

SYNTHESIS, CHARACTERIZATION, AND PHASE STABILITY OF HIGH  
TEMPERATURE THERMOELECTRIC METAL BORIDES AND SILICIDES

by

MALLIKHARJUNA REDDY BOGALA

RAMANA G. REDDY, COMMITTEE CHAIR

SUBHADRA GUPTA

LIN LI

MUHAMMAD A. R. SHARIF

SELVUM PILLAY

A DISSERTATION

Submitted in partial fulfillment of the requirements  
for the degree of Doctor of Philosophy  
in the Department of Metallurgical and Materials Engineering  
in the Graduate School of  
The University of Alabama

TUSCALOOSA, ALABAMA

2016

Copyright Mallikharjuna Reddy Bogala 2016  
ALL RIGHTS RESERVED

## ABSTRACT

Thermoelectric (TE) materials are used for converting waste heat into electricity. The TE technology is attractive because it uses solid-state devices that are immovable, highly reliable, and eco-friendly. Several nations are implementing this renewable technology for processing solar thermal energy into electricity, thereby, it not only reduces the energy costs, but also minimizes the global warming caused due to combustion of natural fuels.

Currently, TE materials have very low conversion efficiencies at higher temperatures and uses expensive elements (Te, Ge, etc.) for TE power generation. Several studies have been conducted on metal borides and silicides as potential TE materials because of their low cost, high thermal stabilities, and good transport properties. In the present study, a preliminary investigation was carried out on selected alkaline earth metal borides ( $\text{CaB}_6$ , and  $\text{SrB}_6$ ) and silicides ( $\text{Mg}_2\text{Si}$  and  $\text{CaSi}$ ) and transition metal borides and silicides of ABX-type ( $A = \text{Ti/ Nb/ Mn}$ ;  $B = \text{Co}$ ;  $X = \text{B/Si}$ ). Screening of the alloys were done based on the available literature/calculations of energy band gaps, crystal structure, transport, and thermodynamic properties.

Experiments were conducted on alkaline earth metal silicides ( $\text{Mg}_2\text{Si}$  and metal-doped  $\text{Mg}_2\text{Si}$ ), transition metal boride ( $\text{TiB}_2$ ), and transition metal silicide ( $\text{Mn}_4\text{Si}_7$ ). The selected alloys were synthesized *via* one-step simple, and fast procedure that involves cold-pressing, sintering, or arc-melting of the elemental mixture under inert argon atmosphere. The samples were characterized using scanning electron microscopy, energy-dispersive spectroscopy, and X-ray diffraction methods.

Thermodynamic properties of the alloys were determined at higher temperatures using differential scanning calorimetry (DSC), differential thermal analyzer (DTA), and EMF cell methods. Reaction kinetics of  $\text{Mg}_2\text{Si}$  and metal-doped  $\text{Mg}_2\text{Si}$  ( $\text{Mg}_2\text{Si}: m\text{X}$ ;  $\text{X} = \text{Ti, Nb, Mn, Co}$ ;  $m = 0 - 0.08 \text{ mol}$ ) were conducted using DTA technique. The reaction mechanism, the effect of metal-dopant on the formation activation energy, and thermal stability of  $\text{Mg}_2\text{Si}: m\text{X}$  were determined. Thermodynamic modelling tools were used to calculate thermodynamic properties and phase equilibria of the alloys. In addition, thermoelectric properties were determined for  $\text{TiB}_2$  and  $\text{Mn}_4\text{Si}_7$ . This research work provide fundamental knowledge on thermodynamic and thermoelectric properties of metal borides and silicides.

## DEDICATION

To my father, mother, sister, brother, and friends for their timely support.

## LIST OF ABBREVIATIONS AND SYMBOLS

$a_x$	Activity of element (X)
$C_p$	Specific Heat
$\Delta H$	Change in Enthalpy
$\Delta G$	Change in Gibbs Energy
$\Delta S$	Change in Entropy
$EMF$	Electromotive Force
$T$	Temperature
$TE$	Thermoelectric
$X_A$	Mole fraction of element A
$ZT$	Figure of Merit
$\alpha/S$	Seebeck coefficient or thermoelectric power or degree of conversion
$\sigma$	Electrical conductivity
$\kappa$	Thermal conductivity
$\eta_{TE}$	Maximum conversion efficiency
$\Pi$	Thermoelectric refrigeration
$\beta$	scan rate or heating rate
$g(\alpha)$	conversion function
$\gamma_x$	Activity Coefficient of element (X)
$\theta_{hkl}$	Diffraction angle of X-rays from (h k l) plane

## ACKNOWLEDGMENTS

I consider this as a great opportunity to acknowledge the faculty members, staff, friends, and colleagues for their help in completion of the research project. I would like to thank my graduate research advisor, and chairman of the dissertation committee, Prof. Ramana G. Reddy, for his guidance, support, and encouragement during my doctoral study at The University of Alabama. I am greatly benefited from his knowledge and experience in research, teaching, and administration, which will remain as tokens of motivation for my future career.

I would like to extend my sincere thanks to all other members of the committee, Prof. Subhadra Gupta, Prof. Lin Li, Prof. Muhammad A. R. Sharif, and Prof. Selvum Pillay for serving in my dissertation supervisory committee. I appreciate for their valuable input, comments, and suggestions on the research work.

I want to thank Prof. Laurentiu Nascac for his generosity in allowing me to use the Differential Thermal Analysis instrument from his research laboratory. This not only helped me to finish the studies in time, but also formed a considerable portion of the current research work.

My sincere thanks to all the past and the current members of Dr. Reddy's research group i.e., Dr. Murali Ramachandran, Dr. Tao Wang, Dr. Hoaxing Yang, Dr. Min Li, Dr. Liang Li, Mr. Jacob Young, Mr. Yuxiang Peng, Mr. Yudong Li, Mr. Andrew Kim, and Mr. Muhammad A. Imam for their help, suggestions, and comments on the research project.

I am grateful to all the technical and administrative staff of Department of Metallurgical and Materials Science Engineering (MTE), and Central Analytical Facility (CAF) at The

University of Alabama. The timely assistance from the engineering and technical staff (Mr. Robert Fanning, Mr. Richard Colquitt, Ms. Kim Clary, Mr. Wade Compton, Mr. Johnny Goodwin, Mr. Rich Martins, and Rob Holler), and the administrative staff (Ms. Jan Creitz, Ms. Susan Noble, and Ms. Kim Walker) are valuable in the completion of this study.

I would like to extend my gratitude to Department of Metallurgical and Materials Engineering, and Center for Materials for Information Technology (MINT) at The University of Alabama for offering me the full-time graduate teaching/research assistantships. In addition, I am thankful for the financial support from the National Science Foundation (NSF) agency, Grant No. DMR-1310072, during the course of the current research project.

Finally, I want to thank my friends and colleagues for their guidance during my stay at The University of Alabama. This research would not have been possible without the support and constant encouragement from my friends, fellow graduate students, and family members.

## CONTENTS

ABSTRACT .....	ii
DEDICATION .....	iv
LIST OF ABBREVIATIONS AND SYMBOLS .....	v
ACKNOWLEDGMENTS .....	vi
LIST OF TABLES .....	xiii
LIST OF FIGURES .....	xv
CHAPTER 1: INTRODUCTION .....	1
1.1 Electricity .....	2
1.1.1 Fossil Fuels .....	2
1.1.2 Global Warming .....	3
1.2 Renewable Energy .....	4
1.2.1 Renewable Energy Sources .....	4
1.2.2 Harvesting of Waste Heat .....	6
1.3 Thermoelectric Technology .....	7
1.3.1 Seebeck Effect .....	8
1.3.2 Peltier Effect .....	9
1.3.3 Thompson Effect .....	10
1.4 Thermoelectric Device .....	12
1.4.1 Figure of Merit .....	14

1.4.2 Conversion Efficiency .....	15
1.5 Thermoelectric Materials .....	17
1.5.1 Seebeck Coefficient .....	18
1.5.2 Electrical Conductivity .....	18
1.5.3 Thermal Conductivity .....	19
1.5.4 ZT vs. Temperature of TE Alloys.....	22
1.5.5 State-of-Art TE Materials .....	26
1.6 Engineering TE Alloys .....	28
CHAPTER 2: LITERATURE REVIEW .....	29
2.1 Boride TE Alloys .....	30
2.1.1 Properties of TE Borides.....	30
2.1.2 Titanium Diboride.....	37
2.2 Silicide TE Alloys.....	40
2.2.1 Properties of TE Silicides .....	40
2.2.2 Magnesium Silicides.....	45
2.2.3 Higher Manganese Silicides .....	47
CHAPTER 3: RESEARCH OBJECTIVES.....	49
CHAPTER 4: MATERIALS AND METHODS .....	51
4.1 Mixing of Powders.....	51
4.2 Pelleting of Mixture .....	52
4.3 Sintering of Pellets.....	53
4.4 Arc-melting of Pellets.....	55
4.5 X-ray Diffraction .....	56

4.6 Scanning Electron Microscopy .....	58
4.7 Energy Dispersive Spectroscopy .....	59
4.8 Thermal Analysis of TE Alloys .....	59
4.8.1 Differential Scanning Calorimetry.....	59
4.8.2 Differential Thermal Analysis .....	61
4.9 Solid-state Galvanic or EMF Cell.....	65
4.10 Thermodynamic Modelling .....	67
CHAPTER 5: A PRELIMINARY STUDY .....	68
5.1 Arrhenius Relation .....	68
5.2 Group (II) Borides and Silicides .....	69
5.3 Log (TE property) vs. 1/T Plots .....	70
5.4 Evaluation of TE Properties.....	72
5.5 Estimation of Efficiencies.....	73
5.6 Comparison of Properties .....	74
5.7 Thermodynamic Calculations .....	75
5.8 Summary of Preliminary Study .....	77
CHAPTER 6: MAGNESIUM SILICIDE.....	78
6.1 Synthesis of Mg <sub>2</sub> Si.....	80
6.2 Characterization of Mg <sub>2</sub> Si.....	82
6.3 Differential Thermal Analysis of Mg <sub>2</sub> Si.....	88
6.3.1 Reaction Kinetics of Mg <sub>2</sub> Si .....	88
6.3.2 Thermal Stability of Mg <sub>2</sub> Si.....	96
6.3.3 Specific Heat Measurement of Mg <sub>2</sub> Si.....	97

6.4 Differential Scanning Calorimetry of Mg <sub>2</sub> Si .....	104
6.4 Thermodynamic Calculations of Mg <sub>2</sub> Si.....	106
6.5 EMF Study of Mg-Si System.....	109
6.6 Summary of Magnesium Silicide Study .....	119
CHAPTER 7: METAL-DOPED MAGNESIUM SILICIDES .....	121
7.1 Synthesis of Metal-doped Mg <sub>2</sub> Si .....	121
7.2 XRD of Metal-doped Mg <sub>2</sub> Si .....	123
7.3 Lattice Constants of Metal-doped Mg <sub>2</sub> Si.....	124
7.4 DTA of Metal-doped Mg <sub>2</sub> Si .....	125
7.4.1 Formation Kinetics of Mg <sub>2</sub> Si: mX.....	125
7.4.2 Thermodynamic Properties of Mg <sub>2</sub> Si:0.08X .....	129
7.5 Summary of Metal-doped Magnesium Silicides Study .....	131
CHAPTER 8: TRANSITION METAL BORIDES AND SILICIDES....	132
8.1 Thermodynamic Study of Borides and Silicides .....	133
8.2 Synthesis of TiB <sub>2</sub> and Mn <sub>4</sub> Si <sub>7</sub> .....	136
8.3 Characterization of TiB <sub>2</sub> and Mn <sub>4</sub> Si <sub>7</sub> .....	136
8.4 Thermoelectric properties of TiB <sub>2</sub> and Mn <sub>4</sub> Si <sub>7</sub> .....	138
8.5 Summary of Transition Metal Borides and Silicides .....	139
CHAPTER 9: CONCLUSIONS AND FUTURE WORK.....	140
9.1 Conclusions.....	140
9.2 Future Work .....	143
REFERENCES .....	145
APPENDIX A.....	159

APPENDIX B .....	161
APPENDIX C .....	164
APPENDIX D .....	167

## LIST OF TABLES

1.1	Global Electricity Generation from Different Types of Renewable Energy Sources .....	6
1.2	Transport Properties of Selected Metals, Semiconductors, and Insulators at 300 K.....	21
1.3	Maximum Figure of Merit and Temperatures Reported for Different Type of TE Alloys.....	24
2.1	A List of Metal Borides and Silicides Studied as TE Materials .....	29
2.2	Properties of $\beta$ -Boron and Some Selected TE Metal Borides at 300 K.....	33
2.3	TE Properties of Polycrystalline $\text{TiB}_2$ obtained from 280 K to 400 K.....	38
2.4	Properties of Some Selected TE Metal Silicides at 300 K.....	40
4.1	Parameters of DSC and DTA Instruments used in Current Study....	64
5.1	Linear relationship of $\ln(P)$ vs. $1/T$ for $\text{CaB}_6$ , $\text{SrB}_6$ , $\text{Mg}_2\text{Si}$ , and $\text{CaSi}$ .....	72
5.2	Thermoelectric Parameters of Borides ( $\text{CaB}_6$ and $\text{SrB}_6$ ) and Silicides ( $\text{Mg}_2\text{Si}$ and $\text{CaSi}$ ) .....	72
5.3	Crystal Structure and Thermodynamic Data of $\text{CaB}_6$ , $\text{SrB}_6$ , $\text{Mg}_2\text{Si}$ , and $\text{CaSi}$ .....	75
6.1	Sintering Parameters (Temperature and Time) of Samples Tested for Synthesis of $\text{Mg}_2\text{Si}$ . .....	81
6.2	A List of Vital Reaction Mechanisms, Kinetic Models, and Conversion Functions, $g(\alpha)$ .....	93
6.3	List of Coats-Redfern Equations for $\text{Mg}_2\text{Si}$ obtained at Different Scan Rates .....	95
6.4	A Comparison of Activation Energies for Formation of $\text{Mg}_2\text{Si}$	

with the Literature Data .....	95
6.5 Conversion Factor $\left[\frac{K_2}{K_2'} = f(T)\right]$ determined using Graphite as Standard Material .....	102
6.6 Specific Heat of Mg <sub>2</sub> Si from DTA Method (This Study) and Literature .....	104
6.7 Change in Gibbs Energy $\Delta G(T)$ and Thermodynamic Properties of Mg <sub>2</sub> Si at 298.15 K .....	108
6.8 EMF Constants A and B obtained from the Straight Lines of $E$ vs. $T$ in Figure 6.18 .....	111
6.9 List of Activities, and Activity Coefficients of Mg and Si for Selected [Mg-Si] <sub>alloy</sub> Compositions at 973 °C .....	116
6.10 A Comparison of Mg Activities, and Enthalpy of Mixing for Mg <sub>0.66</sub> Si <sub>0.33</sub> Composition.....	116
7.1 List of Metal-Doped Magnesium Silicides considered in the Present Study .....	121
7.2 List of Coats-Redfern Equations for Metal-Doped Magnesium Silicides at $\beta = 20$ K/min .....	126
7.3 Thermodynamic Properties given as a Function of Temperature from 473 K to 1073 K.....	130
7.4 Parameters (A, B, C and D) of Thermodynamic Property Functions from Table 7.3 .....	130
8.1 A Comprehensive List of Binary and Ternary Metal Boride and Silicide Alloy Phases .....	133
8.2 Gibbs Energy Function Parameters of Selected Borides .....	135
8.3 Gibbs Energy Function Parameters of Selected Silicides.....	135

## LIST OF FIGURES

1.1	A Plot of Total Energy Consumption and GDP per Captia of 20 Selected Nations.....	1
1.2	Schematic of Electricity Generation Process in a Typical Thermal Power Plant.....	2
1.3	A Pie Chart of Electricity Generation from Fuel Sources in U.S. during Year 2014 .....	3
1.4	Percent CO <sub>2</sub> Emissions by Different Nations of World during 2010 .....	4
1.5	A Schematic of Different Renewable Energy Sources for Electricity Generation .....	5
1.6	Thermoelectric Technology for Waste Heat Recovery from Different Sources .....	7
1.7	Seebeck Effect: Voltage is observed between Hot and Cold Junctions of Metals A and B.....	8
1.8	Peltier Effect: Temperature change due to Voltage across Junctions of Metals A and B.....	10
1.9	Thomson Effect: A Temperature Gradient along <i>X</i> -Direction of a Conducting Wire causes Gradient in Seebeck Coefficient.....	11
1.10	A TE Device displaying Hot and Cold Sides; <i>p</i> - and <i>n</i> -type Elements, Foil, Ceramic Substrate, and +/- Wires.....	12
1.11	A Thermoelectric Couple showing Current ( <i>I</i> ) Flow, Charge Carriers in <i>n</i> -type ( <i>e</i> <sup>-</sup> ), and <i>p</i> -type ( <i>h</i> <sup>+</sup> ) Elements.....	13
1.12	TE Module from Marlow Industries Inc., (a) Before and (b) After opening AlN Plates; showing Bi <sub>2</sub> Te <sub>3</sub> Elements.....	14
1.13	Variation of Maximum Conversion Efficiency, $\eta_{TE}$ (%), with Temperature ( $T_h$ ); $ZT = 1.0 - 4.0$ , and $T_c = 300$ K .....	16
1.14	Variation of TE Properties ( $\alpha$ , $\sigma$ , $\kappa$ , $\alpha^2\sigma$ , and $ZT$ ) with	

Concentration ( $n_i$ ) for Insulators, Semiconductors and Metals.....	17
1.15 Variation of Thermal Conductivities ( $\kappa$ , $\kappa_e$ , and $\kappa_l$ ) with Carrier Concentration ( $n_i$ ) for Insulators, Semiconductors and Metals.....	20
1.16 Figure of Merit (ZT) of some Existing TE Alloys at Different Temperatures.....	22
1.17 Abundance of Elements in the Earth's Crust.....	26
2.1 Crystal Structures of Unit Cell: (a) $\beta$ -Boron, and Multiple Unit Cell: (b) $\text{CaB}_6$ , (c) $\text{YbB}_6$ , and (d) $\text{SmB}_6$ .....	31
2.2 Effect of Temperature on (a) Seebeck Coefficient, and (b) Electrical Conductivity of $\beta$ - Boron, and Metal Borides .....	34
2.3 Effect of Temperature on (a) Thermal Conductivity, $\kappa$ and (b) Figure of Merit, ZT of $\text{CaB}_6$ , $\text{SrB}_6$ , and $\text{BaB}_6$ .....	36
2.4 Multiple Unit Cell Crystal Structure of $\text{TiB}_2$ .....	37
2.5 Calculated (a) Energy Band Structure, and (b) Density of States (DOS) of $\text{TiB}_2$ .....	39
2.6 Crystal Structures of Unit Cell: (a) $\text{Mg}_2\text{Si}$ , (b) $\text{MnSi}_{1.7}$ , (c) $\beta$ - $\text{FeSi}_2$ , and Multiple Unit Cell: (d) $\text{ReSi}_{1.75}$ , and (e) $\text{CoSi}$ .....	41
2.7 Effect of Temperature on (a) Seebeck Coefficient, and (b) Electrical Conductivity of Metal Silicides.....	42
2.8 Effect of Temperature on (a) Thermal Conductivity ( $\kappa$ ), and (b) ZT of $\text{Mg}_2\text{Si}$ , $\text{CrSi}_2$ , $\text{MnSi}_{1.73}$ , $\beta$ - $\text{FeSi}_2$ , $\text{CoSi}$ , and $\text{Ru}_2\text{Si}_3$ .....	44
2.9 Effect of Metal-doping on ZT of $\text{Mg}_2\text{Si}$ at Different Temperatures.....	45
2.10 Calculated (a) Energy Band Structure, and (b) Density of States (DOS) of $\text{Mg}_2\text{Si}$ .....	46
2.11 Formation of Nowotny Chimney Ladder Crystal Structure of $\text{Mn}_4\text{Si}_7$ , and Four HMS Phases with their Relative Size .....	47
2.12 Calculated (a) Energy Band Structure, and (b) Density of States (DOS) of $\text{Mn}_4\text{Si}_7$ .....	48
3.1 A Schematic Outlining the Specific Tasks of Current Research Project .....	50

4.1	An Image of Labconco Glove Box used for Mixing of Metal Powders.....	52
4.2	An Image of (a) Carver Press, and (b) Schematic of Pelleting the Metal Powders.....	53
4.3	An Image of (a) Fischer Scientific furnace, and (b) Schematic of Pellet Sintering.....	54
4.4	Images of (a) electric arc furnace, (b) bell jar chamber, and (c) schematic of the furnace.....	55
4.5	Principle of (a) XRD, and (b) Image of X'Pert MPD used in Current Study.....	57
4.6	Image of (a) JEOL 7000F SEM, and (b) Working Principle of SEM for Sample Analysis.....	58
4.7	Image of (a) Pyris Diamond PerkinElmer DSC, and (b) Schematic of DSC Apparatus.....	59
4.8	Image of (a) Linseis PT 1600 DTA, and (b) Schematic of DTA Furnace.....	62
4.9	An Image of PerkinElmer DTA7 with a Blow-up View of Ref. & Sample Crucibles & DTA calibration curve of Al standard.....	63
4.10	A Schematic of (a) EMF Cell, and (b) Blow-up View of Cell Assembly, and (c) Image of Experimental Set-up.....	65
5.1	A Flow Chart of the Procedure Used to Evaluate the TE Properties from Arrhenius Relation.....	69
5.2	Plots of $S$ , $\sigma$ , $\kappa$ and $ZT$ vs. Temperature ( $T$ ) for Borides (■CaB <sub>6</sub> , & ●SrB <sub>6</sub> ) and Silicides (▲Mg <sub>2</sub> Si, & ▼CaSi).....	70
5.3	$\ln(P)$ vs. $1/T$ ( $-S$ , $\sigma$ , $\kappa$ & $ZT$ ) of Data (■CaB <sub>6</sub> , ●SrB <sub>6</sub> , ▲Mg <sub>2</sub> Si, & ▼CaSi) and Fit (●●●CaB <sub>6</sub> , ●●●SrB <sub>6</sub> , ●●●Mg <sub>2</sub> Si, & ●●●CaSi).....	71
5.4	$S$ , $\sigma$ , $\kappa$ and $ZT$ vs. $T$ for Data (■CaB <sub>6</sub> , ●SrB <sub>6</sub> , ▲Mg <sub>2</sub> Si, & ◆CaSi) & Predicted (●●●CaB <sub>6</sub> , ●●●SrB <sub>6</sub> , ●●●Mg <sub>2</sub> Si, & ●●●CaSi).....	73
5.5	A Plot of Efficiency ( $\eta_{TE}$ ) vs. $T$ for Borides (■CaB <sub>6</sub> , & ●SrB <sub>6</sub> ) & Silicides (▲Mg <sub>2</sub> Si, & ▼CaSi).....	74
5.6	Gibbs Energy at Different Temperatures for ▲Mg <sub>2</sub> Si, ■CaB <sub>6</sub> , & ▼CaSi.....	76

5.7	Activities of B in Ca-B and Sr-B and Si in Mg-Si and Ca-Si Solid Solutions at 1000 K .....	77
6.1	Binary Phase Diagram of Mg-Si System obtained at 1 bar using FactSage 6.3 .....	79
6.2	A Schematic showing the Experimental Procedure for Synthesis of Mg <sub>2</sub> Si Powder .....	81
6.3	Images of (2Mg + Si) and Mg <sub>2</sub> Si Pellets before & after Sintering at 500 °C and 5 min .....	82
6.4	XRD Spectra of (a) 2Mg + Si & (b) Mg <sub>2</sub> Si Powders from Sintering at 500 °C for 5 min .....	83
6.5	SEM Image of Mg <sub>2</sub> Si Powder obtained from Sintering at 500 °C for 5 min.....	84
6.6	SEM and Particle Size Distribution of (a) Mg, (b) Si, and (c) Mg <sub>2</sub> Si Samples .....	85
6.7	Image of (a) Mg <sub>2</sub> Si Suspension after Ultrasonication, & (b) High Magnification SEM Image displaying Mg <sub>2</sub> Si Nanoparticles.....	86
6.8	A Schematic illustrating Ultra-sonication Mediated conversion of Mg <sub>2</sub> Si Aggregates/agglomerates to NanoMg <sub>2</sub> Si .....	87
6.9	EDS Spectrum of Mg <sub>2</sub> Si Powder obtained from Sintering at 500 °C for 5 min.....	87
6.10	DTA Heat Flow vs. Temperature of (2Mg + Si) Mixture at Different Scan Rates .....	89
6.11	DTA Heat Flow vs. Time Plot of (2Mg + Si) Mixture at Different Scan Rates .....	90
6.12	Ln( $\beta$ ) vs $-1.0516/RT_{max}$ (Ozawa Equation) Plot for the Formation of Mg <sub>2</sub> Si. ....	91
6.13	Ln( $\beta/T_{max}^2$ ) vs $-1/RT_{max}$ (KAS Equation) Plot for the Formation of Mg <sub>2</sub> Si. ....	92
6.14	Ln [(g ( $\alpha$ )/T <sup>2</sup> ] vs. $-1/RT$ (CR Equation) Plot for the Formation of Mg <sub>2</sub> Si. ....	94
6.15	DTA Curve of Mg <sub>2</sub> Si obtained from Sintering at 500 °C for 5 min. ....	96

6.16 A Schematic of Cross-sectional View of Linseis PT1600 DTA Furnace .....	97
6.17 DTA Heat Flow Measurements of Graphite using Mass Difference Baseline Method .....	99
6.18 DTA Heat Flow Measurements of Mg <sub>2</sub> Si using Mass Difference Baseline Method .....	103
6.19 Specific Heat vs T plot of Mg <sub>2</sub> Si obtained from DTA, DSC, HSC, and Literature .....	105
6.20 Change in Gibbs Energy vs. Temperature for Mg <sub>2</sub> Si obtained at 500 °C and 5 min.....	108
6.21 A Schematic displaying the Procedure for Preparation of EMF Electrodes. ....	109
6.22 A Plot of EMF vs. Temperature for Different Compositions of Mg-Si System. ....	111
6.23 XRD Plots of Reference Electrode of Mg <sub>0.66</sub> Si <sub>0.33</sub> (a) Before & (d) After the EMF Experiment.....	112
6.24 XRD Plots of Working Electrode of Mg <sub>0.66</sub> Si <sub>0.33</sub> (a) Before and (d) After the EMF Experiment. ....	113
6.25 An Overlay of Calculated and Experimental Activities of Mg-Si System at 973 °C.....	115
6.26 A Plot of Gibbs Energy of Mixing ( $\Delta G^M$ ) vs. X <sub>Si</sub> of Mg-Si System at 973 °C.....	117
6.27 A Plot of Enthalpy of Mixing ( $\Delta H^M$ ) vs. X <sub>Si</sub> of Mg-Si System at 973 °C.....	118
7.1 A Flow Chart of the Procedure used to Synthesize TE Alloys in Current Study .....	122
7.2 Images of (a) (2Mg + Si + mTi) Pellets, and (b) Mg <sub>2</sub> Si: mTi Powders Before and After Sintering at 773 - 873 K for 5 min.....	122
7.3 XRD of Mg <sub>2</sub> Si: mX; X = (a) Ti, (b) Mn, (c) Nb, and (d) Co, m = 0 - 0.08 mol.....	123
7.4 Lattice Constant vs. % Atomic Fraction of Dopant (X) Plot of Mg <sub>2</sub> Si: mX; X = (a) Ti, (b) Mn, (c) Nb, and (d) Co.....	124
7.5 DTA Curves of (2Mg + Si + mX); X = (a) Ti, (b) Mn, (c) Nb,	

and (d) Co at 20 K/min .....	125
7.6 Formation Activation Energy vs. Dopant Moles of (a) Mg <sub>2</sub> Si: mTi, and (b) Mg <sub>2</sub> Si: mCo.....	127
7.7 Formation Activation Energy vs. Dopant Moles of (a) Mg <sub>2</sub> Si: mNb, and (b) Mg <sub>2</sub> Si: mMn .....	128
7.8 DTA Curves of Un-doped Mg <sub>2</sub> Si, & Mg <sub>2</sub> Si:0.08X; X = Ti, Nb, Mn & Co at 20 K/min .....	129
8.1 Schematic of Transition Metal Boride/Silicide System Considered in the Current Study.....	132
8.2 Change in the Gibbs energy of Selected (a) Borides, and (b) Silicides .....	134
8.3 XRD Spectrum and Image of (a) TiB <sub>2</sub> and (b) Mn <sub>4</sub> Si <sub>7</sub> obtained by Arc-Melting Method .....	137
8.4 TE Properties (a) S, (b) $\sigma$ , (c) $\kappa$ and (d) ZT of TiB <sub>2</sub> , and Mn <sub>4</sub> Si <sub>7</sub> .....	138

# CHAPTER 1

## INTRODUCTION

Energy is very essential for human life. There is a huge demand for energy across the world. By the year 2035, the estimated global demand for energy reaches to 770 quadrillion British thermal units (Btu). Figure 1.1 shows the plot of total energy consumption, and GDP per capita of 20 selected nations in year 2010. Evidently, the nations with higher energy consumption are wealthier countries. Hence, the economy of a nation is directly related to its energy consumption.

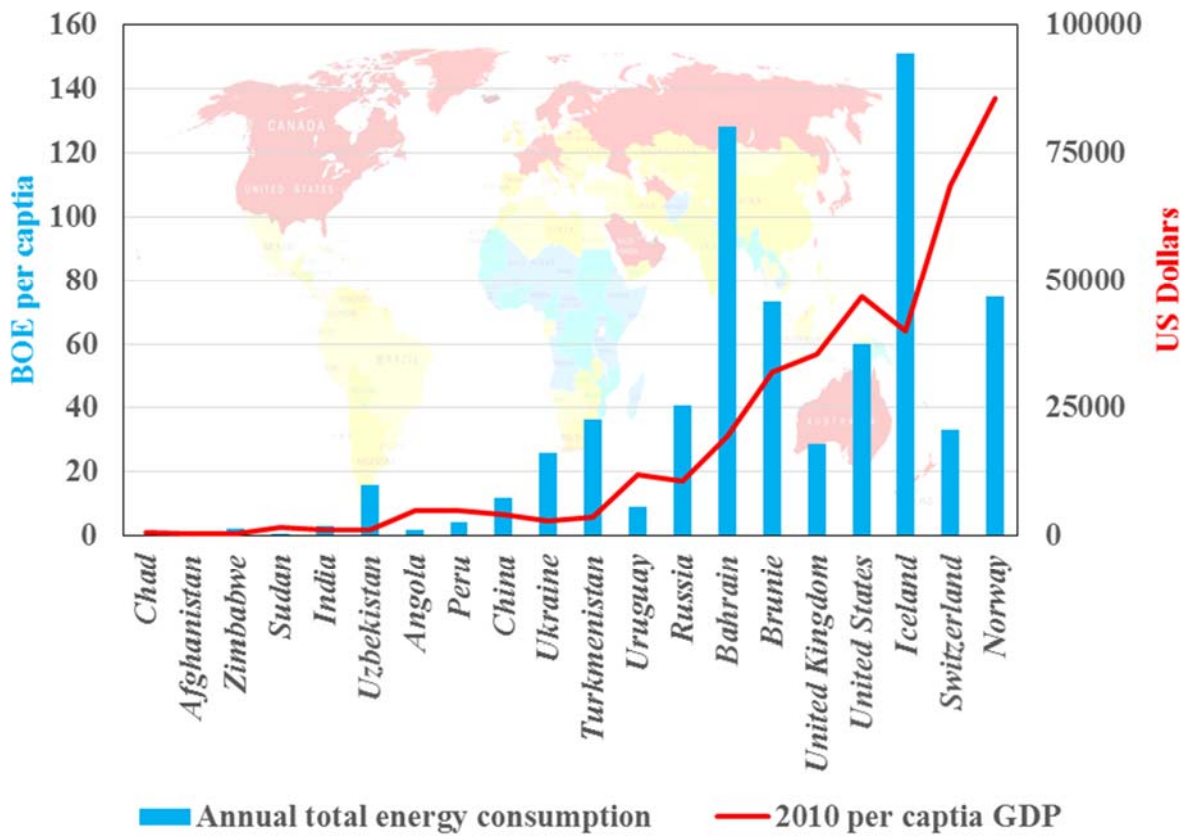


Figure 1.1 A Plot of Total Energy Consumption and GDP per Capita of 20 Selected Nations [1]

## 1.1. Electricity

About 90% of the U.S's electricity is generated from thermal energy of power plants, which is obtained through combustion of natural resources like coal, nuclear, natural gas, and oil. Conventionally, the thermal energy is produced from combustion of fossil fuels in heat engines [2]. The extracted heat is used to raise the steam from water and the thermal energy of steam is converted to kinetic energy in steam turbines. The rotary electrical generators of power plants transform the mechanical energy of steam turbines into electrical energy. Figure 1.2 shows the schematic of the process for electricity generation from burning coal in a thermal power plant.

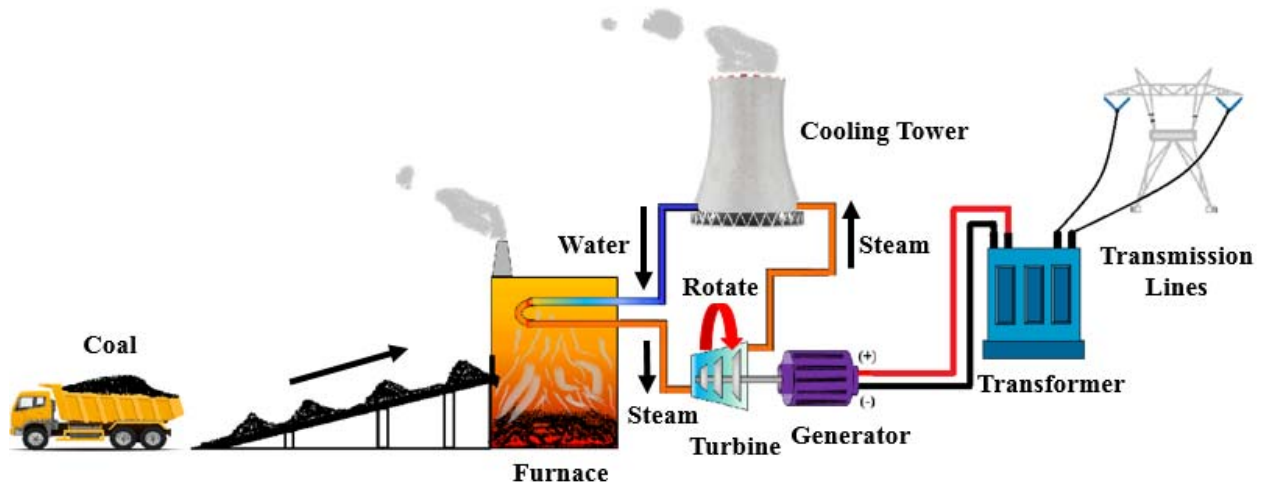


Figure 1.2 Schematic of Electricity Generation Process in a Typical Thermal Power Plant [2].

### 1.1.1. Fossil Fuels

According to the annual energy outlook (AEO) 2015 report, published by U.S. energy information administration (USEIA), the total electricity usage increases from 3,836 billion kilowatt hours (BkW.h) in 2013 to 4,797 BkW.h in 2040, at an average rate of 0.8% per year [3].

About 68% of the required electricity is produced from burning of fossil fuels (coal, natural gas and petroleum products). Figure 1.3 displays the pie chart of total electricity generated in U.S.

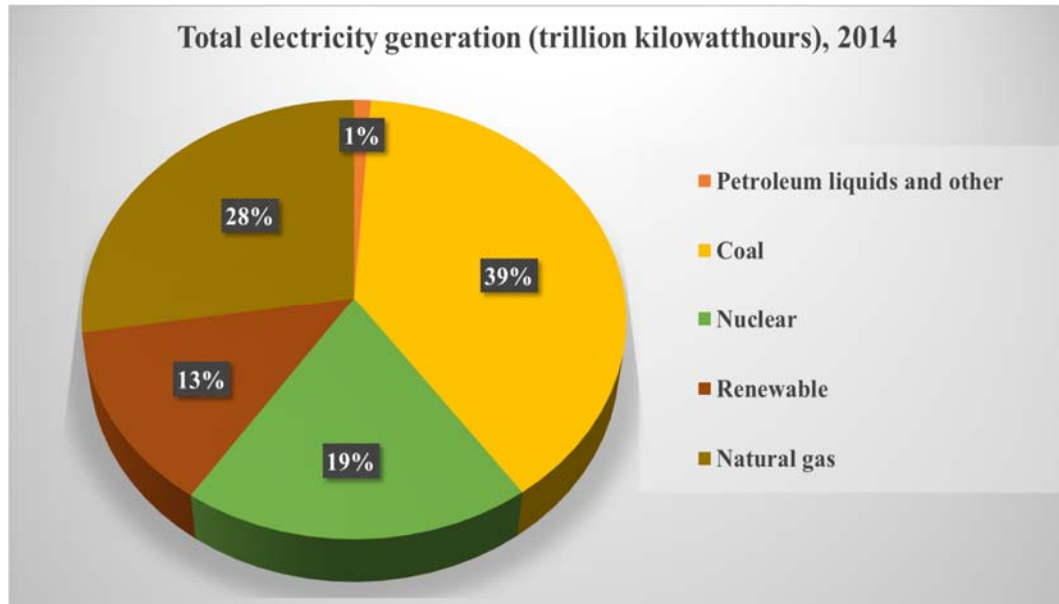


Figure 1.3 A Pie Chart of Electricity Generation in U.S. from Fuel Sources during 2014.

during the year 2014 from different energy sources. However, the energy-associated CO<sub>2</sub> emissions in the world are projected to increase from 30.2 billion metric tons (BMt) in 2007 to 43.2 BMt in 2035 [3].

### 1.1.2. Global Warming

The burning of fossil fuels results in the emission of greenhouse gases (carbon dioxide, CO<sub>2</sub>) into earth's atmosphere [4]. The CO<sub>2</sub> gas promotes the absorption and emission of infrared radiation in the atmosphere, which causes global warming and a climate change at the earth's surface. Figure 1.4 displays bar graph of percentage CO<sub>2</sub> emissions from different countries of the world in 2010 [4]. Developing nations, like China and India, which still depends on the fossil fuels, as main energy source, are new big contributors for the increase in global CO<sub>2</sub> emissions. Whereas, developed nations such as U.S., EU, Russia, and Japan have significant amount of emissions per capita and therefore, these countries account for higher fossil fuel consumption per person.

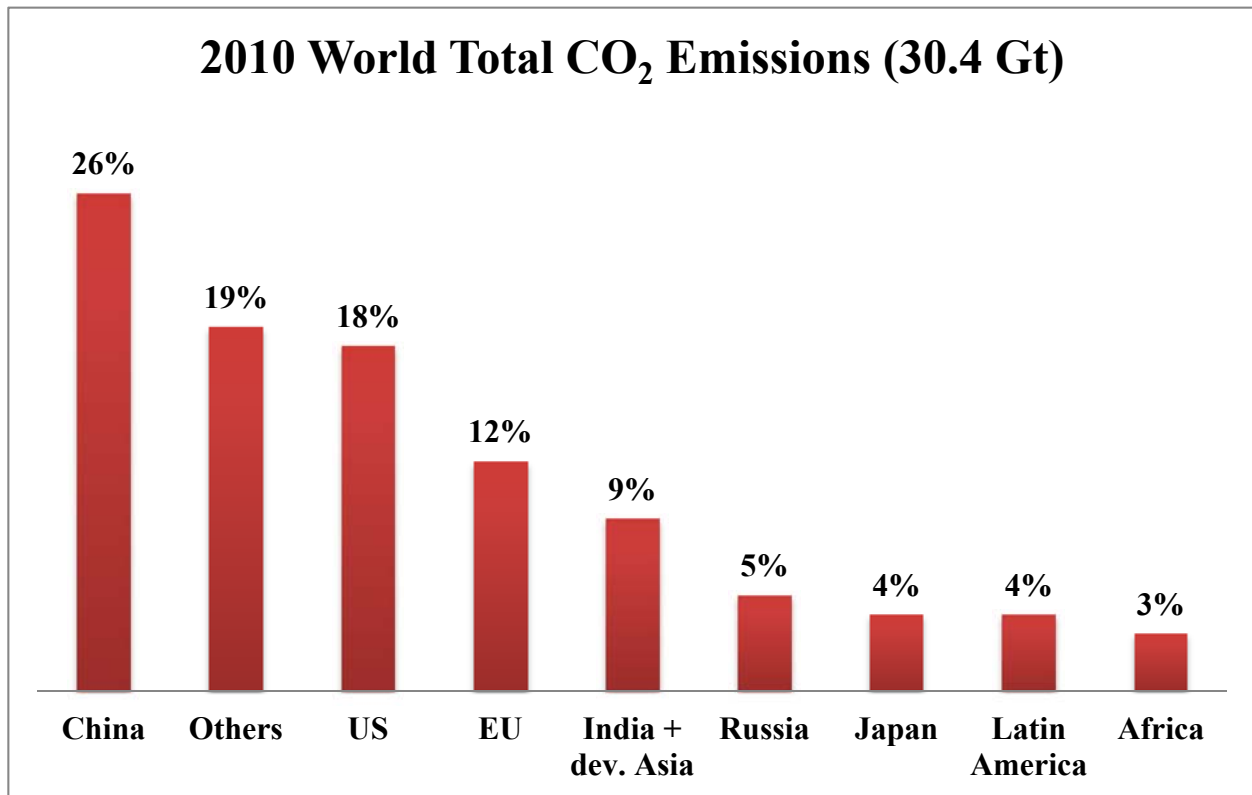


Figure 1.4 A Bar Graph of Percent CO<sub>2</sub> Emissions by Different Nations of World during 2010.

## 1.2. Renewable Energy

Because of the problems associated with the increase in global warming, change in climate, and depletion of natural resources, there is a need to discover and develop renewable energy technologies for addressing these issues. The primary advantages of using renewable energy technologies are: (a) decrease in the energy costs, (b) reduction of the CO<sub>2</sub> emissions, (c) minimization of the global warming and climate change, and (d) conservation of the natural resources. Therefore, the renewable energy is good for both human progress and environment.

### 1.2.1. Renewable Energy Sources

Renewable energy not only substitutes fossil fuels for electricity generation, but also used in other applications like air and water heating/cooling, motor biofuels, and rural energy off-grid

services [5]. Unlike fossil fuels, the renewable energy sources are spread across wide geographical areas, and are not limited to fewer nations. The main renewable energy sources are (1) solar energy, (2) biomass, (3) wind, (4) ocean, (5), geothermal, and (6) hydropower [6]. Figure 1.5 shows the electricity generation from different renewable energy sources.



Figure 1.5 Schematic showing Different Renewable Energy Sources for Electricity Generation.

The global electricity generation from the renewable energy sources is likely to increase 2.7 times from 2010 to 2035. Table 1.1 shows different types of renewable energy resources, the amount of electricity generated in 2010, and the projections for 2020 and 2035 [7].

Although a significant progress have been made in renewable energy technologies, approximately 59% of the total energy in U.S. is lost to the surroundings as thermal energy such as waste heat from industrial process (steel, Al and glass) and vehicle exhaust (automobiles) [8].

Hence, there is a need for the discovery and development of processing technologies that converts waste heat to electricity.

Table 1.1 Global Electricity Generation from Different Types of Renewable Energy Sources.

Renewable energy sources	Electricity (TW.h)		
	2010	2020	2035
Solar energy	34	382	824
Biomass	331	696	1,487
Wind	342	1,272	2,681
Ocean	1	5	57
Geothermal	68	131	315
Hydropower	3,431	4,513	5,677
Electricity generation	4,207	6,999	11,341
% Share of total electricity	20%	25%	31%

### 1.2.2. Harvesting of Waste Heat

The main sources of waste heat in industries are hot combustion gases, heated products, and heated equipment surfaces. Some examples include glass melting furnace, cement kiln, furnace incinerator, Al reverbaratory furnace, boilers, steel electric-arc furnace, reactors, hot cokes, blast furnace slags, air compressors, separators, internal combustion engines, dryers, motors, pumps, and heat exchange pipes [9]. A considerable amount (20 - 50%) of total industrial energy consumption is lost in the form of waste heat. Although some heat losses in the industries are uncontrollable, certain amount of the dissipated heat can be retrieved/recovered through installation of the waste heat recovery units. As a result, the industries are benefited from lowering of the operation costs, improvement of the efficiencies, and increase in the energy savings.

### 1.3. Thermoelectric Technology

Several heat recovery technologies have been investigated to recover waste heat from the industries. They involve components such as regenerators, piezoelectric devices, recuperators, thermoelectric generators, waste heat boilers, thermionic modules, and economizers [9]. The conventional methods involve power cycles, such as Rankine cycle and Kalina cycle, which converts waste heat to mechanical energy, and eventually to electrical energy [9]. Whereas, the newly developed technologies convert waste heat to electrical energy directly, without involvement of any intermediate processes. These heat recovery units contain piezoelectric (PE), thermionic, and thermoelectric (TE) devices [9]. The PE devices are applicable for low-temperature (100 - 150 °C) heat conversion, while thermionic modules are suitable for high-temperature (> 1000 °C) applications. The conversion efficiencies of PE devices are low, and due to their high manufacturing costs, these devices are limited to fewer applications. The thermionic

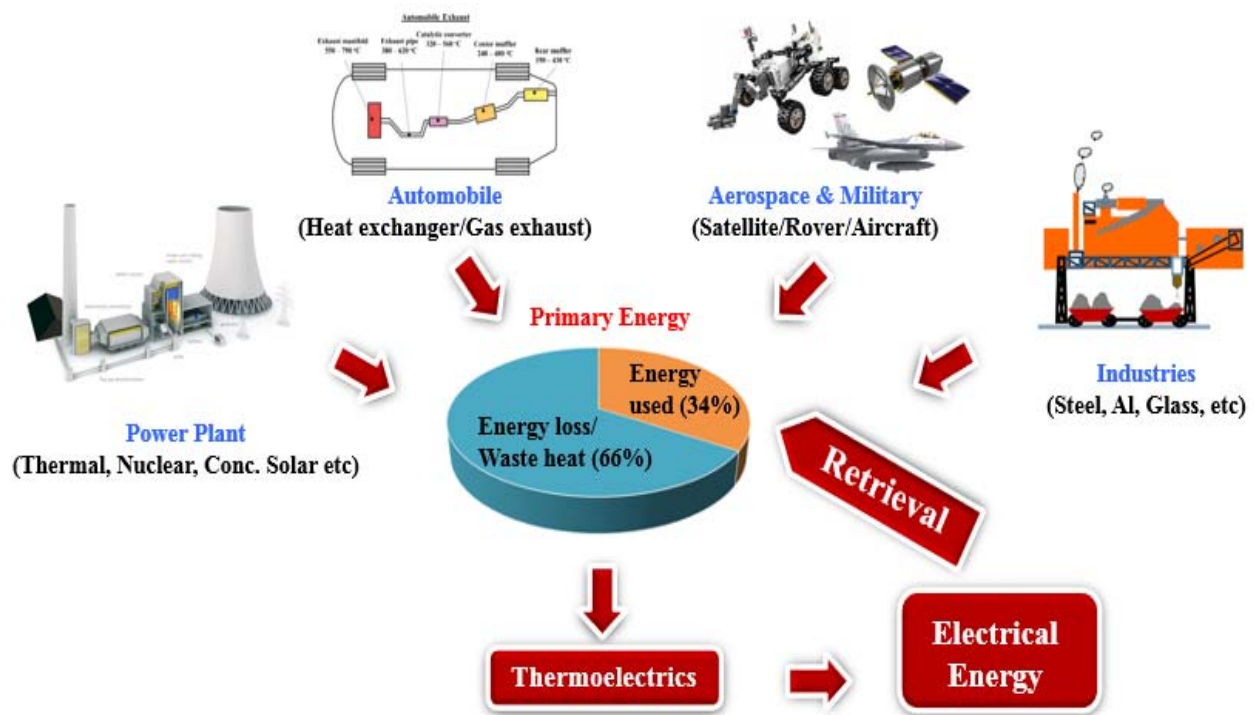


Figure 1.6 Thermoelectric Technology for Waste Heat Recovery from Different Resources.

modules operate under high vacuum conditions, and are not suitable for medium-temperatures of industrial processes. The TE devices are very attractive because of their ability to operate at all temperatures i.e., low-temperatures ( $< 300\text{ }^{\circ}\text{C}$ ), medium-temperatures ( $300 - 600\text{ }^{\circ}\text{C}$ ), and high-temperatures ( $600 - 1200\text{ }^{\circ}\text{C}$ ). The TE materials comprises of wider class of alloys with different thermal and electrical properties. As shown in Figure 1.6, the TE technology is a promising method for electricity generation from waste heat in automobile, aerospace, military and other industries.

The TE technology relates to three separate phenomena: Seebeck effect, Peltier effect, and Thomson effect. Although the underlying principles of TE devices have been known to the scientists for more than 150 years, the development and wider applications of the TE devices only started in 1900s, due to the advancements in new material synthesis and processing methods.

### 1.3.1. Seebeck Effect

In 1821, a Baltic German physicist, Thomas Johann Seebeck, discovered that the needle of a magnetic compass deflected due to the electromotive force or thermoelectric voltage generated from the temperature difference between the junctions of a closed loop formed from two dissimilar metals [10]. Figure 1.7 shows the principle of Seebeck effect. Different metals respond in different ways to the temperature gradients and thus, produces different current loops and magnetic fields.

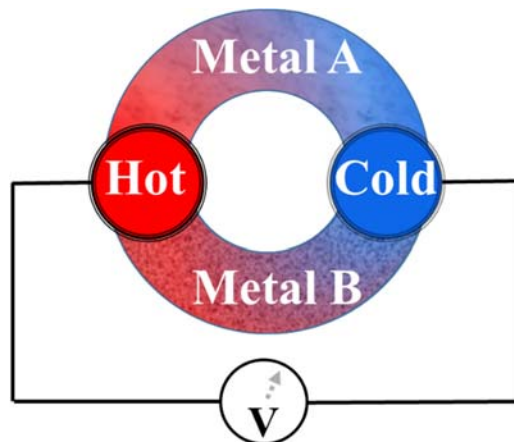


Figure 1.7 Seebeck Effect: Voltage is observed between Hot & Cold Junctions of Metals A & B.

Initially, Seebeck mistakenly believed that the voltage is mainly due to the magnetic fields and did not recognize the involvement of currents from the loop, and so he called the phenomenon as ‘thermomagnetic effect’. Later, a Danish physicist, Hans Christian Ørsted, found that the current is due to thermally induced voltage and thus, coined the term ‘thermoelectricity’. In 1851, Lord Kelvin further explored this phenomenon in semiconductors, and extended the ‘Seebeck effect’ to other non-metals [11]. Also, the ‘Seebeck effect’ is the basic working principle of a thermocouple.

The thermoelectric voltage generated in the closed circuit of Figure 1.6 is called ‘Seebeck electromotive force’. The electric potential gradient ( $\nabla V$ ) is directly proportional to the temperature gradient ( $\nabla T$ ) between the hot and cold junctions, and depends on the type of materials connected to form the closed circuit. The negative ratio of potential gradient ( $\nabla V$ ) and temperature gradient ( $\nabla T$ ) is known as ‘Seebeck coefficient ( $\alpha$ )’ and is given by equation (1.1) [12].

$$\alpha = - \frac{\nabla V}{\nabla T} \quad (1.1)$$

The Seebeck coefficient is an intrinsic property of a given material, and is also denoted by the symbol ‘ $S$ ’ with S.I units of  $\mu V/K$ . In general, if the hot side of the junction contain positive charge, then the sign of ‘ $S$ ’ is negative. The value of ‘ $S$ ’ for metals ( $\sim 10 \mu V/K$ ) is small, while compared with the value of ‘ $S$ ’ for semiconductors ( $\sim 100 \mu V/K$ ).

### 1.3.2. Peltier Effect

In 1834, a French physicist, Jean-Charles-Athanase Peltier, discovered the reverse phenomenon of Seebeck effect, known as ‘Peltier effect’ i.e., a temperature difference is created between the junctions of two dissimilar materials with the application of potential difference across the junctions [13]. Figure 1.8 show Peltier effect observed at the junctions of two dissimilar metals.

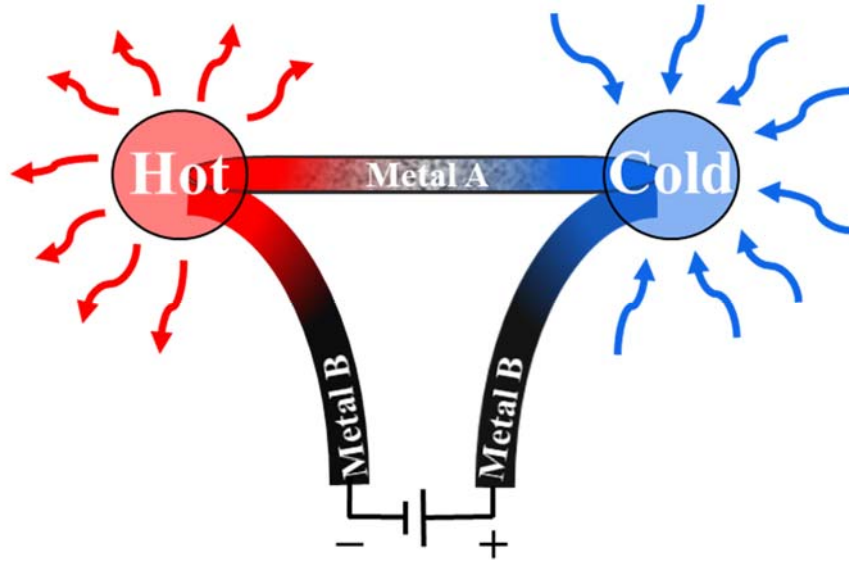


Figure 1.8 Peltier Effect: Temperature change due to Voltage across Junctions of Metals A & B.

Heating or cooling of the junction(s) occurs depending on the direction of current flow and the type of materials. The rate ( $Q_p$ ) of heating or cooling at the junction is proportional to the amount of current ( $I$ ) flowing through the metals, and is given by equation (1.2) [12, 14].

$$Q_P = (\Pi_A - \Pi_B)I = \Pi_{AB}I \quad (1.2)$$

where  $\Pi_A$ , and  $\Pi_B$  are Peltier coefficients of metals A and B and  $\Pi_{AB}$  is relative Peltier coefficient of metals A and B. Peltier effect is widely used in TE refrigeration, IR detector cooling, etc.

### 1.3.3. Thomson Effect

The value of Seebeck coefficient changes with the temperature in many materials. As a result of the spatial gradient in temperature of a material, a gradient in Seebeck coefficient also occurs along three-dimensions (3-D) of the material. Thomson effect was observed by William Thomson (Lord Kelvin) in 1851 [11]. Thomson effect is applicable to all heating or cooling materials with temperature gradient in space, which results from the flow of current through them.

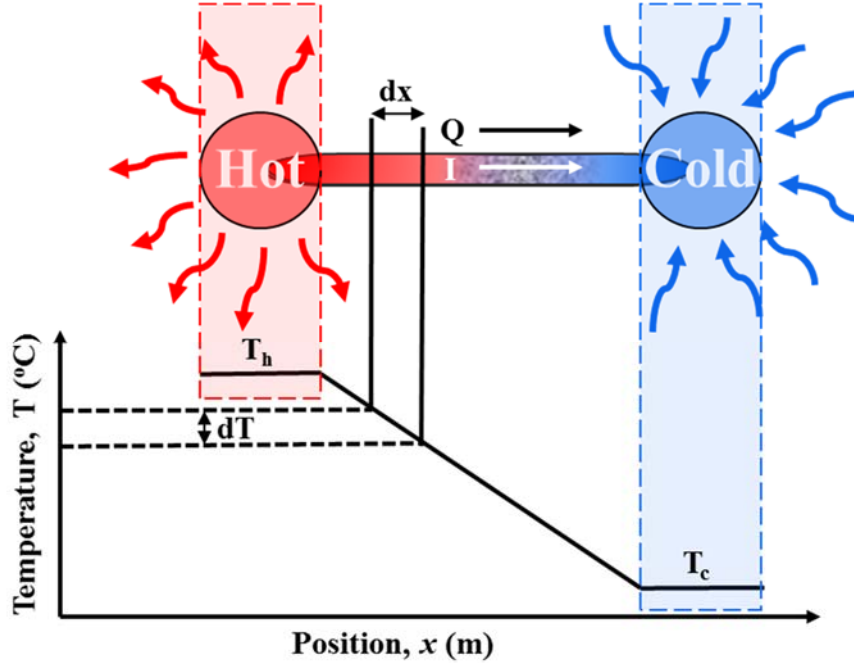


Figure 1.9 Thomson Effect: A Temperature Gradient along  $X$ -direction of a Conducting Wire causes a Gradient in the Seebeck Coefficient.

For a 1-D homogeneous material, the gradient of heat flux ( $dQ/dx$ ) is given by equation (1.3) as:

$$\frac{dQ}{dx} = \tau_{th} I \frac{dT}{dx} \quad (1.3)$$

where  $I$  is the current,  $\tau_{th}$  is the Thomson coefficient, and  $dT/dx$  is the temperature gradient along the  $x$ -dimension of the material. The sign of gradient of heat flux is positive or negative depending on the direction of flow of electrical current ( $I$ ) in the material. Figure 1.9 shows the schematic of Thomson effect in a wire. Unlike Seebeck or Peltier coefficients, Thomson coefficient is directly measured for a given material. The Seebeck, Peltier, and Thomson coefficients are interdependent, and the relationship for a closed loop of metals A and B is given by equation (1.4).

$$\tau_A - \tau_B = \frac{\pi_{AB}}{\alpha_{AB}} \times \frac{d\alpha_{AB}}{dT} \quad (1.4)$$

The above equation (1.4) gives the fundamental connection between thermoelectric power generation ( $\alpha$ ), and thermoelectric refrigeration ( $\Pi$ ) of a TE device.

#### 1.4. Thermoelectric Device

Thermoelectric devices or thermoelectric modules are used for inter-conversion of energy i.e., thermal energy to electrical energy or electrical energy to thermal energy. Thus, the TE devices operate not only in the power generation mode, but also in the refrigeration mode. Figure 1.10 depicts the schematic of a typical TE device and respective components. The temperature gradient is introduced between the hot and cold sides of a TE device. These two substrate plates are made-up of ceramic material such as AlN. An array consisting of *p*-type and *n*-type semiconducting segments are sandwiched between the ceramic substrates of TE device [16]. These segments are inter-connected electrically in series, and thermally in parallel by conducting foil/strips, made-up

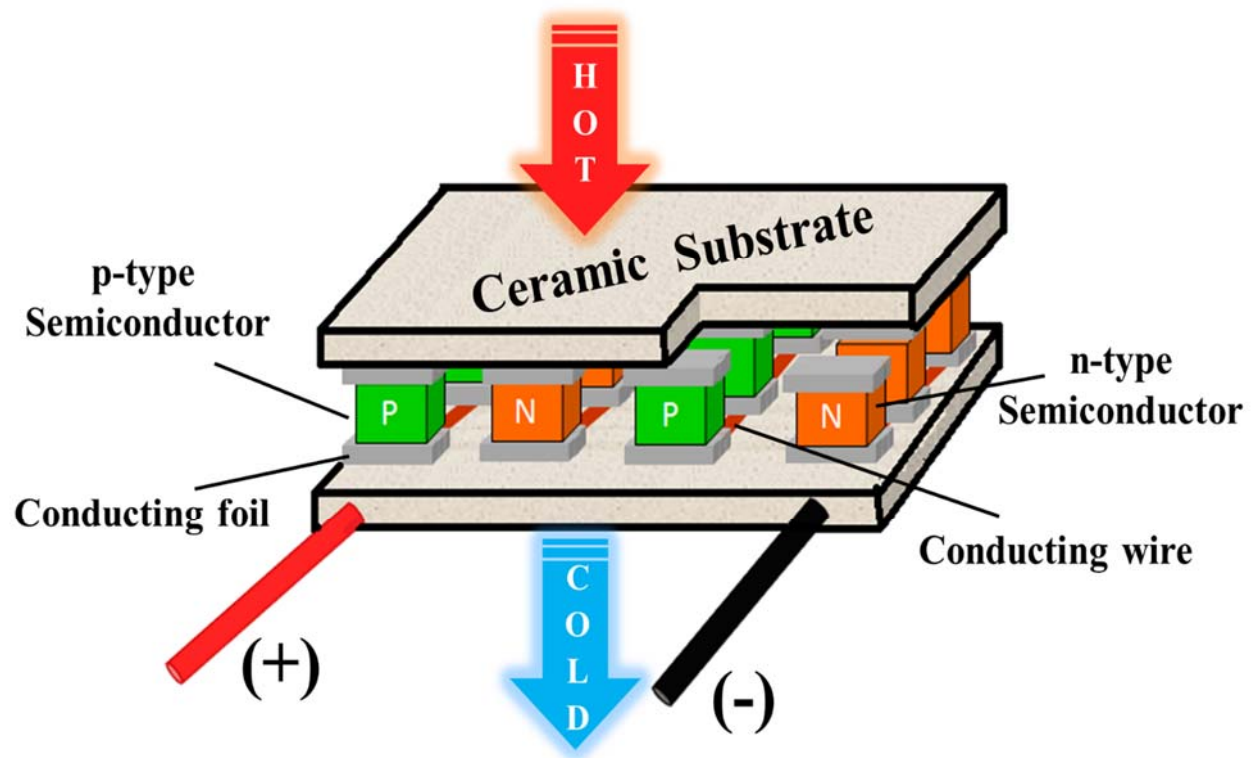


Figure 1.10 A TE Device displaying Hot and Cold Sides; *p*- and *n*-type Elements, Foil, Ceramic Substrate, and +/- Wires [15].

of metals like Cu or Ni. Basically, each connected pair of the  $p$ -type and  $n$ -type semiconducting segments serves as a ‘thermocouple’. Thus, both the Seebeck effect and the Peltier effect can be realized with such a configuration. The temperature difference between the hot and cold sides of a TE device establishes the Seebeck voltage. The  $p$ -type and  $n$ -type semiconducting segments have positive and negative Seebeck coefficients respectively. As a result, the type, the concentration, and the mobility of carriers also differ for each element. Holes ( $h^+$ ) are the main carriers in  $p$ -type semiconductors, while electrons ( $e^-$ ) are the predominant charge carriers in  $n$ -type semiconductors. As shown in Figure 1.11,  $p$ -type and  $n$ -type semiconducting segments are joined together to form a TE couple. Both, holes and electrons flow from the hot side to the cold side of a TE device, thus establishing electric voltage in the circuit. Figure 1.12 show the images of actual TE module from Marlow Industries Inc. that contain silver-colored bismuth telluride semiconducting elements.

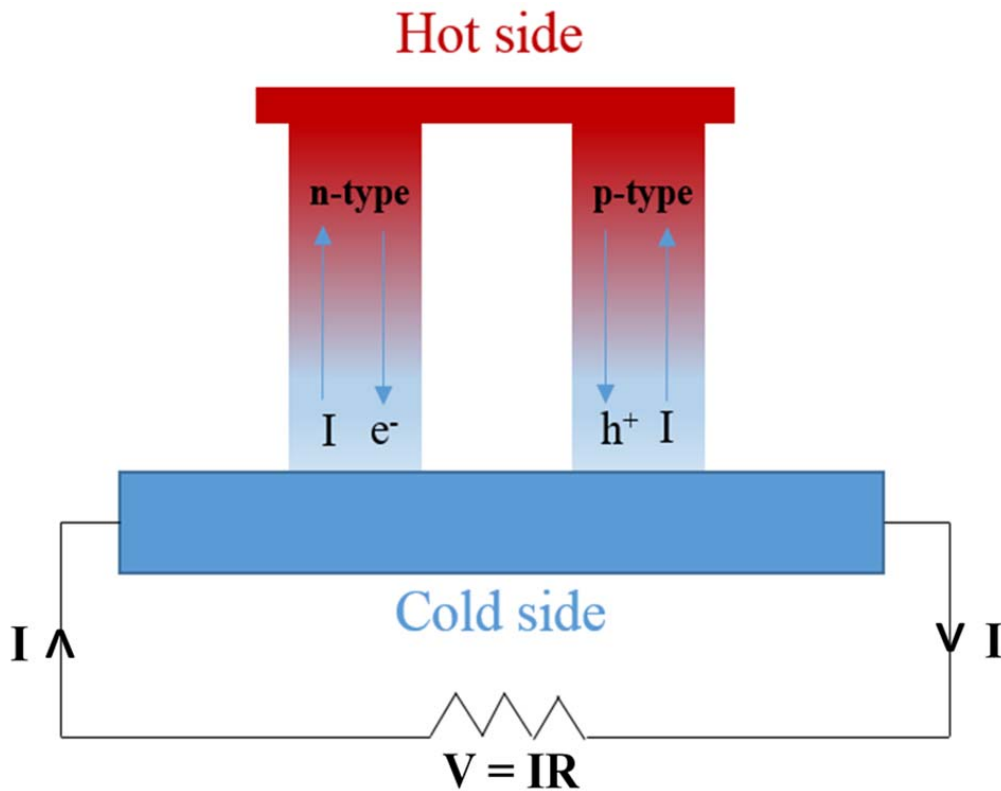


Figure 1.11 A Thermoelectric Couple showing Current ( $I$ ) Flow, Charge Carriers in  $n$ -type ( $e^-$ ), and  $p$ -type ( $h^+$ ) Elements.

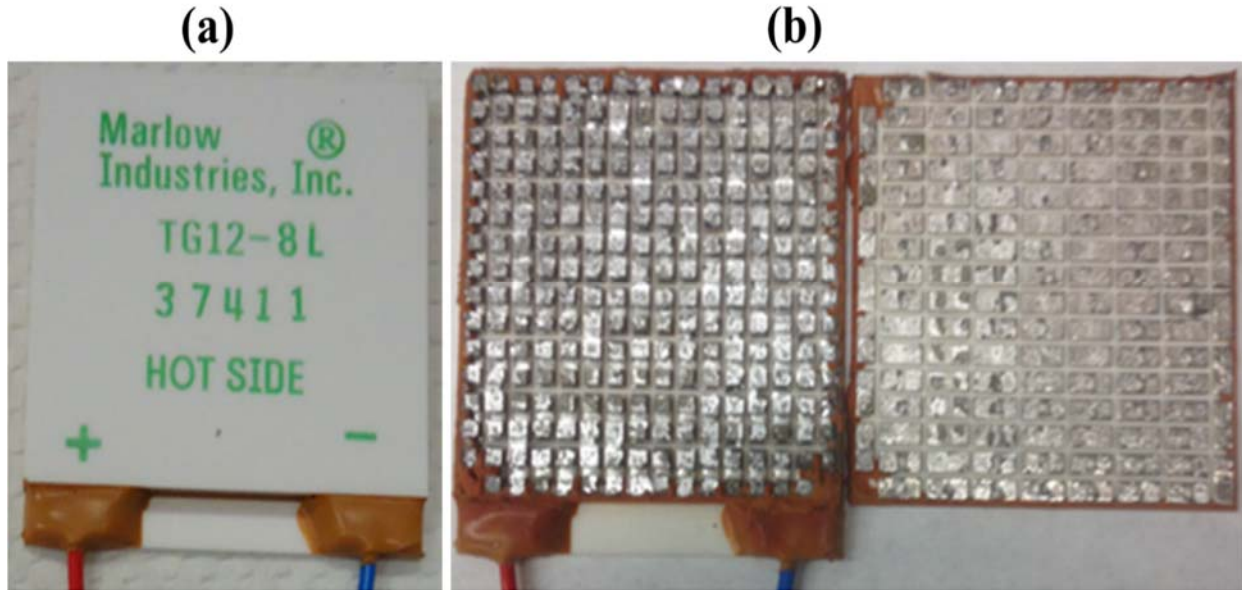


Figure 1.12 TE Module from Marlow Industries Inc., (a) Before and (b) After opening AlN plates; showing Bi<sub>2</sub>Te<sub>3</sub> Elements.

#### 1.4.1. Figure of Merit

In 1949, a Russian Physicist, Abram Fedorovich Ioffe, formulated  $Z$ -parameter and developed the modern concept of dimensionless figure of merit,  $ZT$  [17]. The ability or potential of a material to generate TE power is determined from the  $ZT$ , given by equation (1.5) [18 - 21].

$$ZT = \frac{\alpha^2 \sigma T}{\kappa} \quad (1.5)$$

where

$\alpha$  or  $S$  is the Seebeck coefficient ( $\mu\text{VK}^{-1}$ ),

$\sigma$  is the electrical conductivity ( $\text{Ohm}^{-1}\text{m}^{-1}$ )

$\kappa$  is the total thermal conductivity ( $\text{Wm}^{-1}\text{K}^{-1}$ ) and

$T$  is the absolute temperature (K).

The product ' $\alpha^2\sigma$ ' is also known as the power factor ( $PF$ ), and it represents the electrical transport properties of the TE material. From equation (1.5), it is evident that the  $ZT$ -value of a TE material can be improved by: (a) increasing both Seebeck coefficient (power of 2), and electrical conductivity (linearly), and (b) decreasing the thermal conductivity (linearly) of TE material. Furthermore, the transport properties ( $S$ ,  $\sigma$ , and  $\kappa$ ) of a given TE material depends on the carrier concentration ( $n_i$ ), and the temperature ( $T$ ). For a TE device containing both  $p$ -type and  $n$ -type segments, the dimensionless figure of merit from equation (1.5), is rewritten as equation (1.6).

$$ZT = \frac{(\alpha_p - \alpha_n)^2 T}{[(\rho_p \kappa_p)^{\frac{1}{2}} + (\rho_n \kappa_n)^{\frac{1}{2}}]^2} \quad (1.6)$$

where parameters ( $\alpha_p$ ,  $\rho_p$ , and  $\kappa_p$ ) and ( $\alpha_n$ ,  $\rho_n$ , and  $\kappa_n$ ) represents Seebeck coefficient, resistivity, and thermal conductivity of  $p$ - and  $n$ -type segments of the TE device.

#### 1.4.2. Conversion Efficiency

The maximum conversion efficiency ( $\eta_{TE}$ ) of an ideal TE device, with a negligible contact resistance, is obtained from the ratio of power ( $W$ ) input to the load, and total heat flow rate ( $Q_h$ ) of the TE device. The maximum conversion efficiency is given as the product of two terms i.e., (a) Carnot efficiency, and (b)  $ZT$  - dependent term. The  $\eta_{TE}$  is calculated by using equation (1.7).

$$\eta_{TE} = \frac{W}{Q_h} = \frac{T_h - T_c}{T_h} \times \frac{\sqrt{1 + ZT_m} - 1}{\sqrt{1 + ZT_m} + \frac{T_c}{T_h}} \quad (1.7)$$

where

$T_h$  is temperature of hot side of TE device,

$T_c$  is temperature of cold side of TE device,

$T_m$  is the average temperature of cold side, and hot side of a TE device,  $T_m = \frac{T_h + T_c}{2}$

$ZT_m$  is the dimensionless figure of merit at the mean temperature,  $T_m$  [18, 20, 21]

As shown in Figure 1.13, with the cold-side temperature ( $T_c$ ) kept constant at 300 K, the calculated maximum conversion efficiency,  $\eta_{TE}$  (%) of a TE device is plotted as a function of hot-side temperature ( $T_h$ ) for different values of  $ZT$ . Theoretically, the conversion efficiency of a TE device increases with the increase in  $ZT$  value of the TE material, which has no upper limit. However, the existing TE devices have low conversion efficiencies of  $\sim 7 - 8\%$ , which imposes a huge set back to the wide spread applications of TE devices at high temperatures [20]. Therefore, several research efforts are being made to improve the  $ZT$  of TE alloys to much higher values, such that the  $\eta_{TE}$  (%) of the TE device approaches to its Carnot efficiency at higher temperatures.

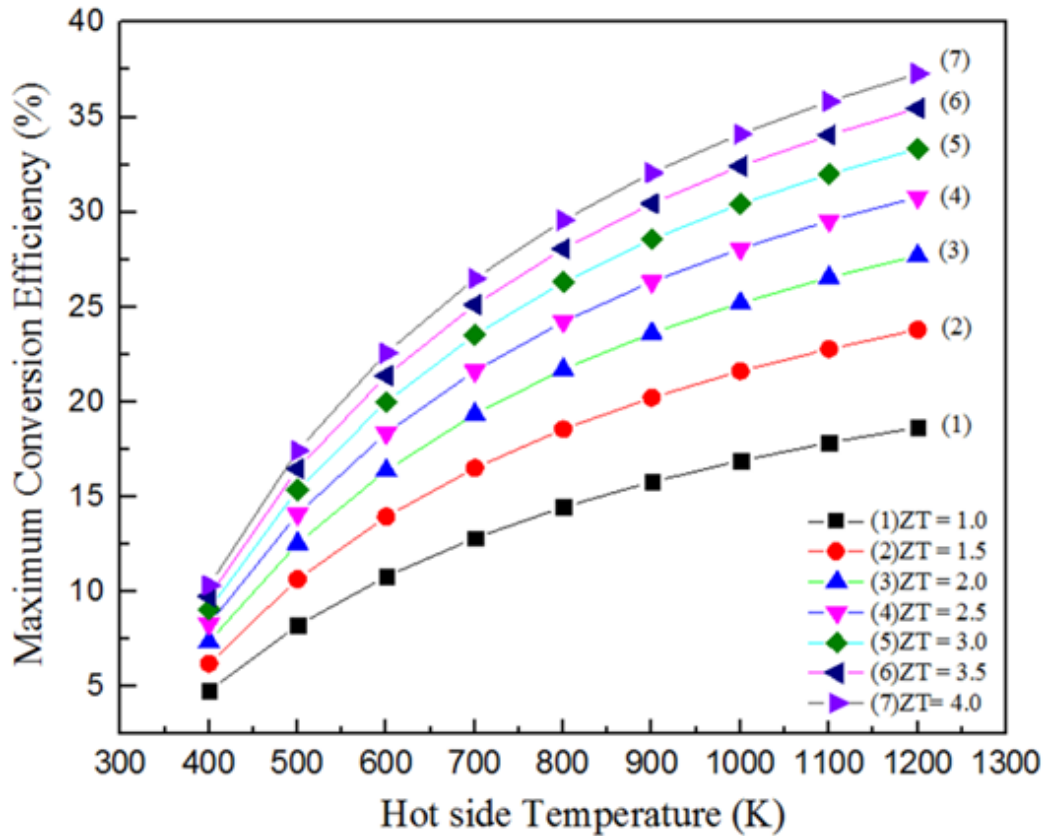


Figure 1.13 Variation of Maximum Conversion Efficiency,  $\eta_{TE}$  (%), with Temperature ( $T_h$ );  $ZT = 1.0 - 4.0$ , and  $T_c = 300$  K.

## 1.5. Thermoelectric Materials

From the previous sections (1.4.1 and 1.4.2), it is evident that the performance and conversion efficiency of a TE device, for power generation, is dependent on the transport properties of the material. These include Seebeck coefficient, electrical conductivity, and thermal conductivity. An ideal TE material conducts electricity like a crystal, and transfers heat like a glass [21]. The TE material can be categorized into ‘phonon-glass electron-crystal (PGEC)’ type. The electron-crystal requirement improves both the  $\alpha$ - and the  $\sigma$ -values resulting in higher power factors, while the phonon-glass prerequisite decreases the  $\kappa$ -values, thus enhancing overall  $ZT$  of the TE material. Figure 1.14 shows the interdependence of the transport properties ( $\alpha$ ,  $\sigma$ , and  $\kappa$ ), power factor ( $\alpha^2\sigma$ ), and  $ZT$  on carrier concentration for insulators, semiconductors, and metals.

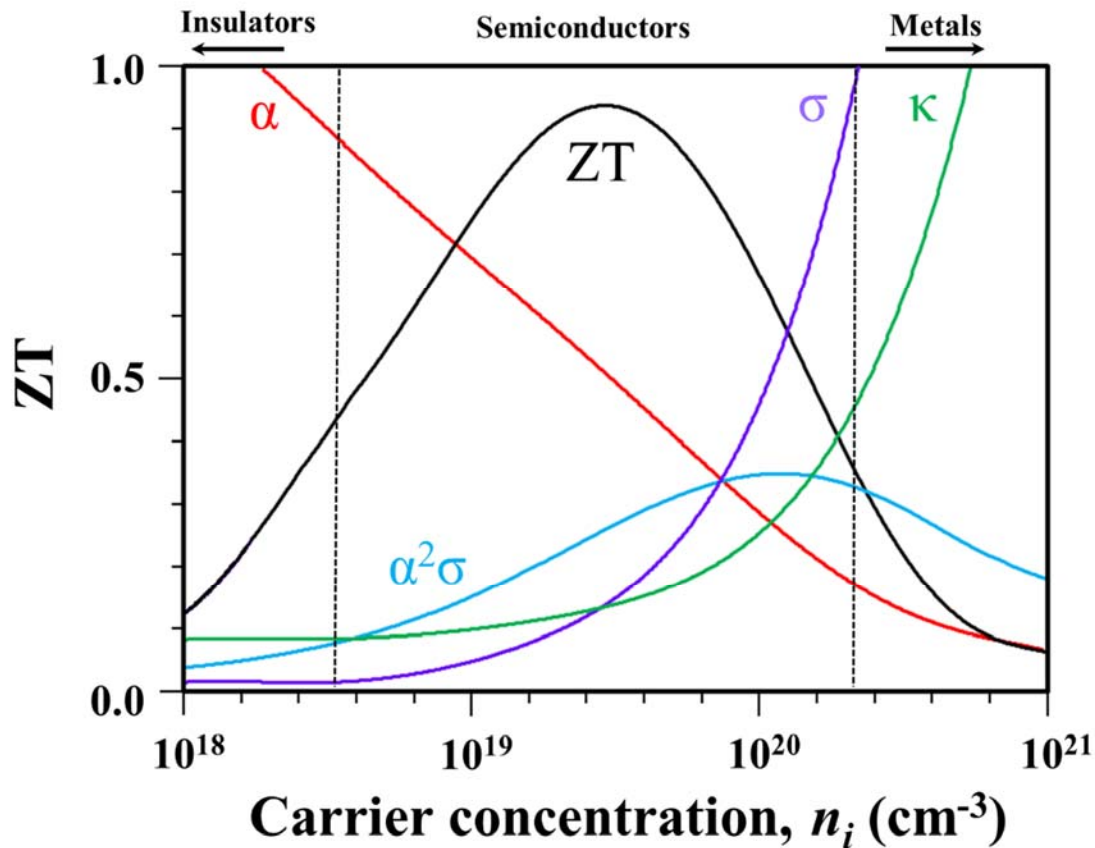


Figure 1.14 Variation of TE Properties ( $\alpha$ ,  $\sigma$ ,  $\kappa$ ,  $\alpha^2\sigma$ , and  $ZT$ ) with Carrier Concentration ( $n_i$ ) for Insulators, Semiconductors, and Metals.

To attain good  $ZT$  values, the TE material must possess: (i) high  $\alpha$  for maximum conversion of heat to electric power, (ii) high  $\sigma$  to reduce Joule heating, and (iii) low  $\kappa$  to avoid thermal shorting, and maintain thermal gradient across the TE device. For a given TE material, a decrease in  $\alpha$  value is associated with the simultaneous increase in  $\sigma$ - and  $\kappa$ -values. Insulators exhibit poor  $\sigma$ -values, whereas metals contain low  $\alpha$ -values. Heavily doped TE alloys have optimum  $ZT$  with  $n_i$  ( $10^{19}$  -  $10^{20}$  per  $cm^3$ ),  $\alpha$  ( $150 - 230 \mu VK^{-1}$ ),  $\sigma$  ( $1 - 3 m\Omega^{-1}cm^{-1}$ ), and  $\kappa$  ( $1.5 - 3 WmK^{-1}$ ).

### 1.5.1. Seebeck Coefficient

The Seebeck coefficient of metals or degenerate semiconductors depends on the carrier concentration ( $n_i$ ), the effective mass of carriers ( $m^*$ ), and the temperature ( $T$ ), according to the Mott formula given by equation (1.8) [22].

$$\alpha = \frac{\pi^2 k_B^2}{3e} T \left\{ \frac{d[\ln \sigma(E)]}{dE} \right\}_{E=E_f} \quad (1.8)$$

The above equation (1.8) is further simplified to equation (1.9) as:

$$\alpha = \frac{8\pi^2 k_B^2}{3eh^2} m^* T \left( \frac{\pi}{3n_i} \right)^{2/3} \quad (1.9)$$

where  $k_B$  is the Boltzmann's constant,  $e$  is the charge of an electron,  $\sigma(E)$  is the energy dependent electrical conductivity,  $E_f$  is the fermi energy, and  $h$  is the Planck's constant.

### 1.5.2. Electrical Conductivity

The electrical conductivity ( $\sigma$ ) of a TE alloy indicates its ability to conduct charge. The electrical conductivity or reciprocal of resistivity ( $\rho$ ) of a material, with length ' $l$ ' and cross-sectional area ' $A$ ', is defined by equation (1.10) [23].

$$\sigma = \frac{1}{\rho} = \frac{l}{R \times A} \quad (1.10)$$

where ‘ $R$ ’ is the electrical resistance of the material in *Ohms* ( $\Omega$ ). In addition, the electrical conductivity of a TE material is directly proportional to its carrier concentration ‘ $n_i$ ’ and mobility of carriers ‘ $\mu$ ’, and is given by equation (1.11) [21].

$$\sigma = n_i e \mu \quad (1.11)$$

Also, the electrical conductivity of a semiconducting material is temperature dependent, and is calculated using equation (1.12) [24].

$$\sigma(T) = (\sigma_o T) e^{-\frac{E_g}{RT}} \quad (1.12)$$

where  $\sigma_o$  is proportionality constant,  $E_g$  is the energy band gap, and  $R$  is universal gas constant.

The interdependence of Seebeck coefficient, and electrical conductivity is realized from the occurrence of common terms ‘ $e$ ’ and ‘ $n_i$ ’ in equations (1.9 and 1.11) for the transport properties.

### 1.5.3. Thermal Conductivity

The thermal conductivity of a TE material indicates the ability of the alloy to conduct thermal energy. Heat transport occurs within the material *via* movement of charge carriers, such as electrons, and vibrations of crystal lattice or phonon-phonon scattering. The total thermal conductivity ( $\kappa$ ) of a TE alloy is the sum of its (i) electronic thermal conductivity ( $\kappa_e$ ), and (ii) lattice or phonon thermal conductivity ( $\kappa_l$ ) and is given by equation (1.13) [21].

$$\kappa = \kappa_e + \kappa_l \quad (1.13)$$

According to Wiedemann-Franz law, the electronic thermal conductivity is directly proportional to electrical conductivity, and is given by equation (1.14) [21] as:

$$\kappa_e = L\sigma T = Lne\mu T \quad (1.14)$$

where  $L$  is the Lorenz number ( $2.45 \times 10^{-8} \text{ J}^2\text{K}^{-2}\text{C}^{-2}$ ) for free electrons. The  $L$ -value depends on material type and temperature [25]. It also varies with the Seebeck coefficient (equation 1.15) [26].

$$L (\times 10^{-8} \text{ W}\Omega\text{K}^{-2}) = 1.5 + \exp\left[-\frac{|S| (\mu\text{V}/\text{K})}{116}\right] \quad (1.15)$$

The lattice thermal conductivity of a material is calculated from the specific heat capacity ( $C$ ) of the material, velocity of phonons ( $v$ ), and mean free path ( $\lambda$ ) of phonons in the material and is given by the equation (1.16) [21].

$$\kappa_l = \frac{1}{3} C v \lambda \quad (1.16)$$

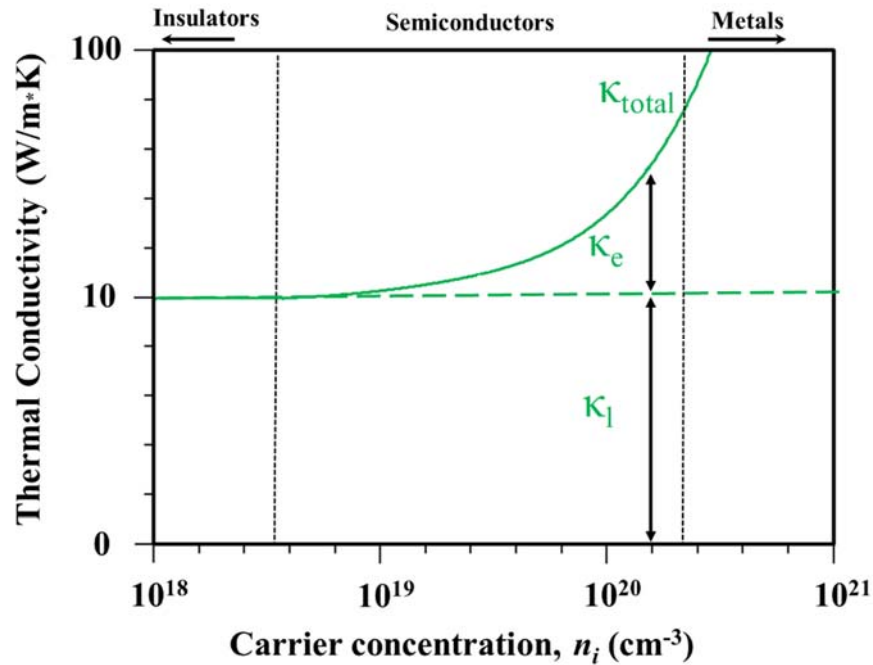


Figure 1.15 Variation of Thermal Conductivities ( $\kappa$ ,  $\kappa_e$ , and  $\kappa_l$ ) with Carrier Concentration ( $n_i$ ) for Insulators, Semiconductors and Metals.

Table 1.2 Transport Properties of some Metals, Semiconductors, & Insulators at 298.15 K [27-29].

<b>Material</b>	<b>Seebeck coefficient (<math>\mu\text{V/K}</math>)</b>	<b>Electrical conductivity (<math>\times 10^6 \text{ Sm}^{-1}</math>)</b>	<b>Thermal conductivity (<math>\text{W/mK}</math>)</b>
Mg	-1.46	22.6	156
Sb	47	2.88	24.3
Pb	-1.05	4.81	35.3
Ti	9.1	2.34	21.9
Nb	-0.44	6.93	53.7
Mn	-9.8	0.695	7.82
Co	-30.8	17.2	100
B	700	$1 \times 10^{-10}$	27
Si	300 (n), -500 (p)	$2.5 \times 10^{-10}$	130
Se	900	$1 \times 10^{-10}$	2.04
Te	500	$2 \times 10^{-4}$	2.35
Ge	600 (n), -830 (p)	$1.45 \times 10^{-6}$	59.9
Bi	-72	0.867	7.87
$\text{Bi}_2\text{Te}_3$	-162	0.182	4.68
PbTe	-180	0.532	2.3
SiGe	121	0.085	2.45
$\text{Mg}_2\text{Si}$	-178	0.082	7.25
$\text{MnSi}_{1.73}$	130	0.047	2.70
$\text{TiB}_2$	-2.7	11.49	116
ZnO	-301	$3.8 \times 10^{-4}$	48.7

Table 1.2 gives the list of transport properties of metals, semiconductors, and insulators at 298.15 K. The transport properties differs widely among the materials. This is because the electrons that carry charge in materials are also responsible for the simultaneous transport of thermal energy (equation 1.14). As shown in Figure 1.15, the metals exhibit high  $\kappa$ -values, the semiconductors contain medium  $\kappa$ -values, and the insulators have low  $\kappa$ -values. At higher temperatures, the  $\kappa$ -value of a semiconductor decreases due to increase in the number of phonons, while the  $\sigma$ -value increases in most cases because of increase in the number of intrinsic carriers.

#### 1.5.4. ZT vs. Temperature of TE Alloys

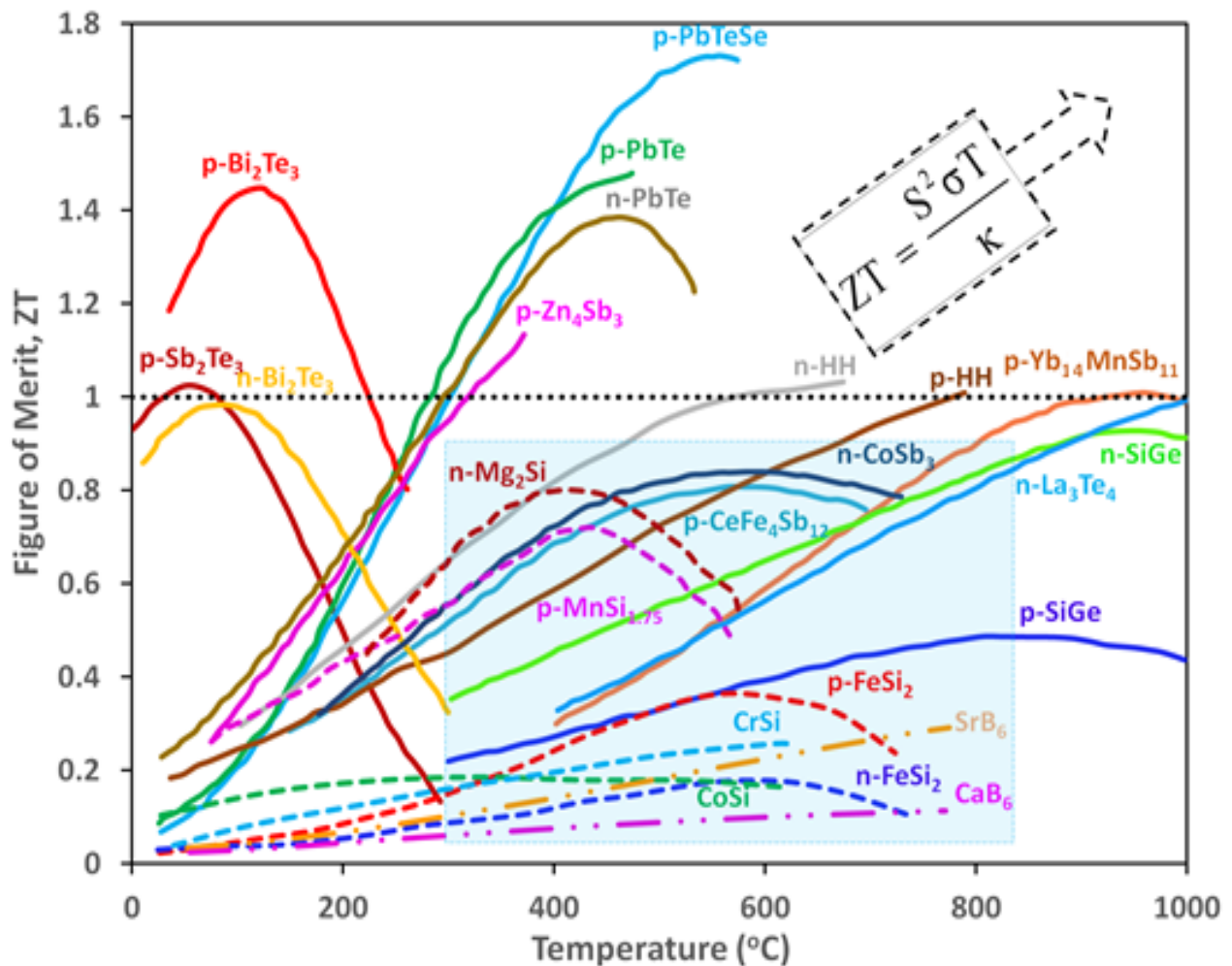


Figure 1.16 Figure of Merit (ZT) for some Existing TE Alloys at Different Temperatures.

Although many materials have tendency to show thermoelectric effect, only some of them are feasible for the conversion of waste heat to electrical energy. In general, the TE alloys are both *p*-type semiconductors ( $\text{Bi}_2\text{Te}_3$ ,  $\text{Sb}_2\text{Te}_3$ ,  $\text{Bi}_2\text{Se}_3$ ,  $\text{PbTe}$ ,  $\text{PbTeSe}$ ,  $\text{CeFe}_4\text{Sb}_{12}$ ,  $\text{Zn}_4\text{Sb}_3$ ,  $\text{SiGe}$ ,  $\text{MnSi}_{1.75}$ ,  $\text{Yb}_{14}\text{MnSb}_{11}$  etc.), and *n*-type semiconductors ( $\text{Bi}_2\text{Te}_3$ ,  $\text{PbTe}$ ,  $\text{CoSb}_3$ ,  $\text{Mg}_2\text{Si}$ ,  $\text{SiGe}$ ,  $\text{La}_2\text{Te}_3$ ,  $\text{La}_3\text{Te}_4$  etc.) with narrow energy band gaps that can facilitate good carrier concentration ( $10^{25}$  -  $10^{27}$   $\text{m}^{-3}$ ) at the operational temperatures [21]. Figure 1.16 shows the overlay of *ZT* curves as a function of temperature for some existing bulk TE materials.

Conventional TE materials such as  $\text{Bi}_2\text{Te}_3$  and  $\text{Sb}_2\text{Te}_3$  are suitable for low temperature (< 200 °C) applications [30], like cooling effect in refrigerators and recovery of waste-heat from steam pipes etc. Both *p*- and *n*-type tellurides such as  $\text{PbTe}$ ,  $\text{PbTeSe}$ ,  $\text{Zn}_4\text{Sb}_3$ ,  $\text{GeTe}$ , and  $\text{SnTe}$  are applied for power generation at temperatures of 300 - 600 °C [31]. Other TE alloys in this range include cage-like structures of skutterudites ( $\text{CoSb}_3$ -based) [32], clathrates ( $\text{Ga}_{16}\text{Ge}_{30}$ -based) [33], tellurides ( $\text{Tl}_2\text{Te}_5$ -based) [34], and Mo-clusters ( $\text{Mo}_6\text{X}_8$ -type) [35]. For high temperature (600 – 1000 °C) applications, a variety of materials have been considered as TE alloys. These include  $\text{SiGe}$ -based [36], cobaltites ( $\text{CoO}_2$ -based) [37], antimonides ( $\text{MnSb}_{11}$ -,  $\text{Zn}_4\text{Sb}_3$ -based) [38, 39], half-Heusler (HH) alloys i.e.  $(\text{Ti}, \text{Zr}, \text{Hf})\text{NiSnSb}$ , and  $(\text{Ti}, \text{Zr}, \text{Hf})\text{CoSnSb}$  [40], selenides ( $\text{Cu}_2\text{Se}$ ) [41], and tellurides ( $\text{LaTe}$ -based) [42].

Higher *ZT* values have been reported with layered super-lattice structures of thin-film, and nanostructured bulk TE materials. Table 1.3 summarizes the maximum *ZT*, and respective temperatures reported for different material family of TE alloys. Venkatasubramanian *et al.* have reported a *ZT* of ~ 2.4 for *p*-type chalcogenides ( $\text{Bi}_2\text{Te}_3/\text{Sb}_2\text{Te}_3$ ) super lattices at 300 K [43]. In another study, Biswas *et al.* studied TE properties of controlled doped  $\text{PbTe}$  – based hierarchical

Table 1.3 Maximum Figure of Merit and Temperatures Reported for Different Type of TE Alloys.

<b>Material family</b>	<b>TE Alloy</b>	<b>Maximum <math>ZT</math></b>	<b>Temperature (K)</b>	<b>Ref.</b>
Chalcogenides	<i>p</i> -type Bi <sub>2</sub> Te <sub>3</sub> /Sb <sub>2</sub> Te <sub>3</sub>	2.4	300	[43]
Tellurides	PbTe-SrTe (4 mol%) with 2% Na	2.2	915	[44]
Clathrates	<i>n</i> -doped Sr <sub>8</sub> Ga <sub>16</sub> Ge <sub>30</sub> /Ba <sub>8</sub> In <sub>16</sub> Sn <sub>30</sub>	1.7	900	[45]
Metal oxides	Ca <sub>2</sub> Co <sub>2</sub> O <sub>5</sub>	1.2 - 2.7	≥ 873	[46]
Half-heuslers	Sb-doped (Ti, Zr, Hf) NiSn	1.5	700	[47]
Selenides	SnSe	2.6	923	[48]
Skutterudites	<i>n</i> -type (In, Sr, Ba, Yb) <sub>y</sub> Co <sub>4</sub> Sb <sub>12</sub>	1.8	823	[49]
Antimonides	β-Zn <sub>4</sub> Sb <sub>3</sub>	1.3	670	[50]
	Mg <sub>2</sub> Si <sub>0.53</sub> Sn <sub>0.4</sub> Ge <sub>0.05</sub> Bi <sub>0.02</sub>	1.4	823	[55]
	<i>n</i> -type Mg <sub>2.16</sub> (Si <sub>0.4</sub> Sn <sub>0.6</sub> ) <sub>0.985</sub> Sb <sub>0.015</sub>	1.3	740	[56]
Metal Silicides	Complex doped MnSi <sub>1.75</sub>	~ 1.0	675	[57]
	B-doped Si <sub>80</sub> Ge <sub>20</sub>	~ 1.0	1073 - 1173	[58]
Si <sub>x</sub> Ge <sub>1-x</sub> based alloys	2 mol % P-doped Si <sub>80</sub> Ge <sub>20</sub>	1.3	1173	[59]

structures and their results showed a maximum  $ZT$  of  $\sim 2.2$  for spark-plasma-sintered (SPS) 2% Na-doped PbTe-SrTe (4 mol%) bulk alloy at 915 K [44]. Blake *et al.* conducted density functional calculations on the band structures and TE properties of Ba-based and Sr-based inorganic clathrates and their predictions indicate that  $n$ -doped  $\text{Sr}_8\text{Ga}_{16}\text{Ge}_{30}/\text{Ba}_8\text{In}_{16}\text{Sn}_{30}$  may reach a maximum  $ZT$  of 1.7 at 900 K [45]. Funahashi *et al.* have shown that the layered oxide thermoelectric material i.e.  $\text{Ca}_2\text{Co}_2\text{O}_5$  or Co-225 whiskers, contain an estimated  $ZT$  values of 1.2 to 2.7 at temperatures,  $T \geq 873$  K [46]. Sakurada and Shutoh have reported a maximum  $ZT$  value of 1.5 for Sb-doped (Ti, Zr, Hf) NiSn half-Heusler compounds at 700 K [47]. In SnSe crystal, the figure of merit is anisotropic or varies directionally along different crystallographic axis. Recently, Zhao *et al.* have reported an unprecedented  $ZT$  of  $\sim 2.6$  along  $b$ -axis at 923 K, a high  $ZT$  of  $\sim 2.3$  along  $c$ -axis, and a relatively low  $ZT$  of 0.8 along  $a$ -axis [48]. In another study, Rogl *et al.* synthesized  $n$ -type skutterudites  $(\text{In}, \text{Sr}, \text{Ba}, \text{Yb})_y\text{Co}_4\text{Sb}_{12}$  via high-energy ball milling (HB) that exhibited low thermal conductivity, and an outstanding high  $ZT$  of 1.8 at 823 K, with a maximum TE conversion efficiency ( $\eta_{max}$ ) equivalent to 17.5 % [49]. In 1997, Caillat *et al.* prepared zinc antimonide,  $\beta\text{-Zn}_4\text{Sb}_3$ , which exhibited a maximum  $ZT$  of 1.3 at 670 K [39].

Although the aforementioned TE materials possess higher  $ZT$  values, it is very difficult to find suitable TE alloys with reproducible  $ZT \geq 1.5$  for high temperature applications. In recent years, there is a huge demand for efficient bulk TE materials in aerospace, military, automobile, and consumer-based industries for waste heat processing at higher temperatures [50, 20]. The electricity generated from the waste-heat components, such as exhaust pipes of automobiles, concentrated solar and thermal power plants, incinerators, and steel industry furnaces [9, 51, 52], can be used as auxiliary source for operating low power systems like air condition, audio/video systems etc. Heat recovery methods, like TE technology, aim at minimizing the waste heat,

improving the energy efficiency, reducing the energy emissions, and lowering the energy cost [53]. Therefore, the new frontiers of TE research include the discovery of high performance TE alloys for high temperature applications.

### 1.5.5. State-of-Art TE Materials

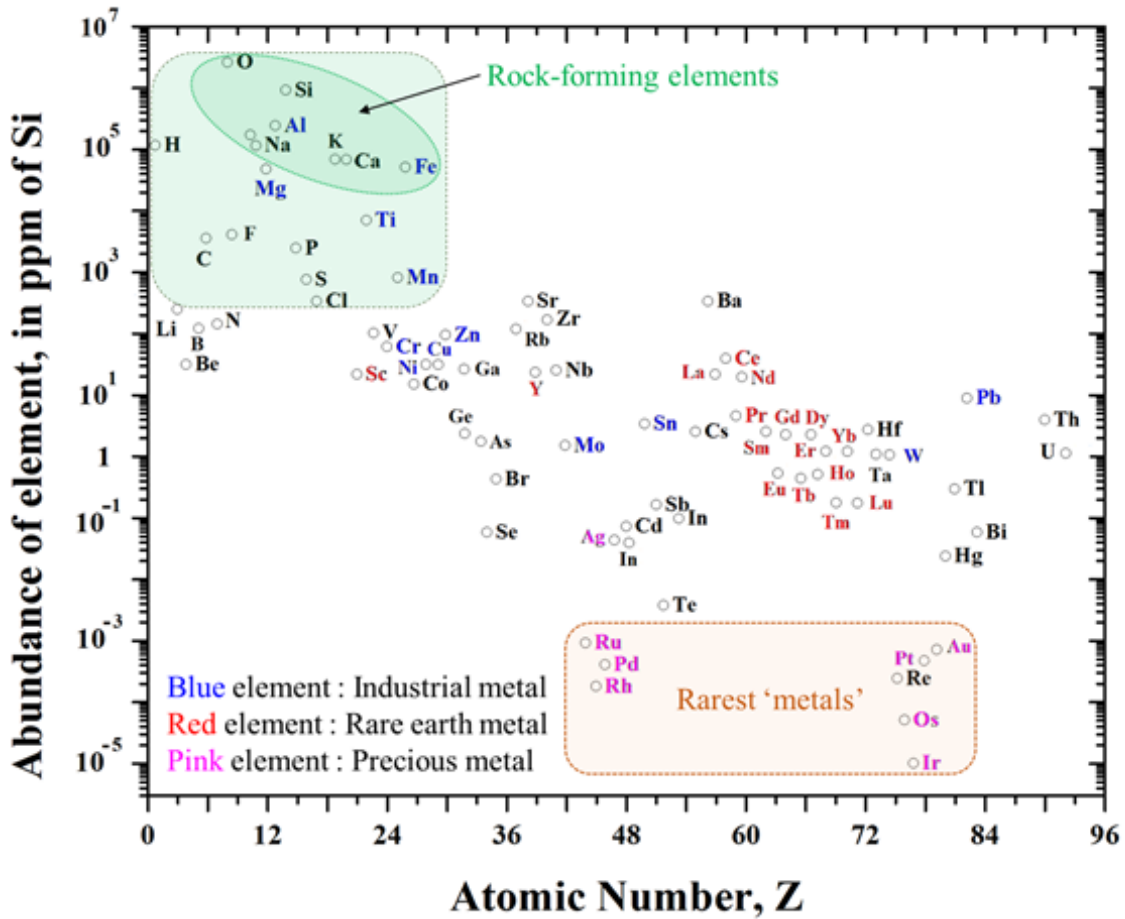


Figure 1.17 Abundance of Elements in the Earth's Crust [54].

The commercially available state-of-art materials for thermoelectric power generation mainly consists of telluride-based ( $\text{Bi}_2\text{Te}_3$ ,  $\text{Sb}_2\text{Te}_3$ ,  $\text{PbTe}$ ,  $\text{PbTeSe}$ ,  $\text{La}_3\text{Te}_4$  etc.), antimony-based ( $\text{Sb}_2\text{Te}_3$ ,  $\text{Zn}_4\text{Sb}_3$ ,  $\text{CoSb}_3$ ,  $\text{CeFe}_4\text{Sb}_{12}$ ,  $\text{Yb}_{14}\text{MnSb}_{11}$ , half-Heuslers etc.), and SiGe-based ( $\text{Si}_x\text{Ge}_{1-x}$ ) TE materials, which exhibits high  $ZT \sim 1.0 - 1.7$  (from Figure 1.15). But, the constituent elements (Te, Sb, and Ge) of above TE materials are costly due to their low abundance in the earth's crust.

In order to reduce the manufacturing cost of TE devices, a good direction for TE research is to start with the low-cost, and high-abundant raw materials. As shown in the Figure 1.16, the natural abundance of important elements (with respective Si) as a function of the atomic number [54]. Economically, the TE materials constituting the rock forming elements (Si, Mg, Al, Na, K, Ca, Ti, Mn, Fe, C, O, S, and P) are preferred over the rare metals like Te and Sb. Therefore, several research studies have been primarily concentrated on silicon-based, boron-based, and oxygen-based inexpensive thermoelectric materials.

Khan *et al.* have reported a maximum  $ZT$  value of 1.4 for  $\text{Mg}_2\text{Si}_{0.53}\text{Sn}_{0.4}\text{Ge}_{0.05}\text{Bi}_{0.02}$ , and a high  $ZT$  of 1.2 for  $\text{Mg}_2\text{Si}_{0.5375}\text{Sn}_{0.4}\text{Ge}_{0.05}\text{Sb}_{0.0125}$  at 823 K [55]. Likewise, Liu *et al.* have reported high  $ZT$  value of 1.3 for  $n$ -type  $\text{Mg}_{2.16}(\text{Si}_{0.4}\text{Sn}_{0.6})_{0.985}\text{Sb}_{0.015}$  at 740 K [56]. Zaitsev conducted studies on TE properties of anisotropic higher manganese silicide (HMS),  $\text{MnSi}_{1.75}$  and showed that the introduction of complex dopants into  $\text{MnSi}_{1.75}$  crystal structure resulted in the enhancement of  $ZT$  to 0.97 at 675 K [57]. In 2008, two research groups have conducted independent studies on improving  $ZT$  via nano-structuring approach. Joshi *et al.* have reported enhanced  $ZT$  of  $\sim 1.0$  for  $p$ -type nanostructured boron doped- $\text{Si}_{80}\text{Ge}_{20}$  bulk alloy at 1073 - 1173 K [58], while Wang *et al.* have synthesized  $n$ -type nanostructured 2 mol % phosphorus doped- $\text{Si}_{80}\text{Ge}_{20}$  bulk alloy that exhibited an enhanced  $ZT$  of 1.3 at 1173 K [59]. Doped  $\text{Si}/\text{Si}_x\text{Ge}_{1-x}$  alloys have been used by National Aeronautics and Space Administration (NASA) in radioisotope thermoelectric generator (RTG) of satellites, during deep space missions for TE conversion at temperature of  $\sim 1000$  K [60].

Metal oxides are interesting newcomers in the field of thermoelectrics. Ternary and quaternary cobaltates, such as  $\text{Na}_x\text{CoO}_2$ ,  $\text{Ca}_2\text{Co}_2\text{O}_5$ ,  $\text{Ca}_3\text{Co}_4\text{O}_9$ , and  $\text{Bi}_2\text{Sr}_2\text{Co}_2\text{O}_7$ , have promising  $ZT$  because of high  $S$ - and low  $\kappa_T$ -values [61]. The crystal lattice of these oxide materials have (a) common  $\text{CoO}_2$  layers that facilitates good electron-transport, and (b) the intercalated metals (Na,

Ca, Bi, and Sr) layers that act as phonon-scattering regions thus resulting in lower  $\kappa_l$ -values. These factors are responsible for good performance of the oxide TE alloys. Although the oxides appeal for high temperature TE applications due to their good thermal and chemical stabilities, most of these materials: (i) are insulators with low  $n_i$  values, (ii) have high contact resistance at the metal/oxide electrode junction, and (iii) suffer from cracking or exfoliation, due to poor thermal expansion during the operation cycles [62].

Although metal borides are not classified under the state-of-art materials (with  $ZT \geq 1$ ), they are still attractive because of their good stabilities, mechanical and transport properties. In 2003, Takeda *et al.* have studied TE properties of divalent hexaborides, and they discovered that SrB<sub>6</sub> exhibit  $ZT$  of  $\sim 0.3$  at 1000 K [63]. Recently, Sussardi *et al.* reported that the boron-rich cluster compound, SmB<sub>62</sub>, have extrapolated  $ZT$  of  $\sim 0.4$  at 1500 K [64].

## 1.6. Engineering TE Alloys

A paradigm shift in bulk TE material research include: (a) consideration of low-cost starting materials, like metal silicides and borides, and (b) engineering the thermoelectric properties of the alloys for high temperature waste-heat recovery applications by

- (i) increasing carrier concentration ( $n_i$ ) through metal-doping, which in turn enhances the thermoelectric power ( $S^2\sigma$ ; increase in both  $S$  and  $\sigma$  values), and
- (ii) altering the crystal lattice structure *via* appropriate material synthetic procedures (nano-structuring/grain size modification) to increase phonon scattering, thus decreasing the overall  $\kappa_l$  value of the material.

Therefore, the current research work mainly focuses on synthesis, characterization, phase stability, thermodynamic, and thermoelectric aspects of selected transition metal borides and silicides.

CHAPTER 2  
LITERATURE REVIEW

Table 2.1 lists several semiconducting metal borides and silicides that have been examined as TE materials [63, 65-73]. The metal borides show (i) increasing of  $S$  and  $\sigma$ , (ii) lowering of  $\kappa$ , and (iii) good thermal stabilities at higher temperatures [65]. Likewise, the metal silicides have been studied because of their (i) low toxicity, (ii) high natural abundance, (iii) good transport properties, and (iv) better thermal stabilities at higher temperatures [65].

Table 2.1. A List of Metal Borides and Silicides studied as TE Materials

TE alloys	Type	Constituent metal (M)
<b>Metal Borides</b>	MB	Ti, V, Cr, Mn, Fe, Co, Ni, Mo, and W
	MB <sub>2</sub>	Mg, Al, Sc, Ti, V, Cr, Mn, Tc, and Re
	MB <sub>4</sub>	Mg, Cr, Y, and W
	MB <sub>6</sub>	Ca, Sr, Ba, La, Ce, Sm, Eu, and Yb
	Other	Mg <sub>2</sub> B <sub>105</sub> , AlB <sub>12</sub> , AlMgB <sub>14</sub> , Ba <sub>1-x</sub> Ca <sub>x</sub> B <sub>6</sub> , Sr <sub>1-x</sub> CaB <sub>6</sub> , Ba <sub>1-x</sub> Sr <sub>x</sub> B <sub>6</sub> , SmB <sub>62</sub> , YB <sub>48</sub> , ZrB <sub>12</sub> , and Y <sub>x</sub> Al <sub>y</sub> B <sub>14</sub> ,
<b>Metal Silicides</b>	MSi	Na, Ca, Sr, Co, and Ba
	M <sub>2</sub> Si	Mg, Ca, and Sr
	MSi <sub>2</sub>	Ca, Ti, Cr, Mn, Fe, Co, Sr, Zr, Mo, Ru, Ba, W, Re, and Os
	Other	Ca <sub>3</sub> Si <sub>4</sub> , Ca <sub>5</sub> Si <sub>3</sub> , Mg <sub>2-x</sub> Ca <sub>x</sub> Si, MnSi <sub>2-x</sub> , RuSi <sub>2-x</sub> , Ru <sub>2</sub> Si <sub>3</sub> , Os <sub>2</sub> Si <sub>3</sub> , ReSi <sub>1.75</sub> , Rh <sub>3</sub> Si <sub>4</sub> , Rh <sub>4</sub> Si <sub>5</sub> , IrSi <sub>3</sub> , Ir <sub>3</sub> Si <sub>5</sub> , Mg <sub>127</sub> Si <sub>64</sub> , Mg <sub>127</sub> Al <sub>1</sub> Si <sub>64</sub> , Mg <sub>129</sub> Si <sub>63</sub> , Mg <sub>128</sub> Al <sub>1</sub> Si <sub>63</sub> , Mg <sub>127</sub> Si <sub>64</sub> , Co <sub>1-x</sub> Pt <sub>x</sub> Si, Co <sub>1-x</sub> Ni <sub>x</sub> Si, Co <sub>1-x</sub> Pd <sub>x</sub> Si, Fe <sub>1-x</sub> Os <sub>x</sub> Si <sub>2</sub> , and Ru <sub>2-x</sub> Os <sub>x</sub> Si <sub>3</sub>

The cyan-colored region of Figure 1.15 highlights the  $ZT$  curves of some TE metal silicides ( $n$ -type  $Mg_2Si$ ,  $p$ -type  $MnSi_{1.75}$ ,  $p$ - and  $n$ -type  $FeSi_2$ ,  $CrSi$ ,  $CoSi$ ,  $p$ - and  $n$ -type  $SiGe$ ), and TE metal borides ( $CaB_6$ , and  $SrB_6$ ), which are promising for mid- and high-temperature waste heat recovery applications. Although Pb – based, and La – based tellurides exhibit good  $ZT$  (1 - 1.8) at mid/high temperatures while compared to the metal borides and silicides, they have disadvantages of toxicity, high cost, low abundance, and high density. Implementing advanced nanostructure strategies, such as introduction of (i) point defects, vacancies, rattling structures within the unit cell, (ii) dopants or disordered structures that do not alter the electron-transport region of the crystal, and (iii) super lattice structures or nanocomposites with multi-interfaces that can enhance the scattering of phonons in the crystal lattice of metal borides and silicides. This further results in lowering of lattice thermal conductivity ( $\kappa_l$ ), and hence, an overall improvement in the  $ZT$ -value can be achieved for the TE alloys.

## 2.1. Boride TE Alloys

Until now, most of the boron thermoelectric research have been conducted on boron carbides [74, 75], metal-doped  $\beta$ -rhombohedral boron [76, 77], boron cluster compounds [78-82], and metal borides [63-67], due to their physical properties (high melting points, good mechanical strength, chemical and thermal stabilities), and TE properties (large  $S$  and low  $\kappa$ ). Maruyama *et al.* showed that excellent  $p$ - $n$  control can be achieved with TE boride ( $Y_xAl_yB_{14}$ ) at high temperature [73]. Takeda *et al.* reported that divalent metal borides ( $CaB_6$ ,  $SrB_6$ ,  $YbB_6$ ,  $EbB_6$ ,  $SmB_6$ ,  $CeB_6$  and  $BaB_6$ ) are  $n$ -type TE materials, with large negative  $S$ , and high  $\sigma$  values [63, 67, and 83].

### 2.1.1. Properties of TE Borides

Metal borides contain one-, two-, and three-dimensional network of boron atoms, which are inter-linked through strong covalent bonds [84]. The complex structural behavior arises due to

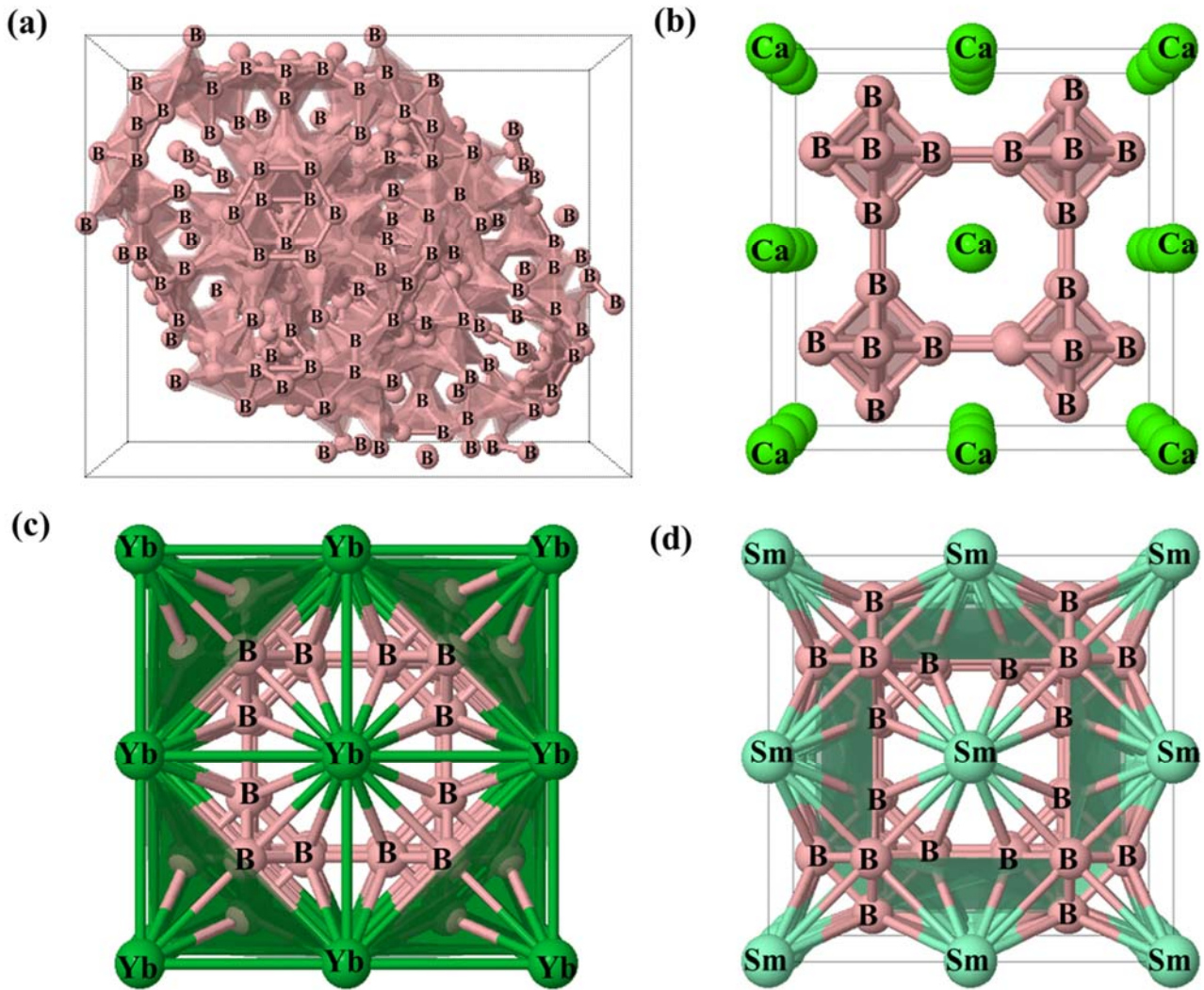


Figure 2.1 Crystal Structures of Unit Cell of (a)  $\beta$ -Boron, and Multiple Unit Cell of (b)  $\text{CaB}_6$ , (c)  $\text{YbB}_6$  and (d)  $\text{SmB}_6$  [29].

the valance saturation requirements of electron-deficient boron atoms [85]. Figure 2.1 shows the crystal structures of  $\beta$ -boron, and metal borides ( $\text{CaB}_6$ ,  $\text{YbB}_6$ , and  $\text{SmB}_6$ ) [29]. To obtain high temperature  $n$ -type TE materials, Nakayama *et al.* doped  $\beta$ -rhombohedral boron with metals (V, Cr, Fe or Zr), and studied the relationship between the electrical properties, and site occupancy of the metals in the crystal structure at temperatures  $< 300$  K [77]. The  $\sigma$ -values of the metal doped  $\beta$ -rhombohedral boron increases with the corresponding increase in the occupancy of A-1 sites.

The  $S$ -values of these materials decreases with the increase in metal concentration (exception for  $Zr$ ). The authors concluded that both the  $\sigma$ -, and the  $S$ -values increases as a function of temperature. This is mainly due to the variable-range hopping conduction that occurs within the metal doped  $\beta$ - boron crystal. The  $S$ -value of  $\beta$  - boron changes from positive to the negative value after doping with Fe, V, and Cr metals [76, 77]. Also, the power factor ( $S^2\sigma$ ) increases with the temperature. The  $S^2\sigma$ -values for  $n$ -type heavily V/Cr-doped  $\beta$  - boron are three times larger while compared to that of pure  $\beta$  - boron crystal (Figure 2.1a). In another study, Kim and Kimura doped  $\beta$  - rhombohedral boron with 1 % metal (Al, Co, Cr, Cu, Mo, Nb, Ni, Ru, Si, V, W, and Zr) and the TE properties of metal –doped  $\beta$  - rhombohedral boron were examined from 353 K to 1073 K [86]. The authors showed that V-doped  $\beta$ -boron exhibited highest  $ZT$  among all the metal-doped  $\beta$  - boron materials. Also, the  $S$ -value decreased from positive to negative, the  $\sigma$ -value increased, and the  $\kappa$ -value decreased as a result of V-doping in the  $\beta$  – boron crystal.

Because of the restriction in the maximum amount of metal-dopant in the crystal structures of both  $\beta$  – boron, and boron carbide (unit cell not shown) to a few percent, it is very difficult to further increase the doping-level (due to limited dopant-sites), and achieve the desired  $n$ -type TE properties for these materials [67]. Alternatively, the metal hexaborides have been considered as  $n$ -type TE materials, because of their relatively less structural-complexity, and good  $S$ -values. The TE properties of  $CaB_6$ ,  $SrB_6$ ,  $BaB_6$ ,  $LaB_6$ ,  $EuB_6$ ,  $YbB_6$ ,  $CeB_6$ , and  $SmB_6$  have been thoroughly investigated [63-67]. The multiple unit cell structures of the divalent alkaline earth metal hexaborides ( $SrB_6$ , and  $BaB_6$ ) are similar to that of other group (II) metal hexaboride,  $CaB_6$  (Figure 2.1b). Likewise, among the lanthanide hexaborides, both  $LaB_6$ , and  $EuB_6$  have multiple cell structures that are analogous to that of  $YbB_6$  (Figure 2.1c), while  $CeB_6$  have comparable multiple

unit cell structure to that of SmB<sub>6</sub> (Figure 2.1d). The percent metallic/non-metallic contribution to the overall structure of the TE boride materials can directly be inferred from the polyhedral shaded regions of the unit cell structures. Also, the structural frame work of the metal hexaborides effects their physical, mechanical, and chemical properties.

Table 2.2 Properties of  $\beta$ -Boron and Some Selected TE Metal Borides at 300 K [29, 63, 87-90].

<b>Metal Borides</b>	<b><math>M.P^{\dagger}</math> (K)</b>	<b><math>\rho^{\#}</math> (g/cm<sup>3</sup>)</b>	<b><math>E^*</math> (GPa)</b>	<b><math>\alpha^{\diamond}</math> (10<sup>-6</sup>/K)</b>	<b><math>-\Delta_f H^{\circ \S}</math> (kJ/mol)</b>	<b><math>C_p^{\dagger}</math> (J/mol*K)</b>	<b><math>n_i^{\blacklozenge}</math> (10<sup>20</sup>/cm<sup>3</sup>)</b>	<b><math>E_g^{\blacksquare}</math> (eV)</b>
<b><math>\beta</math>- Boron</b>	2365	2.34	482.6	4.3	0.00	11.19	0.0025 <sup>b</sup>	1.78
<b>CaB<sub>6</sub></b>	2235	2.49	219.1	6.2	167.3	85.5	~3.3	0.93
<b>SrB<sub>6</sub></b>	2508	3.39	272.3	6.7	247	0.043 <sup>a</sup>	~2.4	0.95
<b>BaB<sub>6</sub></b>	2540	4.36	305.4	6.2	202.1	253.75	6.0	0.97
<b>LaB<sub>6</sub></b>	2210	4.72	452.0	6.4	259.4	97.33	~130	2.0
<b>EuB<sub>6</sub></b>	2520	5.00	267.4	6.9	223.8	136.16	1200	~ 1.0
<b>YbB<sub>6</sub></b>	2800	5.61	226.9	5.8	179.9	96.56	1.2	0.14
<b>CeB<sub>6</sub></b>	2550	4.80	393.0	7.3	255.2	103.9	150	0.045 <sup>c</sup>
<b>SmB<sub>6</sub></b>	2740	5.11	253.5	6.8	230.1	92.31	400	0.045 <sup>c</sup>

<sup>†</sup> $M.P$  - Melting point; <sup>#</sup> $\rho$  -Density; <sup>\*</sup> $E$  -Young's Modulus; <sup>◇</sup> $\alpha$  -Linear thermal expansion coefficient; <sup>§</sup> $\Delta_f H^{\circ}$  -Heat of formation; <sup>†</sup> $C_p$  -Specific heat (<sup>a</sup> $C_p$  at 12.5 K); <sup>◆</sup> $n_i$ - Charge carrier concentration (300 K); <sup>b</sup>( $n_i$  at 600 K) ; <sup>■</sup> $E_g$ -Energy band gap, <sup>c</sup>( $E_g$  at 13 - 53 K).

Specifically, the transition metal hexaborides are characterized by high strength, refractory behavior, chemical and thermal stability, thermionic emission, and conductivities. Table 2.2 lists

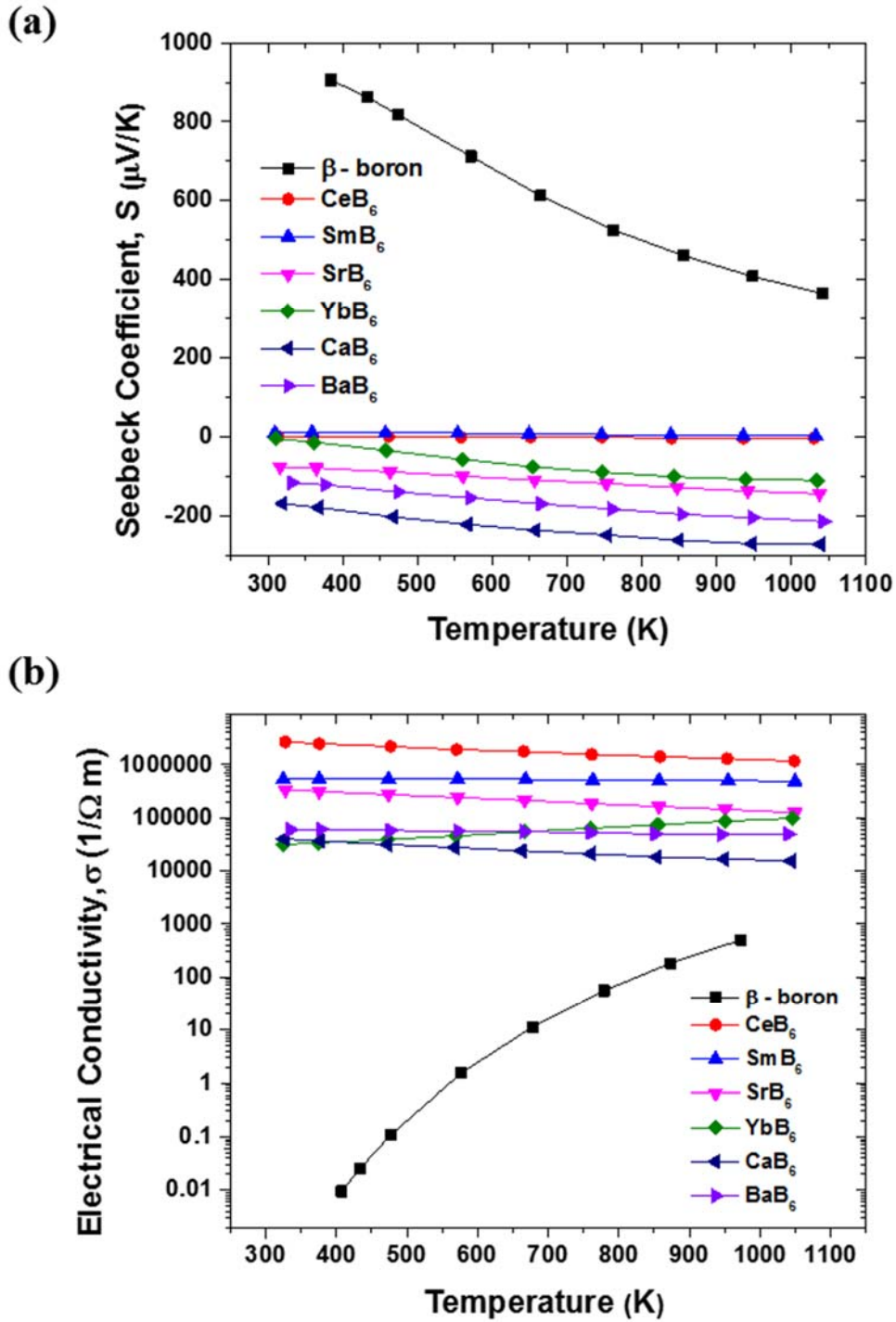


Figure 2.2 Effect of Temperature on (a) Seebeck Coefficient, and (b) Electrical Conductivity of  $\beta$ -Boron, and Metal Borides [63, 91].

the important properties of  $\beta$  - boron, and some selected TE metal borides. These alloys possess very high melting points, low densities, high Young's moduli, low thermal expansion coefficients, high heat of formation, and heat capacities. All these properties suggest that the TE metal borides are good candidates for high temperature applications. In addition, the availability of good charge carrier concentration, and the narrow energy band gap values indicate that the metal borides are suitable TE materials for waste heat recovery at high temperatures.

As shown in the Figure 2.2(a), the Seebeck coefficient of (i) *p*-type  $\beta$  - boron, and (ii) *n*-type metal borides (CeB<sub>6</sub>, SmB<sub>6</sub>, SrB<sub>6</sub>, YbB<sub>6</sub>, CaB<sub>6</sub> and BaB<sub>6</sub>) [63, 91]. With the addition of the metal atoms to the  $\beta$  - boron, the *S*-value changes from positive to negative values. CaB<sub>6</sub>, BaB<sub>6</sub>, and SrB<sub>6</sub> have good negative *S*-values, while compared to  $\beta$  - boron, and other selected TE metal borides at higher temperatures. Similarly, Figure 2.2 (b) shows the effect of temperature on the electrical conductivity of the TE materials [63, 91]. The electron-deficient boron contains very low  $\sigma$ -values in comparison to that of the electron rich metal hexaborides. The  $\sigma$ -value of  $\beta$  - boron increases slightly at higher temperatures. Among the metal hexaborides, CeB<sub>6</sub>, SmB<sub>6</sub>, and SrB<sub>6</sub> showed good electrical conductivity in comparison to the YbB<sub>6</sub>, BaB<sub>6</sub>, and CaB<sub>6</sub>. Hence, the metal hexaborides with relatively larger *S*-values have relatively smaller  $\sigma$ -values.

In general, the metal hexaborides exhibit low  $\kappa$ -values ( $< 50$  W/m $\cdot$ K) at different temperatures [92]. Figure 2.3(a) shows the thermal conductivities of CaB<sub>6</sub>, SrB<sub>6</sub>, and BaB<sub>6</sub> from 320 to 1080 K [91]. The thermal conductivities of all the alkaline-earth metal hexaborides decrease with the increase in temperature. SrB<sub>6</sub> has a relatively lower  $\kappa$ -value, while compared to that of BaB<sub>6</sub> and CaB<sub>6</sub>. However, at higher temperatures of  $\sim 1080$  K, the  $\kappa$ -values of both CaB<sub>6</sub>, and SrB<sub>6</sub> are the same, and they are slightly more than the  $\kappa$ -value of BaB<sub>6</sub>. As shown in the Figure 2.3(b), the *ZT* values of the alkaline earth metal hexaborides increase with the temperature [91].

Although the  $ZT$ -values of  $\text{CaB}_6$ ,  $\text{SrB}_6$  and  $\text{BaB}_6$  are very similar at 320 K,  $\text{CaB}_6$  have relatively higher  $ZT$  ( $\sim 0.3$ ) at 1080 K, while compared to the  $ZT$  of other ( $\text{BaB}_6$ , and  $\text{SrB}_6$ ) alloys.

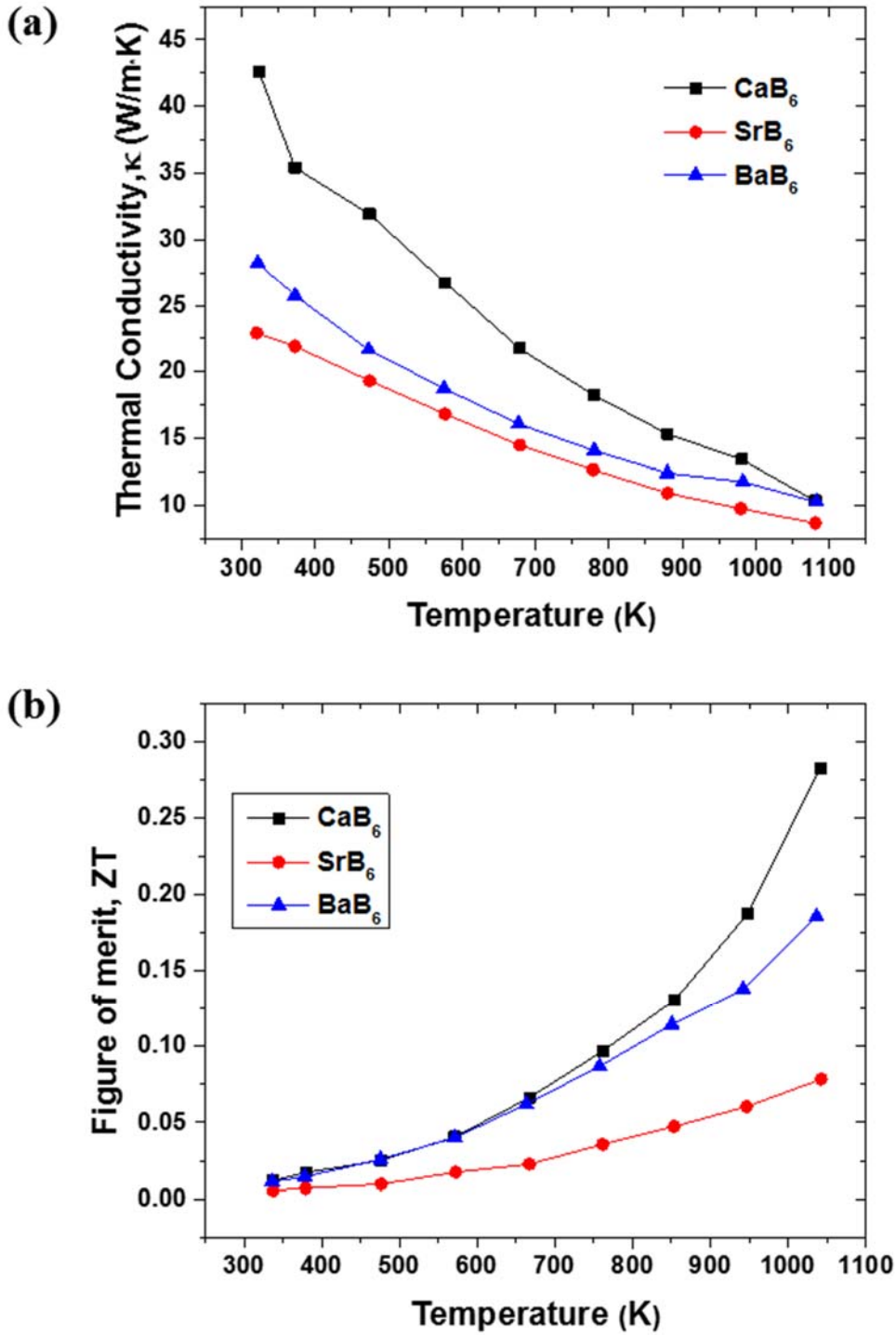


Figure 2.3 Effect of Temperature on (a) Thermal Conductivity,  $\kappa$  and (b) Figure of Merit,  $ZT$  of  $\text{CaB}_6$ ,  $\text{SrB}_6$ , and  $\text{BaB}_6$  [91].

### 2.1.2. Titanium Diboride

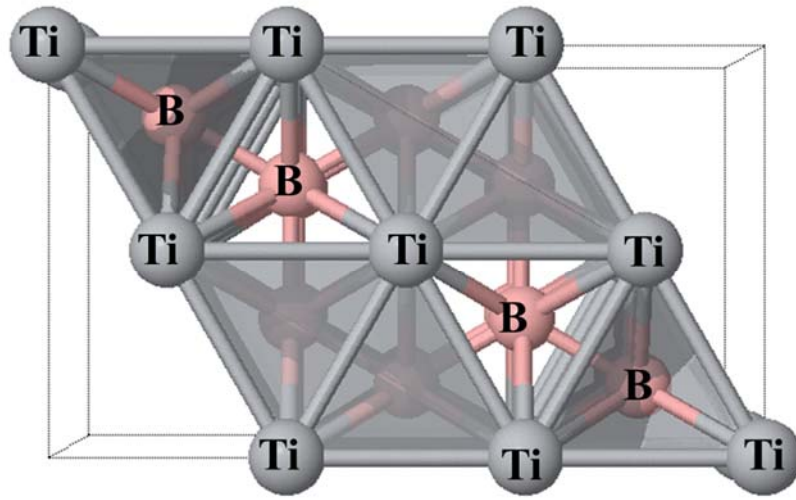


Figure 2.4 Multiple Unit Cell Crystal Structure of TiB<sub>2</sub> [29].

Titanium diboride (TiB<sub>2</sub>) is an important metal boride, which has been less extensively studied as a TE material. Figure 2.4 shows the multiple unit cell crystal structure of TiB<sub>2</sub>. It consists of atoms linked *via* both covalent, and ionic bonds [93]. The grey-colored shaded region of the TiB<sub>2</sub> polyhedron represents the metallic nature of the alloy. The space group of TiB<sub>2</sub> is  $P6/mmm$ , and the unit cell parameters of TiB<sub>2</sub> are:  $a = b = 0.303 \text{ \AA}$ , and  $c = 0.323 \text{ \AA}$ , and  $\alpha = \beta = 90^\circ$ , and  $\gamma = 120^\circ$ . The density of TiB<sub>2</sub> is  $4.50 \text{ g/cm}^3$ , and the unit cell volume is  $25.68 \text{ \AA}^3$  [29]. TiB<sub>2</sub> is characterized by very high melting point (3498 K), high chemical stability (oxidation resistance up to 1273 K), good hardness at high temperatures, better electrical, and thermal conductivities. All these properties prompted several researchers to study the transport properties of the material [29]. Williams *et al.* have studied the transport properties of high pure, and polycrystalline TiB<sub>2</sub> alloy [94]. Seebeck coefficient ( $S$ ) measurements were carried out from 0 K to 1500 K. Electrical resistivity data was collected from 300 to 1800 K, and thermal conductivity readings were obtained from 80 to 400 K.

Table 2.3 TE Properties of Polycrystalline TiB<sub>2</sub> obtained from 280 K to 400 K [94].

Temperature (K)	$S$ ( $\mu\text{V}/\text{K}$ )	$\sigma \times 10^6$ ( $1/\text{Ohm}\cdot\text{m}$ )	$\kappa$ ( $\text{W}/\text{m}\cdot\text{K}$ )	$ZT$ ( $\times 10^{-3}$ )
280	-2.22	12.56	118	0.15
300	-2.70	11.49	116	0.22
320	-3.13	10.58	114	0.29
340	-3.54	9.80	112	0.37
360	-3.92	9.12	110	0.46
380	-4.26	8.52	109	0.54
400	-4.60	8.00	108	0.63

Table 2.3 lists the TE properties of TiB<sub>2</sub> obtained at 280 K to 400 K. Although TiB<sub>2</sub> have very high  $\sigma$ -values, it shows low  $S$ -values, and high  $\kappa$ -values that resulted in poor  $ZT$  values. Increasing trend of  $S$ , and decreasing trend of  $\kappa$  with the increase in temperature, suggests that TiB<sub>2</sub> is a good promising material for high temperature application. As shown in the Figure 2.5(a), the semi-local density functional calculations (DFT) of the energy band structure of TiB<sub>2</sub> do not reveal any significant energy band gap ( $\sim 0$  eV). This further confirms the previous observation that the TiB<sub>2</sub> crystal contain large number of charge carriers (Figure 2.4 and Table 2.3). From Figure 2.5(b), the density functional theory (DFT) calculations of the density of states (DOS) indicates that the fermi level of TiB<sub>2</sub> is located just in the dip between the two large peaks of the DOS curve [66]. As the temperature coefficient of electronic contribution to the specific heat is proportional to the DOS at the fermi level, TiB<sub>2</sub> has the minimum temperature coefficient value

( $1.08 \text{ mJ/K}^2$ ) relative to the temperature coefficients of other transition metal diborides ( $\text{ScB}_2$ ,  $\text{VB}_2$ ,  $\text{CrB}_2$ , and  $\text{MnB}_2$ ) [66]. In addition,  $\text{TiB}_2$  have been used as an additive to improve the TE performance of the composite materials, like  $\text{B}_4\text{C-TiB}_2$  [96], and  $\beta\text{-FeSi}_2\text{-TiB}_2$  [97].

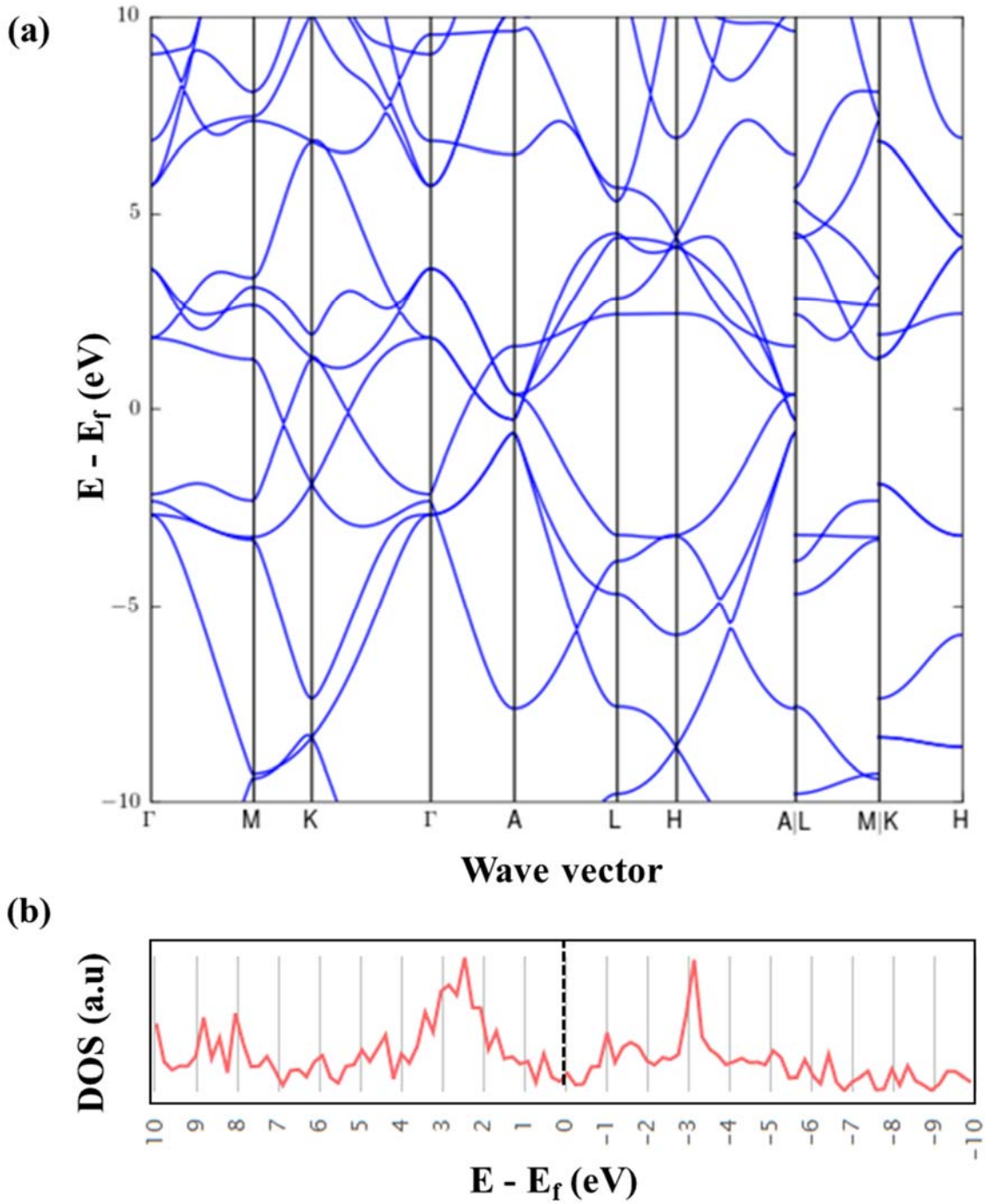


Figure 2.5 Calculated (a) Energy Band Structure, and (b) Density of States (DOS) of  $\text{TiB}_2$  [95].

## 2.2. Silicide TE Alloys

In 1958, Nikitkin E.N conducted first thermoelectric property study on silicides by measuring the electrical conductivity, and thermal power at different temperatures [98]. The author revealed that CrSi<sub>2</sub>, MnSi, MnSi<sub>2</sub>, and CoSi are promising materials for the TE application at mid/high temperatures. Then, several other researchers have shown interest in developing metal silicides as TE materials. Metal silicides are attractive due to (a) low-cost, (b) abundance in earths cost, (c) eco-friendly, (d) high mechanical strength, and (e) good chemical stability [68, 99-103].

### 2.2.1. Properties of TE Silicides

Table 2.4 Properties of some Selected TE Metal Silicides at 300 K [29, 68, 100, 102-105].

Metal Silicides	$M.P^{\dagger}$ (K)	$\rho^{\#}$ (g/cm <sup>3</sup> )	$-\Delta_f H^{\circ\&$ (kJ/mol)	Type	$\kappa_l^{\ddagger}$ (W/mK)	$\mu_i^{\diamond}$ (cm <sup>2</sup> /Vs)	$E_g^{\blacksquare}$ (eV)	$ZT_{\max}$
Mg <sub>2</sub> Si	1358	1.98	26	n	~ 8	65	0.7	0.9
CrSi <sub>2</sub>	1763	4.98	108	p	6.8	0.15 - 15	0.7	0.25
MnSi <sub>1.7</sub>	1430	5.18	33	p	2.9	40	0.66	0.9
$\beta$ -FeSi <sub>2</sub>	1490	4.93	74	n, p	4.0	2 - 4	0.87	<sup>a</sup> 0.4, <sup>b</sup> 0.2
CoSi	1700	6.56	100	n	~1.5	~43	0.01	0.2
Ru <sub>2</sub> Si <sub>3</sub>	1970	6.96	134	n, p	4.0	10 - 29	1.1	<sup>a</sup> 0.4, <sup>b</sup> 0.2
ReSi <sub>1.75</sub>	2213	10.44	70	p	~5.5	~105	0.15	0.8

<sup>\dagger</sup> $M.P$  - Melting point; <sup>\#</sup> $\rho$  -Density; <sup>\&</sup> $\Delta_f H^{\circ}$  -Heat of formation; <sup>\ddagger</sup> $\kappa_l$ -Lattice thermal conductivity; <sup>\diamond</sup> $\mu_i$ - Carrier mobility; <sup>\blacksquare</sup> $E_g$ -Energy band gap, <sup>a</sup>(n-type), <sup>b</sup>(p-type).

Extensive research have been conducted on alkaline earth metal silicide ( $Mg_2Si$ ), and transition metal silicides ( $MnSi_{1.73}$ ,  $ReSi_{1.75}$ ,  $\beta$ - $FeSi_2$ ,  $Ru_2Si_3$ ,  $CrSi_2$ , and  $CoSi$ ) because of high  $ZT$  at mid/high temperatures. Table 2.4 lists some important properties of the selected metal silicides.

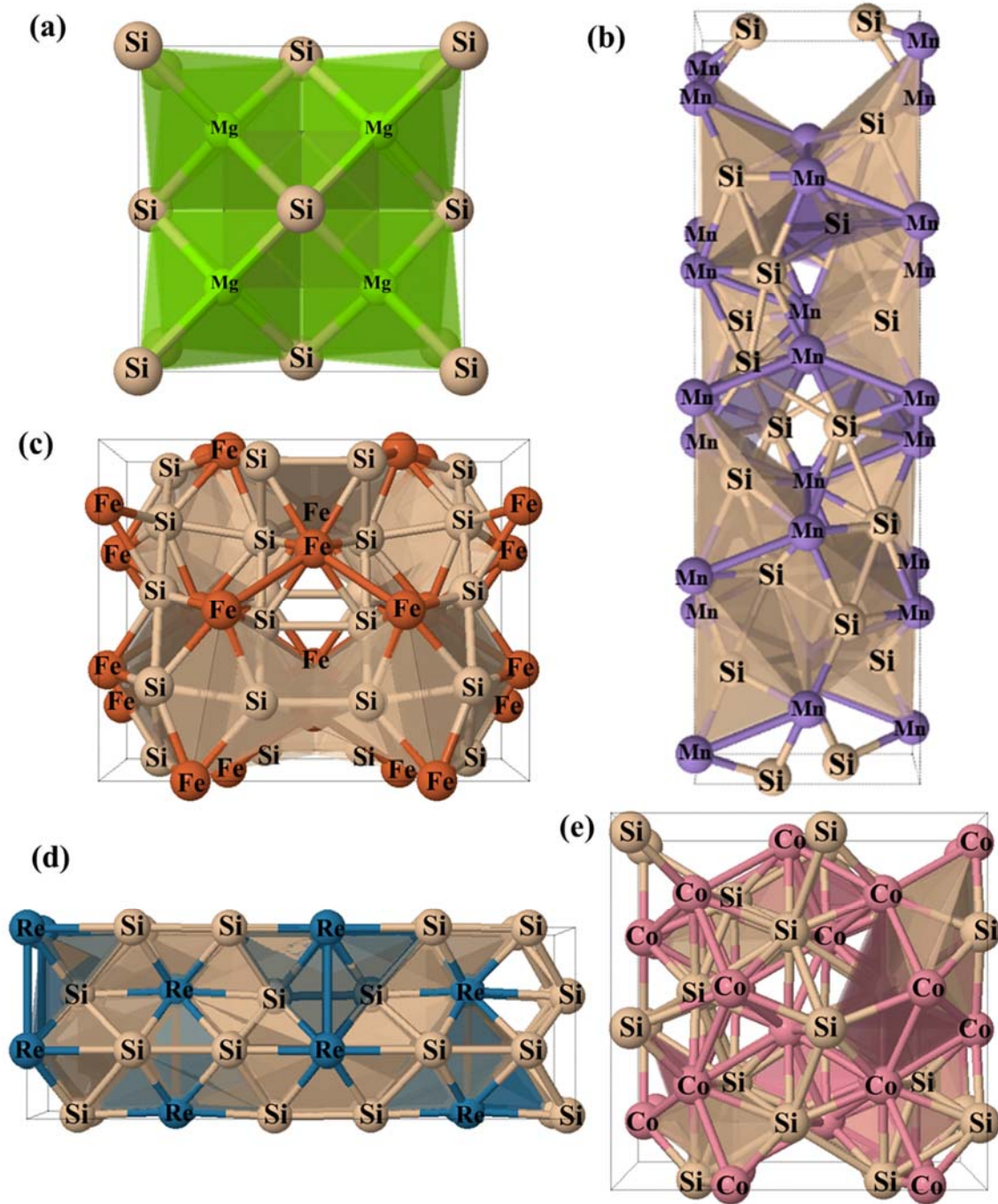


Figure 2.6 Crystal Structures of Unit Cell of (a)  $Mg_2Si$ , (b)  $MnSi_{1.7}$ , (c)  $\beta$ - $FeSi_2$ , and Multiple Unit Cell of (d)  $ReSi_{1.75}$ , and (e)  $CoSi$  [29].

$Mg_2Si$  have relatively low melting point, low density, low heat of formation, and high  $ZT$  in comparison to the transition metal silicides.  $MnSi_{1.7}$ , and  $ReSi_{1.75}$  are other high performing TE materials with  $ZT_{max}$  comparable to that of  $Mg_2Si$ .

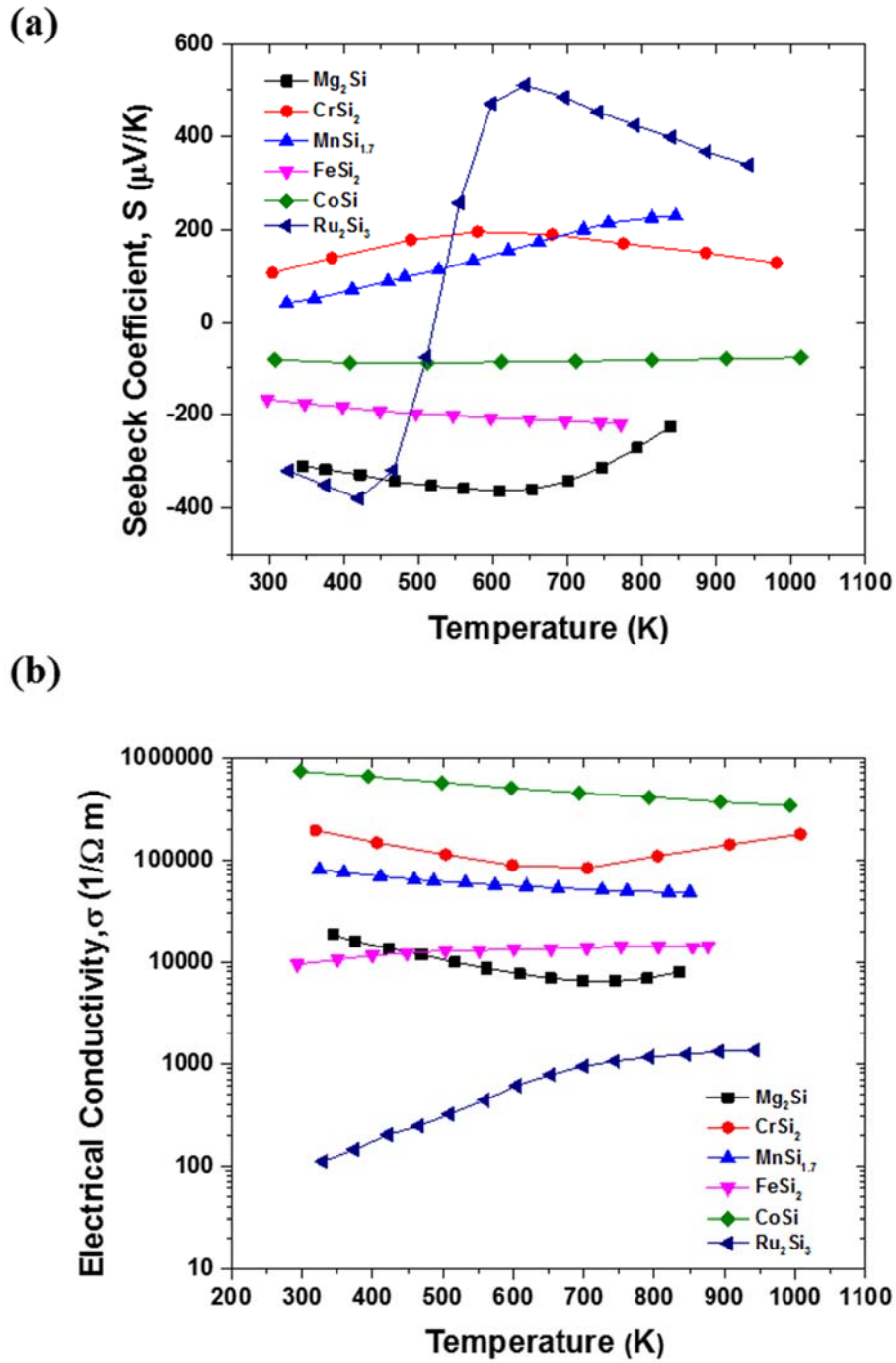


Figure 2.7 Effect of Temperature on (a) Seebeck Coefficient, and (b) Electrical Conductivity of Metal Silicides [68, 97, 100, 101].

Figure 2.6 shows the crystal structure of unit cell of (a)  $\text{Mg}_2\text{Si}$ , (b)  $\text{MnSi}_{1.7}$ , and (c)  $\beta\text{-FeSi}_2$ , and multiple unit cell of  $\text{ReSi}_{1.75}$ , and (e)  $\text{CoSi}$  [29]. From the polyhedron structures, the proportion of metallic component (green-shaded region) in  $\text{Mg}_2\text{Si}$  structure is relatively high, while compared to that in transition metal silicides (other than sand-colored region). Therefore, it is directly related to the molar ratio of metal to silicon in the metal silicides. The structural frame work also influences the thermoelectric properties of the metal silicides. As shown in the Figure 2.7(a), the Seebeck coefficients of six selected metal silicides ( $\text{Mg}_2\text{Si}$ ,  $\text{CrSi}_2$ ,  $\text{MnSi}_{1.73}$ ,  $\beta\text{-FeSi}_2$ ,  $\text{CoSi}$ , and  $\text{Ru}_2\text{Si}_3$ ) are plotted from 300 K to 1030 K.  $\text{Mg}_2\text{Si}$ ,  $\beta\text{-FeSi}_2$ ,  $\text{Ru}_2\text{Si}_3$ , and  $\text{CoSi}$  have negative  $S$ -values (or  $n$ -type), while  $\text{MnSi}_{1.7}$ ,  $\text{CrSi}_2$ , and  $\text{Ru}_2\text{Si}_3$  have positive  $S$ -values (or  $p$ -type).  $\text{Ru}_2\text{Si}_3$  contain high  $S$ -values and therefore can be used as both  $n$ -type ( $T < \sim 550$  K), and  $p$ -type ( $T > \sim 550$  K) TE material. Other materials with better  $S$ -values are  $\text{Mg}_2\text{Si}$ , and  $\text{MnSi}_{1.7}$ . Figure 2.7(b) displays the effect of temperature on the  $\sigma$ -values of the metal silicides.  $\text{CoSi}$  and  $\text{CrSi}_2$  have very high  $\sigma$ -values, and  $\text{Ru}_2\text{Si}_3$  have the least  $\sigma$ -value. With the increase in temperature, an increase in  $\sigma$ -value was observed for  $\text{Ru}_2\text{Si}_3$ , and  $\beta\text{-FeSi}_2$ , while decrease in the  $\sigma$ -value was noticed in case of  $\text{CoSi}$  and  $\text{MnSi}_{1.7}$ . The  $\sigma$ -value of  $\text{Mg}_2\text{Si}$  and  $\text{CrSi}_2$  decreased up to 700 K, and then, a further increase in the temperature resulted in an increase in their electrical conductivities.

Metal silicides are characterized by low thermal conductivities. As shown in Figure 2.8(a), the effect of temperature on the  $\kappa$ -values of  $\text{Mg}_2\text{Si}$ ,  $\text{CrSi}_2$ ,  $\text{MnSi}_{1.73}$ ,  $\beta\text{-FeSi}_2$ ,  $\text{CoSi}$ , and  $\text{Ru}_2\text{Si}_3$ .  $\text{MnSi}_{1.7}$  exhibited lowest  $\kappa$ -values, followed by  $\text{Ru}_2\text{Si}_3$ ,  $\text{FeSi}_2$ , and  $\text{Mg}_2\text{Si}$  at all temperatures.  $\text{CoSi}$  and  $\text{CrSi}_2$  have relatively higher thermal conductivities. The selected metal silicides have good  $ZT$  from 500 K to 800 K. As shown in the Figure 2.8(b), the  $ZT$  vs. temperature plot of  $\text{Mg}_2\text{Si}$ ,  $\text{CrSi}_2$ ,  $\text{MnSi}_{1.73}$ ,  $\beta\text{-FeSi}_2$ ,  $\text{CoSi}$ , and  $\text{Ru}_2\text{Si}_3$ .  $\text{Mg}_2\text{Si}$  and  $\text{MnSi}_{1.7}$  have high  $ZT$  values, while other metal silicides exhibited relatively low  $ZT$  values. Although  $\text{Ru}_2\text{Si}_3$ ,  $\text{FeSi}_2$ , and  $\text{CrSi}_2$  have low  $ZT$  at  $T <$

600 K, the TE performance of these silicides increases with further increase in the temperature.

No appreciable change in the  $ZT$ - value of  $\text{CoSi}$  was observed with the increase in temperature.

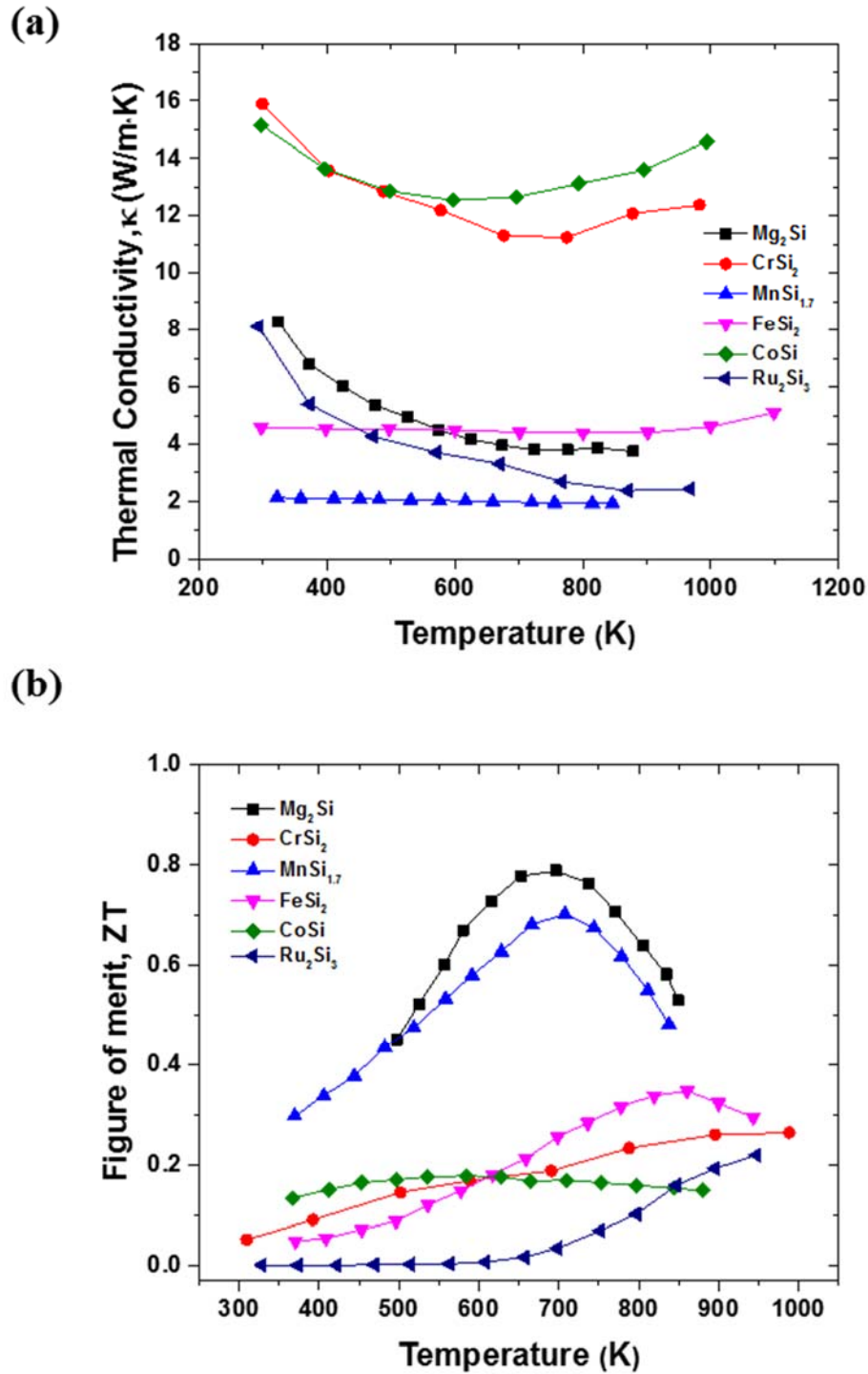


Figure 2.8 Effect of Temperature on (a) Thermal Conductivity,  $\kappa$  and (b)  $ZT$  of  $\text{Mg}_2\text{Si}$ ,  $\text{CrSi}_2$ ,  $\text{MnSi}_{1.73}$ ,  $\beta\text{-FeSi}_2$ ,  $\text{CoSi}$ , and  $\text{Ru}_2\text{Si}_3$  [68, 97, 100, 101].

### 2.2.2. Magnesium Silicides

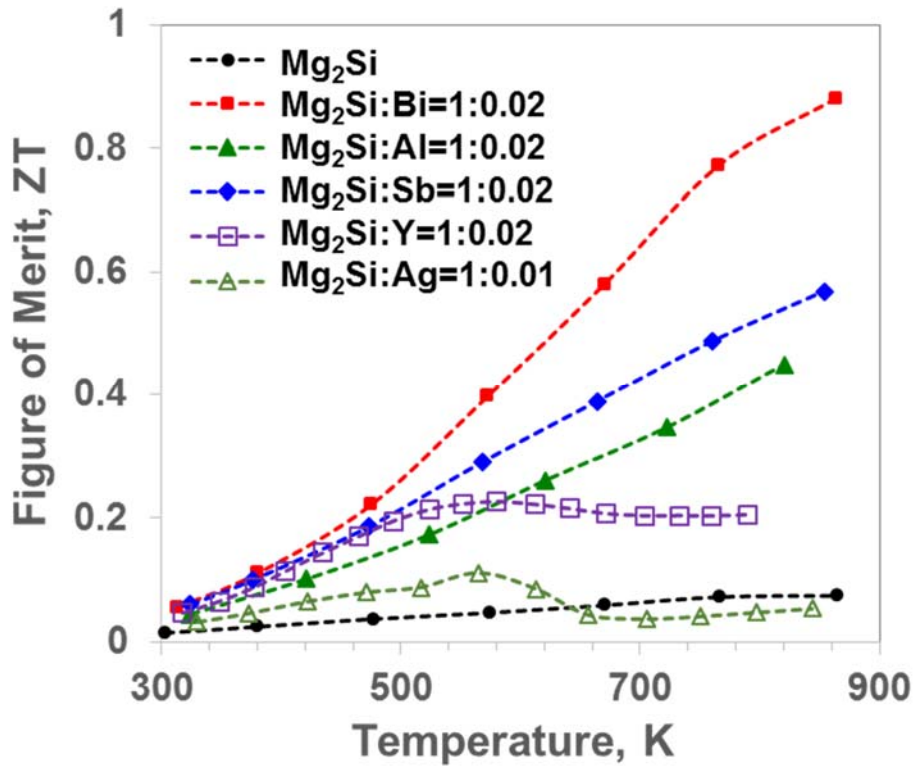


Figure 2.9 Effect of Metal-doping on  $ZT$  of  $Mg_2Si$  at Different Temperatures [106-110].

The TE performance of  $Mg_2Si$  can be altered *via* doping with small amounts of metal (donor or acceptor), which effect the carrier concentration of the alloy. Metal-doped magnesium silicides ( $Mg_2Si: X = 1: m$ ;  $X =$  dopant metal,  $m =$  dopant concentration) are increasingly attractive for TE applications at high temperatures (500 - 800 K) because of their low density, large natural abundance, non-toxicity, good thermal stability, and transport properties [106 - 110]. As plotted in Figure 2.9, the effect of five different metal dopants (Bi, Al, Sb, Y, and Ag) on  $ZT$  of  $Mg_2Si$  is shown at different temperatures. The concentration of metal dopants used are:  $m = 0.02$  moles (Bi, Al, Sb, and Y), and  $m = 0.01$  mol (Ag). A significant improvement in the  $ZT$  was observed with the addition of metals to  $Mg_2Si$  crystal structure.  $Mg_2Si: Bi$  exhibited relatively higher

enhancement in  $ZT$ - values compared to pure  $Mg_2Si$  (un-doped). Other alloys ( $Mg_2Si$ : Sb,  $Mg_2Si$ : Al, and  $Mg_2Si$ : Y) have similar positive effect on the  $ZT$  of  $Mg_2Si$ , while  $Mg_2Si$ : Ag showed small, and negative effect on the  $ZT$  enhancement of  $Mg_2Si$  at higher temperatures.

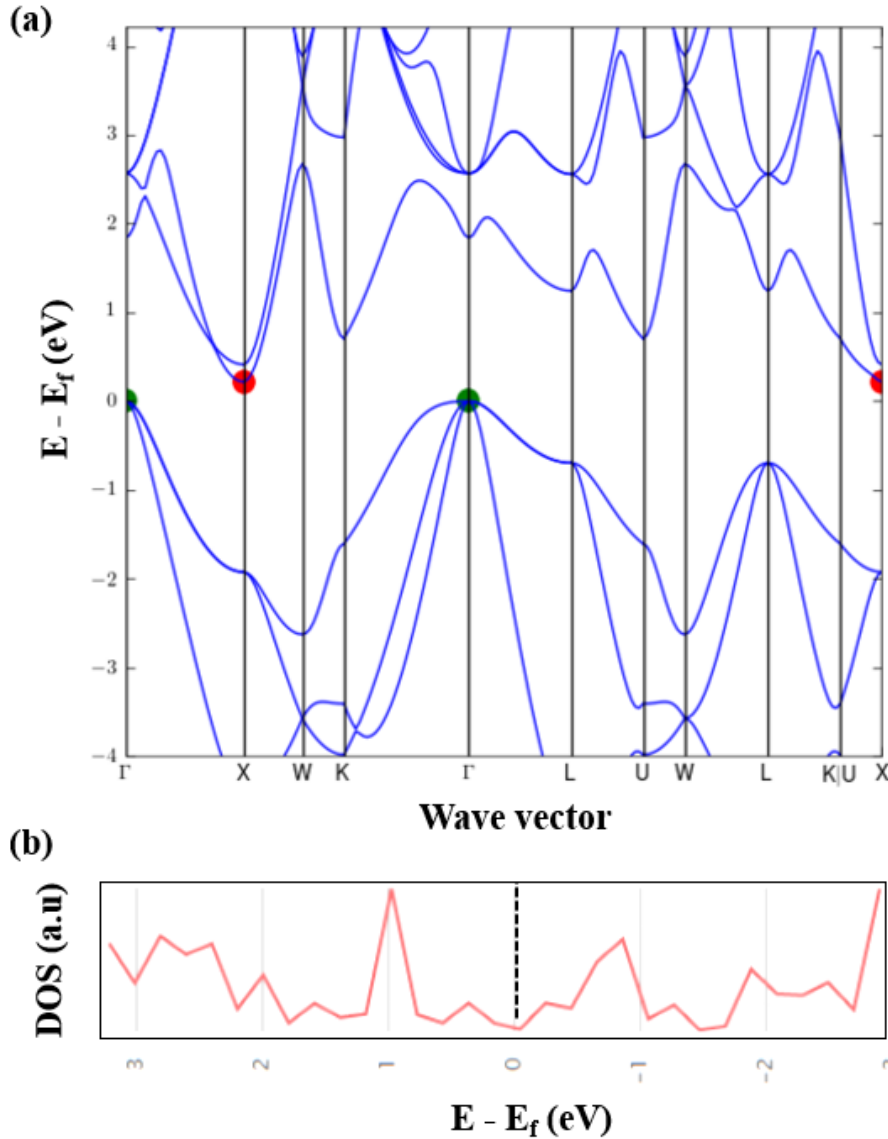


Figure 2.10 Calculated (a) Energy Band Structure, and (b) Density of States (DOS) of  $Mg_2Si$  [95].

As shown in the Figure 2.10, the calculations for the band structure, and density of states of  $Mg_2Si$  shows the existence of narrow indirect energy band gap (0.218 eV) for  $Mg_2Si$ . Also, the calculated formation energy of  $Mg_2Si$  is -1.60 eV per atom [95].

### 2.2.3. Higher Manganese Silicides

Higher manganese silicide (HMS) assume Nowotny chimney ladder structure, in which Mn atoms form the chimney, and Si atoms spiral around them as the ladder [111]. Figure 2.11 shows the formation of chimney ladder crystal structure of  $Mn_4Si_7$  from constituent Mn and Si structures. As shown in the Figure 2.11, the crystal structures and the relative sizes of four HMS phases ( $MnSi_{2-x}$ ), namely  $Mn_4Si_7$ ,  $Mn_{11}Si_{19}$ ,  $Mn_{15}Si_{26}$ , and  $Mn_{27}Si_{47}$ . Besides having complicated crystal structure, HMS show distinct anisotropy of the TE properties. HMS have good potential for TE heat recovery from 573 - 873 K. Zaitsev *et al.* have shown that the doping of HMS with the metals (Al, Mo, and Ge) can further improve the TE performance of the HMS alloys [112].

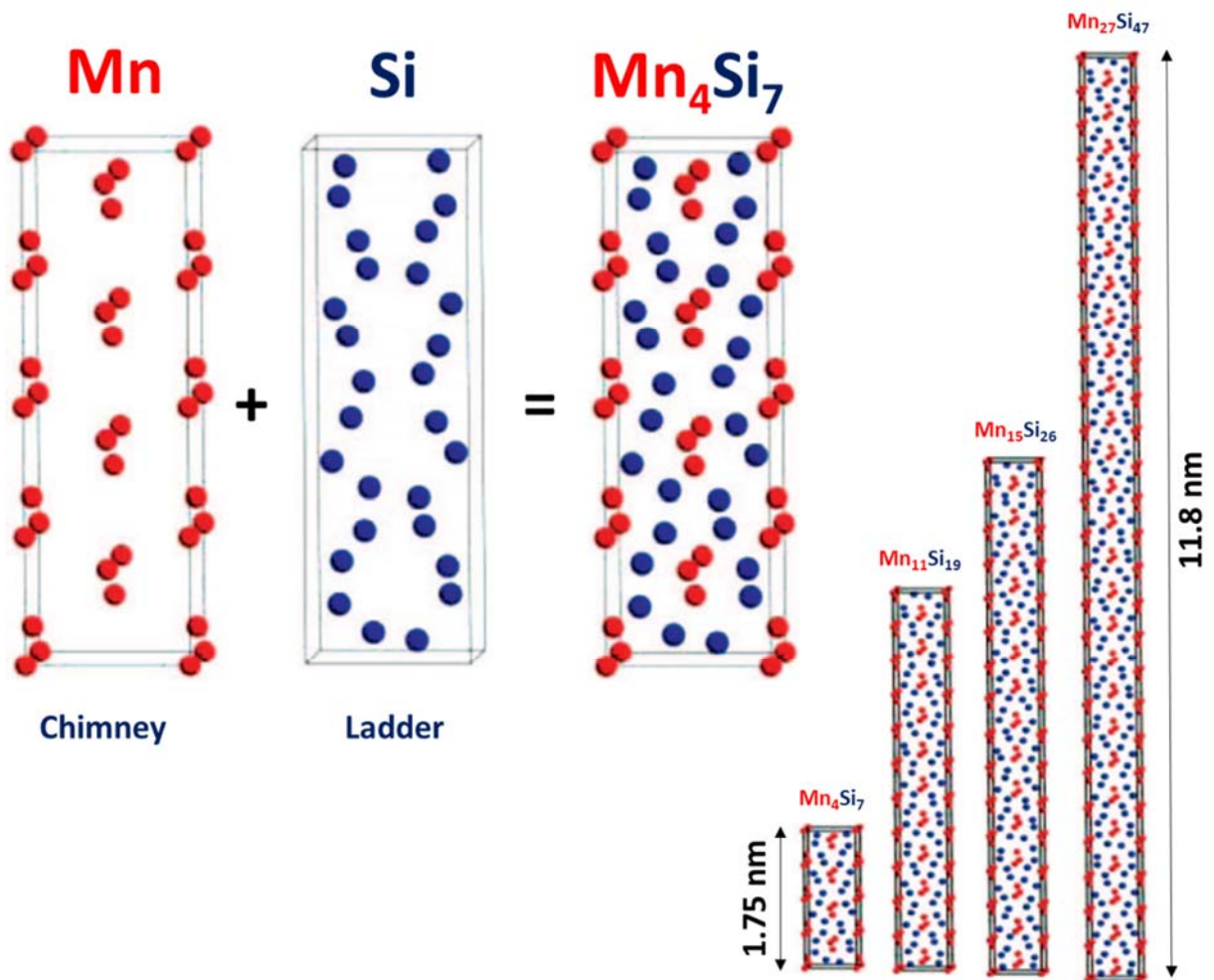


Figure 2.11 Formation of Nowotny Chimney Ladder Crystal Structure of  $Mn_4Si_7$ , and Four HMS Phases with their Relative Size [111].

As shown in the Figure 2.12, the DFT calculations of (a) band structure, and (b) density of states reveal that the HMS ( $\text{Mn}_4\text{Si}_7$ ) alloy possesses an indirect narrow energy band gap of 0.779 eV with the fermi energy level located next to the peak ( $\Delta E = E - E_f = \sim 0$ ). Unlike the band structure of  $\text{Mg}_2\text{Si}$  (Figure 2.10a), the band structure of  $\text{Mn}_4\text{Si}_7$  is much more complicated with larger number of energy levels in both valance and conduction bands. The evaluation also predicts that the energy required for the formation of the  $\text{Mn}_4\text{Si}_7$  is - 0.433 eV per atom.

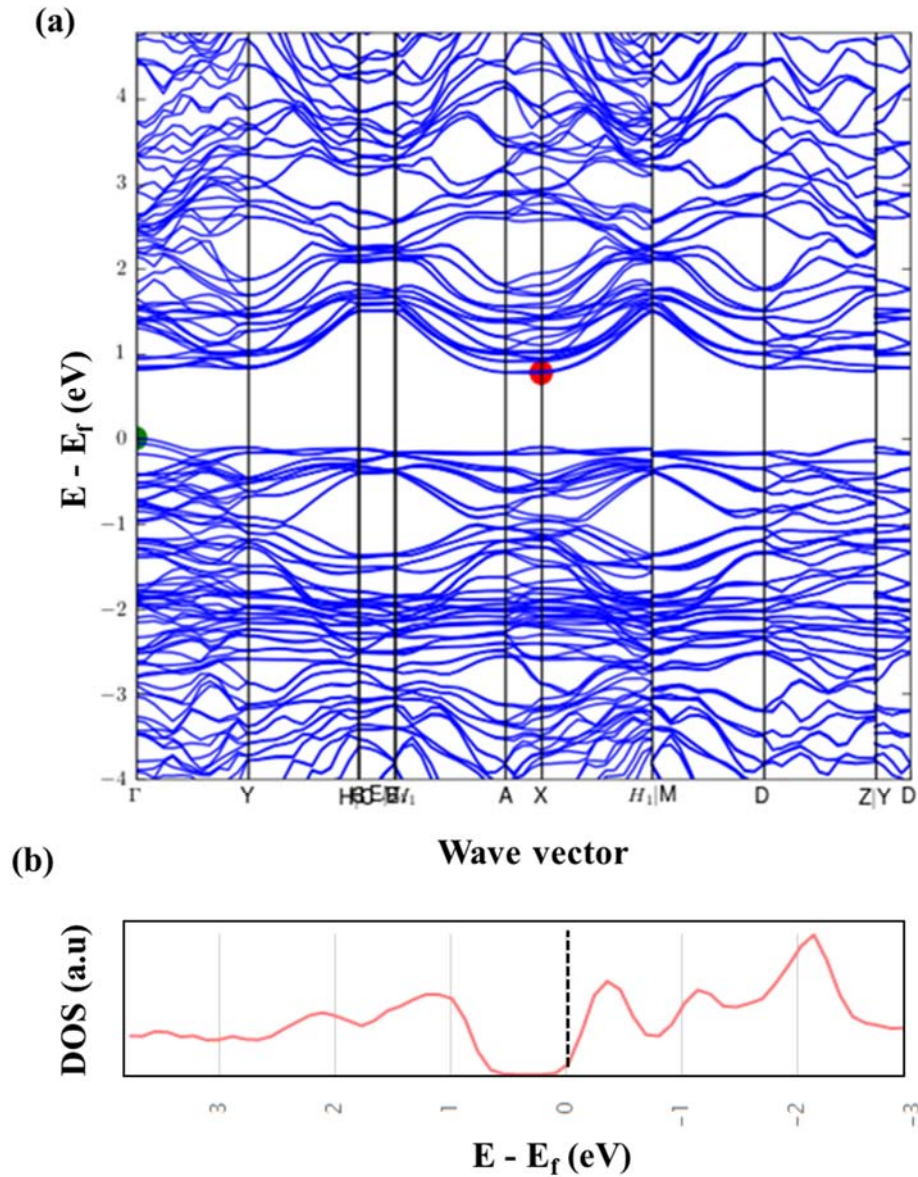


Figure 2.12 Calculated (a) Energy Band Structure, & (b) Density of States (DOS) of  $\text{Mn}_4\text{Si}_7$  [95].

## CHAPTER 3

### RESEARCH OBJECTIVES

The main objective of current research is to develop thermoelectric metal borides and silicides with good figure of merit ( $ZT$ ) for high temperature applications. Borides and silicides of alkaline earth, and transition metals are considered as potential TE materials in the present study. These include binary alloys of the systems: Mg-Si, and Ti/Nb/Mn – Co – B/Si. In addition, the current study focuses on the development of synthesis methods, characterization, phase stability, reaction kinetics, thermodynamic, and thermoelectric property studies of the metal borides and silicides. The solid-state TE devices fabricated from the metal borides and silicides are not only cheaper, durable, and eco-friendly, but also are expected to show good performance in waste heat recovery application at higher temperatures.

As shown in the Figure 3.1, the specific tasks of the current research project are:

1. To select potential metal borides and silicides with good  $ZT$  for high temperature (400 – 1000 °C) applications. Screening of alkaline earth metal borides and silicides ( $\text{CaB}_6$ ,  $\text{SrB}_6$ ,  $\text{Mg}_2\text{Si}$  and  $\text{CaSi}$ ), and binary alloys of transition metal borides and silicides of ABX-type ( $A = \text{Ti/ Nb/ Mn}$ ;  $B = \text{Co}$ ;  $X = \text{B/Si}$ ) were carried out based on the available literature for energy band gaps, crystal structure, transport, and thermodynamic properties of the TE alloys, and from the evaluations using Arrhenius relation.
2. To synthesize the potential TE metal borides and silicides ( $\text{Mg}_2\text{Si}$ , metal-doped  $\text{Mg}_2\text{Si}$ ,  $\text{TiB}_2$ , and  $\text{Mn}_4\text{Si}_7$ ) using cold-pressing, sintering, and arc-melting methods.

- To determine the experimental parameters (sintering temperature, sintering time, arc-melter power, Ar gas pressure, etc.) for production of the alloys.
- To experimentally determine the phase equilibria, and thermodynamic properties of the metal borides and silicides using characterization techniques, such as SEM, EDS, XRD, DSC, DTA, and EMF cell.
- To study reaction kinetics and thermal stability of metal silicides ( $\text{Mg}_2\text{Si}$ ,  $\text{Mg}_2\text{Si}:m\text{X}$ ;  $\text{X} = \text{Ti/Nb/Mn/Co}$ ,  $m = 0 - 0.08 \text{ mol}$ ) using heat flow measurements of DSC/DTA, and EMF data of solid-state galvanic cell. Thermodynamic quantities such as specific heat ( $C_p$ ), change in enthalpy ( $\Delta H$ ), change in entropy ( $\Delta S$ ) and change in Gibbs energy ( $\Delta G$ ), activity ( $a_i$ ), and activity coefficient ( $\gamma_i$ ) are determined for the alloys.
- To determine the thermoelectric properties (Seebeck coefficient, electrical conductivity, thermal conductivity, and figure of merit,  $ZT$ ) of arc-melted samples of transition metal boride ( $\text{TiB}_2$ ), and transition metal silicide ( $\text{Mn}_4\text{Si}_7$ ) using the  $ZT$ -Scanner instrument.

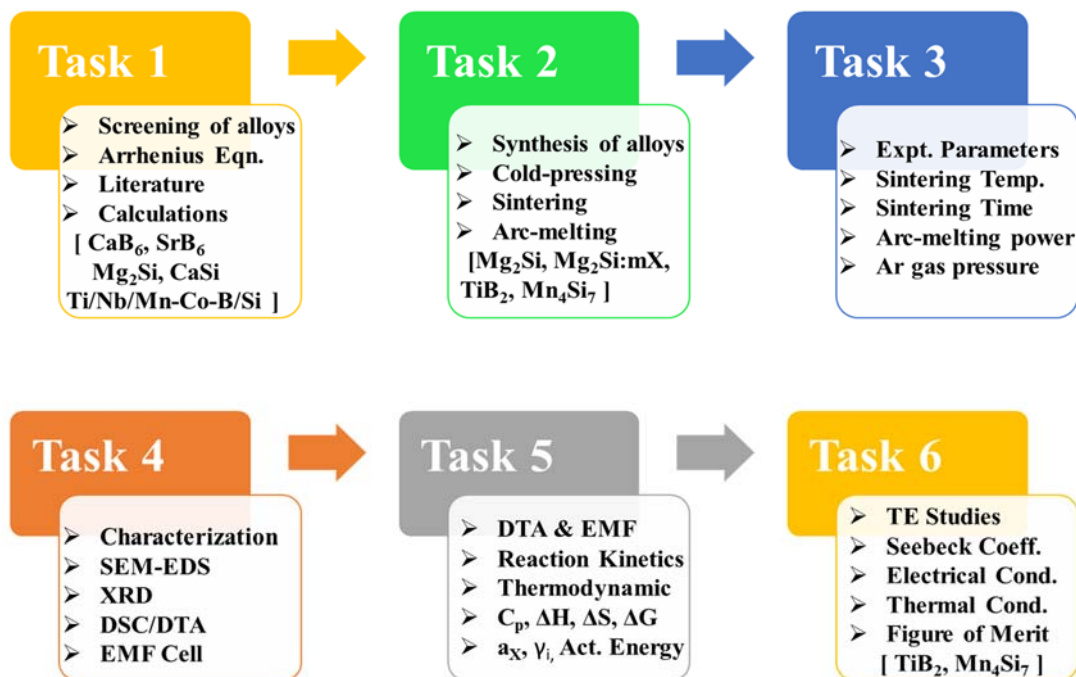


Figure 3.1 A Schematic Outlining the Specific Tasks of Current Research Project.

## CHAPTER 4

### MATERIALS AND METHODS

The raw materials, instruments, and methods used for the synthesis, and characterization of thermoelectric materials play a critical role in determination of their thermodynamic, and thermoelectric properties. This chapter addresses various principles, experimental procedures, precautions that are considered during the synthesis, and analysis of pure, and metal-doped  $\text{Mg}_2\text{Si}$ ,  $\text{TiB}_2$ , and  $\text{MnSi}_{1.7}$  alloys. In addition, the modelling tools considered for estimation of the thermodynamic properties of TE alloys are also described.

All the raw materials and instruments needed for the preparation, and characterization of the TE alloys were purchased from various vendors. Metal powders of magnesium (-325 mesh, 99.8%), silicon (-325 mesh, 99.5%), titanium (-325 mesh, 99%), manganese (-325 mesh, 99.3%), niobium (-325 mesh, 99.8%), and cobalt (-325 mesh, 99.5%) were purchased from Alfa Aesar, MA, U.S.A.  $\text{CaF}_2$  powder (99%),  $\text{MgF}_2$  powder (99.9%), and  $\text{CaF}_2$  crystal optical disc (1.3 cm diameter x 1 mm thickness) for preparation of EMF cell electrodes of were procured from Alfa Aesar.  $\text{Al}_2\text{O}_3$  (reference), and graphite (standard) for DTA study were obtained from PerkinElmer.

#### 4.1. Mixing of Powders

Certain metals, like magnesium, reacts with atmospheric oxygen to form a thin oxide surface layer, which further inhibits their reactivity. Hence, weighing and mixing of stoichiometric amounts of as-received elemental powders of the metals were carried out in a Labconco glove box (Kansas City, MO, U.S.A) under ultra-high pure argon gas atmosphere. Figure 4.1 shows the

image of Labconco glove box used in the current study for the preparation of TE materials. First, the glove box was vacuumed to remove any residual oxygen, and then argon gas was filled inside the chamber. Appropriate amounts of the raw materials were weighted using the microbalance, and the powders were mixed uniformly in Pyrex glass vials using Fischer Scientific Vortex tool.



Figure 4.1 An Image of Labconco Glove Box used for Mixing of Metal Powders.

#### **4.2. Pelleting of Mixture**

After the mixing step, about 1 - 3 g of the powder mixture was placed in a cylindrical stainless steel die of 1.3 cm inner diameter and then, subjected to a uni-axial force of 5.8 ksi using

Carver press at room temperature for 2 minutes. Figure 4.2 displays the image of Carver press used in the present study.

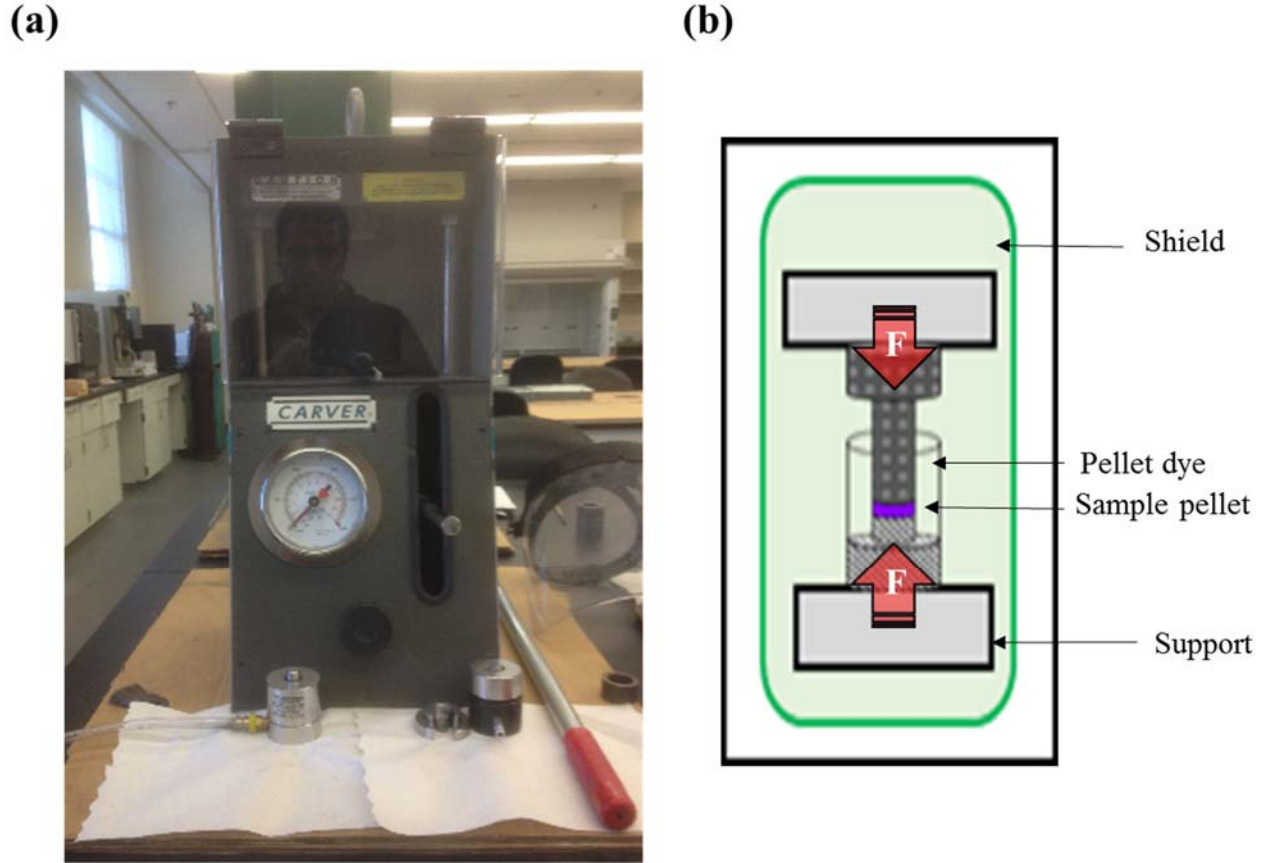


Figure 4.2 An Image of (a) Carver Press, and (b) Schematic of Pelleting the Metal Powders.

In case of the pellets that were not compressed strongly, few drops of acetone solvent (binder) was added to the sample mixture, and the powders were re-pressed for additional timings to obtain better compact pellets.

### 4.3. Sintering of Pellets

The cold-pressed sample pellets were wrapped with a tantalum foil (0.001" thickness, 99.5% Alfa Aesar) to avoid any surface oxidation. The wrapped pellets were placed in a Pyrex

glass vials and then, vacuum sealed with glass lids using Labanco glove box. Sintering of the cold-pressed pellets were conducted using Fischer Scientific box furnace. Figure 4.3 displays the image of box furnace used for sintering of the pellets. The desired temperature, and time for the sintering process are set using the programmable temperature controller that is attached to the furnace. The sealed glass vials containing the sample pellets were placed in ceramic boats. Then, the sample boats were carefully kept inside the box furnace using metal tongs, and high-temperature gloves.

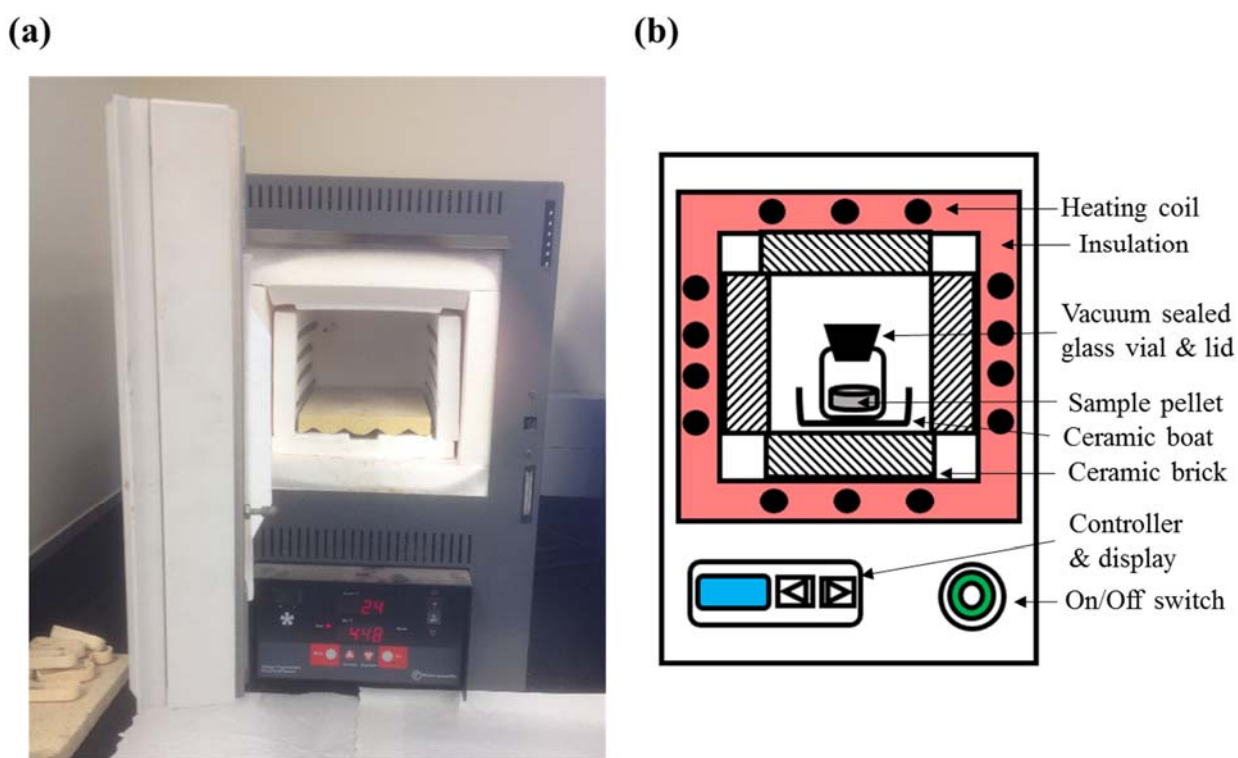


Figure 4.3 An Image of (a) Fischer Scientific furnace, and (b) Schematic of Pellet Sintering.

Any residual oxygen present in the sealed glass vials reacts with tantalum metal to produce white tantalum pentoxide ( $Ta_2O_5$ ) powder on the surface of the pellets. After the sintering process, the glass lids of the vials were removed from the glove box, and the pellets were carefully separated from the white tantalum pentoxide powders by using the forceps/tweezers.

#### 4.4. Arc-melting of Pellets

Metal boride ( $\text{TiB}_2$ ), and metal silicide ( $\text{Mn}_4\text{Si}_7$ ) samples were synthesized by mixing the elemental powders in stoichiometric proportions, cold-pressing the mixture to pellets, and heating up of the pellets in small bell jar arc-melt furnace (ABJ338, Materials Research Furnaces Inc.) under ultra-high pure argon atmosphere. Figure 4.2 (a and b) shows the images of the electric arc furnace, and its open bell jar chamber that was used for the synthesis of metal boride and silicide samples. Figure 2(c) shows the schematic of electric arc furnace with important parts labeled. The arc-furnace consists of Cu stinger or handle with its inside end attached to a pointed thorium-doped tungsten rod electrode. The metal boride or silicide sample was placed onto custom-made

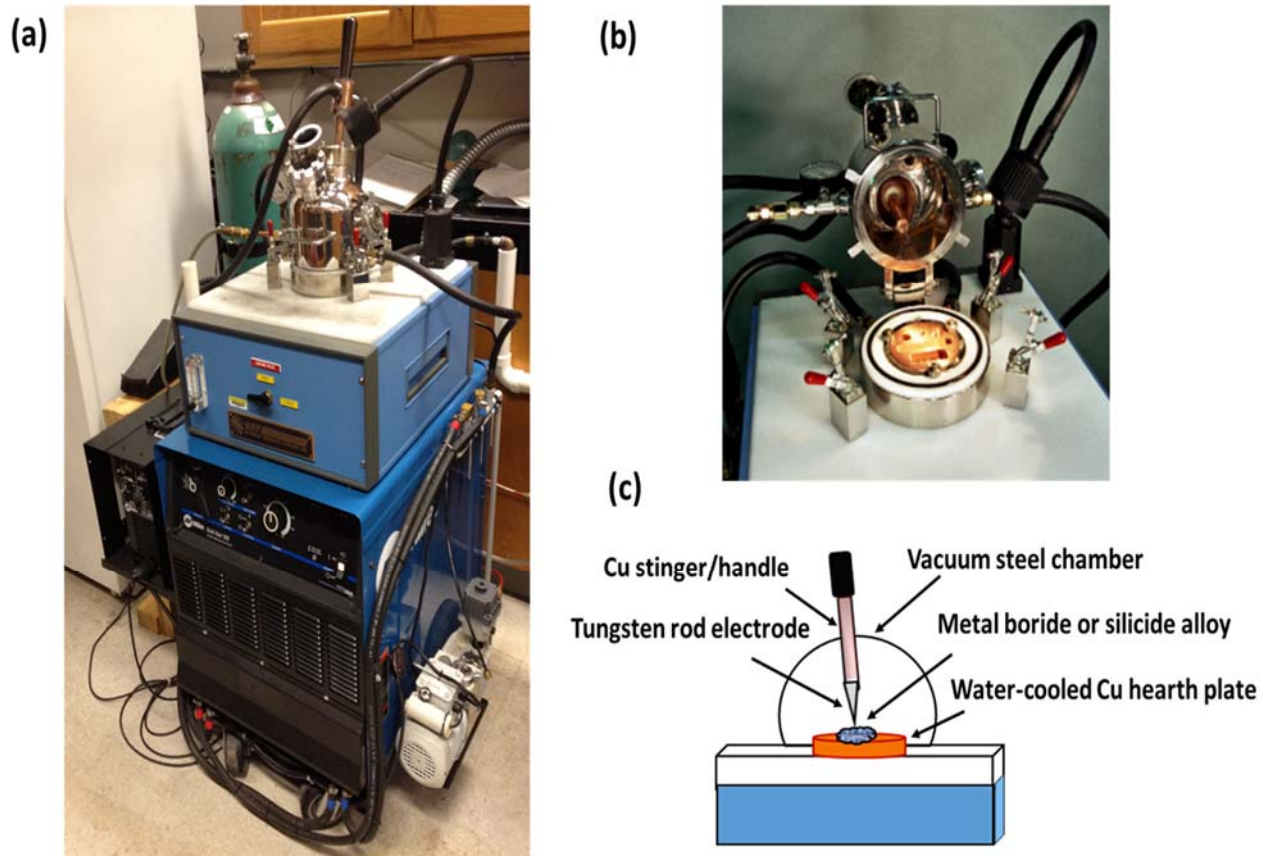


Figure 4.4 Images of (a) electric arc furnace, (b) bell jar chamber, and (c) a schematic of the furnace

cavities of water-cooled copper hearth plate (8.5 cm diameter). The 304L stainless steel bell jar chamber was closed with the metal clamps, and then, it was water-cooled to maintain the temperature of the chamber below 50 °C throughout the experiment. An evacuation pump (56 LPM) was used to create the vacuum inside the chamber. Prior to the start of the experiments, the furnace pressure was reduced to 30 mm Hg to remove any ambient air present inside the chamber. The compartment was refilled with inert argon gas for at least three times. The thorium-doped tungsten rod tip of the water-cooled stringer was placed over the oxygen getter (titanium sponge), and an electric-arc was struck to melt the titanium metal. This process removes any residual oxygen from the chamber. Later, under a standard positive argon pressure (2 psig), and by passing a current (200 A), an electric-plasma arc was struck on one edge of the sample pellet. When the temperature of the pellet reached the formation temperature of metal boride ( $\text{TiB}_2$ ) or silicide ( $\text{Mn}_4\text{Si}_7$ ), self-propagating high-temperature synthesis (SHS) of  $\text{TiB}_2$  or  $\text{Mn}_4\text{Si}_7$  took place, and the pellet was completely converted to a button-shaped ingot (alloy). After the initial melting of the pellet, the ingot button was flipped up-side down, and re-melted for at least 2-3 times in order to obtain homogeneous composition of the alloy.

#### **4.5. X-ray Diffraction**

The product samples (sintered powders/crushed ingots/pellets) were analyzed for the presence of different alloy phases using X-ray diffraction (XRD) method. Figure 4.5 shows the image of XRD, model Philips X'Pert MPD instrument. The instrument uses monochromatic radiation from Cu-K $\alpha$  source with a wavelength of 1.540 Å. The MPD instrument was operated at a voltage of 45 kV and a current of 40 mA. The samples were spread uniformly on a glass mounting slide holder, and the XRD data was acquired at different diffraction angles ( $2\theta = 20^\circ$  to  $120^\circ$ ) using the scan rate of 0.01° per sec. High-Score plus software was used to adjust the baseline threshold

of the XRD spectra. Identification of different phases present in the sample were performed manually using the International Center for Diffraction Data (ICDD) cards that are available in PDF2014 software database.

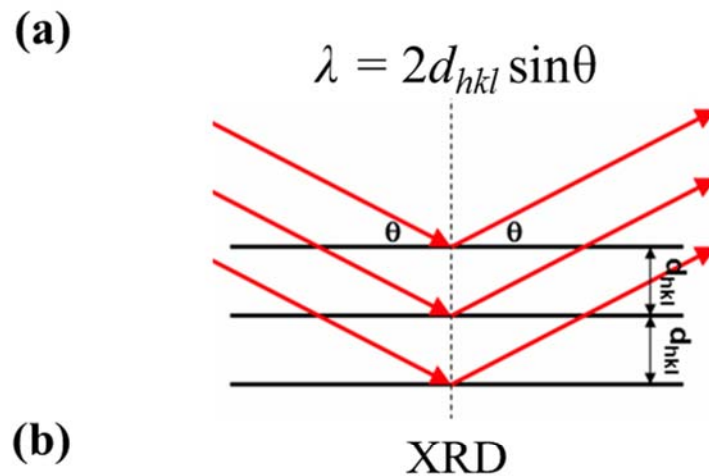


Figure 4.5 Principle of (a) XRD, and (b) an Image of X'Pert MPD used in Current Study.

#### 4.6. Scanning Electron Microscopy

The surface morphology determination, and elemental composition analysis of the samples were conducted using scanning electron microscope (SEM), model JEOL JSM 7000F that is equipped with the energy dispersive spectrometer (EDS). Figure 4.6 shows the image of JEOL 7000F SEM, and various detectors attached to it. Small amounts of the product samples were held on to the top surface of a conducting carbon tape, whose bottom surface was stuck to the sample holder. The samples were then mounted onto sample holder and then inserted into the JEOL SEM instrument. The images of microparticles of the product samples were taken at higher resolution (1500X) by setting the accelerating voltage to 20 kV, and working distance to 10.0 mm.

(a)



(b)

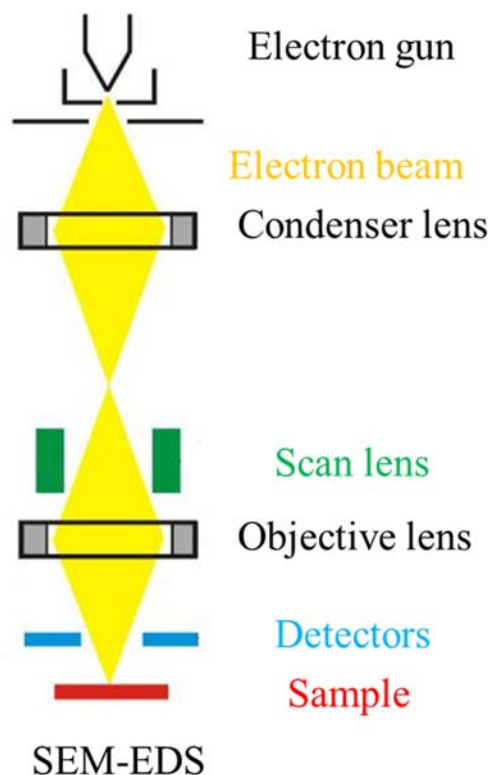


Figure 4.6 An Image of (a) JEOL 7000F SEM, and (b) Working Principle for Sample Analysis.

#### 4.7. Energy Dispersive Spectroscopy

The composition of different elements present in the sample was quantitatively determined by using the EDS detector attached to the SEM instrument. INCA analyzer software tool was used to acquire the EDS spectra from the selected region/spot of interest on the sample's SEM image.

#### 4.8. Thermal Analysis

The two types of thermal analytical techniques used in the current study are: (i) Differential Scanning calorimeter (DSC), and (ii) differential thermal analysis (DTA). PerkinElmer Diamond DSC was used to measure the heat capacities of Mg<sub>2</sub>Si powder from 50 to 350 °C, while Linseis PT1600 DTA, and PerkinElmer DTA7 were used to study the reaction kinetics, and to measure the heat capacities, and thermal stability of the samples at higher temperatures (< 850 °C). Reddy *et al.* conducted thermal studies of different samples using DSC and DTA methods [113-118].

##### 4.8.1. Differential Scanning Calorimetry

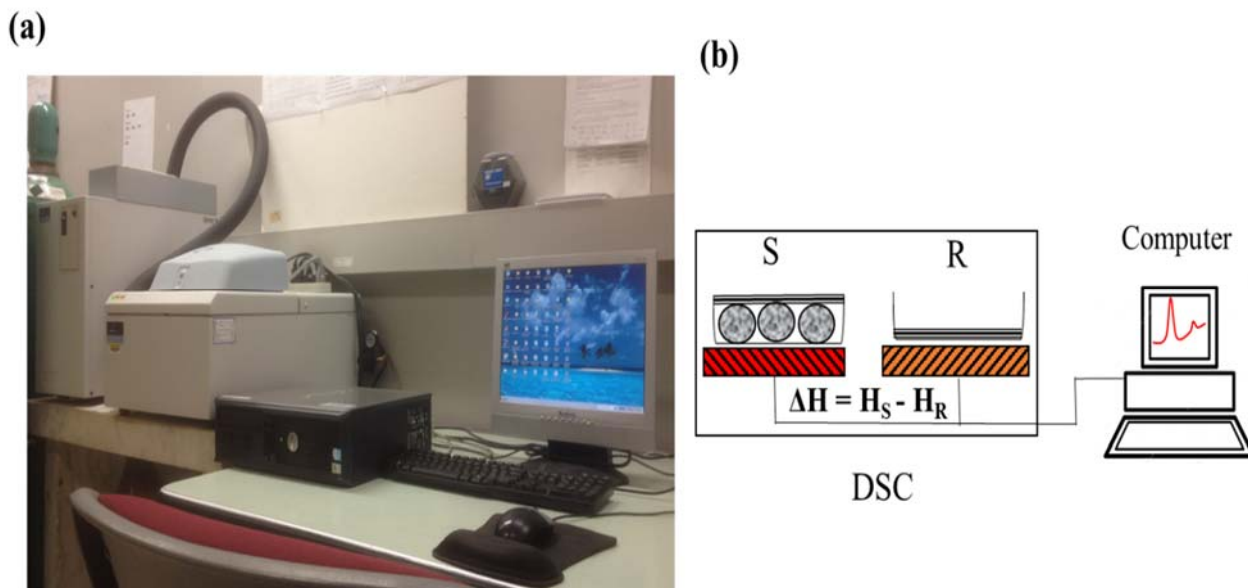


Figure 4.7 An Image of (a) Pyris Diamond PerkinElmer DSC, and (b) a Schematic of DSC Apparatus.

Figure 4.7 (a) shows the image of actual experimental set-up of the DSC instrument used in the current research. As shown in Figure 4.7(b), the DSC measures the difference in the amount of heat or differential heat flow ( $\Delta H = H_S - H_R$ ) between the sample ( $S$ ), and the reference ( $R$ ) as a function of temperature ( $T$ ). Throughout the experiment, both sample pan and reference pan are kept at the same temperature ( $\Delta T = T_S - T_R = 0$ ). DSC is mainly used for quantitative measurements of energy or heat flow due to endothermic (heat transfer to the sample) or exothermic (heat transfer from the sample) physical changes or chemical reactions, which in turn depends on the nature of the sample used for thermal analysis. DSC requires no mass change in sample for measuring the differential heat flow or energy. Using the DSC instrument, it is possible to accurately monitor the heat flow, and the temperature of sample up to lower limits of 0.0001 mW and 0.01 K respectively.

Measurements were taken under argon gas atmosphere at a flow rate of 20 cc/min. Standard aluminum pans (PerkinElmer), with the aluminum lids, were used for holding the samples during the DSC experiments. Both the sample and the reference Al pans, along with the Al lids, were weighed prior to the starting of the DSC measurements. About 10 mg of the synthesized  $Mg_2Si$  powder was placed in the sample pan and then, closed with the lid. Using the PerkinElmer sample press, the lid was crimped tightly on to the pan. To prevent any sample loss during the heating process, enough care was taken to eliminate any voids/gaps at the joints. The reference Al pan (with the lid) and the crimped sample pan were placed in the DSC instrument. Pyris7 software was used to set the temperature program under ‘*iso-scan-iso*’ mode, with a constant heating or scan rate ( $\beta$ ) of 5 K/min, and a hold time of 1 min. The temperature program of DSC is mathematically expressed in terms of a simple linear relationship between temperature ( $T$ ) and time ( $t$ ), and is given by equation (4.1) as:

$$T(t) = T_o + \beta t \quad (4.1)$$

where  $T_o$  is the initial temperature, and  $\beta$  is the heating or scan rate. The sample is (a) heated for  $\beta > 0$ , (b) at isothermal temperature ( $T_o$ ) for  $\beta = 0$ , and (c) cooled for  $\beta < 0$ . Before running the temperature program in 'iso-scan-iso' mode, the heat flow between the sample, and the reference pans were made 'zero' at the initial temperature ( $T_o$ ).

The specific heat measurements were measured from 50 °C to 350 °C. After calibration of the DSC instrument, with the known standard material (Indium), measurements were carried out to obtain the baseline, and the heat flow curves of the samples. The difference between sample, and baseline DSC curves gives the actual heat flow of sample at different temperatures. From the equilibrium thermodynamics, heat capacity or specific heat of a substance is defined as the amount of heat required to raise the temperature of one gram of the substance by one degree Kelvin. Therefore, the specific heat of a sample at a constant pressure is given by equation (4.2) as:

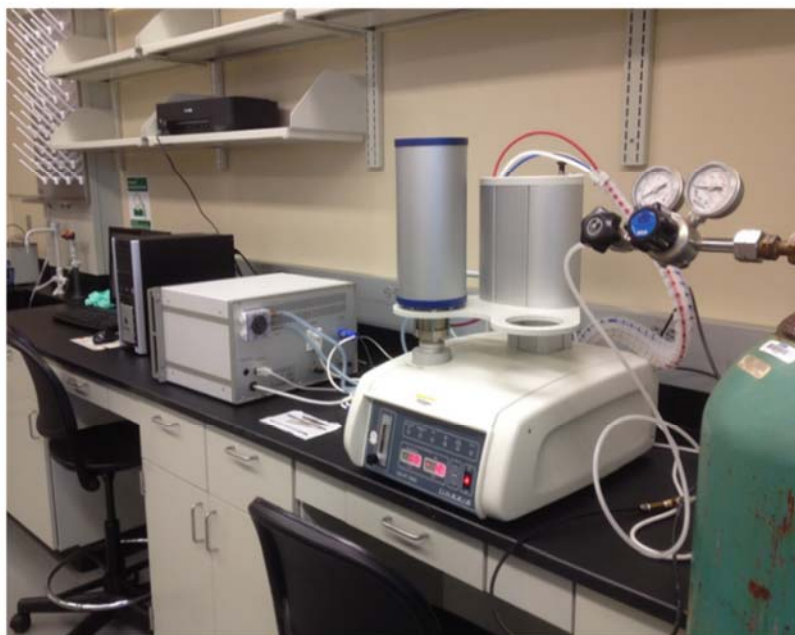
$$C_p = \frac{1}{m} \times \left( \frac{\partial H}{\partial T} \right)_p = \frac{1}{m} \times \left( \frac{\partial H / \partial t}{\partial T / \partial t} \right)_p = \frac{1}{m} \times \frac{\Delta P}{\beta} \quad (4.2)$$

where ' $m$ ' is mass of sample,  $H$  is the enthalpy of sample, and ' $\Delta P$ ' is the absolute heat flow or DSC signal of sample.

#### 4.8.2. Differential Thermal Analysis

DTA is another thermal analytical technique, which possess many similar features to those of the DSC technique. In DTA method, the temperature difference ( $\Delta T = T_S - T_R$ ) between the sample ( $S$ ) and reference ( $R$ ) materials is measured by maintaining the same heat flow ( $\Delta H = H_S - H_R = 0$ ) between sample and reference. DTA measures the change in temperature between sample and reference, when both are supplied with same amount of heat. Any phase changes, and thermal processes that occur within sample are directly related to increase or decrease in the temperature

(a)



(b)

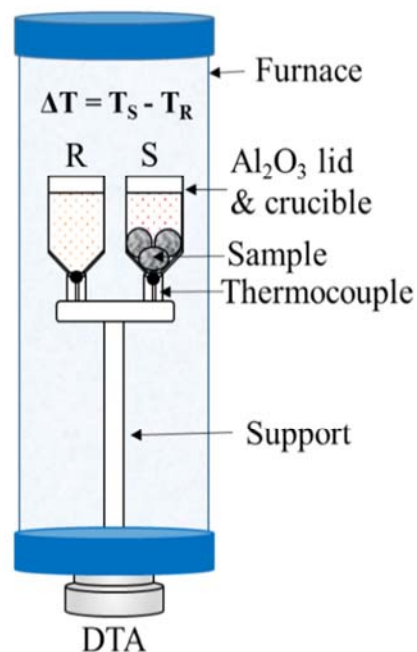


Figure 4.8 An Image of (a) Linseis PT 1600 DTA, and (b) a Schematic of DTA Furnace.

difference ( $\Delta T$ ). The DTA instrument is easy to use i.e. samples are kept in the open system, and it can be used under different experimental conditions such as high temperature, high pressure, and vacuum. DTA is mainly used for qualitative measurements of the heat flow that occur during the physical changes/chemical reactions of the samples. Figure 4.8(a) shows the actual experimental setup (Linseis PT1600) used for the DTA measurements of the TE materials. Figure 4.8(b) shows the schematic of DTA furnace with all important parts labelled i.e. sample, reference, crucibles, lids, thermocouples, and support. DTA experiments were carried out in an inert Ar gas atmosphere and at a flow rate of 4 cc/min.

The Linseis DTA instrument was used for: (a) measuring the reaction kinetics, and (b) determination of heat capacities of magnesium silicides. 100 mg of  $\text{Al}_2\text{O}_3$  was used as the reference

material, and 10 mg of pure/metal-doped  $\text{Mg}_2\text{Si}$  was used as the analyte. 10 mg of pure Al was used to calibrate the DTA apparatus, and 10 mg /20 mg of graphite was used as standard material

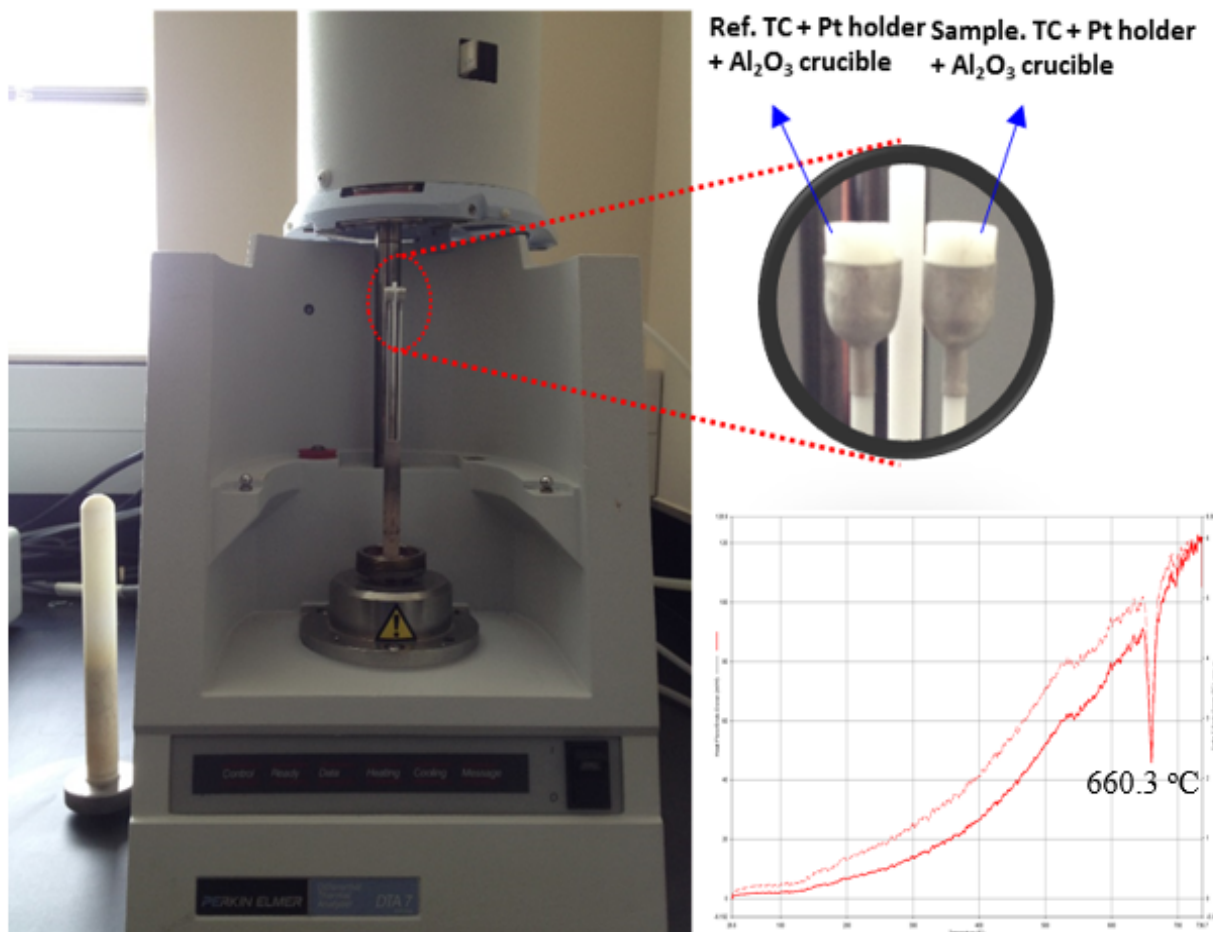


Figure 4.9 An Image of PerkinElmer DTA7 with a Blow-up View of Reference, and Sample Crucibles and DTA calibration curve of Al standard.

for specific heat ( $C_p$ ) measurements. The decomposition experiment of  $\text{Mg}_2\text{Si}$  was carried out using Perkin Elmer DTA 7 from 50 °C to 1150 °C, under Ar gas atmosphere, at a scan rate of 40 °C/min. Figure 4.9 shows the image of PerkinElmer DTA7 instrument used in current study, a blow-up view of reference, and sample crucibles with the furnace in open position, and the DTA heat flow calibration curve of Al standard showing the melting point of Al at ~ 660 °C. Table 4.1 lists the instrumental parameters of DSC, and DTA instruments used for the thermal analysis.

Table 4.1 Parameters of DSC and DTA Instruments used in Current Study.

<b>Parameters</b>	<b>Diamond DSC</b>	<b>Linseis DTA</b>	<b>PerkinElmer DTA7</b>
Scan rate ( $\beta$ ), K/min	5	5, 10, 15 and 20	40
Purging gas	Ultra-high pure Ar	Ultra-high pure Ar	Ultra-high pure Ar
Purge gas flow rate, cc/min	20	20	20
Sample/Reference container	Aluminum pan with Al cover lid	Al <sub>2</sub> O <sub>3</sub> crucible with Al <sub>2</sub> O <sub>3</sub> cover lid	Al <sub>2</sub> O <sub>3</sub> crucible with Pt holder (no lid)
Calibration standard	Indium	Aluminum	Aluminum, gold
Reference material	None	Al <sub>2</sub> O <sub>3</sub>	Al <sub>2</sub> O <sub>3</sub>
Temperature range	50 °C - 350 °C	30 °C - 850 °C	30 °C - 1200 °C
Raw thermal data	Differential heat	Temperature difference	Temperature difference
Thermal analysis	Specific heat, enthalpy, entropy, and Gibbs energy	Reaction kinetics, temperature, activation energy, specific heat, enthalpy, entropy, and Gibbs energy	Melting point

#### 4.9. Solid-state Galvanic or Electrochemical Cell

Reddy *et al.* have conducted extensive experimental studies on determination of thermal stability of Ti-Al, and Nb-Al binary systems using solid-state galvanic cell method (or EMF cell method) [118-121]. The reference and working electrodes of the solid-state galvanic cell were prepared from the chemicals ( $\text{CaF}_2$ ,  $\text{MgF}_2$ , Mg, and Si) obtained from Alfa Aesar (> 99% pure). The optically transparent pure cylindrical  $\text{CaF}_2$  crystal (diameter = 13 mm, and thickness = 2 mm) was also purchased from Alfa Aesar. Equi-molar ratio of  $\text{CaF}_2$ , and  $\text{MgF}_2$  was mixed uniformly, and small amounts of Mg and  $x\text{Mg} + (1-x)\text{Si}$  were added to ( $\text{CaF}_2 + \text{MgF}_2$ ) blend, to prepare 1 g uniform mixture of six reference electrodes (each containing 0.4 g Mg), and six different working electrodes (comprising  $\text{Mg}_x\text{Si}_{1-x}$ ;  $x = 0.10, 0.23, 0.43, 0.67, 0.84, \text{ and } 0.98$ ) respectively. The mixtures were cold-pressed into pellets of 13 mm diameter under uniaxial load of 5.85 ksi. The

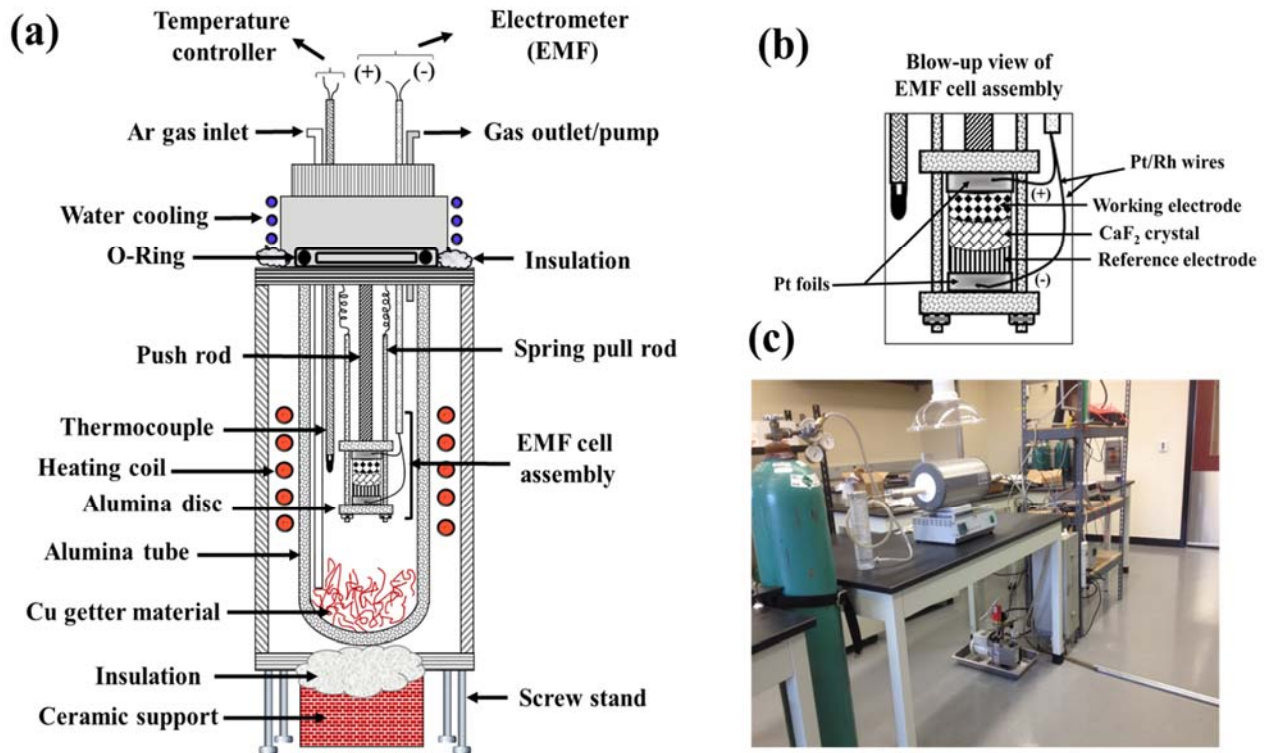


Figure 4.10 A Schematic of (a) EMF Cell, and (b) Blow-up View of Cell Assembly, and (c) Image of Experimental Set-up.

electrode pellets were wrapped in Ta foil, and placed in a vacuum sealed glass vials. The pellets were sintered at 600 °C for 7 days in a Fischer Scientific box furnace.

The design of the EMF cell, and its construction play a critical role in the accurate measurement of the cell EMF voltages. As shown in the Figure 4.10(a), the EMF cell consists of electrode assembly fastened by a pull-push system, and the cell assembly was inserted into the Al<sub>2</sub>O<sub>3</sub> tube of the vertical furnace. Figure 4.10(b) displays a blow-up view of the cell assembly containing a stack of working electrode, CaF<sub>2</sub> crystal, and reference electrode, whose ends are in contact with Pt foils, and Pt/Rh wires for measuring the cell EMF voltage. The other ends of the Pt/Rh leads were connected to Keithley 2700 multimeter, and cell voltages were recorded at different temperatures. Throughout the experiments, ultra-high pure argon gas was purged through (a) derite chamber to remove any moisture, (b) a copper getter furnace to remove trace amount of oxygen, (c) a flow meter (Fischer Scientific) to maintain a constant flow of 1 cc /min, and (d) to copper getter filings placed at the bottom of the Al<sub>2</sub>O<sub>3</sub> tube. In addition, the EMF cell setup is constantly evacuated using a vacuum pump to remove out gasses from the reaction. A K-type thermocouple (Omega Co.) was placed inside the chamber, in such a manner that its tip, and the center of the electrode cell assembly were at the same level. The other end of the thermocouple was connected to a temperature controller (Omega 2270) for monitoring the reaction temperature of the cell. After reaching the equilibrium, the EMF values (within ± 0.05 mV) are measured by using six different working electrode compositions of Mg<sub>x</sub>Si<sub>1-x</sub> (x = 0.101, 0.23, 0.434, 0.666, 0.842, and 0.984 mol) at five different temperatures (923, 947, 973, 997, and 1023 °C). Thermodynamic properties such as activity, activity coefficients, Gibbs energy of mixing, enthalpy of mixing, and entropy of mixing for Mg-Si system, were calculated from the cell EMF voltage at different temperatures to assess the thermal stability of alloy phases in Mg-Si system.

#### 4.10. Thermodynamic Modelling

In a multicomponent system, the phase equilibria is calculated by minimizing the total Gibbs energy ‘ $G$ ’ of all individual components that participates in the equilibrium. The total Gibbs energy is given by equation (4.3) as

$$G = \sum_{i=1}^p n_i G_i^o = \text{minimum} \quad (4.3)$$

where  $n_i$ , and  $G_i^o$  are the number of moles, and Gibbs energy of individual phase ‘ $i$ ’[122]. Thermodynamic tools (HSC and FactSage) were used to model the thermodynamic properties, and phase equilibria of binary alloys from Mg-Si, and transition metal borides and silicides of (Ti/Nb/Mn) - Co- (B/Si) systems. Change in Gibbs energy of Mg<sub>2</sub>Si, 9 binary metal borides (Co<sub>2</sub>B, CoB, TiB, TiB<sub>2</sub>, NbB<sub>2</sub>, Mn<sub>2</sub>B, MnB, Mn<sub>3</sub>B<sub>4</sub>, and MnB<sub>2</sub>), and 12 binary silicides (NbSi<sub>2</sub>, Nb<sub>5</sub>Si<sub>3</sub>, CoSi<sub>2</sub>, CoSi, Co<sub>2</sub>Si, Ti<sub>5</sub>Si<sub>3</sub>, TiSi, TiSi<sub>2</sub>, MnSi, Mn<sub>5</sub>Si<sub>3</sub>, Mn<sub>3</sub>Si, and MnSi<sub>1.73</sub>) were evaluated using ‘Reaction Equations’ module of HSC 7.1 software tool. The change in Gibbs energy of the selected borides and silicides were calculated from 25 °C to 1500 °C at 1 bar pressure. The positive/negative sign of change in Gibbs energy indicates the thermal stability of the metal borides and silicides.

From all stable binary alloys of (Ti/Nb/Mn – Co – B/Si) systems, 5 borides (Co<sub>2</sub>B, CoB, TiB, TiB<sub>2</sub>, and NbB<sub>2</sub>) and 9 silicides (CoSi, Ti<sub>5</sub>Si<sub>3</sub>, TiSi, TiSi<sub>2</sub>, MnSi, Mn<sub>5</sub>Si<sub>3</sub>, Mn<sub>3</sub>Si, NbSi<sub>2</sub> and Nb<sub>5</sub>Si<sub>3</sub>) were selected to obtain the Gibbs energy as a function of temperature. Using ‘Compound’ module of Factsage 6.3 tool, the Gibbs energy function,  $G(T)$  is given by equation (4.4), and the parameters (A, B, C, D and E) of the temperature polynomial function was estimated for each of the selected metal borides and silicides.

$$G(T), \frac{kJ}{mol} = A + B \times T + C \times T^2 + D \times T^{-1} + E \times T \ln T \quad (4.4)$$

Also, the binary phase diagram, and Mg/Si activities of Mg-Si system were obtained at 1 bar pressure by using ‘Phase Diagram’, and ‘Equilib’ modules of FactSage 6.3 respectively.

## CHAPTER 5

### A PRELIMINARY STUDY

The divalent alkaline earth metal hexaborides are known for their low densities, high melting points, high hardness, large elastic moduli, low thermal expansion coefficients, high chemical stabilities [63, 67]. Also, recent studies indicates that the alkaline earth metal hexaborides are promising *n*-type TE materials with high *S*- and  $\sigma$ - values. Therefore, the group (II) metal hexaborides show greater potential for high temperature TE power generation.

The alkaline earth metal silicides are promising candidates for TE power generation in mid/high temperature range. Group (II) metal silicides are very attractive and have potential to replace lead-based TE materials because of their low cost, non-toxicity, and high abundance in the earth's crust. Moreover, group (II) metal silicides reduces the weight of TE devices, which is an important feature for aerospace, and automobile industries. Group (II) metals are desirable candidates for achieving high *ZT*- values because of their high *S*- and  $\sigma$ - values, low lattice thermal conductivity ( $\kappa_L$ ) values, and high melting points [71, 72].

#### 5.1. Arrhenius Relation

In this study, group (II) metal borides (CaB<sub>6</sub> and SrB<sub>6</sub>), and metal silicides (Mg<sub>2</sub>Si and CaSi) are considered for evaluation of the TE properties, *P* (= *S*,  $\sigma$ ,  $\kappa$  and *ZT*) as a function of temperature. Experimental data for '*P*' is obtained from the literature [63, 67, 71, 72], and fitted to the Arrhenius relation given by equation (5.1) as:

$$P(T) = P_o \times e^{-\left(\frac{Q_P}{R \times T}\right)} \quad (5.1)$$

where  $P_o$  ( $= S_o, \sigma_o, \kappa_o$  and  $(ZT)_o$ ) is the pre-exponential factor (same units as  $P$ ),  $Q_P$  ( $= Q_S, Q_\sigma, Q_\kappa$ , and  $Q_{ZT}$ ) is the activation energy ( $Jmol^{-1}$ ) of  $P$ ,  $R$  is the universal gas constant ( $8.314 Jmol^{-1}K^{-1}$ ), and  $T$  is the temperature ( $K$ ). As shown in the flow chart of Figure 5.1, the experimental data of ‘ $P$ ’ was fitted to Arrhenius relation given by equation (5.1) [123].

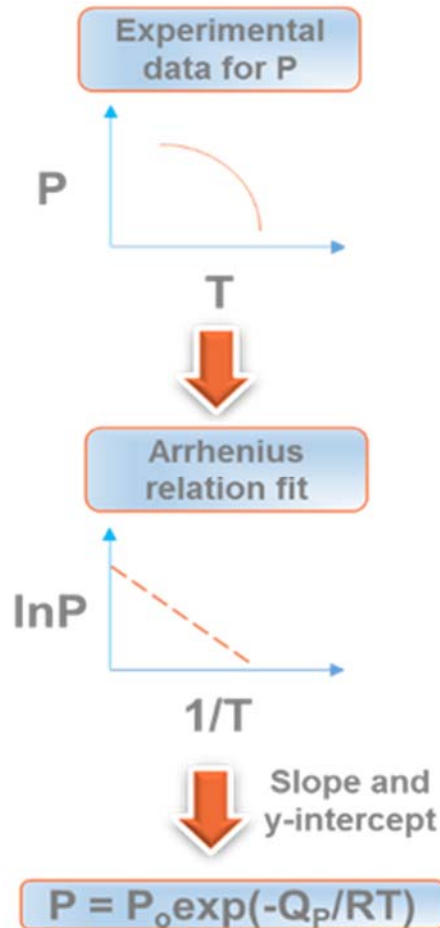


Figure 5.1. A Flow Chart of the Procedure used to Evaluate the TE Properties from Arrhenius Relation.

## 5.2. Group (II) Borides and Silicides

In the current study, experimental data on TE properties ( $P$ ) for borides ( $CaB_6$  and  $SrB_6$ ) and silicides ( $Mg_2Si$ , and  $CaSi$ ) was evaluated as a function of temperature from 300 to 1050 K. Arrhenius relation was used to assess the parameters such as pre-exponential factors ( $P_o$ ), and activation energies ( $Q_P$ ) of the group (II) metal hexaborides, and group (II) metal silicides.

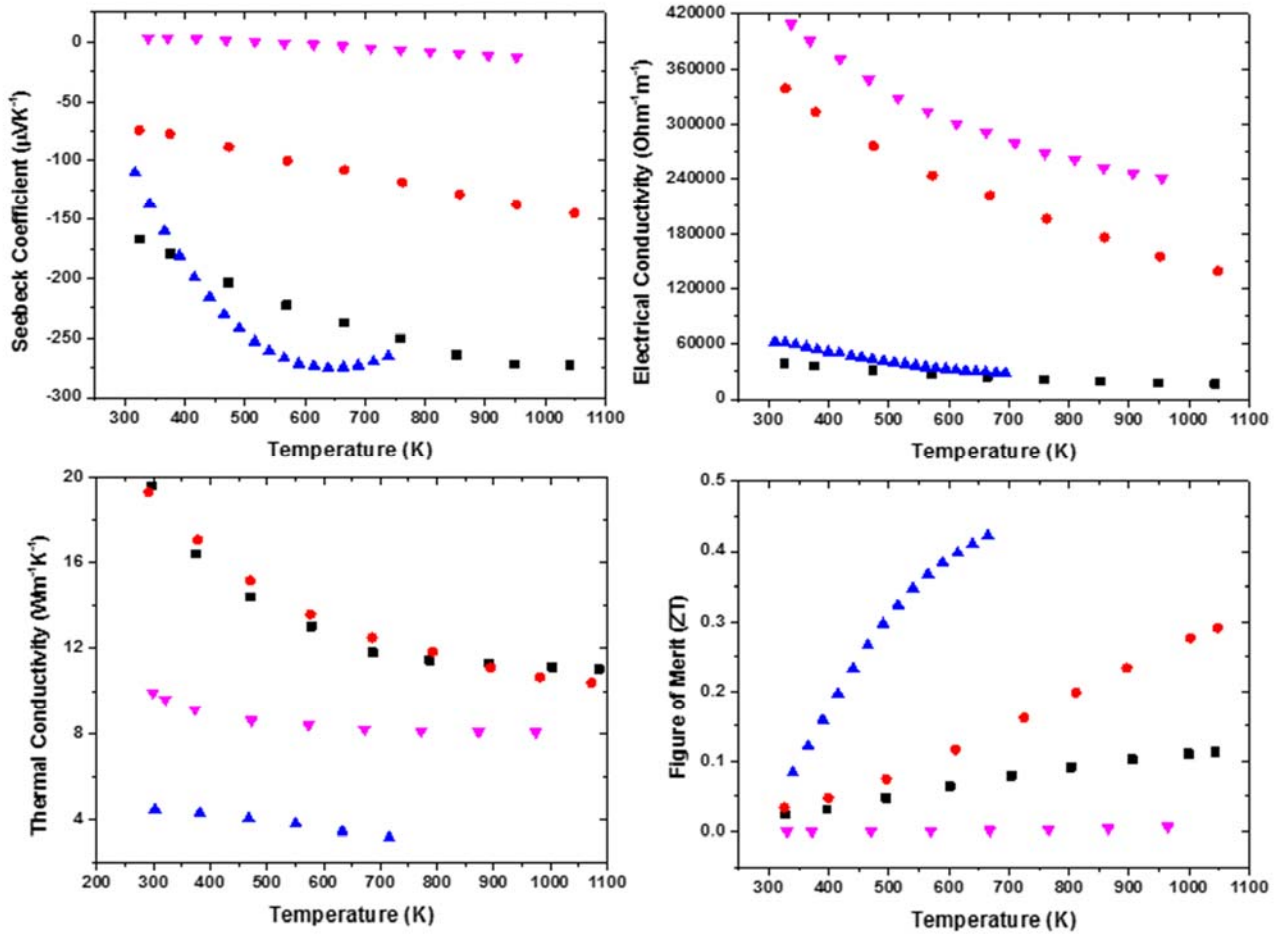


Figure 5.2. Plots of  $S$ ,  $\sigma$ ,  $\kappa$  and  $ZT$  vs. Temperature ( $T$ ) for Borides (■CaB<sub>6</sub> and ●SrB<sub>6</sub>) and Silicides (▲Mg<sub>2</sub>Si and ▼CaSi)

Gibbs energies for the formation of CaB<sub>6</sub>, Mg<sub>2</sub>Si, and CaSi were calculated using the HSC 7.1 tool at temperatures ranging from 300 to 1300 K. Solid solution activities of B and Si in the binary alloys were calculated at 1 bar and 1000 K by using FactSage 6.3 tool. The experimental data on TE properties ( $S$ ,  $\sigma$ ,  $\kappa$  and  $ZT$ ) of CaB<sub>6</sub>, SrB<sub>6</sub>, Mg<sub>2</sub>Si and CaSi at different temperatures is plotted in Figure 5.2 [63, 67, 71, 72].

### 5.3. Log (TE property) vs. 1/T Plots

The prediction of the TE properties was done using Arrhenius relation of equation (5.1). Firstly, the natural logarithm of the TE property ( $\ln(P)$ ) was calculated for each temperature, and

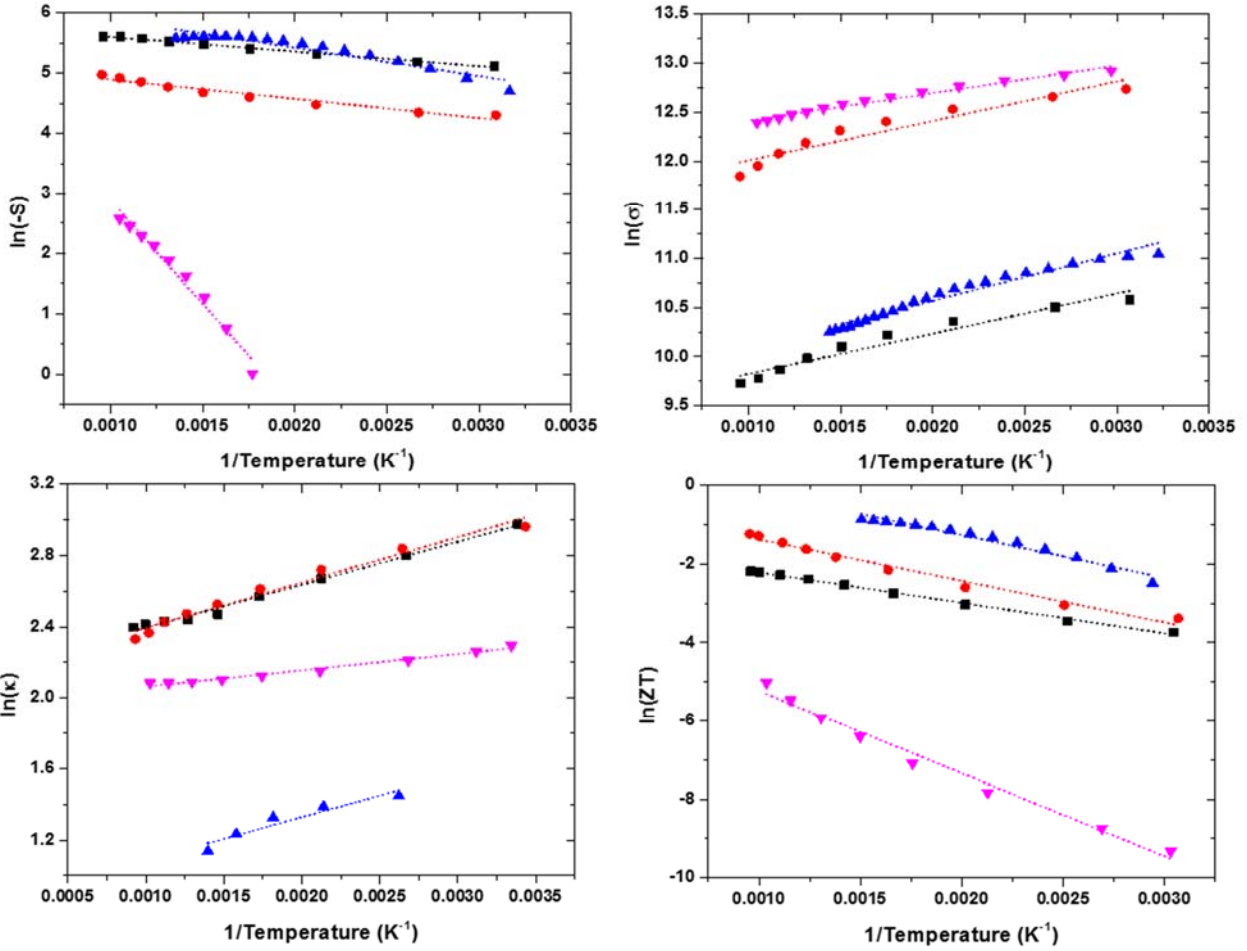


Figure 5.3.  $\ln(P)$  vs.  $1/T$  ( $P = -S, \sigma, \kappa$  and  $ZT$ ) Plots of Experimental Data (■CaB<sub>6</sub>, ●SrB<sub>6</sub>, ▲Mg<sub>2</sub>Si and ▼CaSi) and Linear Fit (●●●CaB<sub>6</sub>, ●●●SrB<sub>6</sub>, ●●●Mg<sub>2</sub>Si and ●●●CaSi)

then plotted as a function of inverse temperature ( $1/T$ ). As shown in Figure 5.3, the plots of  $\ln(P)$  vs.  $1/T$  gives straight line for majority of the TE properties. Table 5.1 lists the linear relationships between  $\ln(P)$  and  $1/T$  with good  $R^2$  values ranging from 0.91 to 0.99. Secondly, the value of the slopes and intercepts from Table 5.2 were used for the calculation of the Arrhenius relation parameters ( $P_o = \exp(\text{intercept})$  and  $Q_P = -R \times \text{slope}$ ). The estimated values of  $P_o$  and  $Q_P$  for the TE alloys are listed in Table 5.2. As shown in the Figure 5.3, the marker points of  $P$  vs.  $T$  plots represents the experimental data, while the extended dotted-straight line shows the predicted values of the TE properties for the alloys using the Arrhenius relation.

Table 5.1. Linear relationship of  $\ln(P)$  vs.  $1/T$  for  $\text{CaB}_6$ ,  $\text{SrB}_6$ ,  $\text{Mg}_2\text{Si}$ , and  $\text{CaSi}$ .

Alloy	$\ln(-S)$ vs. $1/T$	$\ln(\sigma)$ vs. $1/T$	$\ln(\kappa)$ vs. $1/T$	$\ln(ZT)$ vs. $1/T$
<b><math>\text{CaB}_6</math></b>	$\ln(-S) = -242.87/T + 5.84$ $R^2 = 0.99$	$\ln(\sigma) = 410.12/T + 9.41$ $R^2 = 0.94$	$\ln(\kappa) = 240.75/T + 2.15$ $R^2 = 0.99$	$\ln(ZT) = -773.7/T - 1.43$ $R^2 = 0.99$
<b><math>\text{SrB}_6</math></b>	$\ln(-S) = -318.73/T + 5.21$ $R^2 = 0.95$	$\ln(\sigma) = 403.97/T + 11.60$ $R^2 = 0.91$	$\ln(\kappa) = 254.76/T + 2.13$ $R^2 = 0.97$	$\ln(ZT) = -1056.8/T - 0.31$ $R^2 = 0.98$
<b><math>\text{Mg}_2\text{Si}</math></b>	$\ln(-S) = -600.62/T + 6.69$ $R^2 = 0.97$	$\ln(\sigma) = 480.62/T + 9.60$ $R^2 = 0.96$	$\ln(\kappa) = 242.13/T + 0.84$ $R^2 = 0.91$	$\ln(ZT) = -1082.5/T + 0.89$ $R^2 = 0.96$
<b><math>\text{CaSi}</math></b>	$\ln(-S) = -3437.9/T + 6.32$ $R^2 = 0.97$	$\ln(\sigma) = 281.45/T + 12.13$ $R^2 = 0.97$	$\ln(\kappa) = 92.105/T + 1.97$ $R^2 = 0.97$	$\ln(ZT) = -2109.3/T - 3.12$ $R^2 = 0.98$

#### 5.4. Evaluation of TE Properties

The estimated values of  $P_o$ , and  $Q_P$  for the TE alloys are listed in Table 5.2. As shown in Figure 5.4, the marker points of  $P$  vs.  $T$  plots represents the experimental data, while the extended dotted-curve represents the evaluated values of the TE properties for the alloys. At higher temperatures, the Arrhenius relation predicts a relatively high  $ZT$  value for  $\text{Mg}_2\text{Si}$ .

Table 5.2. Thermoelectric Parameters of Borides ( $\text{CaB}_6$  and  $\text{SrB}_6$ ) and Silicides ( $\text{Mg}_2\text{Si}$  and  $\text{CaSi}$ ).

Alloy	S - parameters	$\sigma$ - parameters	$\kappa$ - parameters	ZT- parameters
<b><math>\text{CaB}_6</math></b>	$Q_S = -2019.22 \text{ Jmol}^{-1}$ $S_o = -345.81 \mu\text{VK}^{-1}$	$Q_\sigma = 3409.73 \text{ Jmol}^{-1}$ $\sigma_o = 12244.10 \text{ Ohm}^{-1}\text{m}^{-1}$	$Q_\kappa = 2001.59 \text{ Jmol}^{-1}$ $\kappa_o = 8.62 \text{ Wm}^{-1}\text{K}^{-1}$	$Q_{ZT} = -6432.54 \text{ Jmol}^{-1}$ $(ZT)_o = 0.23$
<b><math>\text{SrB}_6</math></b>	$Q_S = -2649.92 \text{ Jmol}^{-1}$ $S_o = -183.75 \mu\text{VK}^{-1}$	$Q_\sigma = 3358.60 \text{ Jmol}^{-1}$ $\sigma_o = 109316.21 \text{ Ohm}^{-1}\text{m}^{-1}$	$Q_\kappa = 2118.07 \text{ Jmol}^{-1}$ $\kappa_o = 8.48 \text{ Wm}^{-1}\text{K}^{-1}$	$Q_{ZT} = -8786.23 \text{ Jmol}^{-1}$ $(ZT)_o = 0.73$
<b><math>\text{Mg}_2\text{Si}</math></b>	$Q_S = -3912.06 \text{ Jmol}^{-1}$ $S_o = -273.47 \mu\text{VK}^{-1}$	$Q_\sigma = 3995.87 \text{ Jmol}^{-1}$ $\sigma_o = 14884.86 \text{ Ohm}^{-1}\text{m}^{-1}$	$Q_\kappa = 2013.06 \text{ Jmol}^{-1}$ $\kappa_o = 2.32 \text{ Wm}^{-1}\text{K}^{-1}$	$Q_{ZT} = -8999.90 \text{ Jmol}^{-1}$ $(ZT)_o = 2.45$
<b><math>\text{CaSi}</math></b>	$Q_S = -28582.70 \text{ Jmol}^{-1}$ $S_o = -557.63 \mu\text{VK}^{-1}$	$Q_\sigma = 2339.97 \text{ Jmol}^{-1}$ $\sigma_o = 185720.84 \text{ Ohm}^{-1}\text{m}^{-1}$	$Q_\kappa = 765.76 \text{ Jmol}^{-1}$ $\kappa_o = 7.18 \text{ Wm}^{-1}\text{K}^{-1}$	$Q_{ZT} = -17536.72 \text{ Jmol}^{-1}$ $(ZT)_o = 0.04$

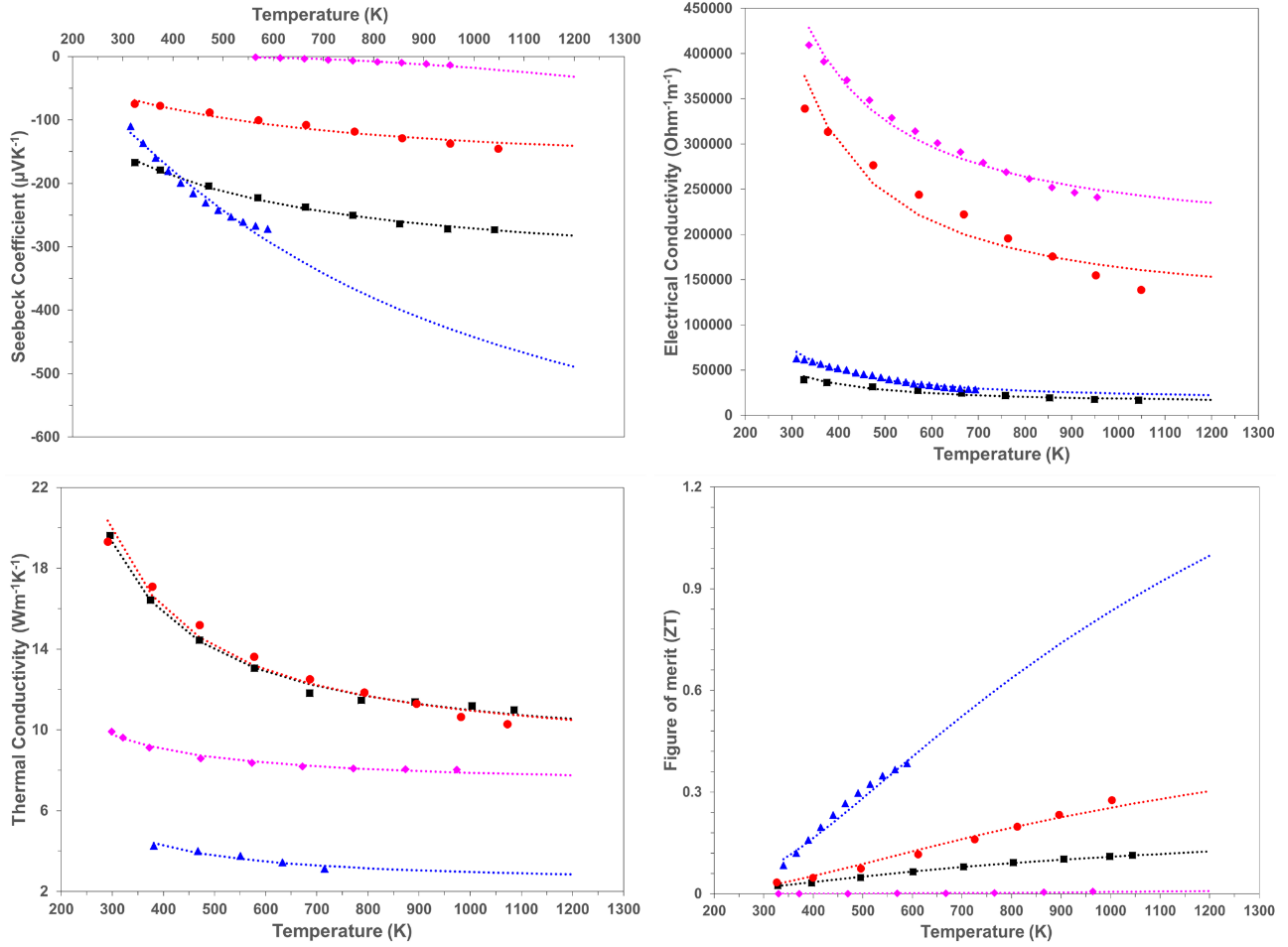


Figure 5.4. Plots of  $S$ ,  $\sigma$ ,  $\kappa$  and  $ZT$  vs.  $T$  for Experimental Data (■CaB<sub>6</sub>, ●SrB<sub>6</sub>, ▲Mg<sub>2</sub>Si and ◆CaSi) and Predicted Values (●●●CaB<sub>6</sub>, ●●●SrB<sub>6</sub>, ●●●Mg<sub>2</sub>Si and ●●●CaSi).

### 5.5. Estimation of Efficiencies

Upon substituting the expression for  $ZT$ , from equation (5.1), into the conversion efficiency ( $\eta_{TE}$ ), of equation (1.7), the formula for maximum conversion efficiency of group (II) borides (CaB<sub>6</sub> and SrB<sub>6</sub>), and silicides (Mg<sub>2</sub>Si and CaSi) was obtained for different hot side temperature ( $T_h$ ) with cold side temperature ( $T_c$ ) kept at 300 K. The  $\eta_{TE}$  as a function of  $T_h$  is given by equation (5.2) as:

$$\eta_{TE} = \frac{T_h - 300 \text{ K}}{300 \text{ K}} \times \frac{\sqrt{1 + (ZT)_o e^{-\left(\frac{Q_{ZT}}{RT}\right)} - 1}}{\sqrt{1 + (ZT)_o e^{-\left(\frac{Q_{ZT}}{RT}\right)} + \frac{300 \text{ K}}{T_h}}} \quad (5.2)$$

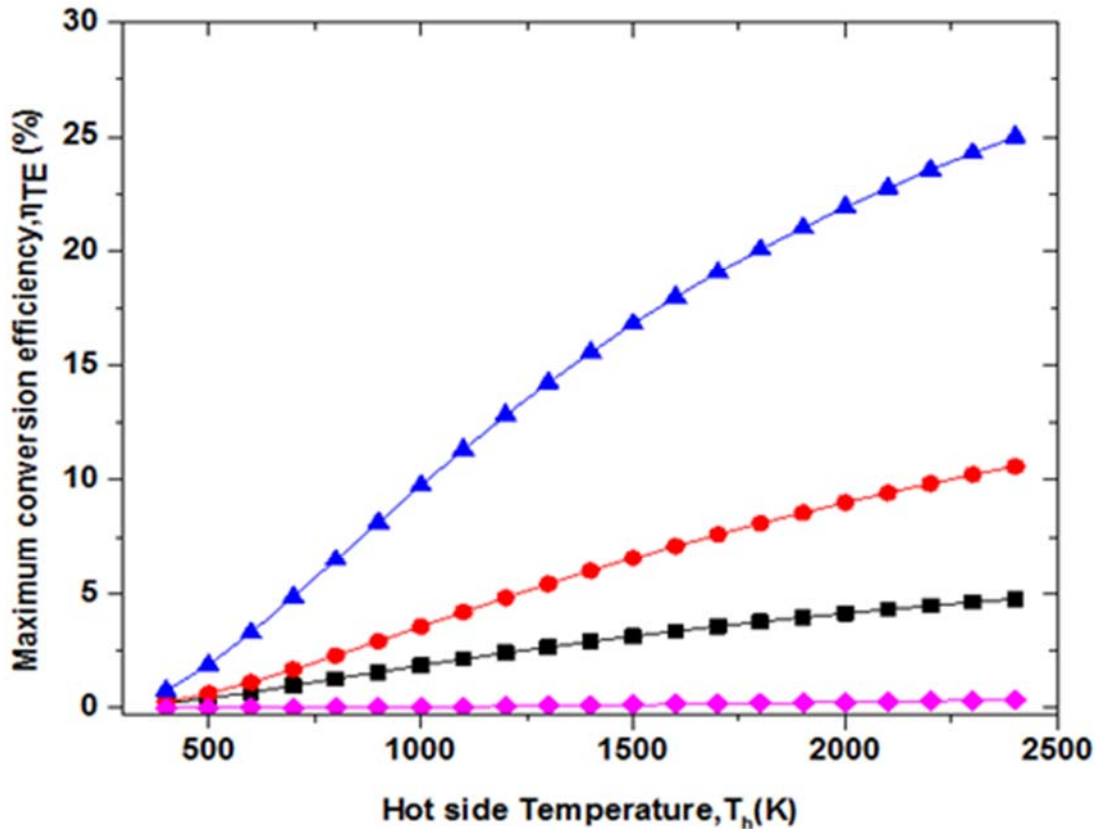


Figure 5.5. A Plot of Efficiency ( $\eta_{TE}$ ) vs. Temperature ( $T$ ) for Borides (■ $CaB_6$ , ● $SrB_6$ ) & Silicides (▲ $Mg_2Si$  & ▼ $CaSi$ )

As shown in Figure 5.5, the plot of ( $\eta_{TE}$ ) vs. temperature ( $T$ ) indicates that  $Mg_2Si$  is relatively more efficient in converting the waste heat into electricity. Therefore, the alloy exhibits a greater potential for power generation at higher temperatures.

### 5.6. Comparison of Properties

The phase stabilities, and crystal structures of  $CaB_6$ ,  $SrB_6$ ,  $Mg_2Si$ , and  $CaSi$  were assessed from the binary alloy phase diagrams [29]. The only stable binary boride alloy phases of Ca, and Sr metals are respective hexaboride phases ( $CaB_6$  and  $SrB_6$ ). Also, the only stable binary silicide alloy phase of Mg is  $Mg_2Si$ . However, the silicides of Ca occur in multiple binary phases ( $Ca_2Si$ ,  $Ca_5Si_3$ ,  $CaSi$ ,  $Ca_3Si_4$ ,  $Ca_{14}Si_{19}$  and  $CaSi_2$ ) with the  $CaSi$  being the most thermally stable phase. Table 5.3 summarizes the crystal structure and physical properties of the group (II) metal borides

and silicides, which includes space group, cell parameters, density, volume, melting point, predicted Gibbs energy of formation, and activities of B/Si in the alloys at 1000 K. CaB<sub>6</sub>, SrB<sub>6</sub>, and Mg<sub>2</sub>Si contain cubic lattice, while CaSi possess orthorhombic unit cell structure. CaB<sub>6</sub>, SrB<sub>6</sub>, Mg<sub>2</sub>Si, and CaSi phases are thermally stable below their melting points 2733, 2773, 1354 and 1553 K respectively. Hence, the alloys are suitable for applications at high temperature (600 to 1200 K).

Table 5.3. Crystal Structure and Thermodynamic Data of CaB<sub>6</sub>, SrB<sub>6</sub>, Mg<sub>2</sub>Si, and CaSi [29].

Alloy	Space group	Cell Parameters	Density (Mg m <sup>-3</sup> )	Volume (Nm <sup>-3</sup> )	Melting point (K)	†ΔG <sub>f</sub> at 1000 K	*Activity of B/Si at 1000 K
CaB <sub>6</sub>	Pm $\bar{3}$ m	a = b = c = 0.414 α = β = γ = 90	2.45	0.071	2733	-94.14	0.03
SrB <sub>6</sub>	Pm $\bar{3}$ m	a = b = c = 0.419 α = β = γ = 90	3.42	0.074	2773	- - -	0.03
Mg <sub>2</sub> Si	Fm $\bar{3}$ m	a = b = c = 0.6351 α = β = γ = 90	1.99	0.256	1354	-67.60	0.0018
CaSi	Cmcm	a = 0.455, b = 1.073, c = 0.389 α = β = γ = 90	2.38	0.190	1553	-134.06	0.27

† Predictions using HSC; \* Predictions using FactSage

## 5.7. Thermodynamic Calculations

In addition, modeling studies were conducted to determine the thermodynamic quantities, such as change in Gibbs energy, and activities of B, Si and metals for the binary TE alloys. To estimate the thermodynamic stabilities of the group (II) metal hexaborides, and group (II) metal silicides, the change in Gibbs energies for the formation of CaB<sub>6</sub>, Mg<sub>2</sub>Si and CaSi were calculated from 300 to 1300 K. As shown in the Figure 5.6, the change in Gibbs energies for CaB<sub>6</sub>, Mg<sub>2</sub>Si, and CaSi are negative, thus suggesting the spontaneous nature, and favorable formation of the stable alloy phases at higher temperatures. Binary alloys of Ca (CaB<sub>6</sub> and CaSi) are more stable than Mg<sub>2</sub>Si alloy, which is in good agreement with experimental melting points (Table 5.3). Mg<sub>2</sub>Si shows a small change in the slope of ΔG vs. T at ~ 900 K, which may be due to the phase change [(Mg) + Mg<sub>2</sub>Si → L + Mg<sub>2</sub>Si] occurring at this temperature.

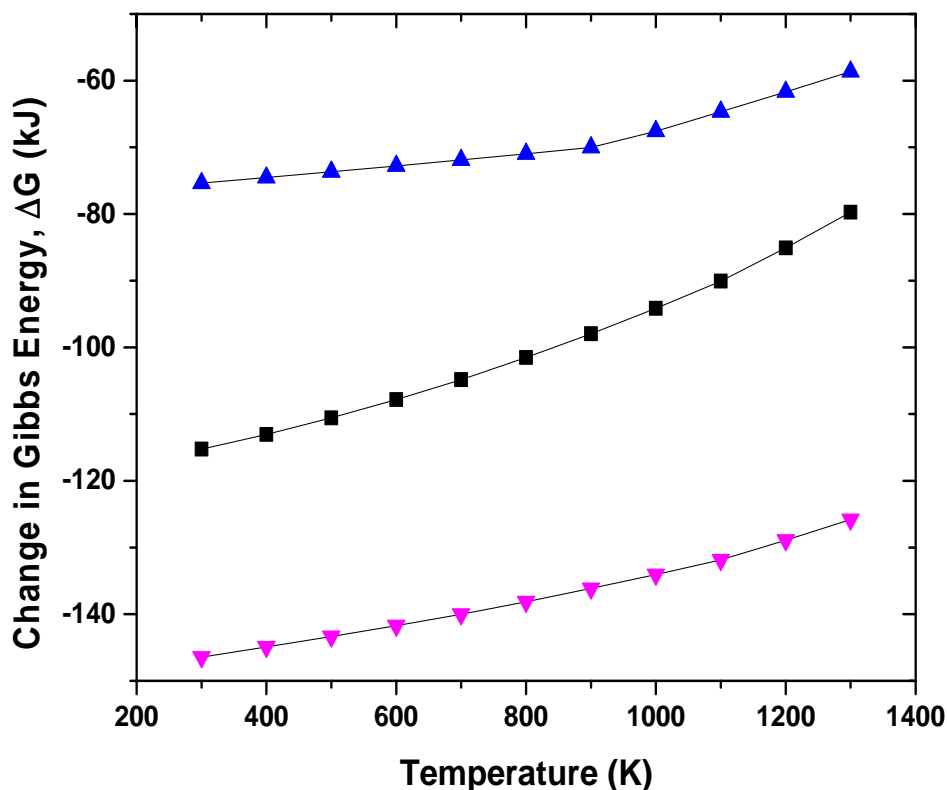


Figure 5.6. Gibbs Energy at Different Temperatures for ▲  $Mg_2Si$ , ■  $CaB_6$  and ▼  $CaSi$

The activities of B in borides and Si in silicides were calculated at 600, 800, 1000 and 1200 K, and at 1 bar pressure. Figure 5.7 shows the plots of solid-solution activities for borides ( $CaB_6$  and  $SrB_6$ ) and silicides ( $Mg_2Si$  and  $CaSi$ ) at 1000 K. Both the activity profiles for mixing of B and metal (Ca or Sr) resulted in a large deviation from the ideality, thus indicating the immiscibility or unmixing of the elements at 1000 K. Although, the activity profiles for the mixing of Si, and metal (Mg or Ca) exhibited non-ideal mixing behavior that is similar to the borides, the deviations in the activities from the ideality are comparatively low for the silicides at 1000 K. No significant changes were observed in the activities of B and Si at other temperatures (activity plots not shown for 600, 800 and 1200 K). The activities of boron in the group (II) metal borides are relatively smaller than the activities of Si in the group (II) metal silicides. The non-ideal behavior of the borides and silicides may be due to the difference in the interactions between the elements of the

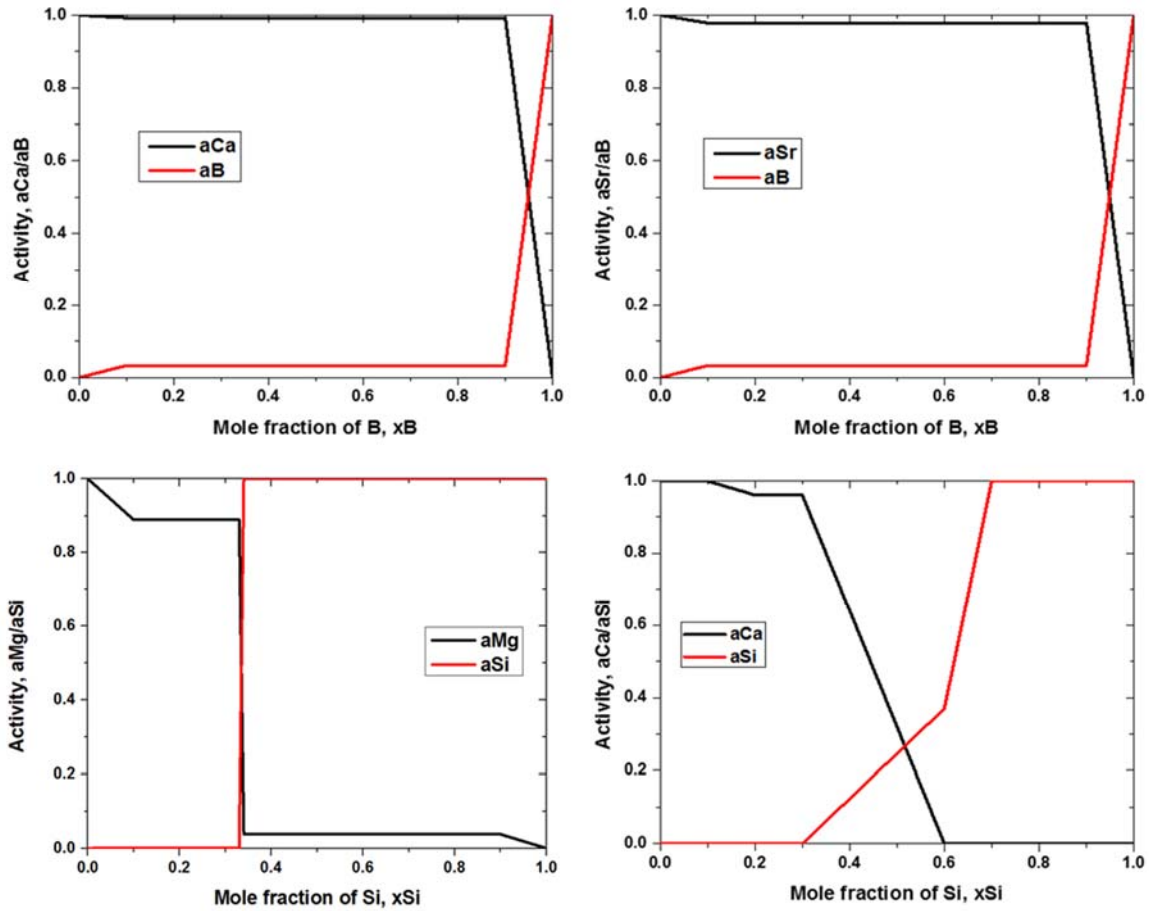


Figure 5.7. Activities of B in Ca-B and Sr-B and Si in Mg-Si and Ca-Si Solid Solutions at 1000 K.

solid-solution, which further effects the reaction energetics (Gibbs energy of mixing) for the system. Therefore, group (II) metal borides are more stable with low activities of B, while group (II) metal silicides are relatively less stable with better activities of Si in the binary alloy solutions.

### 5.8. Summary of Preliminary Study

The thermoelectric and thermodynamic properties of borides ( $CaB_6$  and  $SrB_6$ ), and silicides ( $Mg_2Si$  and  $CaSi$ ) were calculated from 300 to 1050 K. The TE properties ( $S$ ,  $\sigma$ ,  $\kappa$  and  $ZT$ ) for the alloys were obtained from the literature, and the Arrhenius relation was used to evaluate the TE properties as a function of temperature. Phase equilibria, crystal structure, thermodynamic properties (Gibbs energy and activities) was obtained for the alloys. Among the binary alloys studied,  $Mg_2Si$  exhibited greater potential for TE power generation at higher temperatures.

## CHAPTER 6

### MAGNESIUM SILICIDE

Although commercially available Pb-Te and Bi-Te based TE materials exhibits high  $ZT$  - values at low and mid temperatures, they are also toxic, heavy, and less abundant in the earth's crust [30, 31]. Therefore, it is important to develop sustainable TE materials for mid and high temperature applications. Magnesium silicide ( $Mg_2Si$ ) is a promising TE material with high  $ZT$  at mid temperature range of 500 – 800 K [124-128].  $Mg_2Si$  is the only stable binary phase of Mg-Si system.  $Mg_2Si$  contain anti-fluorite  $CaF_2$  type structure with  $Fm\bar{3}m$  space group, and cubic crystal lattice cell parameters ( $a = b = c = 6.351 \text{ \AA}$ , and  $\alpha = \beta = \gamma = 90^\circ$ ) [65]. As shown in the Figure 2.6(a), the Si atoms occupy the corners, and face-centered cubic (FCC) lattice sites of  $Mg_2Si$  unit cell, while Mg atoms occupy eight tetrahedral positions in the interior region of the unit cell. The coordination number of Si, and Mg are eight and four respectively. The cubic lattice of  $Mg_2Si$  transforms to hexagonal lattice at high pressure ( $> 25 \text{ kbar}$ ), and temperature ( $> 900 \text{ }^\circ\text{C}$ ). The density and narrow energy band gap of  $Mg_2Si$  are  $1.99 \text{ gcm}^{-3}$  and  $0.77 \text{ eV}$  respectively [129, 130]. In addition,  $Mg_2Si$  exhibits superior mechanical behavior with high Young's modulus ( $E = 120 \text{ GPa}$ ) and elevated compressional strength ( $= 1640 \text{ MPa}$ ) [129].  $Mg_2Si$  is very attractive candidate due to its low cost, higher abundance, light weight, and non-toxic nature [129, 131]. Therefore,  $Mg_2Si$ - based TE devices have huge potential to replace the existing Pb-Te based TE devices.

As shown in Figure 6.1, the temperature vs. mole fraction plot of Mg-Si system is constructed using the FactSage thermodynamic modelling tool. From the binary phase diagram of

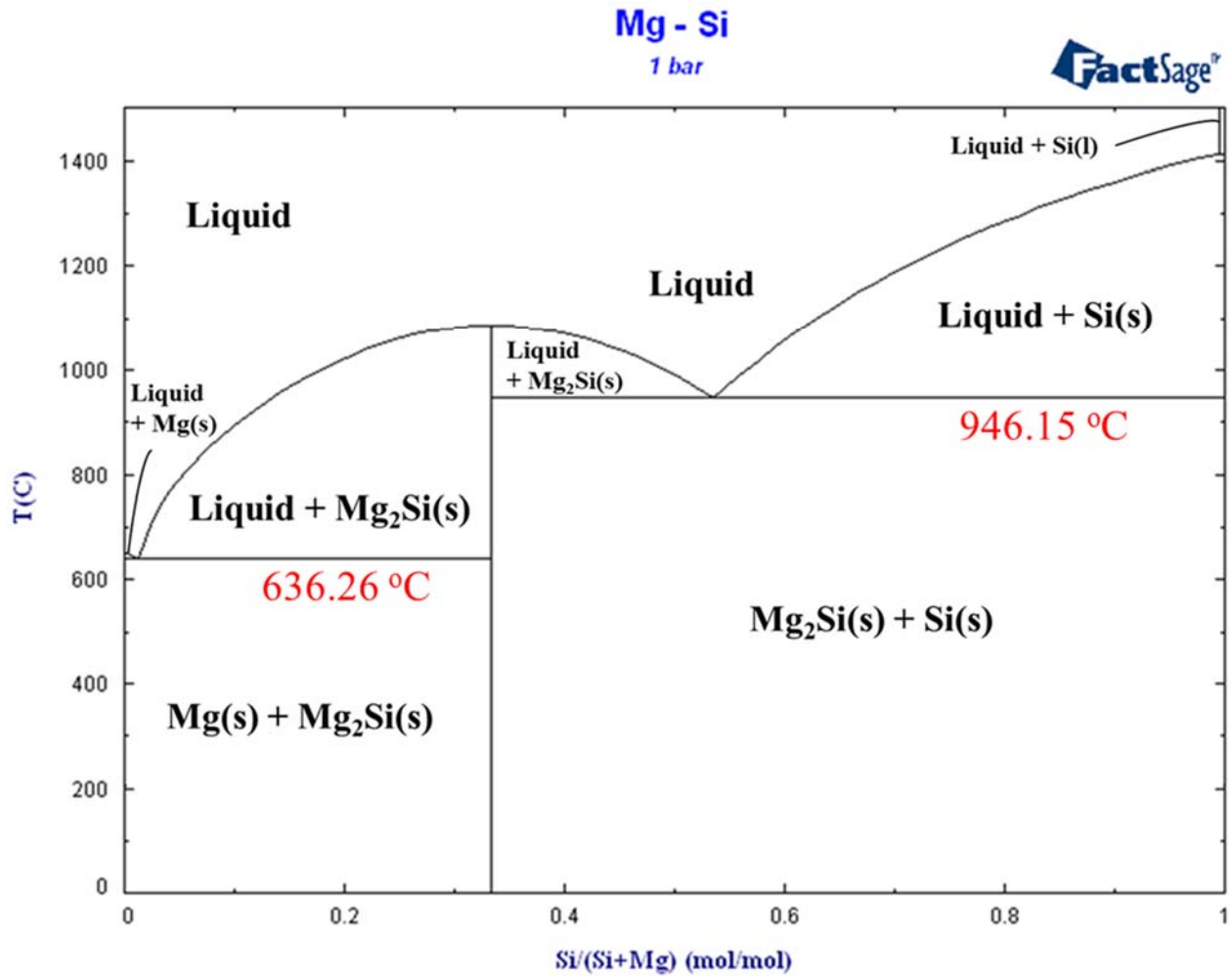


Figure 6.1 Binary Phase Diagram of Mg-Si System obtained at 1 bar using FactSage 6.3

Mg and Si, it is evident that  $Mg_2Si$  is the only binary alloy phase that exists in Mg-Si system. No presence of other binary alloy phases of Mg and Si in the binary phase diagram also indicates the simplicity associated with the synthesis of  $Mg_2Si$ . The formation of  $Mg_2Si$  occur at 66.667% of Mg and below the temperature of  $\sim 637$  °C. The melting point of  $Mg_2Si$  alloy is 1102 °C. Hence,  $Mg_2Si$  is suitable for thermoelectric applications in mid temperature range.

Several synthetic procedures have been used to improve the mechanical, and the TE properties of  $Mg_2Si$  through refinement of grain size, and lowering of thermal conductivity. Some

of these techniques include mechanical alloying or ball milling [132-134], vacuum melting [127], high temperature solid-state reaction [135], spark-plasma-sintering or plasma activated sintering [136, 137], vertical Bridgeman (VB) method [138], and microwave irradiation [139]. Mechanical alloying is a time consuming process and the samples are subjected to easy contamination and oxidation during the synthesis. Using vacuum melting, it is hard to control the synthesis of  $Mg_2Si$ . The structure, composition, and TE performance of  $Mg_2Si$  synthesized from these conventional methods are inconsistent because of (i) large difference in the melting points of Mg (650 °C), and Si (1414 °C), (ii) high volatility or evaporation of Mg at temperature (1090 °C) close to the melting point of  $Mg_2Si$  (1085 °C), and (iii) easy contamination or oxidation of Mg to MgO [129, 140]. Hence, it is important to develop low temperature, fast, and energy efficient methods for the synthesis of  $Mg_2Si$ .

In this chapter, a simple and rapid procedure is described for the synthesis of  $Mg_2Si$  powders. The product samples were tested for phase analysis, surface morphology and elemental composition using XRD, SEM, and EDS methods. Thermal analysis of the samples were carried out using DSC, DTA, and EMF methods. Thermodynamic properties such as specific heat, change in enthalpy, entropy, Gibbs energy, formation activation energies, activities, activity coefficients are determined for the magnesium silicide samples.

## 6.1. Synthesis of $Mg_2Si$

Elemental powders of magnesium (-325 mesh, 99.8%), and silicon (-325 mesh, 99.5%) were purchased from Alfa Aesar, MA, U.S.A. Figure 6.2 shows the schematic drawing of simple and rapid procedure used for the synthesis of  $Mg_2Si$  alloy. Mg reacts with atmospheric oxygen to form a thin oxide surface layer, which further inhibits the reactivity of the metal. Hence, the mixing of stoichiometric amounts of starting materials i.e., Mg and Si powders (in 2:1 molar ratio) were

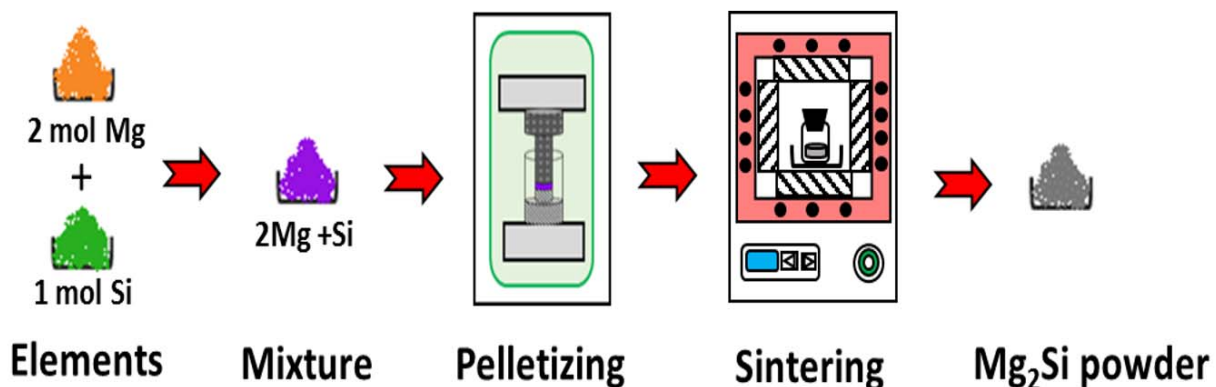


Figure 6.2. A Schematic showing the Experimental Procedure for Synthesis of Mg<sub>2</sub>Si Powder.

carried out in a Labconco glove box (Kansas City, MO, U.S.A) under argon gas atmosphere. About 1 gram of this uniform mixture was placed in a die of 1.3 cm inner diameter, and then cold-pressed at 9.8 ksi using a Carver press. The obtained silver-greyish cylindrical (2Mg + Si) pellet was placed in a glass vial, and sealed under vacuum. Sintering of (2Mg + Si) pellets was carried out using Fischer Scientific furnace to obtain dark-bluish Mg<sub>2</sub>Si powders. Table 6.1 lists the sintering parameters i.e., temperature (300 to 600 °C), and time (0 to 3 hrs) for synthesis of Mg<sub>2</sub>Si powders.

Table 6.1. Sintering Parameters (Temperature & Time) of Samples Tested for Synthesis of Mg<sub>2</sub>Si.

Sample ID	Sintering		Observation
	Temperature (°C)	Time (min)	
1	300	5 and 60	No formation of Mg <sub>2</sub> Si
2	350	5	No formation of Mg <sub>2</sub> Si
3	400	5 and 60	No formation of Mg <sub>2</sub> Si
4	450	5	No formation of Mg <sub>2</sub> Si
5	500	5, 30, 60, 120 and 180	Formation of Mg <sub>2</sub> Si
6	550	5	Formation of Mg <sub>2</sub> Si
7	600	5	Formation of Mg <sub>2</sub> Si

The optimum sintering time and temperature for the synthesis of  $Mg_2Si$  powders are 500 °C and 5 min respectively. Figure 6.3 shows the image of  $(2Mg + Si)$  pellet,  $Mg_2Si$  powder, and  $Mg_2Si$  pellet obtained before and after the sintering process.

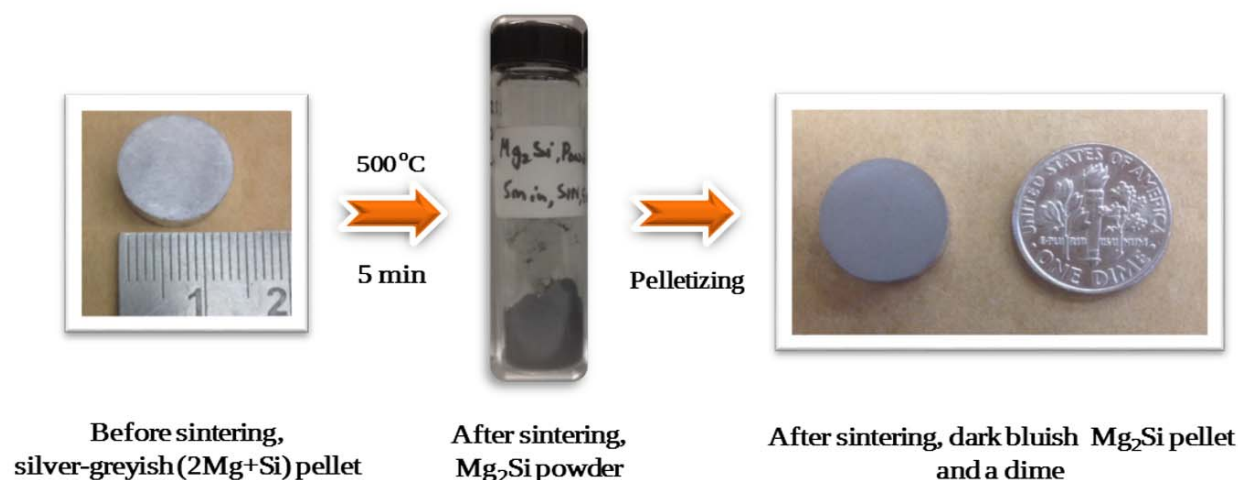


Figure 6.3. Images of  $(2Mg + Si)$  and  $Mg_2Si$  Pellets before & after Sintering at 500 °C and 5 min.

## 6.2. Characterization of $Mg_2Si$

The sample  $Mg_2Si$  powders were characterized for phase analysis, surface morphology, and elemental composition using XRD, SEM, and EDS techniques respectively. Small amounts of the  $Mg_2Si$  powders were used for obtaining X-ray diffraction spectrum using Phillips X'PERT MPD instrument. The XRD data was acquired by using  $Cu K\alpha$  ( $\lambda = 1.5405 \text{ \AA}$ ) source at diffraction angles of  $2\theta$  ( $= 20^\circ - 120^\circ$ ). Phase analysis of the samples was done by manual assignment and comparison of the XRD peak reflections using standard ICDD diffraction data ( $Mg_2Si$ , Mg, and Si). The surface morphology of  $Mg_2Si$  powders was determined using 7000 JEOL FE SEM. Small amounts of the powder sample was adhered on to carbon tape of the holder. The sample was then inserted into the JEOL instrument for SEM imaging, and EDS spectral analysis. A power of 20 kV was applied between the sample, and SEM probe. The working distance was maintained at 10 mm. SEM images of  $Mg_2Si$  sample was captured at higher magnification of 1500X. Figure 6.4 (a & b)

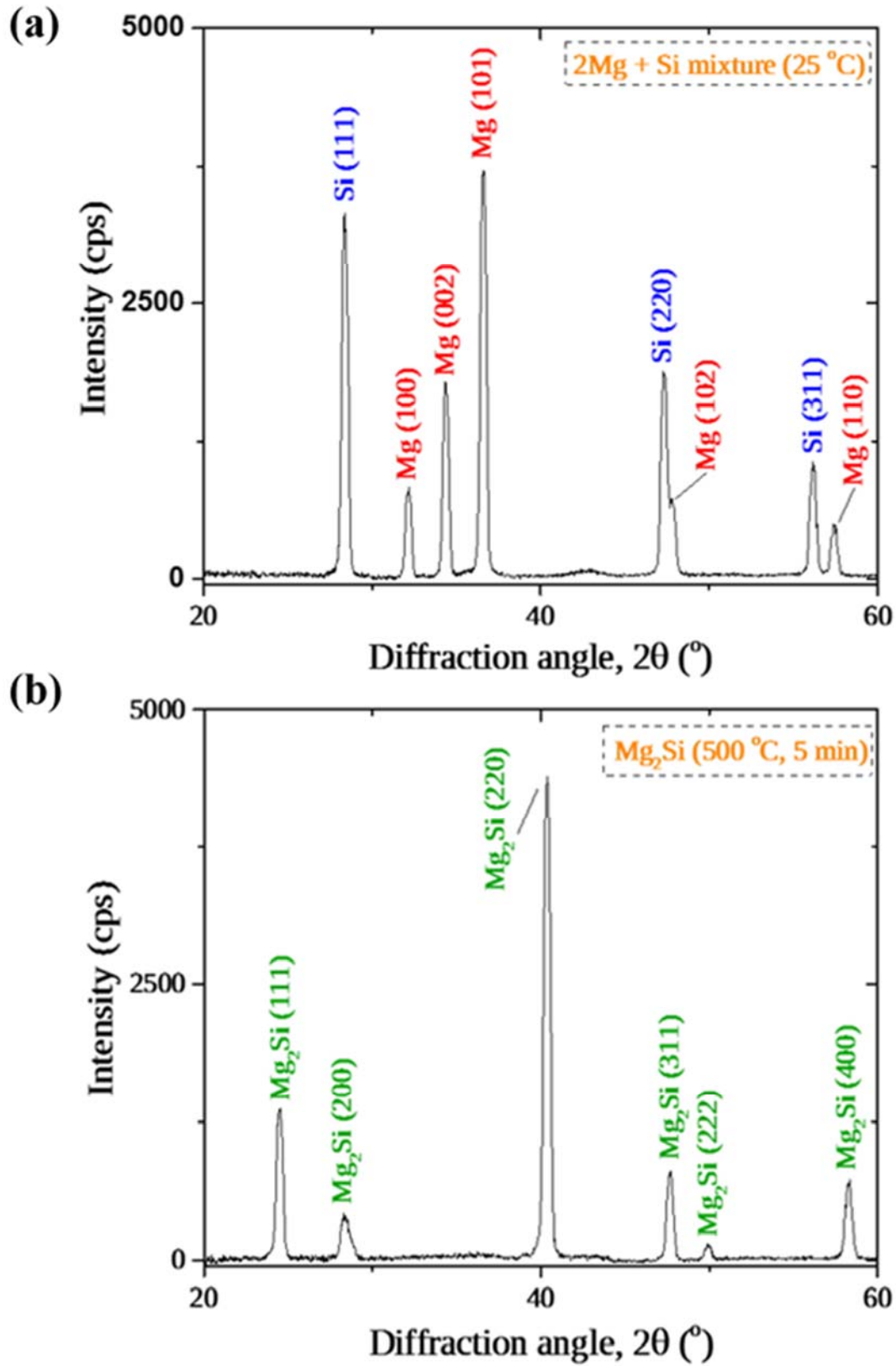


Figure 6.4 XRD Spectra of (a) 2Mg + Si & (b) Mg<sub>2</sub>Si Powders from Sintering at 500 °C for 5 min.

shows the XRD spectra of (2Mg + Si) mixture and Mg<sub>2</sub>Si powder formed after sintering at 500 °C and 5 min. The disappearance of distinct reflections of Mg and Si elements {Mg (101), Mg (002), Mg (100), Si (111) and Si (220)}, and appearance of major characteristic reflection of Mg<sub>2</sub>Si (220) at 2θ ~ 40° in the XRD spectra indicates the formation of single product phase at 500 °C. No other alloy phases of Mg and Si were observed in the spectra. The lattice constant of Mg<sub>2</sub>Si was obtained from strong peak (220) in XRD spectrum of Figure 6.4(b) by using equation (6.1) (Appendix A).

$$a(\text{Å}) = d_{hkl}(\text{Å}) \times (h^2 + k^2 + l^2)^{1/2} = \frac{\lambda}{2 \times \sin(\theta_{hkl})} \times (h^2 + k^2 + l^2)^{1/2} \quad (6.1)$$

The value of lattice constant for Mg<sub>2</sub>Si powder synthesized is 6.278 Å, which is in good agreement with the lattice constant of 6.351 Å reported in standard ICDD database (PDF card 00-034-0458).

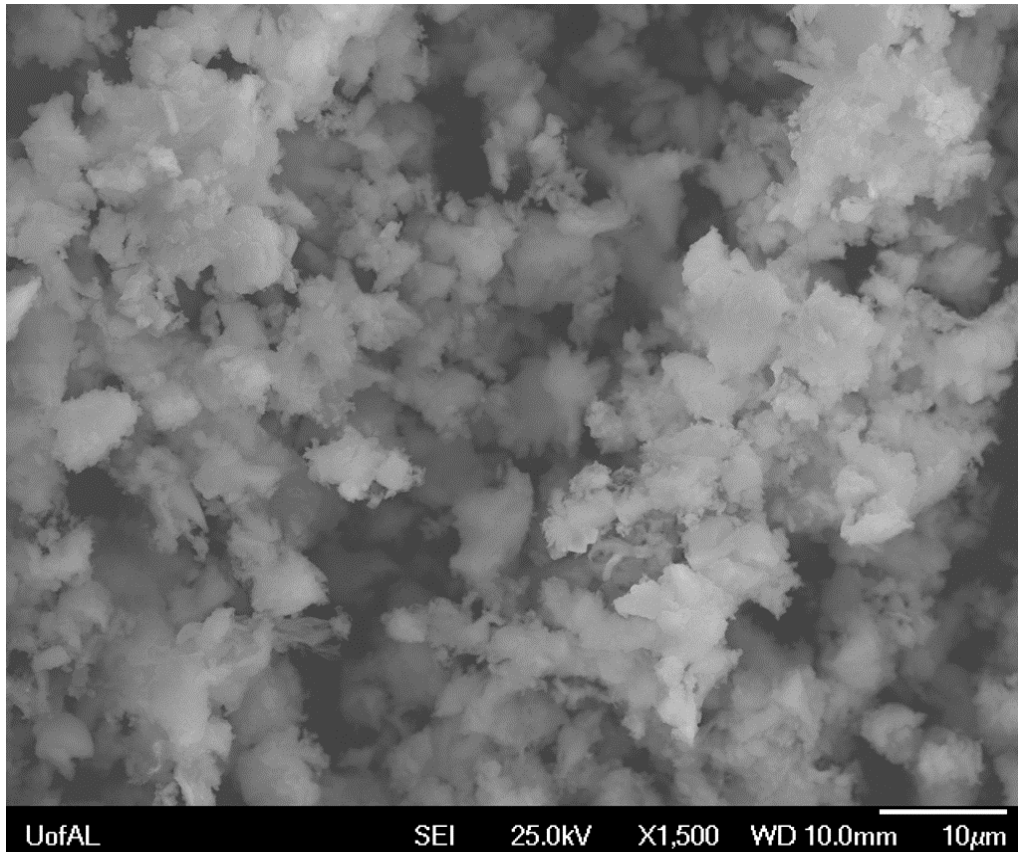


Figure 6.5 SEM Image of Mg<sub>2</sub>Si Powder obtained from Sintering at 500 °C for 5 min.

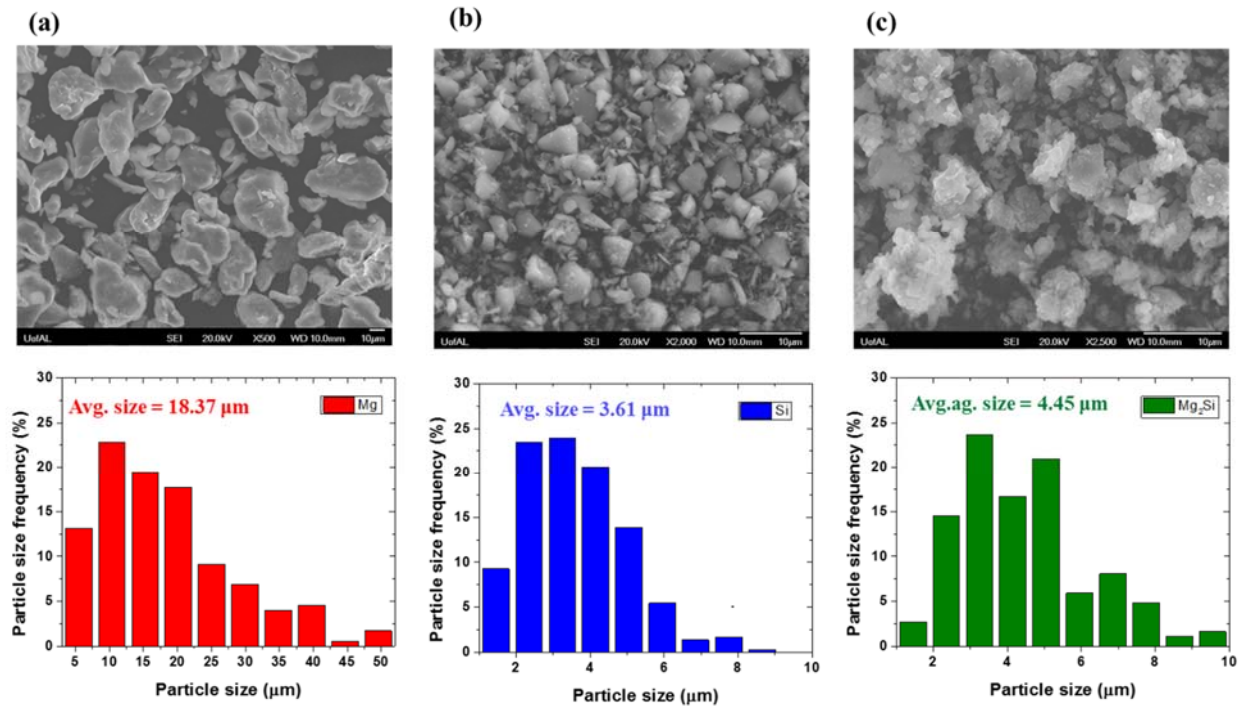
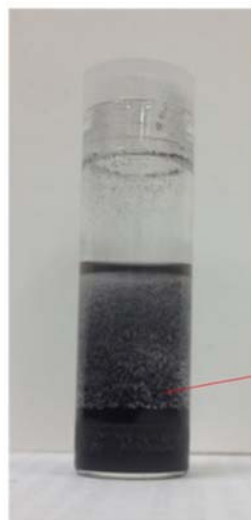


Figure 6.6 SEM and Particle Size Distribution of (a) Mg, (b) Si, and (c) Mg<sub>2</sub>Si Samples.

Figure 6.5 displays the 1500X SEM image of Mg<sub>2</sub>Si powder, obtained from (2Mg + Si) pellet after sintering at 500 °C and 5 min. The size and shape analysis of product Mg<sub>2</sub>Si powders were carried out, and compared with those of the initial raw materials (Mg and Si). Figure 6.6 (a-c) shows the morphologies of the microparticles of Mg, Si, and Mg<sub>2</sub>Si. The SEM images reveal the formation of fine irregular sized microparticles of Mg<sub>2</sub>Si in the product powders obtained from sintering at 500 °C and 5 min. The particle size analysis was determined from the SEM images using ‘Nano Measurer 1.2’ software. The % particle frequency vs. size plots show that the average particle size of Mg, Si, and aggregates of Mg<sub>2</sub>Si are 18.37 μm, 3.61 μm, and 4.45 μm respectively.

Furthermore, experiments were conducted on the breakdown of Mg<sub>2</sub>Si aggregates by using ultra-sonication technique. Figure 6.7(a) shows the image of Mg<sub>2</sub>Si particles suspension after ultra-sonication for 10 hr in hexane solvent. As shown in Figure 6.7(b), the higher magnification SEM image (16000X) of Mg<sub>2</sub>Si was taken from the hexane suspension after ultra-sonication for 10 hr.

(a)



Suspension of Mg<sub>2</sub>Si particles in Hexane

(b)

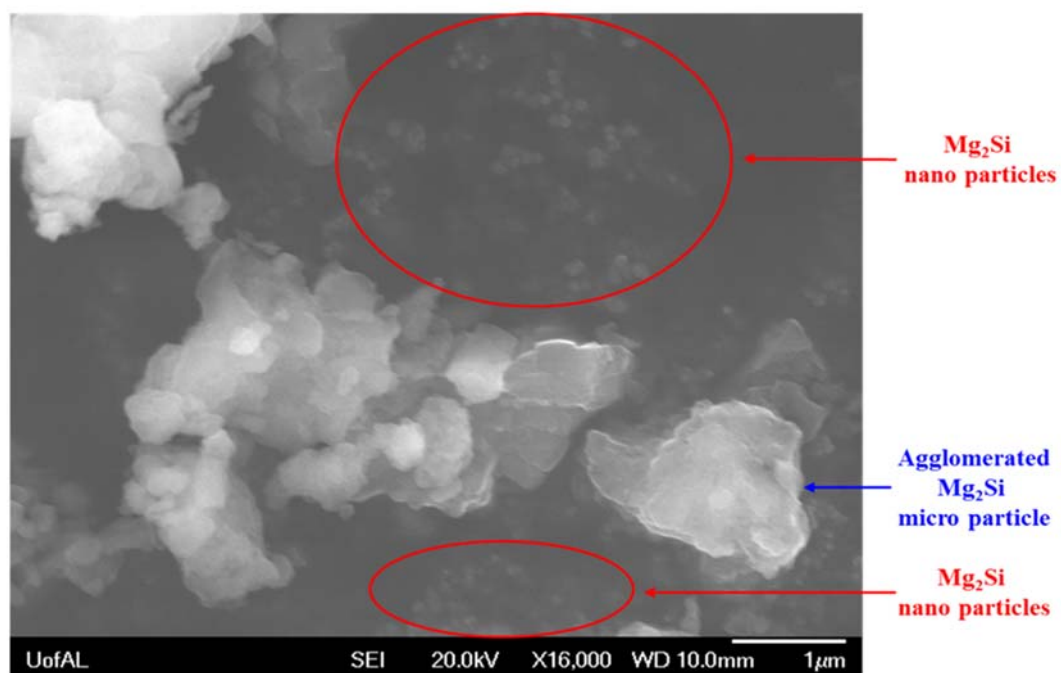


Figure 6.7 Images of (a) Mg<sub>2</sub>Si Suspension after Ultra-sonication, and (b) High Magnification SEM Image displaying Mg<sub>2</sub>Si Nanoparticles.

From the SEM image, the presence of Mg<sub>2</sub>Si nanoparticles with the average size of 215.33 nm was confirmed. Although the breakdown process resulted in Mg<sub>2</sub>Si nanoparticles, the presence of agglomerates were still seen in the ultra-sonicated sample and thus, the method need further improvements. As shown in the Figure 6.8, the separation of nanoMg<sub>2</sub>Si particles from the agglomerates/aggregates of Mg<sub>2</sub>Si occur after subjected to the ultra-sonication dispersion method.

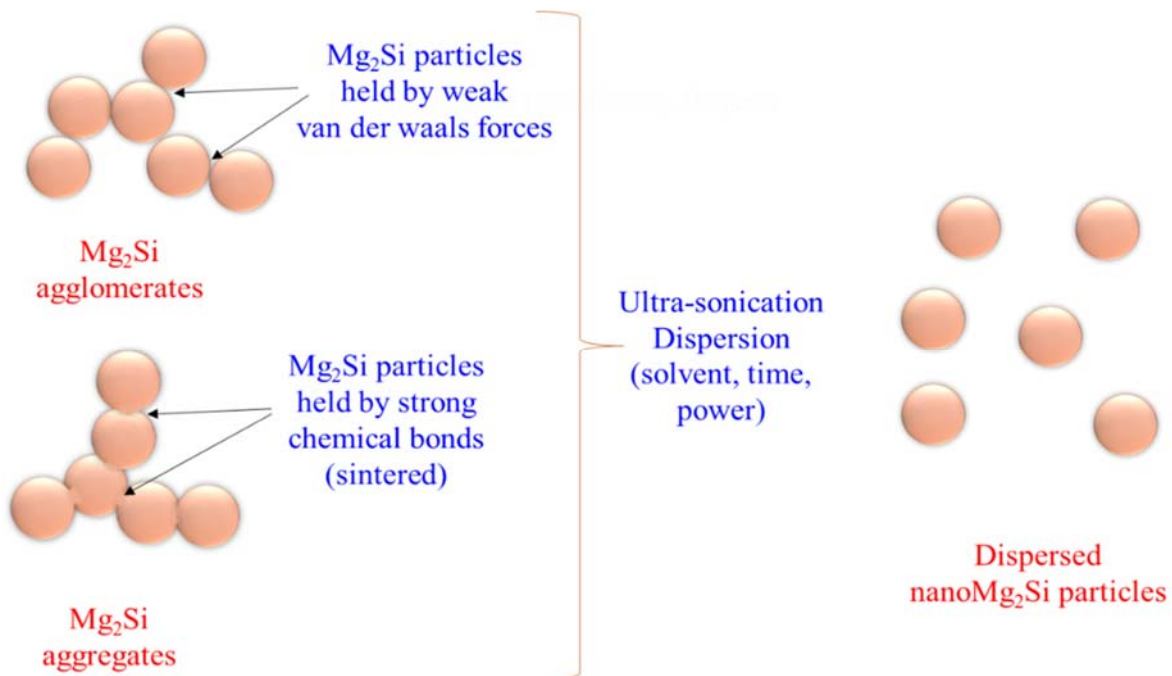


Figure 6.8 A Schematic illustrating Ultra-sonication Mediated conversion of Mg<sub>2</sub>Si Aggregates/agglomerates to NanoMg<sub>2</sub>Si.

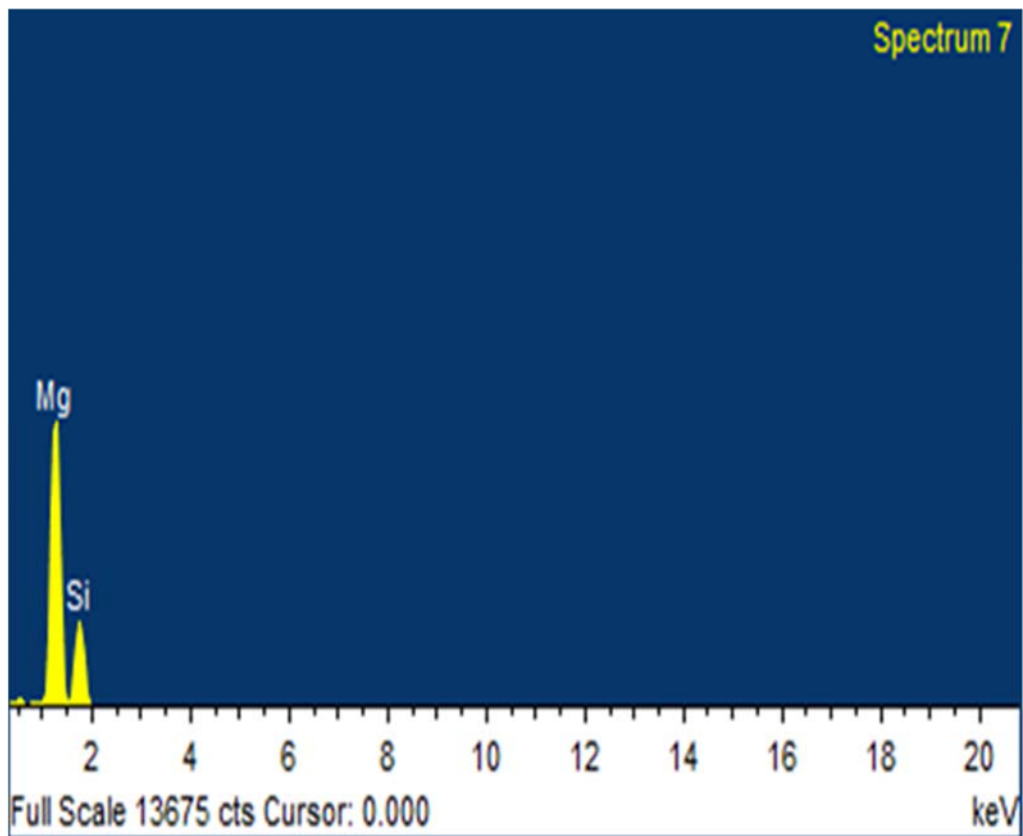


Figure 6.9. EDS Spectrum of Mg<sub>2</sub>Si Powder obtained from Sintering at 500 °C for 5 min.

Since, the Mg<sub>2</sub>Si particles were produced from the sintering process (500 °C, 5 min), the particles were held by stronger chemical bonds and therefore, additional modification of experimental parameters (solvent, pH, additives, time, and power etc.) in the existing ultrasonication method may probably result in the complete breakdown of Mg<sub>2</sub>Si aggregates into the nanoparticles of magnesium silicide.

The Mg<sub>2</sub>Si sample was later subjected to the elemental analysis using the EDS detector, attached to the 7000 JEOL FE SEM. Figure 6.9 corresponds to the total area EDS spectrum of the SEM image (shown in Figure 6.5). The elemental composition of the powder reveals the formation of ultra-high pure Mg<sub>2</sub>Si at the sintering conditions of 500 °C and 5 min.

### **6.3. Differential Thermal Analysis of Mg<sub>2</sub>Si**

The DTA experiments were conducted (*a*) to study the reaction kinetics, and estimate the formation activation energy of Mg<sub>2</sub>Si, and (*b*) to assess the thermal stability of Mg<sub>2</sub>Si, and (*c*) to determine the thermodynamic properties based on the acquired heat flow data.

#### **6.3.1. Reaction Kinetics of Mg<sub>2</sub>Si**

The DTA experiments were carried out on (2Mg + Si) mixture to study the solid-state reaction kinetics of Mg<sub>2</sub>Si formation (equation 6.2) at different scan rates of 5, 10, 15, and 20 K/min using Linseis PT 1600 DTA instrument.



As shown in the Figure 6.10, the heat flow data is plotted at different temperatures (100 - 600 °C) for varying scan rates ( $\beta = 5, 10, 15, \text{ and } 20 \text{ K/min}$ ). A positive shift in the exothermic peak of Mg<sub>2</sub>Si formation to higher temperatures, and an increase in the peak area of the heat flow curves were observed with increase in the scan rate. Similarly, as shown in Figure 6.11, the DTA

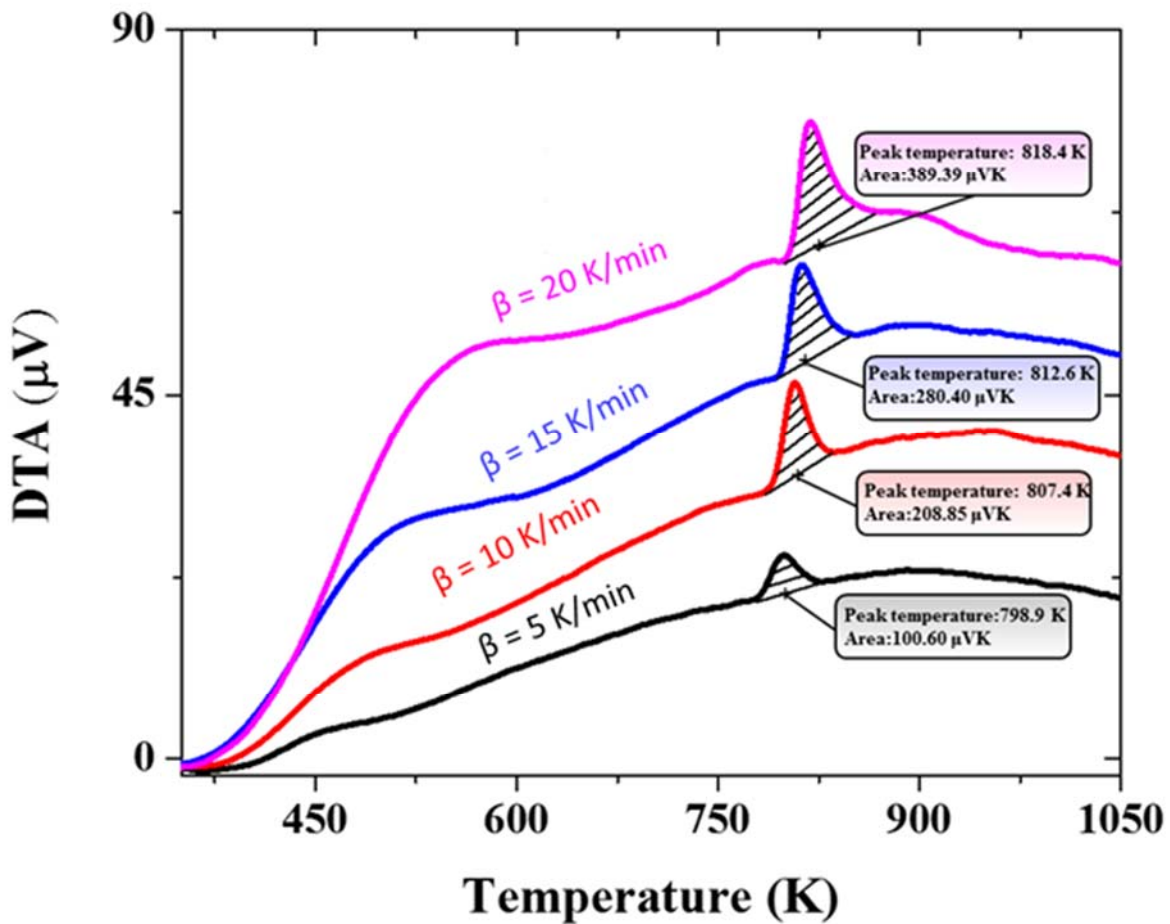


Figure 6.10: DTA Heat Flow vs. Temperature of (2Mg + Si) Mixture at Different Scan Rates.

heat flow vs. time curves showed the negative shifts in the time corresponding to the peak maximum. The peaks are sharper and the reaction process take less time for the completion at higher scan rates ( $\beta = 10, 15,$  and  $20$  K/min), while compared to that at lower scan rate ( $\beta = 5$  K/min). The peak area also increases proportionately with the increase in the scan rate. The XRD spectra (not shown) of DTA samples obtained after the solid-state reaction ( $T > 850$  K) mainly shows the reflections corresponding to reference material ( $\text{Al}_2\text{O}_3$ ), and product sample ( $\text{Mg}_2\text{Si}$ ).

The reaction rate ( $da/dT$ ) of solid-state reaction of  $\text{Mg}_2\text{Si}$  synthesis (equation 6.2) is determined for non-isothermal conditions using equation (6.3) as:

$$\frac{d\alpha}{dT} = \frac{A}{\beta} \times e^{\frac{-E_a}{RT}} \times f(\alpha) \quad (6.3)$$

where  $\alpha$  is degree of conversion,  $A$  is pre-exponential factor,  $\beta$  is heating rate,  $E_a$  is activation energy,  $R$  is gas constant,  $T$  is temperature, and  $f(\alpha)$  is conversion function.

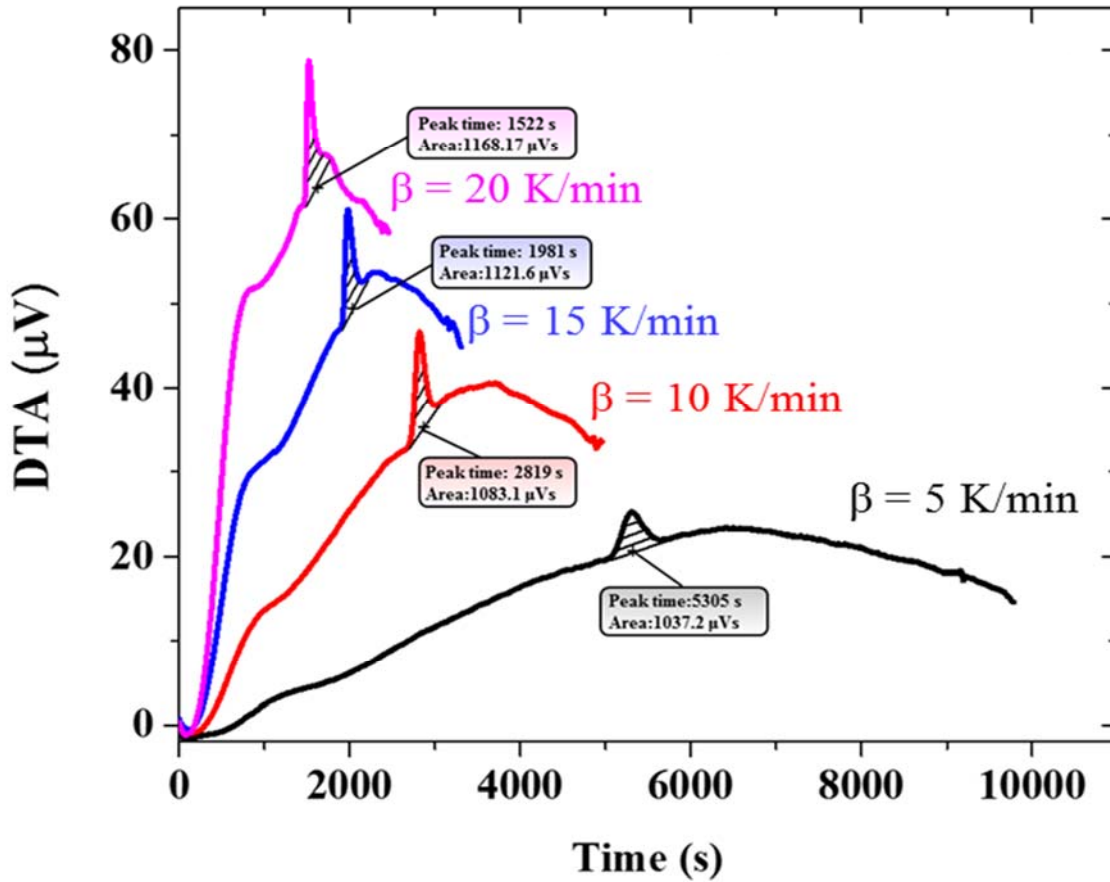


Figure 6.11: DTA Heat Flow vs. Time Plot of (2Mg + Si) Mixture at Different Scan Rates.

The reaction rate given by equation (6.7) is further simplified to calculate the activation energy of formation of  $\text{Mg}_2\text{Si}$  by using several reaction kinetic methods [141, 142]. The common equations used for calculating the activation energy of the solid-state reaction are: (i) Ozawa equation, and (ii) Kissinger-Akahira-Sunrose (KAS) equation. The Ozawa equation [143] that expresses the scan rate ( $\beta$ ) as a function of the peak maximum temperature ( $T_{max}$ ) is given by equation (6.4) as:

$$\ln \beta = \ln \left[ \frac{0.0048 \times A \times E_a}{g(\alpha) \times R} \right] - 1.0516 \frac{E_a}{RT_{max}} \quad (6.4)$$

From the experimental DTA heat flow curves of Figure 6.10, the peak temperature ( $T_{max}$ ) is obtained for different heating or scan rate ( $\beta$ ). As shown in Figure 6.12, the Ozawa equation plot of  $\ln(\beta)$  vs.  $-1.0516 /RT_{max}$  gives a straight line. The slope of the linear plot is equated to that of

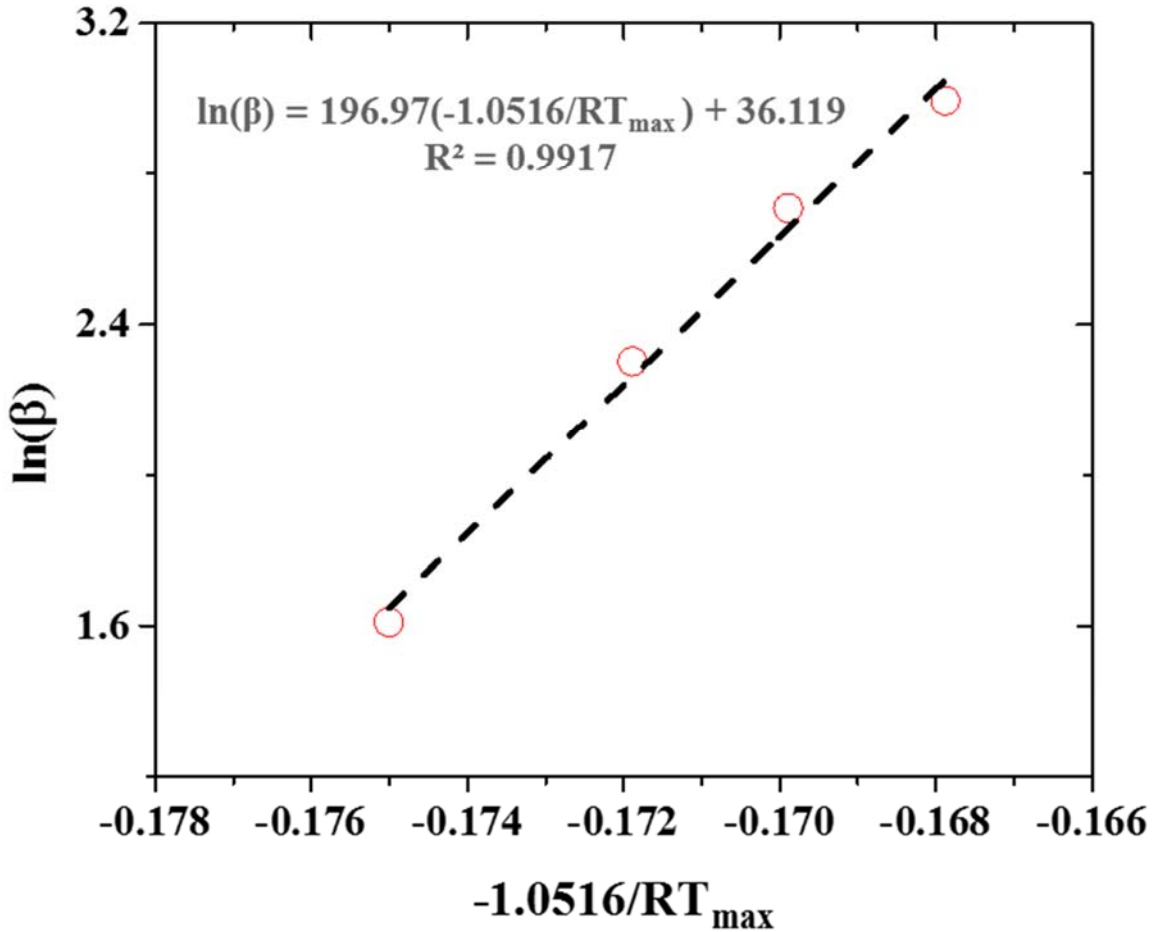


Figure 6.12:  $\ln(\beta)$  vs  $-1.0516/RT_{max}$  (Ozawa Equation) Plot for the Formation of  $Mg_2Si$ .

equation (6.4) to determine the formation activation energy of the reaction. Using the Ozawa equation, the activation energy ( $E_a$ ) for the formation of  $Mg_2Si$  is estimated to be 196.97 kJ/mol.

Similarly, the KAS equation [144] is used to estimate the activation energy for the formation of  $Mg_2Si$ , and is given by equation (6.5) as

$$\ln \frac{\beta}{T_{max}^2} = \ln \left[ \frac{A \times E_a}{g(\alpha) \times R} \right] - \frac{E_a}{RT_{max}} \quad (6.5)$$

From the Figure 6.13, the KAS equation plot of  $\ln(\beta/T^2)$  vs  $1/RT$  gives a straight line, and the slope of which is equated to equation (6.5) to obtain the activation energy for the formation of

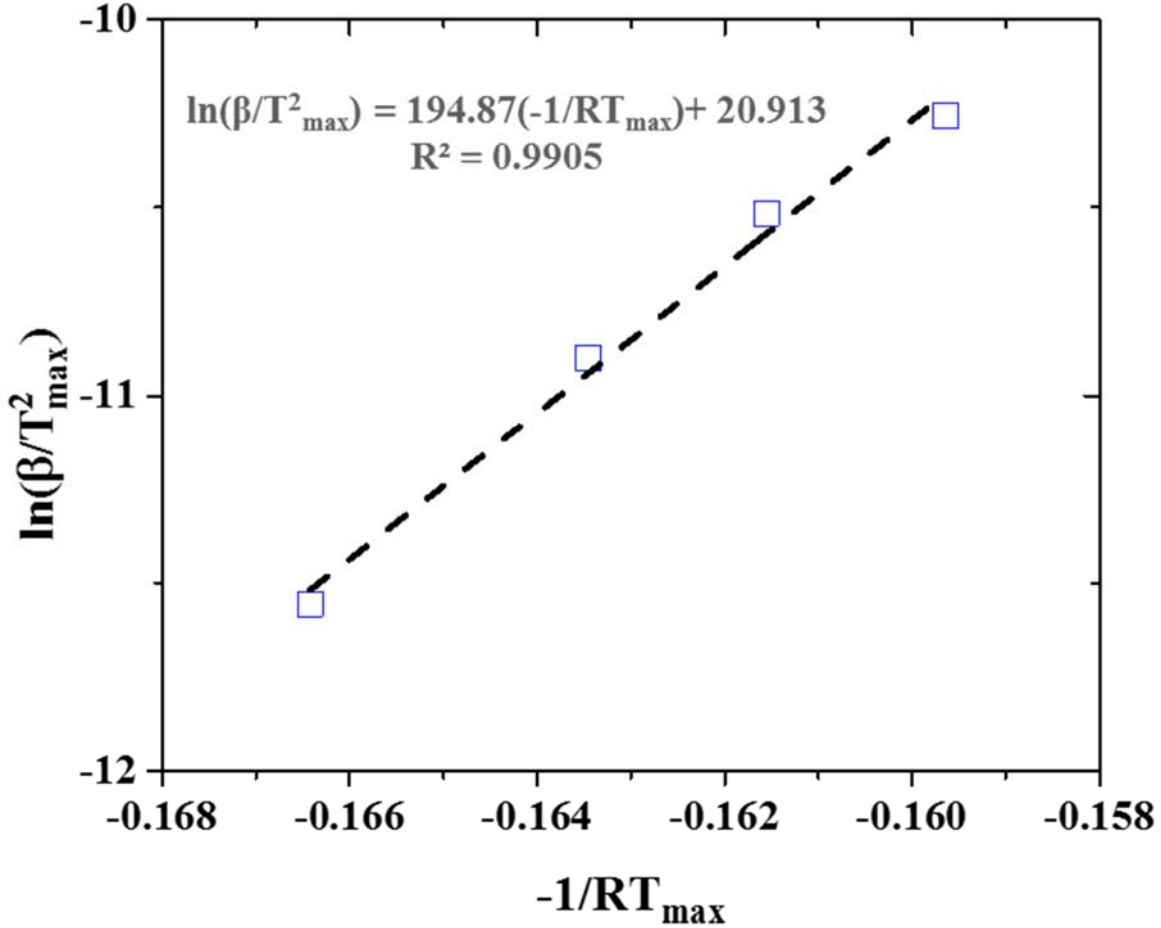


Figure 6.13:  $\ln(\beta/T_{max}^2)$  vs  $-1/RT_{max}$  (KAS Equation) Plot for the Formation of  $Mg_2Si$ .

$Mg_2Si$  as 194.87 kJ/mol. The KAS equation predicts the formation activation energy of  $Mg_2Si$ , whose value differs by 1.07% from that of the formation activation energy estimated using the Ozawa equation. To understand the reaction mechanism, and kinetics of  $Mg_2Si$  synthesis, a model-fitting method based on the Coats-Redfern (CR) equation [145] was studied. The CR equation provides a linear relationship between  $\{\ln [g(\alpha)]/T^2\}$ , and  $1/RT$  and is given by equation (6.6) as:

$$\ln \frac{g(\alpha)}{T^2} = \ln \left[ \frac{A \times R}{\beta \times E_a} \right] - \frac{E_a}{RT} \quad (6.6)$$

Table 6.2: A List of Vital Reaction Mechanisms, Kinetic Models, & Conversion Functions,  $g(\alpha)$

<b>Mechanism</b>	<b>Kinetic Model</b>	<b>Conversion Function, <math>g(\alpha)</math></b>
<b>Nucleation and Growth</b>	Power law (P1)	$\alpha^1$
	Power law (P1.5)	$\alpha^{2/3}$
	Power law (P2)	$\alpha^{1/2}$
	Power law (P3)	$\alpha^{1/3}$
	Power law (P4)	$\alpha^{1/4}$
	Exponential law (E1)	$\ln \alpha$
	Prout-Tompkins (B1)	$\ln[\alpha/(1-\alpha)]$
	Avrami–Erofeev (A0.25)	$[-\ln(1-\alpha)]^4$
	Avrami–Erofeev (A0.33)	$[-\ln(1-\alpha)]^3$
	Avrami–Erofeev (A0.5)	$[-\ln(1-\alpha)]^2$
	Avrami–Erofeev (A1.5)	$[-\ln(1-\alpha)]^{2/3}$
	Avrami–Erofeev (A2)	$[-\ln(1-\alpha)]^{1/2}$
	Avrami–Erofeev (A3)	$[-\ln(1-\alpha)]^{1/3}$
	Avrami–Erofeev (A4)	$[-\ln(1-\alpha)]^{1/4}$
<b>Geometry Contraction</b>	Contracting area/Abstract surface (R2)	$1-(1-\alpha)^{1/2}$
	Contracting/Abstract volume (R3)	$1-(1-\alpha)^{1/3}$
<b>Diffusion Controlled</b>	1-D diffusion (D1)	$\alpha^2$
	2-D diffusion (D2)	$(1-\alpha)\ln(1-\alpha) + \alpha$
	Jander equation (2D, n = 1/2)	$[1-(1-\alpha)^{1/2}]^{1/2}$
	Jander equation (2D, n = 2)	$[1-(1-\alpha)^{1/2}]^2$
	Jander equation (3D, n = 1/2)	$[1-(1-\alpha)^{1/3}]^{1/2}$
	3-D diffusion (D3)/Jander equation (3D, n = 2)	$[1-(1-\alpha)^{1/3}]^2$
	Grinstling-Brouns (D4)	$(1-2\alpha/3)-(1-\alpha)^{2/3}$

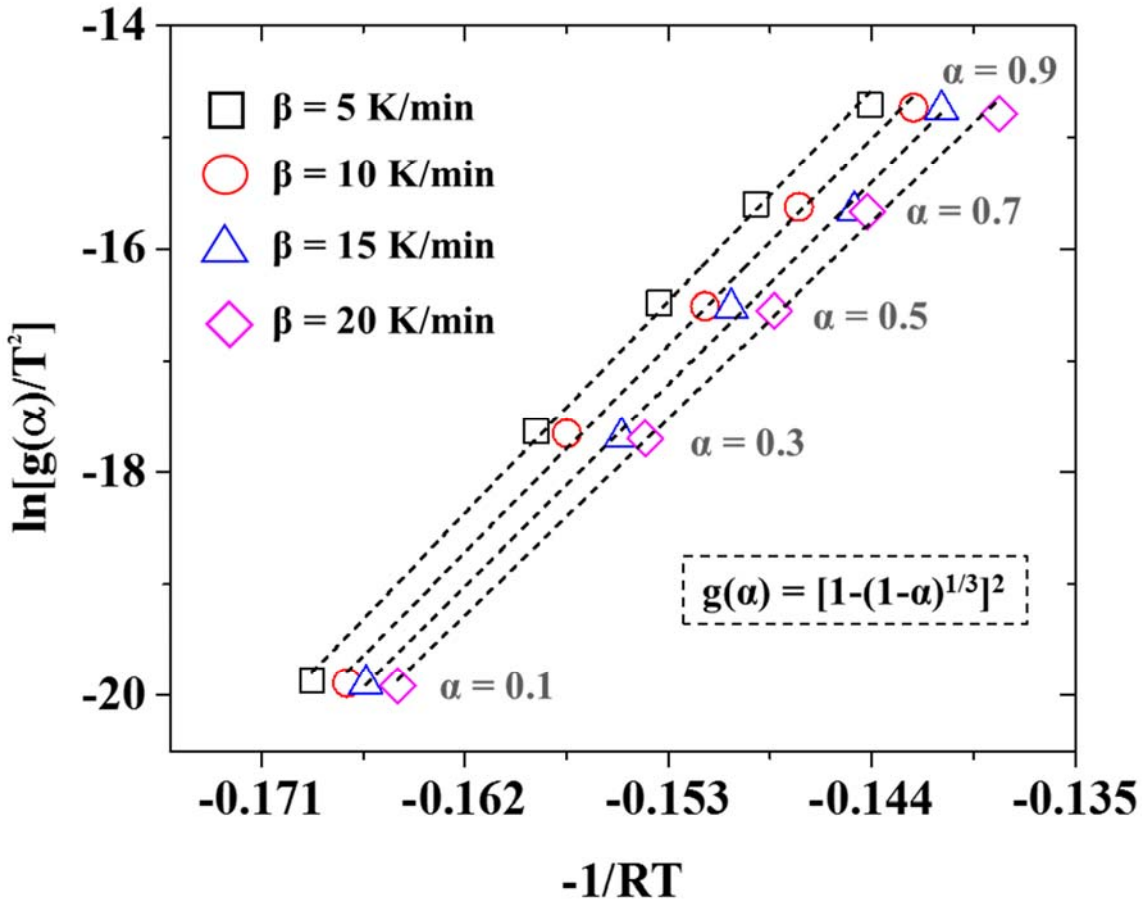


Figure 6.14:  $\ln [g(\alpha)/T^2]$  vs  $-1/RT$  (CR Equation) Plot for the Formation of  $Mg_2Si$ .

Table 6.2 [142, 146, 157] provides the list of some important common forms of the conversion function,  $g(\alpha)$ , that are not only used for modelling the reaction kinetics, but also to understand the underlying mechanism of the solid-state reaction. The conversion functions,  $g(\alpha)$  of Table 6.3, were calculated for five different degree of conversions ( $\alpha = 0.1, 0.3, 0.5, 0.7,$  and  $0.9$ ) and then, the activation energies,  $E_g$ , for all the kinetic models were estimated from the slopes of equation (6.6). Then, the CR equation activation energies were compared with the corresponding activation energies predicted using Ozawa equation, and KAS equation. All the three calculated activation energies were close when the 3-D diffusion i.e.  $g(\alpha) = [1 - (1 - \alpha)^{1/3}]^2$  model was selected as the conversion function. Hence, the formation of  $Mg_2Si$ , in equation (6.2),

is a ‘3-D diffusion controlled’ process. Figure 6.14 shows the plot of  $\{\ln [g(\alpha)]/T^2\}$  vs.  $1/RT$  for four different scan rates ( $\beta = 5, 10, 15, \& 20$  K/min). Table 6.3 lists the linear CR equations for  $Mg_2Si$  at all the scan rates. The activation energy for  $Mg_2Si$  synthesis is obtained from the average of all slopes of the four linear plots. As listed in the Table 6.3, the CR equation activation energy for formation of  $Mg_2Si$  at 20 K/min is 196.01 kJ/mol, which is comparable to the activation energies obtained from the Ozawa, KAS equations, and the literature (Table 6.4) [148-150]. Appendix B provide more details on calculation of the formation activation energies of  $Mg_2Si$ .

Table 6.3: List of Coats-Redfern Equations for  $Mg_2Si$  obtained at Different Scan Rates.

Scan rate ( $\beta$ ), K/min	Coats-Redfern equation	R <sup>2</sup> value
5	$\ln \frac{g(\alpha)}{T^2} = 15.806 - \frac{210.95}{RT}$	0.9981
10	$\ln \frac{g(\alpha)}{T^2} = 14.667 - \frac{206.08}{RT}$	0.9974
15	$\ln \frac{g(\alpha)}{T^2} = 13.575 - \frac{201.21}{RT}$	0.9981
20	$\ln \frac{g(\alpha)}{T^2} = 12.473 - \frac{196.01}{RT}$	0.9976

Table 6.4: A Comparison of Activation Energies for Formation of  $Mg_2Si$  with the Literature Data.

Activation energy (kJ/mol)	Scan rate ( $\beta$ ), K/min	Method	Reference
196.97	20	Ozawa equation, unmilled, DTA curves	This study
194.87	20	KAS equation, unmilled, DTA curves	This Study
196.01	20	CR equation, unmilled, DTA curves	This Study
201.21	15		
206.08	10		
210.95	5		
215	5, 10, 20, & 50	Kissinger approach, ball milled, DSC curves	[148]
190	10, 20, 40, & 80	Kissinger approach, unmilled, DSC curves	[149]
206	~ 400	Reactive forging, ball milled, dT/dt vs. 1/T plot	[150]

### 6.3.2. Thermal Stability of Mg<sub>2</sub>Si

In order to determine the thermal stability of Mg<sub>2</sub>Si at higher temperatures, thermal analysis was conducted on the synthesized Mg<sub>2</sub>Si sample (500 °C and 5 min) using PerkinElmer DTA7 instrument. Figure 6.15 shows the heat flow vs. temperature plot of the Mg<sub>2</sub>Si sample. The maximum of large endothermic peak due to the decomposition of Mg<sub>2</sub>Si occurs at  $T \sim 937$  °C. This is comparable to the reported decomposition peak temperature of Mg<sub>2</sub>Si at 950 °C that was obtained using DSC technique [151]. Also, pure magnesium evaporates at 1091 °C, which is close enough to that of the melting point of pure Mg<sub>2</sub>Si *i.e.*, at 1102 °C. Both the decomposition of Mg<sub>2</sub>Si into Mg and Si elements, and the evaporation of Mg metal takes place at these temperatures. The Mg<sub>2</sub>Si powder is thermally stable up to 850 °C, and therefore, the thermodynamic studies of Mg<sub>2</sub>Si are performed below this critical temperature.

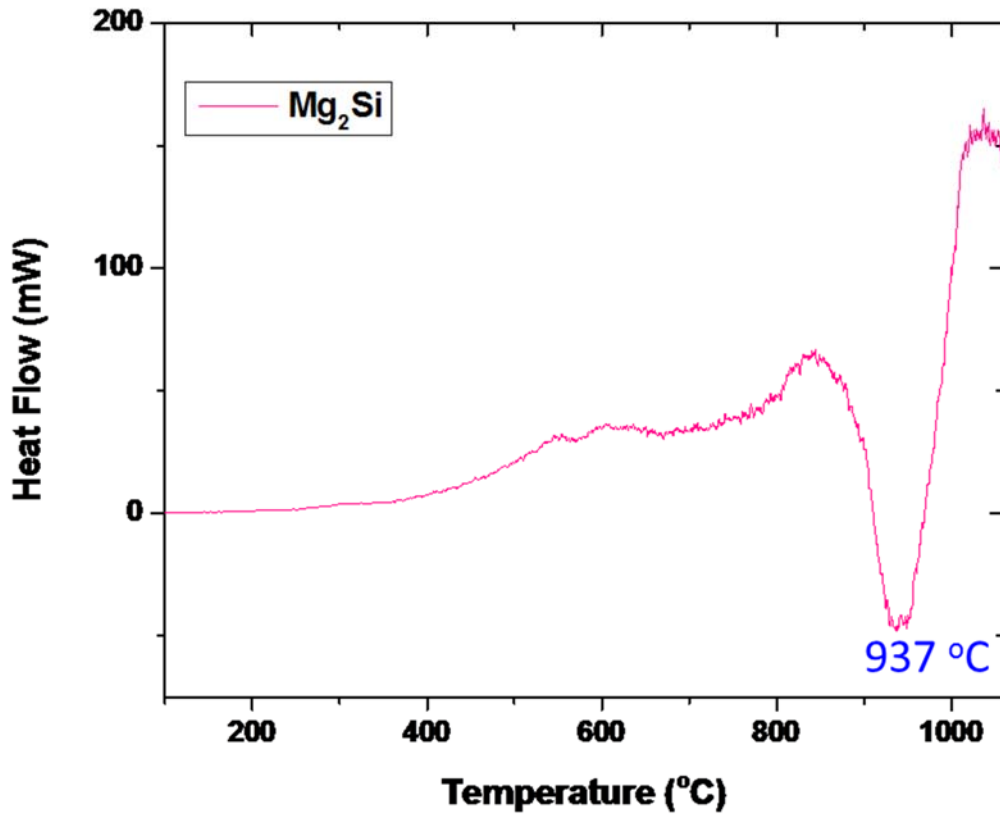


Figure 6.15: DTA Curve of Mg<sub>2</sub>Si obtained from Sintering at 500 °C for 5 min.

### 6.3.3. Specific Heat Measurement of Mg<sub>2</sub>Si

The conventional apparatus for determining the enthalpy change of a sample is DSC, while qualitative measurements of a sample are measured using DTA equipment. But, in the current study, we used Linseis PT1600 DTA instrument for quantitative measurements of the differential heat flow of the Mg<sub>2</sub>Si samples over a wide-temperature range (475 K - 1073 K). A procedure known as ‘*mass-difference baseline method*’ was employed for measuring the quantitative heat flow from the DTA instrument [152-154]. In this method, the DTA curve derived from a small mass sample is used as a baseline for the DTA curve of a large mass sample. The heat flow from the DTA mass-difference baseline method was used to determine the thermodynamic quantities, like specific heat, the changes in standard enthalpy, entropy, and Gibbs energy of Mg<sub>2</sub>Si samples.

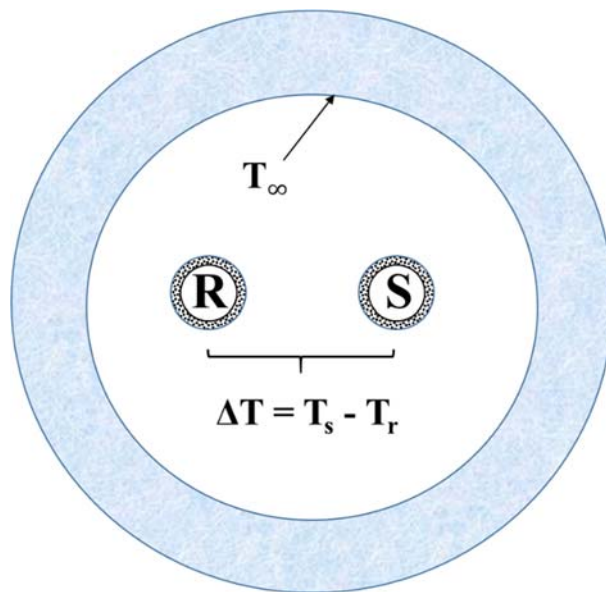


Figure 6.16: A Schematic of Cross-sectional View of Linseis PT1600 DTA Furnace.

As shown in Figure 6.16, both the sample, and reference materials are heated by same heating source ( $T_{\infty}$ ), which is the furnace wall of the DTA instrument. The DTA signal represents the temperature difference ( $\Delta T = T_s - T_r$ ) between sample, and reference materials. The change in enthalpy ( $\Delta H$ ) is then determined from ‘ $\Delta T$ ’ by using conversion factor [155]. Mathematically, the

DTA signal and  $\Delta H$  are related by energy balance equation [155], which after simplification is given by equation (6.7) as:

$$\Delta T = \frac{(\alpha_s - \alpha_r)}{\alpha_s} \times (T_\infty - T_r) - \frac{m_s}{A \times \alpha_s} \times \frac{dH}{dt} \quad (6.7)$$

where

- $\alpha_s$  - overall heat transfer coefficients from furnace to sample side,
- $\alpha_r$  - overall heat transfer coefficients from furnace to reference side,
- $T_\infty - T_r$  - temperature difference between furnace and reference,
- $m_s$  - mass of the sample,
- $A$  - surface area of the sample or the reference,
- $\frac{dH}{dt}$  - rate of the enthalpy.

From the equation (6.11), it is evident that the temperature difference ( $\Delta T$ ) can easily be obtained by knowing the change in the enthalpy ( $\Delta H$ ), and the heat transfer difference between sample and reference  $(\alpha_s - \alpha_r) \times (T_\infty - T_r)$ . Also, the influence of heat transfer term on  $\Delta T$  can be safely neglected by a simple assumption that ‘the value of  $(\alpha_s - \alpha_r)$  is zero’ [156]. Therefore, the equation (6.7) can further be reduced to a much simpler equation (6.8) given as:

$$\Delta T = - \frac{m_s}{A \times \alpha_s} \times \frac{dH}{dt} \quad (6.8)$$

In order to quantitatively determine the change in enthalpy from the DTA measurements over a wide temperature range, the mass difference baseline method was selected in the current study [152-154, 157]. In this method, the DTA curve of the sample, the mass of which is the lower limit for the equipment, is used as a baseline for DTA measurements. As a result, the influence of

asymmetric heat transfer on both the sample and the reference materials can significantly be minimized by subtracting the baseline obtained from using a smaller mass sample under similar experimental conditions. Consequently, the mass difference baseline method improves the linearity between the DTA signal and change in enthalpy of the sample.

In the present study, graphite powder (> 99%, Alfa Aesar) was used to obtain the DTA heat flow measurements. As illustrated in Figure 6.17, the DTA signal of mass difference curve (grey color,  $\Delta m = 10$  mg) was constructed from the DTA signals of 10 mg, and 20 mg graphite samples. Both 10 mg, and 20 mg graphite samples exhibited similar trend in DTA heat flow curves (from 475 K to 1100 K), which indicates the similar heat transfer coefficient ( $\alpha_s$ ) in this temperature range (dotted straight line). The temperature difference between two different samples (1 and 2),

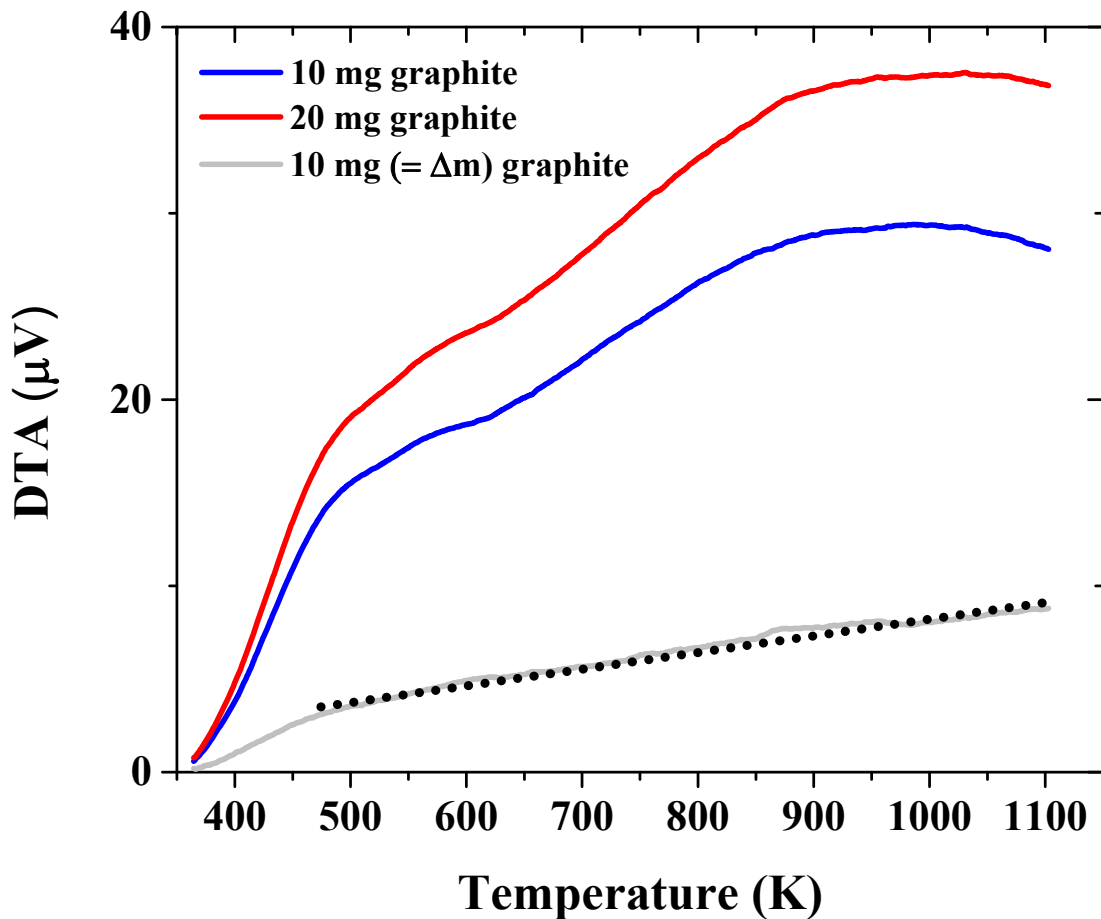


Figure 6.17: DTA Heat Flow Measurements of Graphite using Mass Difference Baseline Method

with similar heat transfer coefficient ( $\alpha_s$ ) for both baseline and sample DTA signals, can be expressed by equation (6.9) as follows [153]:

$$\Delta T_1 - \Delta T_2 = \frac{(m_{s,2} - m_{s,1})}{A \times \alpha_s} \times \frac{dH}{dt} \quad (6.9)$$

where  $\Delta T_1$  and  $\Delta T_2$  are temperature differences between sample and reference materials of two different samples with masses  $m_{s,1}$  and  $m_{s,2}$  ( $m_{s,1} < m_{s,2}$ ) respectively.

Since, the heating rate or scan rate ( $\beta$  or  $K$ ) for the DTA measurements is kept constant throughout the experiment, we consider  $dT = Kdt$ , and the temperature difference ( $\Delta T$ ) between sample and reference materials is proportional to DTA signal ( $D$ ), i.e.  $\Delta T = K_2D$ . Assuming that  $K_1 = A \times \alpha_s$ , equation (6.9) can be rearranged to obtain  $dH/dT$ , and is given by equation (6.10).

$$\frac{dH}{dT} = \frac{K_1 \times K_2}{K} \times \frac{(D_1 - D_2)}{(m_{s,2} - m_{s,1})} \quad (6.10)$$

where

$(D_1 - D_2)$  is the difference between the DTA signals of samples with masses  $m_{s,1}$  and  $m_{s,2}$ ,

$(m_{s,2} - m_{s,1})$  is the mass difference between the samples,

$K_1$  is the heat transfer coefficient that depends on the sample properties and operating conditions,

$K_2$  is the apparatus related parameter, which is function of temperature, and

$K$  is the heating rate constant.

In equation (6.14),  $K_1$  can be assumed to be constant, as the sample properties and operating conditions are fixed for each measurement. Hence, the equation (6.10) can further be simplified to equation (6.11) to obtain the following relationship between enthalpy change and DTA signal.

$$\frac{dH}{dT} = \frac{K_2}{K_2'} \times \left( \frac{dH}{dT} \right)' \times \frac{D}{(D)'} \quad (6.11)$$

where the ratio  $\frac{K_2}{K'_2}$  is a function of temperature that can be determined for a given standard material (like graphite). The ratio is used to calculate the thermodynamic properties of Mg<sub>2</sub>Si from the DTA heat flow. In the equation (6.11), the terms  $(\frac{dH}{dT}, D)$  with primes (') correspond to the graphite material, while those without primes refer to the Mg<sub>2</sub>Si sample.

Table 6.5 shows the conversion factor  $(\frac{K_2}{K'_2})$  for graphite powder from  $T = 473$  K to  $T = 1273$  K calculated by using equation (6.10). The measured DTA and specific heat ( $C_p$ ) of pure graphite from the literature [162] is also listed in the Table 6.5. In calculation of conversion factor, we considered the minimum temperature (473 K) of the dotted straight line in the mass difference ( $\Delta m$ ) curve of Figure 6.17 as the initial temperature. Selection of any temperature below 473 K (non-linear region) as a starting temperature resulted in higher values of the calculated conversion factor ( $> 1$ ) and thus, the enthalpy or specific heat data do not match well with reported literature. Although Table 6.5 gives conversion factor of graphite for  $T > 1100$  K, we only used conversion factor for  $T < 1100$  K, since Mg<sub>2</sub>Si starts decomposing above this temperature (Figure 6.15).

To determine the specific heat ( $C_p$ ) of Mg<sub>2</sub>Si over a wide temperature range of 473 K - 1073 K, DTA heat flow measurements were conducted on two mass samples (10 mg and 20 mg) of Mg<sub>2</sub>Si at a scan rate of 20 K/min. As shown in the Figure 6.18, the mass difference baseline method was used to generate the mass difference ( $\Delta m = 10$  mg) curve. As there are no significant solid-solid, and solid-liquid transitions for graphite (Figure 6.17) and Mg<sub>2</sub>Si (Figure 6.18), the DTA curve profiles for both graphite and Mg<sub>2</sub>Si appear similar except that the Mg<sub>2</sub>Si shows high DTA signal intensity than that of standard graphite. Similar to the mass difference curve of graphite, the mass difference curve of Mg<sub>2</sub>Si also showed a linear trend (dotted straight line) from 473 K to 1073 K. Therefore, thermodynamic calculations such as specific heat, change in standard enthalpy, entropy, and Gibbs energy of Mg<sub>2</sub>Si were carried out from 473 K to 1073 K.

Table 6.5 The Conversion Factor [ $\frac{K_2}{K_2'} = f(T)$ ] determined using Graphite as Standard Material.

T (K)	DTA ( $\mu$ V)	*C <sub>p</sub> (J/g*K)	DTA/†DTA'	C <sub>p</sub> /*C' <sub>p</sub>	K <sub>2</sub> /K <sub>2</sub> '
473	3.07	1.16	1.00	1.00	1.00
523	3.82	1.26	1.24	1.09	0.88
573	4.52	1.36	1.47	1.17	0.80
623	5.07	1.44	1.65	1.24	0.75
673	5.42	1.51	1.76	1.30	0.74
723	5.82	1.57	1.90	1.36	0.71
773	6.46	1.62	2.11	1.40	0.67
823	6.91	1.67	2.25	1.44	0.64
873	7.70	1.71	2.51	1.48	0.59
923	7.85	1.75	2.56	1.51	0.59
973	7.93	1.78	2.58	1.54	0.60
1023	8.23	1.81	2.68	1.56	0.58
1073	8.57	1.84	2.79	1.59	0.57
1123	8.77	1.86	2.86	1.61	0.56
1173	8.94	1.89	2.91	1.63	0.56
1223	8.30	1.90	2.70	1.64	0.61
1273	7.95	1.92	2.59	1.66	0.64

\*C<sub>p</sub>' is specific heat of graphite at 473 K; †DTA' is measured DTA data at T = 473 K.

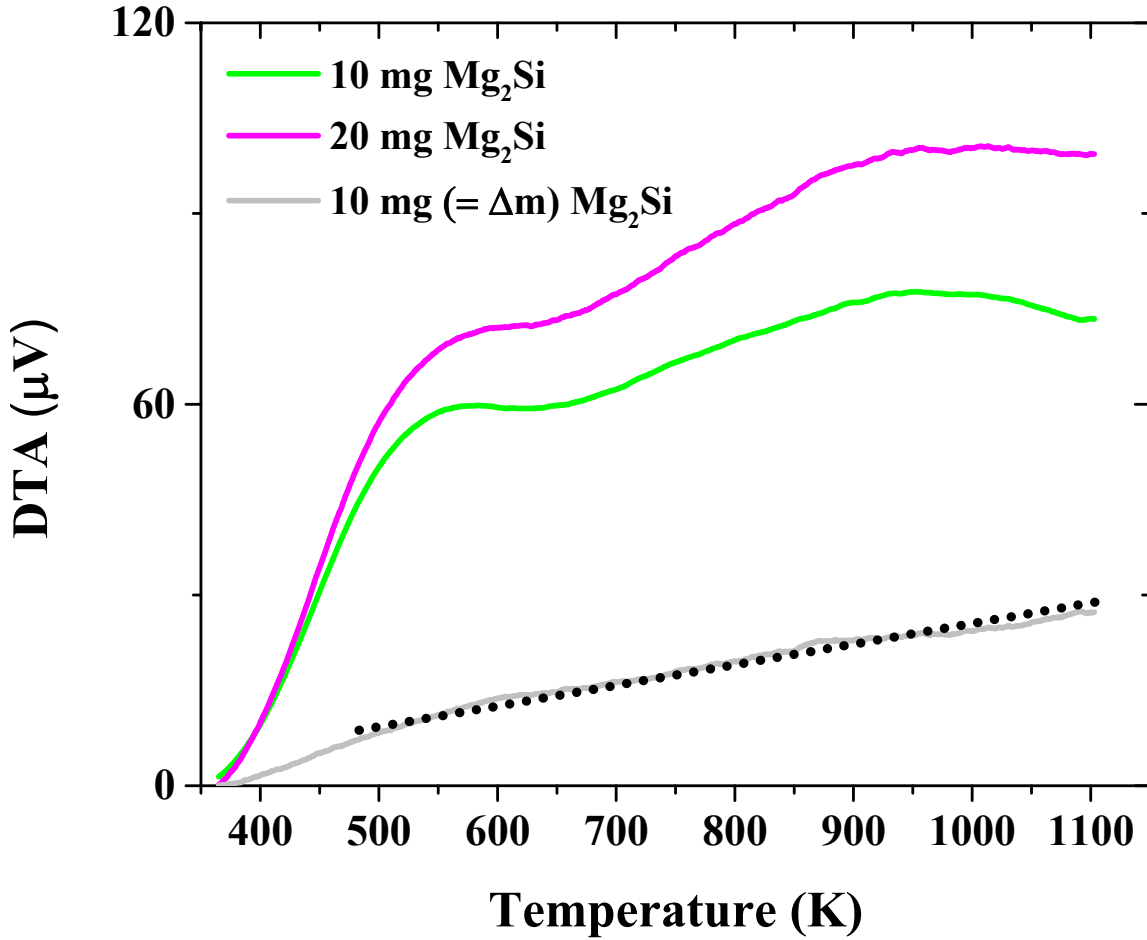


Figure 6.18: DTA Heat Flow Measurements of Mg<sub>2</sub>Si using Mass Difference Baseline Method

From the DTA signal ( $D$ ) of Figure 6.18, and the conversion factor of Table 6.5, the change in enthalpy ( $\frac{dH}{dT}$ ) was calculated for 10 mg Mg<sub>2</sub>Si sample. From equation (4.2), the specific heat ( $C_p$ ) of 10 mg Mg<sub>2</sub>Si sample was determined using ( $\frac{dH}{dT}$ ) data, and the  $C_p$  is expressed as a linear function of temperature ( $T$ ) in equation (6.12) from 473 K to 1073 K.

$$C_p(T), J/mol * K = 0.020 \times T(K) + 68.89 \quad (6.12)$$

Table 6.6 compares the specific heat of Mg<sub>2</sub>Si determined using the DTA mass difference

Table 6.6 The Specific Heat of Mg<sub>2</sub>Si from DTA Method (This Study) and Literature.

Temperature (K)	*C <sub>p</sub> (J/mol*K)	†C <sub>p</sub> (J/mol*K)
473	78.32	76.50
523	79.37	77.96
573	80.35	79.25
623	81.05	80.41
673	82.25	81.48
723	83.07	82.49
773	84.12	83.45
823	85.17	84.37
873	86.22	85.26
923	87.27	86.13
973	88.32	86.99
1023	89.37	87.82
1073	90.42	88.65

\*C<sub>p</sub> – Current DTA study; †C<sub>p</sub> from literature [158]

baseline method of the current study with that of specific heat data reported in the literature [158] for Mg<sub>2</sub>Si at 473 - 1073 K.

### 6.3. Differential Scanning Calorimetry of Mg<sub>2</sub>Si

To determine the phase stability of Mg<sub>2</sub>Si at higher temperatures, thermal analysis was conducted on synthesized Mg<sub>2</sub>Si powder (500 °C and 5 min) using DSC technique from 323 K to 623 K. About 8 mg of sample was placed into Al sample holder of PerkinElmer Diamond DSC instrument. Differential heat flow was acquired in ‘iso-scan-iso’ method using Pyris software.

The heat flow data was used to determine the specific heat capacity ( $C_p$ ) of Mg<sub>2</sub>Si sample from 323 - 623 K. The expression for  $C_p(T)$  is given by equation (6.13) for  $T < 623$  K as:

$$C_p(T), Jmol^{-1}K^{-1} = -0.0001T^2 + 0.1282T + 38.429 \quad (6.13)$$

Figure 6.19 provides the comparison of  $C_p$  vs. temperature plots of  $Mg_2Si$  sample obtained from DSC, DTA, literature [158], and thermodynamic modelling (HSC) tool [161]. At low temperatures (323 K - 573 K), the  $C_p$  values are in agreement with both the literature, and thermodynamic modelling data. The  $C_p$  values obtained from the DTA method are slightly higher in comparison with the corresponding reported, and calculated values. This may be due to the assumption that the influence of heat transfer term on ' $\Delta T$ ' was considered zero, while simplifying the equation (6.7).

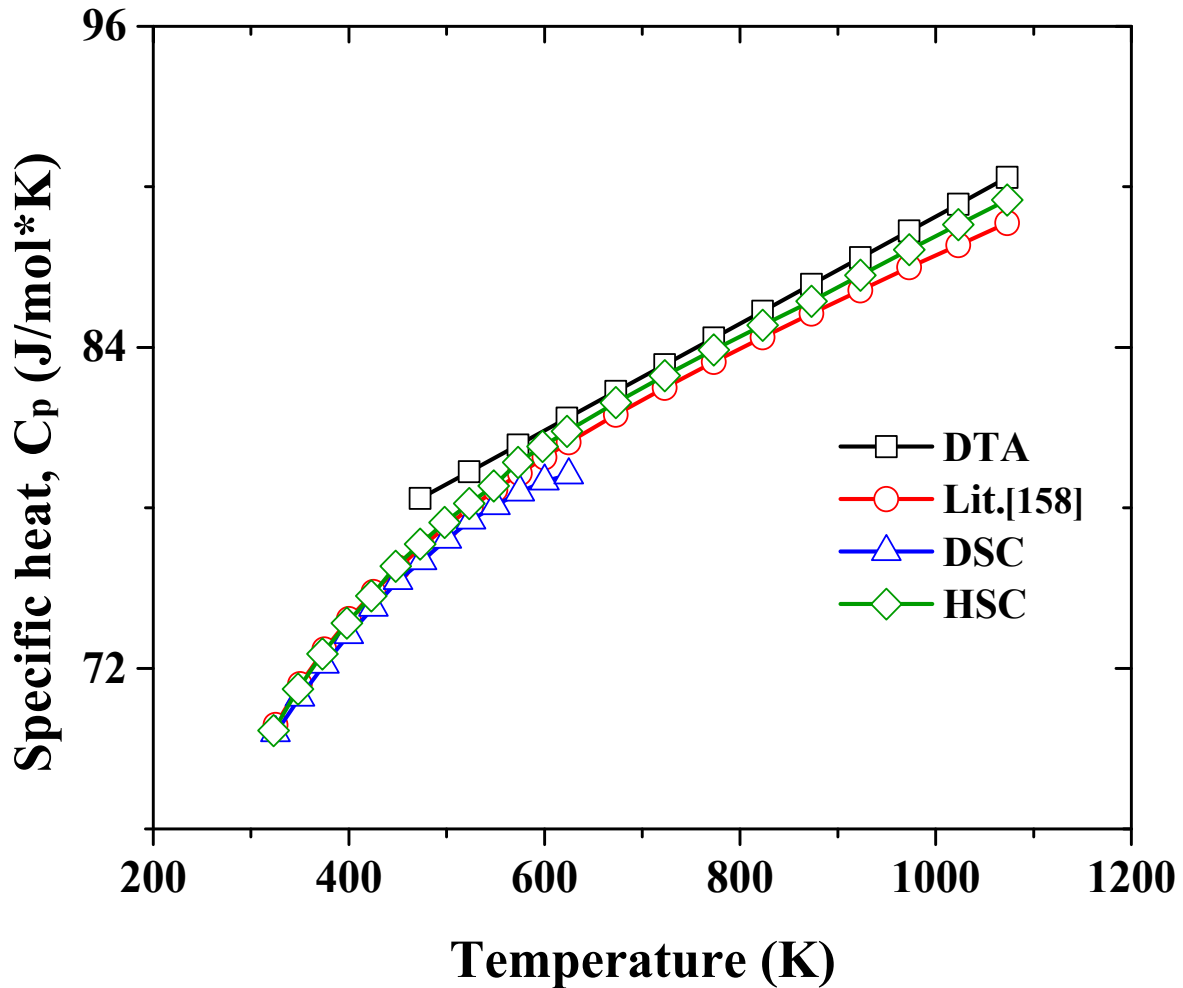


Figure 6.19 Specific Heat vs  $T$  plot of  $Mg_2Si$  obtained from DTA, DSC, HSC & Literature [158].

### 6.3. Thermodynamic Calculations of Mg<sub>2</sub>Si

Thermodynamic calculations were conducted, using  $C_p(T)$  from equations (6.14 and 6.15), to estimate the change in enthalpy ( $\Delta H^o$ ), and the change in entropy ( $\Delta S^o$ ) of Mg<sub>2</sub>Si sample, and Appendix C provide more details of the calculations.

The expressions for  $\Delta H^o(T)$  are given by equations (6.18 and 6.19) respectively.

$$\text{DSC (323 K to 623 K): } \Delta H^o(T), Jmol^{-1} = H_T^o - H_{298.15 K}^o$$

$$= \int_{298.15 K}^T C_p(T) dT$$

$$= -16272.2 + 38.429 \times T + 0.0641 \times T^2 - 0.00003333 \times T^3 \quad (6.14)$$

$$\text{DTA (473 K to 1073 K): } \Delta H^o(T), Jmol^{-1} = H_T^o - H_{473.15 K}^o$$

$$= \int_{473.15 K}^T C_p(T) dT$$

$$= -34834.00 + 68.89 \times T + 0.010 \times T^2 \quad (6.15)$$

The change in standard entropy of Mg<sub>2</sub>Si,  $\Delta S^o(T)$ , is obtained from the equations (6.16 and 6.17) as:

$$\text{DSC (323 K to 623 K): } \Delta S^o(T), Jmol^{-1}K^{-1} = S_T^o - S_{298.15 K}^o$$

$$= \int_{298.15 K}^T [C_p(T)/T] dT$$

$$= -252.731 + 0.1282 \times T - 0.00005 \times T^2 + 38.429 \times \log(T) \quad (6.16)$$

$$\begin{aligned}
\text{DTA (473 K to 1073 K): } \Delta S^o(T), Jmol^{-1}K^{-1} &= S_T^o - S_{473.15 K}^o \\
&= \int_{473.15 K}^T [C_p(T)/T] dT \\
&= -433.79 + 68.89 \times \ln T + 0.020 \times T \quad (6.17)
\end{aligned}$$

The change in Gibbs energy of Mg<sub>2</sub>Si is calculated from equations (6.18 and 6.19) using  $\Delta H^o(T)$  and  $\Delta S^o(T)$  expressions as:

$$\begin{aligned}
\text{DSC (323 K to 623 K): } \Delta G^o(T), Jmol^{-1} &= G_T^o - G_{298.15 K}^o \\
&= (H_T^o - H_{298.15 K}^o) - T(S_T^o - S_{298.15 K}^o) \\
&= -79.412 + 0.0085 T \quad (6.18)
\end{aligned}$$

$$\begin{aligned}
\text{DTA (473 K to 1073 K): } \Delta G^o(T), J/mol &= G_T^o - G_{298.15 K}^o \\
&= \left( H_T^o - H_{473.15 K}^o \right) - T \left( S_T^o - S_{473.15 K}^o \right) \\
&= -34834.00 + 502.68 \times T - 68.89 \times T \times \ln T - 0.010 \times T^2 \quad (6.19)
\end{aligned}$$

Figure 6.20 shows  $\Delta G$  vs. temperature plot of Mg<sub>2</sub>Si powder, which was produced from sintering at 500 °C and 5 min. The negative Gibbs energy values of Mg<sub>2</sub>Si suggests that the obtained Mg<sub>2</sub>Si powder is thermally stable at higher temperatures. Table 6.7 compares the experimental values of thermodynamic properties ( $\Delta G(T)$ ,  $C_p(298.15 K)$ ,  $\Delta_f H^o(298.15 K)$ ,  $\Delta_f S^o(298.15 K)$ , and  $\Delta_f G^o(298.15 K)$ ) with corresponding values from the literature, and the predictions using Gibbs energy minimization tools.

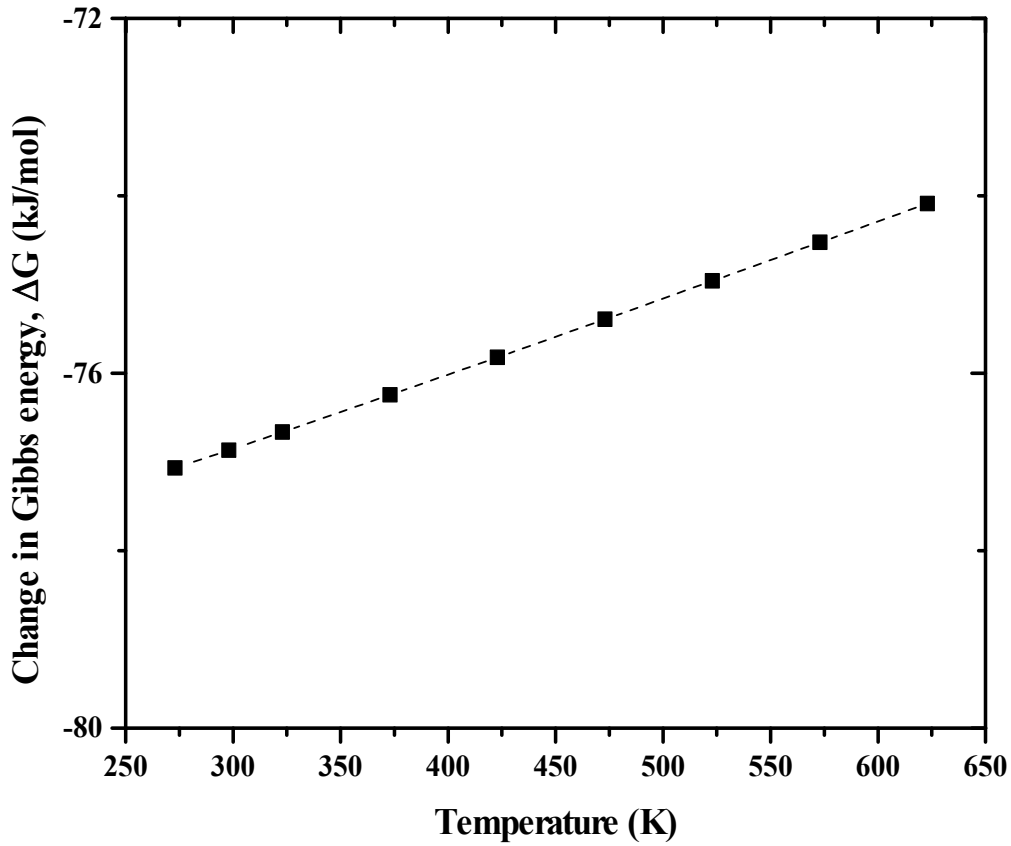


Figure 6.20. Change in Gibbs Energy vs. Temperature for Mg<sub>2</sub>Si obtained at 500 °C and 5 min.

Table 6.7. Change in Gibbs Energy  $\Delta G(T)$  and Thermodynamic Properties of Mg<sub>2</sub>Si at 298.15 K

Mg <sub>2</sub> Si	$\Delta G^\circ(T)$	At 298.15 K			
	(kJ/mol) T = 323 - 623 K	$C_p$ (J/mol*K)	$\Delta_f H^\circ$ (kJ/mol)	$\Delta_f S^\circ$ (J/mol*K)	$\Delta_f G^\circ$ (kJ/mol)
<b>This study</b>	$-79.41 + 0.0085 T$	$67.76 \pm 0.39$	-79.41	-8.50	-76.87
<b>Gerstein et al.[159]</b>	$-77.80 + 0.0080 T$	$68.43 \pm 0.20$	-77.80	-8.05	-75.40
<b>Barin et al.[160]</b>	$-79.29 + 0.0084 T$	67.83	-79.29	-8.40	-76.78
<b>HSC 7.1[161]</b>	$-77.80 + 0.0081 T$	67.84	-77.80	-8.12	-75.38
<b>FactSage 6.3[162]</b>	$-70.82 + 0.0015 T$	67.77	-80.82	-15.06	-76.33

## 6.5. EMF Study of Mg-Si System

Thermodynamic properties of both solid and liquid phases, such as activities, Gibbs energy of mixing etc., can be accurately determined using the electromotive force (EMF) or solid-state galvanic cell method. The EMF cell method uses solid electrolytes like oxides, fluorides etc., which exhibits good ionic conductivities at higher temperatures. Calcium fluoride ( $\text{CaF}_2$ ) is most commonly used as an electrolyte because of its fluoride ion conductivity, which is close to unity for wide-range of temperatures [163, 164]. The design and construction of the EMF cell is critical for precise determination of thermodynamic properties of the Mg-Si system. Figure 4.10 shows EMF cell setup used in the current study. As shown in Figure 6.21, the reference and working electrodes for the EMF cell experiments were prepared using cold-pressing and sintering methods.

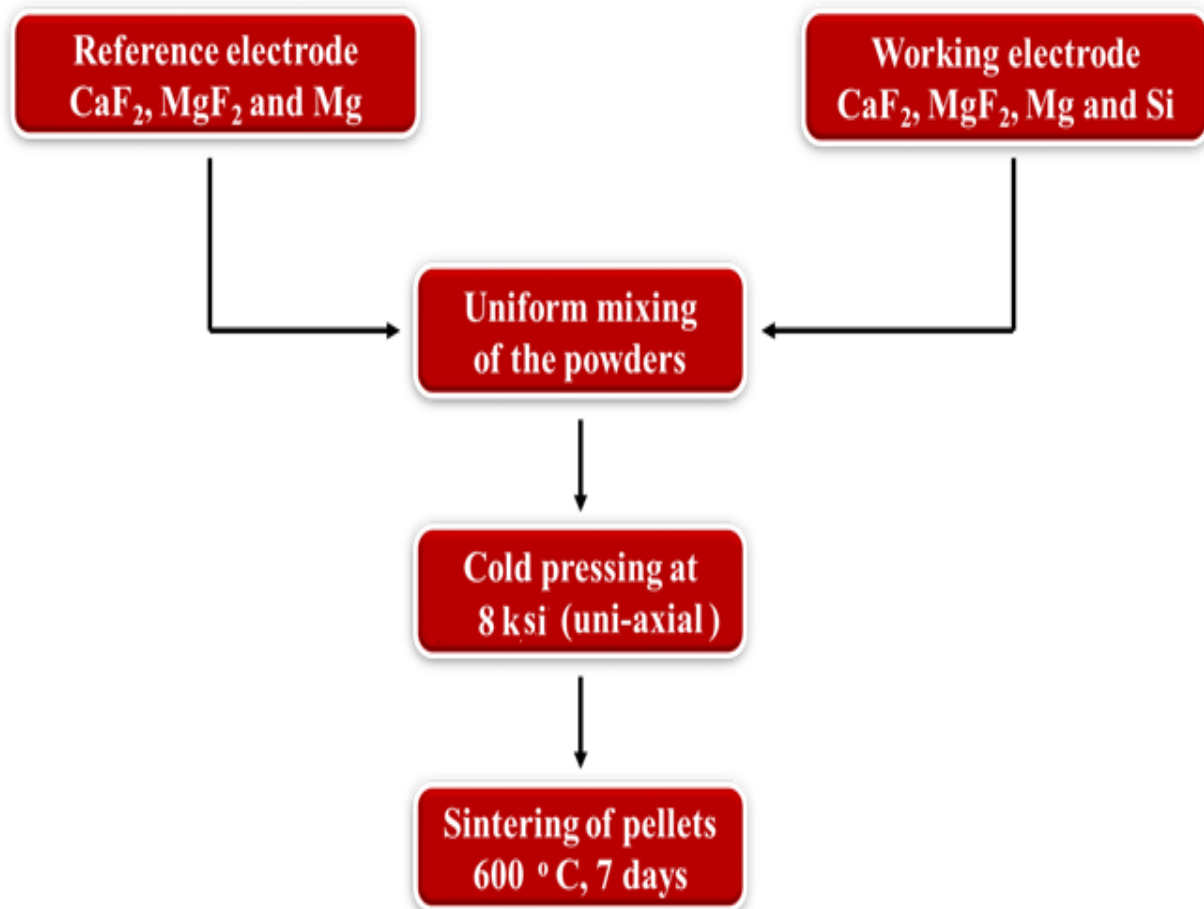


Figure 6.21: A Schematic displaying the Procedure for Preparation of EMF Electrodes.

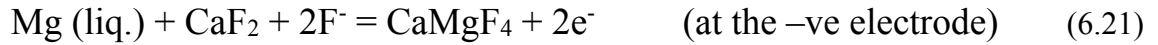
The solid-state galvanic cell is represented by equation (6.20) as

Solid-state galvanic cell:

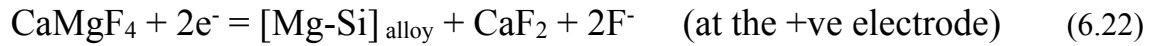


Different half-cell reactions takes place at the reference electrode and the working electrode. The reactions occurring at the reference and the working electrodes are given by equations (6.21 and 6.22) as:

Reference electrode reaction:



Working electrode reaction:



Net cell reaction:



The net cell reaction (equation 6.23) is obtained by adding half-cell reactions of equations (6.21 and 6.22). The variation of EMF as a function of temperature for the above cell with different composition of Mg-Si alloys is shown in Figure 6.22.

The EMF ( $E/mV$ ) for each alloy composition is linearly related to the temperature ( $T/K$ ) by equation (6.24), and Table 6.8 lists the values of constants A and B for each alloy composition.

$$E = A + B \times T \quad (\pm 0.5) \text{ (mV)} \quad (6.24)$$

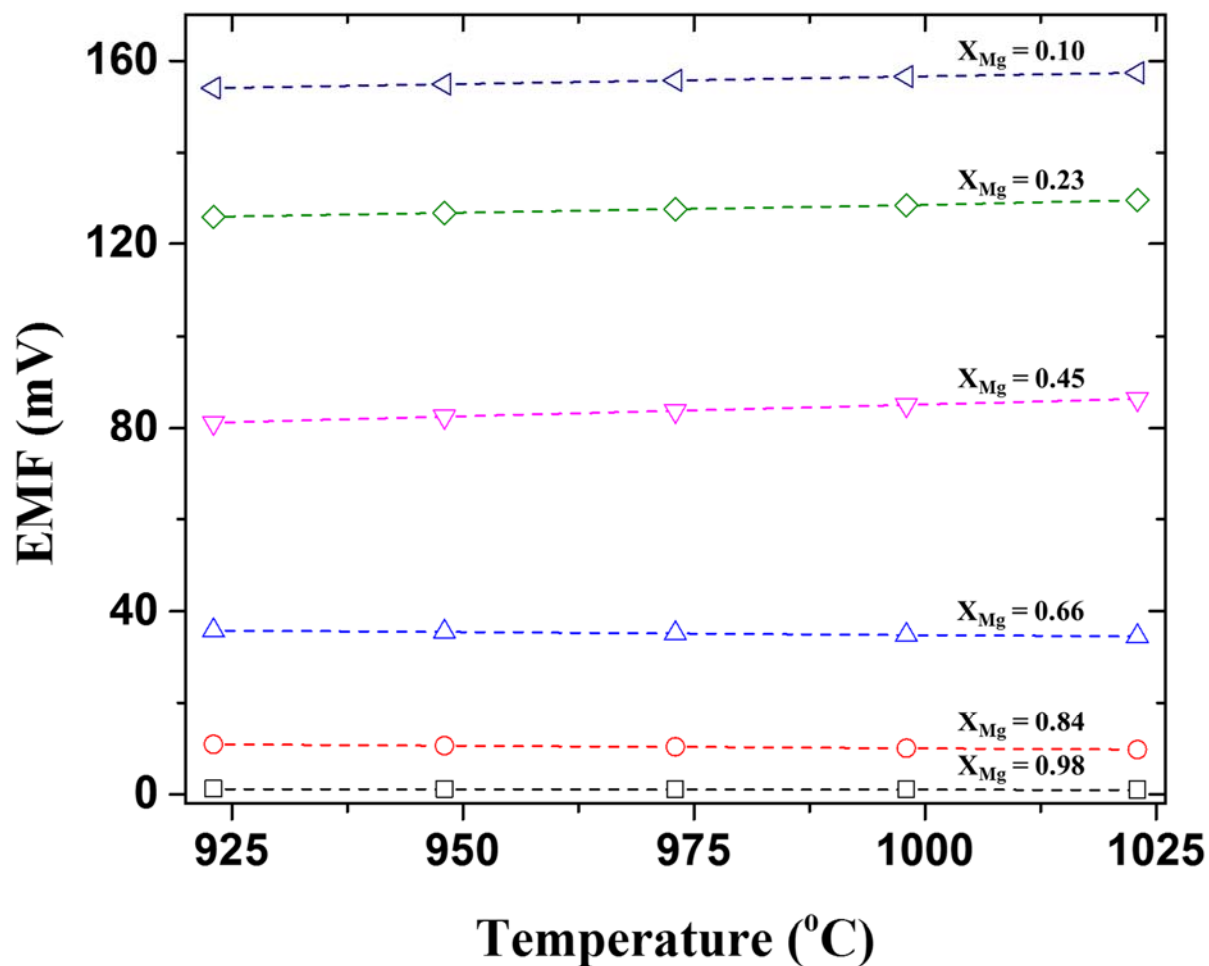


Figure 6.22: A Plot of EMF vs. Temperature for Different Compositions of Mg-Si System

Table 6.8: Values of Constants A and B obtained from the Straight Lines of  $E$  vs.  $T$  in Figure 6.23.

[Mg-Si] <sub>alloy</sub>	A (mV)	B ( $\mu\text{V K}^{-1}$ )
Mg <sub>0.10</sub> Si <sub>0.90</sub>	123.16	33.5
Mg <sub>0.23</sub> Si <sub>0.77</sub>	92.824	35.8
Mg <sub>0.45</sub> Si <sub>0.55</sub>	33.724	51.5
Mg <sub>0.67</sub> Si <sub>0.33</sub>	47.816	-13.0
Mg <sub>0.84</sub> Si <sub>0.16</sub>	21.199	-11.3
Mg <sub>0.98</sub> Si <sub>0.02</sub>	2.7271	-1.70

As shown in Figures 6.23 and 6.24, the XRD spectra of the reference electrode and working electrode before and after the EMF cell experiments respectively. A decrease in signal intensities

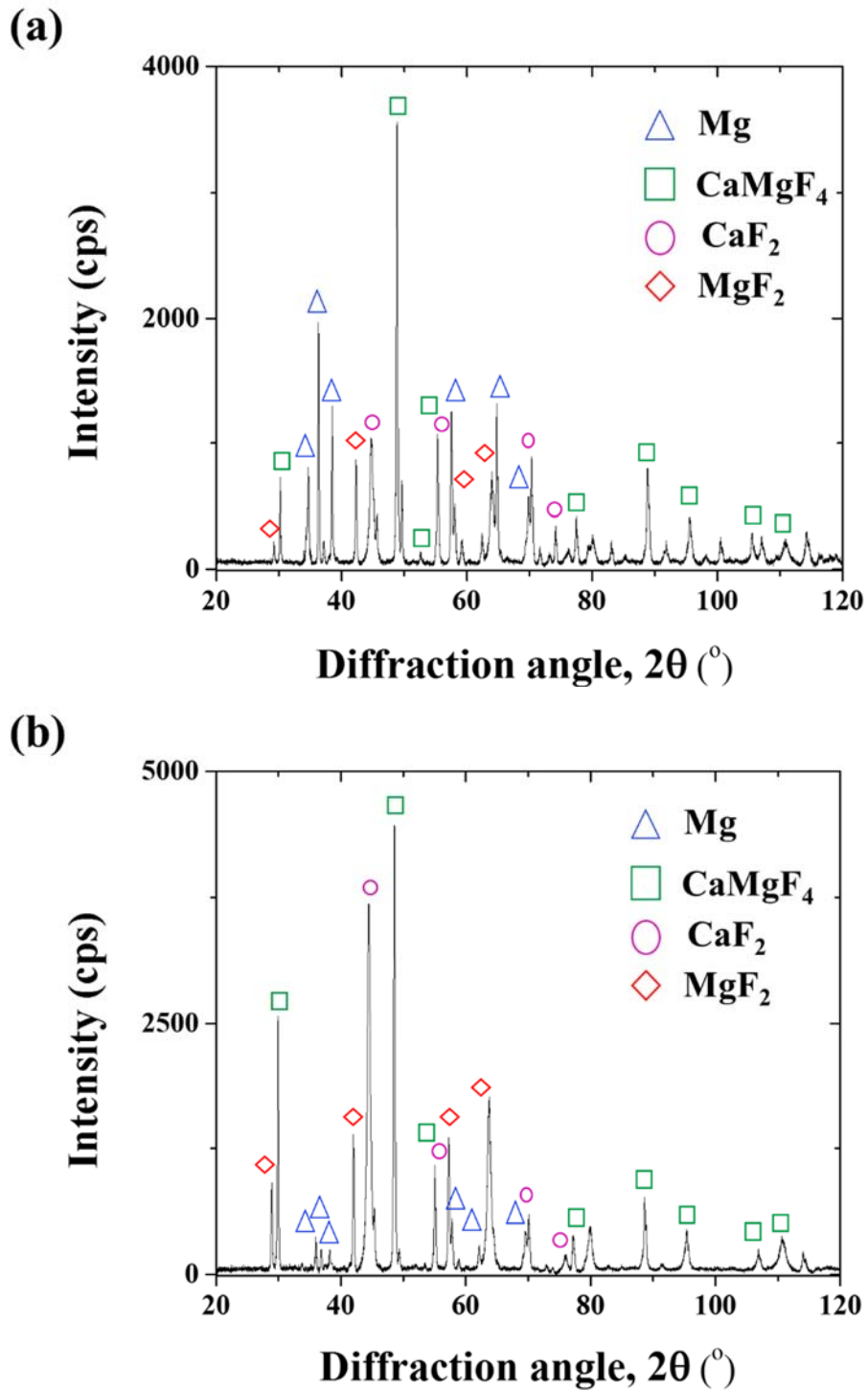


Figure 6.23: XRD Plots of Reference Electrode of Mg<sub>0.66</sub>Si<sub>0.33</sub> (a) Before & (d) After Experiment

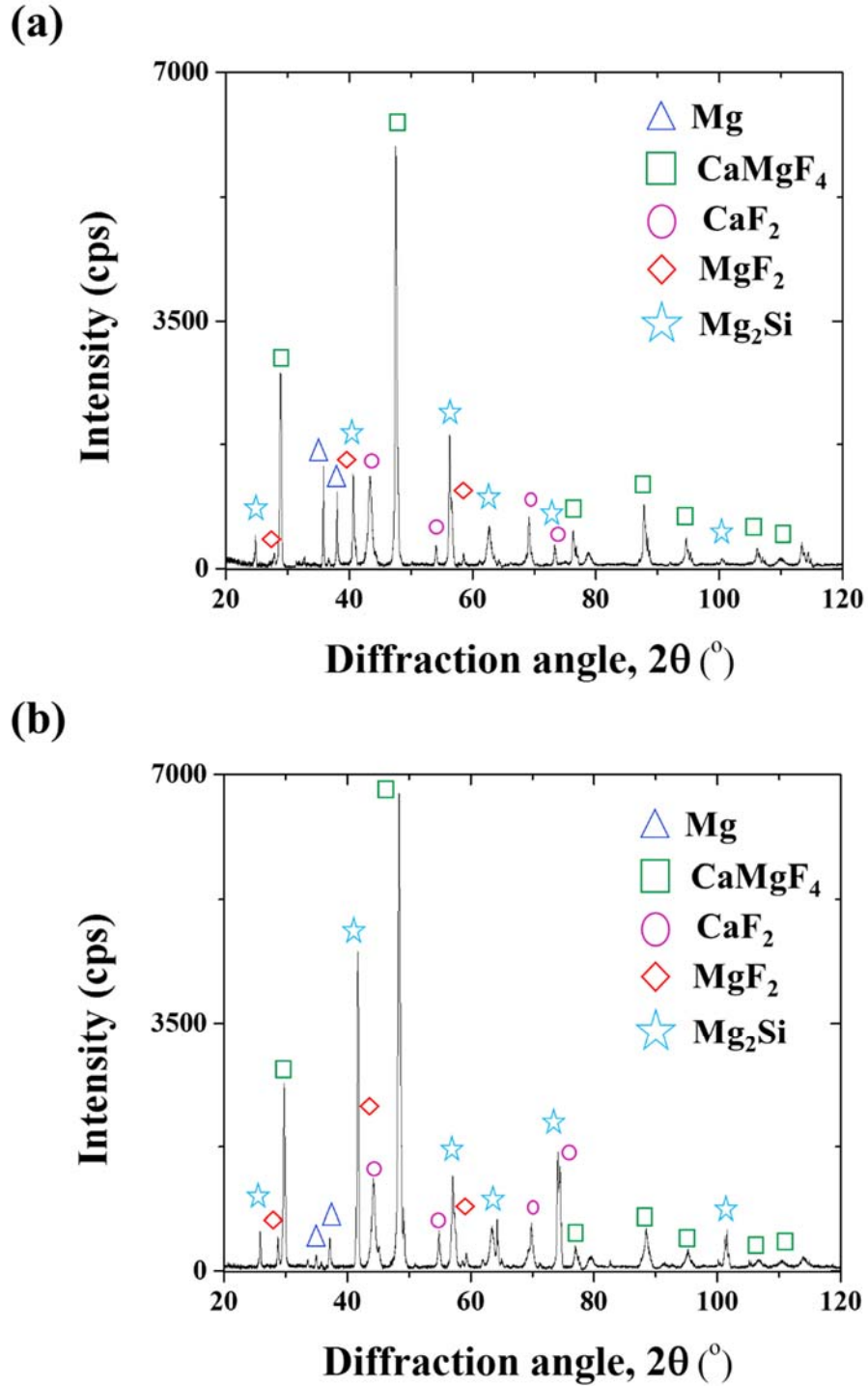


Figure 6.24: XRD Plots of Working Electrode of  $\text{Mg}_{0.66}\text{Si}_{0.33}$  (a) Before & (d) After Experiment.

corresponding to the characteristic reflections of Mg in reference electrode, and an increase in the signal intensities of the characteristic reflections of  $\text{Mg}_2\text{Si}$  in working electrode were observed.

The cell voltage from the solid-state galvanic cell was used for deriving the partial and integral thermodynamic properties of the Mg-Si system. The partial properties of magnesium are directly obtained from the EMF values of equation (6.24). The cell voltage is directly related to the partial Gibbs energy of the least noble element through Nernst equation [165 - 167]. Thus, the partial Gibbs energy of Mg in Mg-Si system can be calculated using equation (6.25) as:

$$\Delta\bar{G}_{Mg} = -nFE \quad (6.25)$$

where  $E$  is the cell voltage,  $n$  is the number of moles of Mg involved, and  $F$  is the Faraday's constant (96845 J/mol V). The activity of Mg is related to the partial Gibbs energy by equation (6.26) as follows.

$$\Delta\bar{G}_{Mg} = RT \ln \left[ \frac{a_{Mg}}{a_{Mg(l)}} \right] \quad (6.26)$$

The activity of Mg in its solid state is assumed to be unity. So, the EMF is related to the activity of Mg in the alloy is obtained from equation (6.27) as follows

$$a_{Mg} = \exp \left[ \frac{\Delta\bar{G}_{Mg}}{RT} \right] = \exp \left[ \frac{-nFE}{RT} \right] \quad (6.27)$$

The activity coefficient of Mg is calculated from the activity of Mg using the relationship given by equation (6.28) as follows:

$$\gamma_{Mg} = \frac{a_{Mg}}{X_{Mg}} = \frac{1}{X_{Mg}} \exp \left[ \frac{-nFE}{RT} \right] \quad (6.28)$$

The activity coefficient of Si is calculated from Gibbs – Duhem relation, and is given by equation (6.29) as:

$$\ln \gamma_{Si} = -X_{Mg} \times X_{Si} \times \left[ \frac{\ln \gamma_{Mg}}{X_{Si}^2} \right] - \int_1^{X_{Si}} \left[ \frac{\ln \gamma_{Mg}}{X_{Si}^2} \right] dX_{Si} \quad (6.29)$$

The activity of silicon is calculated from the activity coefficient values using equation (6.30) given as:

$$a_{Si} = \gamma_{Si} \times X_{Si} \quad (6.30)$$

Figure 6.25 shows the comparison of experimental activities of Mg and Si with those of calculated values at 973 °C [141, 168]. The activity of Mg display a negative deviation from the ideality for all the compositions studied. The activity of Si show a negative deviation from ideality

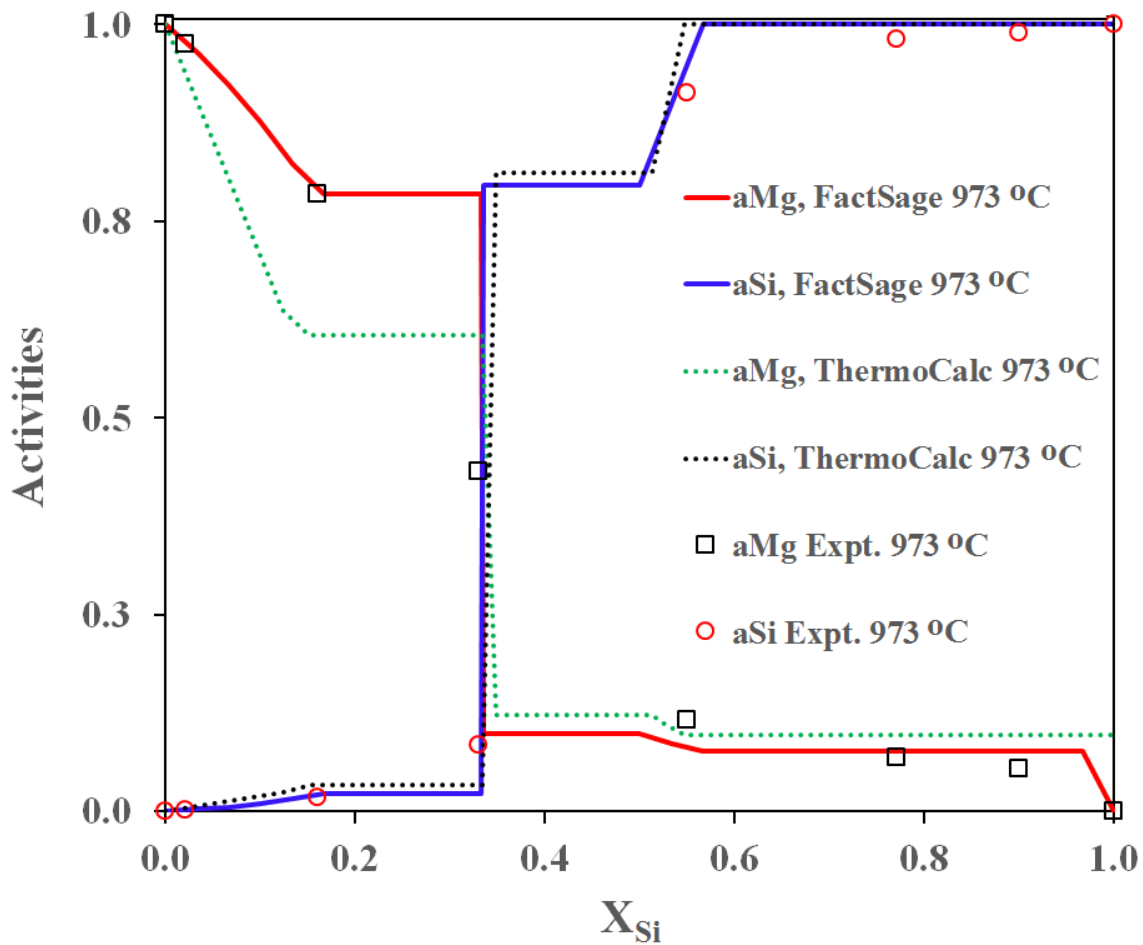


Figure 6.25: An Overlay of Calculated and Experimental Activities of Mg-Si System at 973 °C

Table 6.9: List of Activities, and Activity Coefficients of Mg and Si for Selected [Mg-Si]<sub>alloy</sub> Compositions at 973 °C.

[Mg-Si] <sub>alloy</sub>	X <sub>Mg</sub>	a <sub>Mg</sub>	γ <sub>Mg</sub>	X <sub>Si</sub>	a <sub>Si</sub>	γ <sub>Si</sub>
Mg <sub>0.10</sub> Si <sub>0.90</sub>	0.10	0.044	0.443	0.90	0.989	1.099
Mg <sub>0.23</sub> Si <sub>0.77</sub>	0.23	0.069	0.299	0.77	0.981	1.275
Mg <sub>0.45</sub> Si <sub>0.55</sub>	0.45	0.115	0.256	0.55	0.913	1.659
Mg <sub>0.67</sub> Si <sub>0.33</sub>	0.67	0.432	0.645	0.33	0.085	0.257
Mg <sub>0.84</sub> Si <sub>0.16</sub>	0.84	0.784	0.933	0.16	0.018	0.111
Mg <sub>0.98</sub> Si <sub>0.02</sub>	0.98	0.975	0.995	0.02	0.002	0.116

Table 6.10: A Comparison of Mg Activities, and Enthalpy of Mixing for Mg<sub>0.66</sub>Si<sub>0.33</sub> Composition.

Activity of Mg	Enthalpy of Mixing (ΔH <sup>M</sup> ), kJ/mol	Temperature, K	Reference
0.43	-17.47	1246	This work
0.44	-16.14	1350	[169]
---	-19.82	1350	[170]
0.26	---	1350	[171]
0.37	---	1350	[172]

for low X<sub>Si</sub> (= 0.02, 0.16, and 0.33) values, and a positive deviation from the ideality at high X<sub>Si</sub> (= 0.55, 0.77, and 0.90) values. The negative deviation behavior in activities of Mg and Si is because of the favorable interaction between Mg and Si in binary Mg-Si system, while the positive deviation in the Si activity may be due to preferential interaction of Si with other Si atoms instead of Mg atoms. Table 6.9 lists activities, and activity coefficients of [Mg-Si]<sub>alloy</sub> system at 973 °C.

In addition, Table 6.10 provide a comparison of magnesium activity and enthalpy of mixing ( $\Delta H^M$ ) for  $Mg_{0.66}Si_{0.33}$  composition with corresponding data reported from the literature [169-172].

The partial Gibbs energy of silicon is calculated using equation (6.31) as follows:

$$\Delta \bar{G}_{Si} = RT \ln a_{Si} = RT \ln (\gamma_{Si} \times X_{Si}) \quad (6.31)$$

The Gibbs energy of mixing ( $\Delta G^M$ ) for  $[Mg-Si]_{\text{alloy}}$  system is given by equation (6.32) as:

$$\Delta G^M = X_{Mg} \times \Delta \bar{G}_{Mg} + X_{Si} \times \Delta \bar{G}_{Si} = RT[X_{Mg} \times \ln a_{Mg} + X_{Si} \times \ln a_{Mg}] \quad (6.32)$$

As shown in the Figure 6.26, the Gibbs energy of mixing for the Mg-Si system is plotted against the mole fraction of silicon at 973 °C. The values of  $\Delta G^M$  are negative for all the alloy compositions, which suggests that the mixing process of Mg and Si takes place spontaneously.

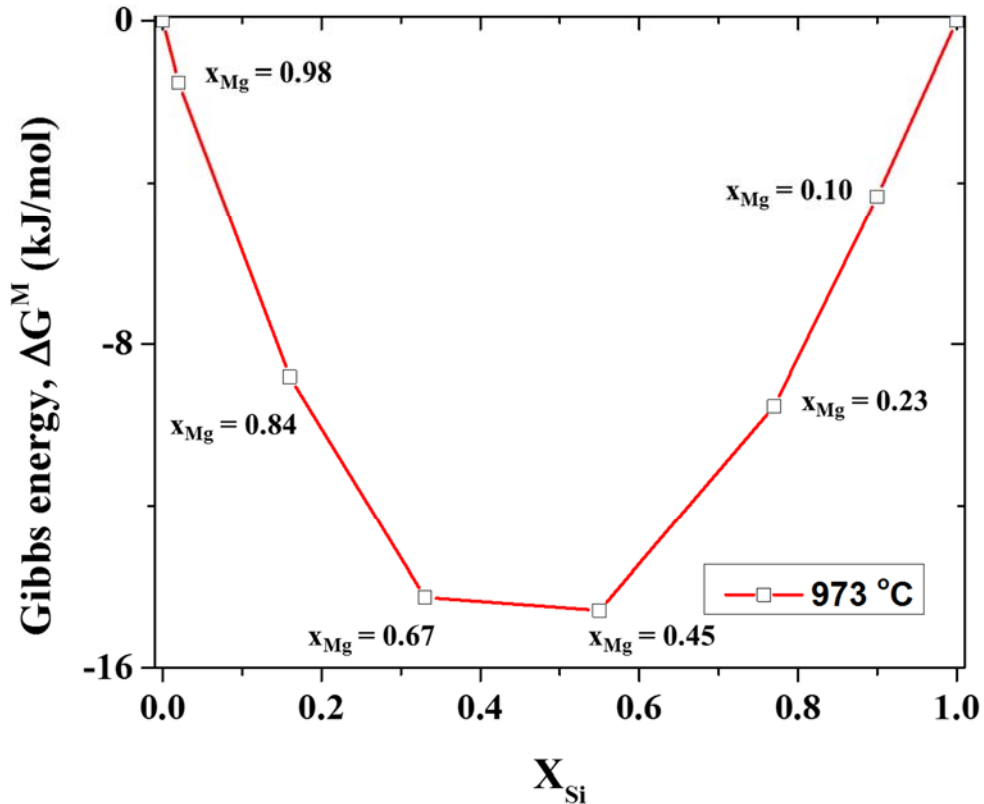


Figure 6.26: A Plot of Gibbs Energy of Mixing ( $\Delta G^M$ ) vs.  $X_{Si}$  of Mg-Si System at 973 °C

The enthalpy of mixing ( $\Delta H^M$ ) of alloys was calculated using the  $\Delta G^M$  values for each composition in the binary Mg-Si system at different temperatures using the equation (6.33) as:

$$\Delta H^M = \frac{\partial \left( \frac{\Delta G^M}{T} \right)}{\partial \left( \frac{1}{T} \right)} \quad (6.33)$$

Figure 6.27 shows the plot of  $\Delta H^M$  vs.  $X_{Si}$  for the Mg-Si system at 973 °C. The value of  $\Delta H^M$  for all the compositions are negative, which indicates that the mixing of Mg and Si occur *via* exothermic reaction. In addition, the negative  $\Delta H^M$  values suggests that the bond energy of Mg-Si is more negative than either Mg-Mg or Si-Si bond energies. This further results in ordering within the solid-solution i.e., Mg atoms prefer to associate with Si atoms, and vice versa.

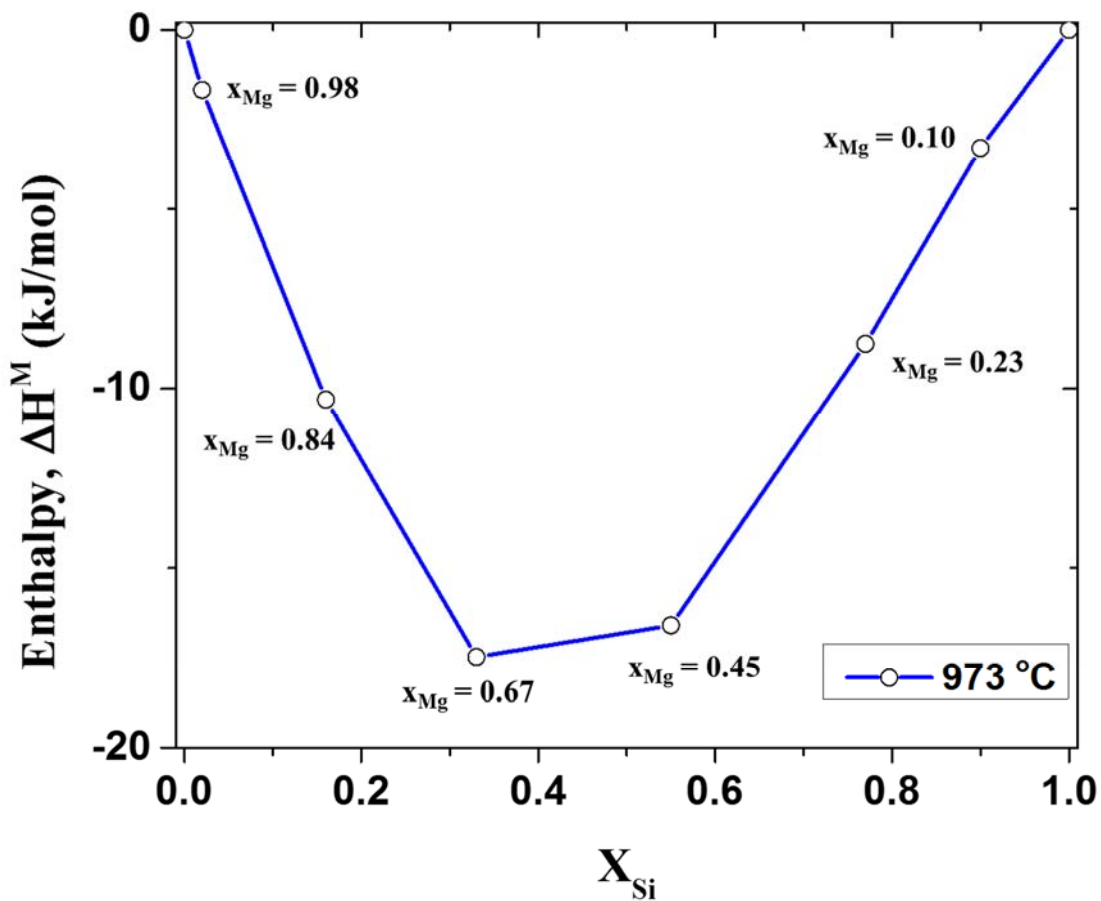


Figure 6.27: A Plot of Enthalpy of Mixing ( $\Delta H^M$ ) vs  $X_{Si}$  of Mg-Si System at 973 °C

At any given temperature ( $T$ ), the entropy of mixing ( $\Delta S^M$ ) of a solution is also related to the enthalpy of mixing ( $\Delta H^M$ ), and the Gibbs energy of mixing ( $\Delta G^M$ ) of the solution.

$$\Delta S^M = \frac{\Delta H^M - \Delta G^M}{T} \quad (6.34)$$

From knowing  $\Delta G^M$  (equation 6.32), and  $\Delta H^M$  (equation 6.33), the entropy of mixing ( $\Delta S^M$ ) for the binary Mg-Si system is calculated from equation (6.34) at 973 °C.

## 6.6. Summary of Magnesium Silicide Study

In this chapter, a simple and rapid synthesis of nanoMg<sub>2</sub>Si powders was carried out using pelleting, and sintering methods. Mg<sub>2</sub>Si was produced from cold-pressing of 2:1 molar mixture of Mg and Si, followed by sintering of the pellet at optimum conditions of 500 °C for 5 min. The Mg<sub>2</sub>Si samples were characterized using XRD, SEM, and EDS methods. Formation of uniform micro-aggregates of pure Mg<sub>2</sub>Si with an average particle size of 215.33 nm was observed.

The reaction kinetics, and thermal stability studies of Mg<sub>2</sub>Si powders was carried out using thermal techniques, such as DTA and DSC methods. The activation energy for the formation of Mg<sub>2</sub>Si was calculated to be 196.01 kJ/mol using CR equation, whose value is in good agreement with those determined from Ozawa equation, KAS equation, and to that of reported literature. Also, a 3-D diffusion controlled mechanism was established for the solid-state reaction kinetics of Mg<sub>2</sub>Si formation. Thermodynamic properties of Mg<sub>2</sub>Si was calculated using both DSC (*iso-scan-iso*) and DTA (*mass difference baseline*) methods. The specific heat of Mg<sub>2</sub>Si determined using both DSC (323 K – 623 K) and DTA (473 K – 1073 K) techniques are in good agreement with the literature reported data, and the thermodynamic modelling data (HSC). The heat capacity ( $C_p$ ), and change in Gibbs energy ( $\Delta G$ ) data suggests that the Mg<sub>2</sub>Si powders are thermally stable at higher temperatures (< 850 °C).

Furthermore, we studied the thermodynamic properties of binary Mg-Si system using EMF or solid-state galvanic cell method. A linear relationship between the cell EMF and temperature was obtained for six selected compositions of the binary alloy system. Activities of the Mg and Si were determined, and compared with the corresponding activity values calculated from thermodynamic modelling tools. Other related thermodynamic quantities such as activity coefficients, change in Gibbs energies, change in enthalpies, and change in entropies of mixing were also estimated for the binary Mg-Si system.

## CHAPTER 7

### METAL-DOPED MAGNESIUM SILICIDES

The mechanical, thermal, and thermoelectric properties of pure nanoMg<sub>2</sub>Si powders can further be improved *via* introduction of trace amounts of metals into the crystal lattice sites of Mg<sub>2</sub>Si. As discussed in the Chapter 2 (section 2.2.2), the metal-doped magnesium silicides (Mg<sub>2</sub>Si: X = 1: m; X = dopant metal, m = dopant concentration) are preferred over un-doped Mg<sub>2</sub>Si because of good control of the TE properties *via* proper selection of the metal-dopant type, and its concentration. The focus of this chapter is primarily on the effect of selected metal-dopants on the synthesis, characterization, and thermodynamic properties (activation energy, specific heat, and Gibbs energy) of magnesium silicide powders.

#### 7.1. Synthesis of Metal-doped Mg<sub>2</sub>Si

The raw materials required for the synthesis of metal-doped Mg<sub>2</sub>Si (high pure elemental powders of Mg, Si, Ti, Nb, Mn, and Co) were purchased from Alfa Aesar. Table 7.1 shows the list

Table 7.1: List of Metal-Doped Magnesium Silicides considered in the Present Study.

Mg <sub>2</sub> Si: mX alloys		Doping concentration, m (moles)			
		0	0.02	0.04	0.08
<b>Metal, X</b>	<b>Ti</b>	Mg <sub>2</sub> Si	Mg <sub>2</sub> Si:0.02Ti	Mg <sub>2</sub> Si:0.04Ti	Mg <sub>2</sub> Si:0.08Ti
	<b>Mn</b>	Mg <sub>2</sub> Si	Mg <sub>2</sub> Si:0.02Mn	Mg <sub>2</sub> Si:0.04Mn	Mg <sub>2</sub> Si:0.08Mn
	<b>Nb</b>	Mg <sub>2</sub> Si	Mg <sub>2</sub> Si:0.02Nb	Mg <sub>2</sub> Si:0.04Nb	Mg <sub>2</sub> Si:0.08Nb
	<b>Co</b>	Mg <sub>2</sub> Si	Mg <sub>2</sub> Si:0.02Co	Mg <sub>2</sub> Si:0.04Co	Mg <sub>2</sub> Si:0.08Co



## 7.2. XRD of Metal-doped Mg<sub>2</sub>Si

Small amounts of the powder samples were used for the phase analysis using XRD diffraction. As shown in Figure 6.4(b), all the samples showed the XRD reflections that are similar to that of Mg<sub>2</sub>Si powder obtained from sintering at 500 °C for 5 min. No XRD reflections corresponding to the metal-dopants or other alloy phases was observed in the spectra. The appearance of major characteristic reflection of Mg<sub>2</sub>Si: mX (220) at  $2\theta \sim 40^\circ$  in the XRD spectra suggests the formation of single product phase at 500 - 550 °C. However, from Figure 7.3, some minor changes in the position of the peak maxima for (220) reflection were observed due to the increase in concentration of the metal-dopants. This suggests that the metal-dopants have small effect on changing the crystal lattice of Mg<sub>2</sub>Si. Furthermore, the minor shifts in the peak maxima of XRD signals were used to calculate the lattice constants of Mg<sub>2</sub>Si: mX alloys.

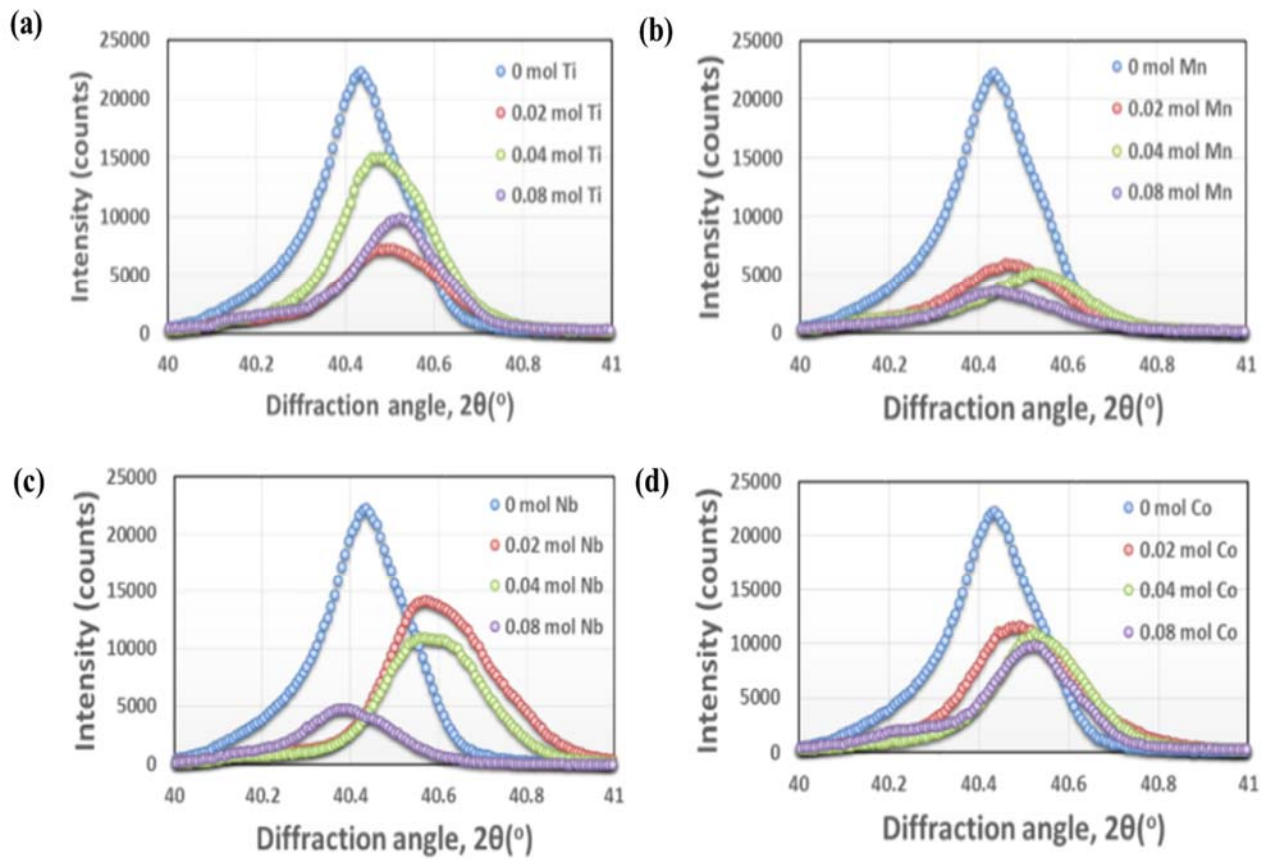


Figure 7.3: XRD of Mg<sub>2</sub>Si: mX; X = (a) Ti, (b) Mn, (c) Nb, and (d) Co, m = 0 - 0.08 mol.

### 7.3. Lattice Constants of Metal-doped Mg<sub>2</sub>Si

From the  $\theta_{hkl}$  values and using equation (6.1), the lattice constants of cubic Mg<sub>2</sub>Si: mX unit cell was calculated based on the (220) XRD reflections. Figure 7.4 (a - d) shows the plots of lattice constants of Mg<sub>2</sub>Si: mX (X = Ti, Nb, Mn & Co; m = 0, 0.02, 0.04 & 0.08 mol) samples. The dotted line is a linear fit of calculated lattice constants (open data points) from the XRD data. The Ti-doped Mg<sub>2</sub>Si shows an increase in the lattice constant with increase in the dopant concentration, while other metal (Mn, Nb, and Co)-doped Mg<sub>2</sub>Si showed a decreasing trend in lattice constant upon increasing the dopant concentration. The observed expansion or contraction in lattice constants of Mg<sub>2</sub>Si: mX may be due to (i) the substitution of metal-dopant of different ionic radius relative to that of host atoms in unit cell, and (ii) electronic properties (electron affinity, & valance state) of the constituent atoms can alter the bond lengths and hence, the structure of the unit cell.

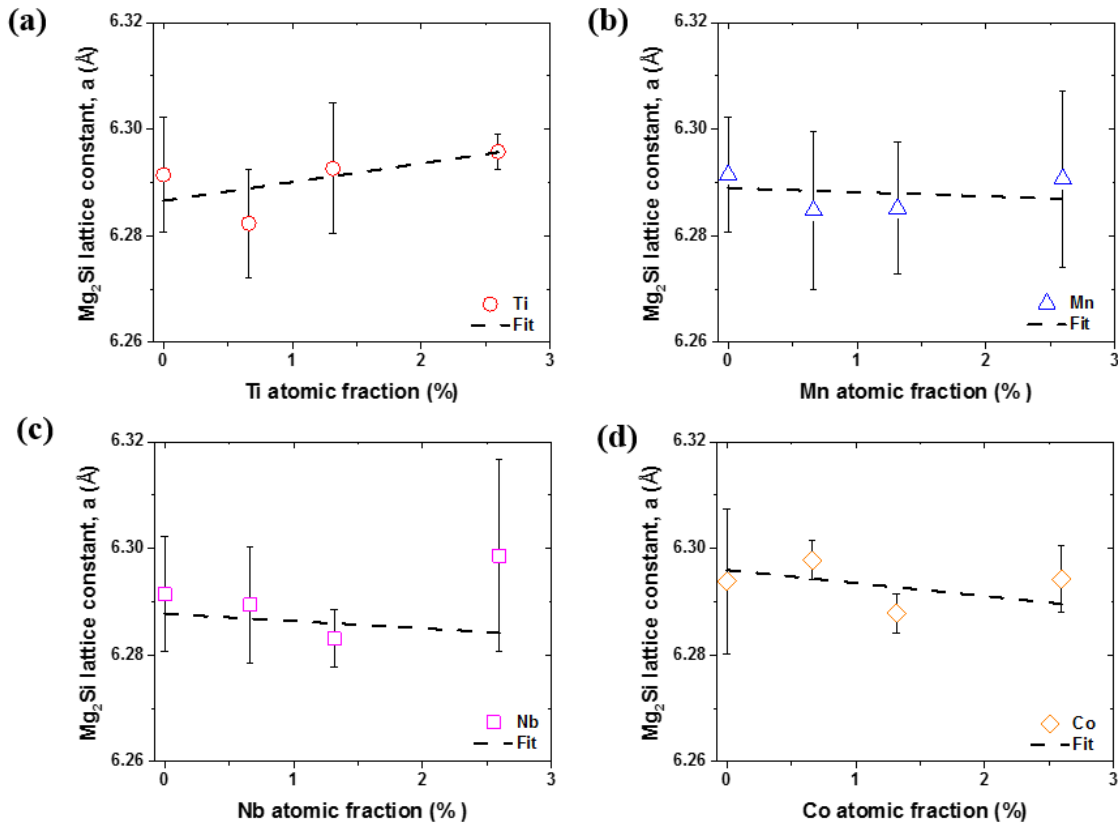


Figure 7.4: Lattice Constant vs. % Atomic Fraction of Dopant (X) Plot of Mg<sub>2</sub>Si: mX; X = (a) Ti, (b) Mn, (c) Nb and (d) Co.

## 7.4. DTA of metal-doped Mg<sub>2</sub>Si

The DTA experiments were conducted to study the effect of metal-doping on (a) formation activation energy of Mg<sub>2</sub>Si: mX, and (b) to determine the thermal properties of Mg<sub>2</sub>Si: mX from the heat flow data.

### 7.4.1. Formation Kinetics of Mg<sub>2</sub>Si: mX

The DTA experiments were carried out on (2Mg + Si + mX) mixture to study the solid-state reaction kinetics of Mg<sub>2</sub>Si: mX formation (equation 7.1) at a scan rate ( $\beta$ ) of 20 K/min using Linseis PT 1600 DTA instrument.

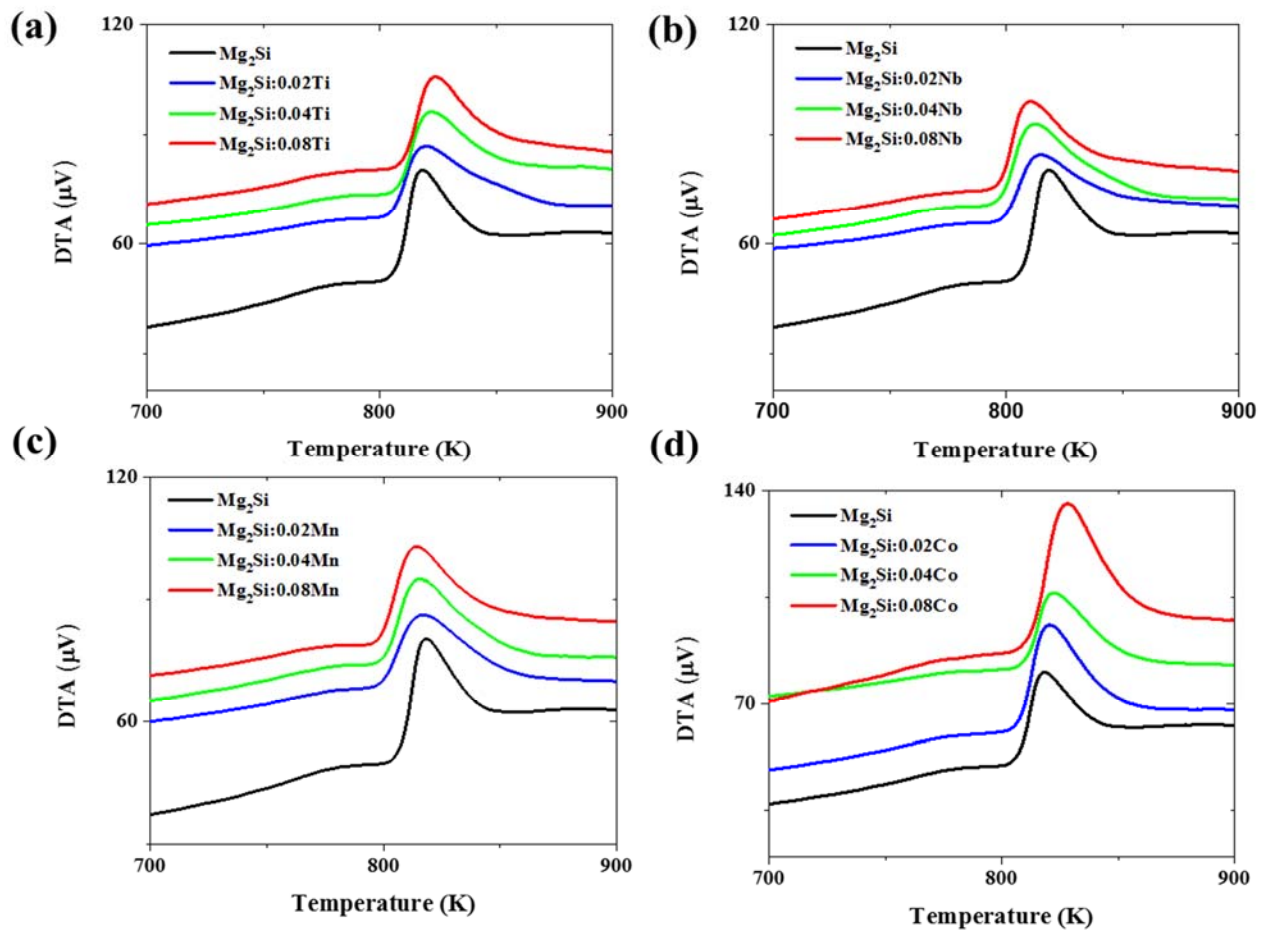
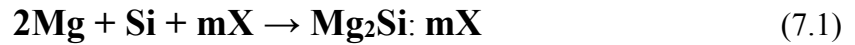


Figure 7.5: DTA Curves of (2Mg + Si + mX); X = (a) Ti, (b) Mn, (c) Nb, & (d) Co at 20 K/min.

As shown in the Figure 7.5, the differential heat flow data from the DTA experiments of (2Mg + Si + mX) samples were plotted at different temperatures (700 - 900 K) for a scan rate ( $\beta$ ) of 20 K/min. All the samples displayed an increase in the exothermic peak area with an increase in dopant concentration (m). A positive shift in the exothermic peak to higher temperatures was observed for the formation of Mg<sub>2</sub>Si: mTi and Mg<sub>2</sub>Si: mCo samples, while a negative shift in the exothermic peak to lower temperatures was noticed for the formation of Mg<sub>2</sub>Si: mNb and Mg<sub>2</sub>Si: mMn samples. Furthermore, the Coats-Redfern (CR) equation, from the Chapter 6 (equation 6.6),

Table 7.2: List of Coats-Redfern Equations for Metal-Doped Magnesium Silicides at  $\beta = 20$  K/min.

<b>Metal-dopant</b>	<b>Mg<sub>2</sub>Si:mX</b>	<b>Coats-Redfern equation</b>
<b>Un-doped</b>	Mg <sub>2</sub> Si	$\ln \frac{g(\alpha)}{T^2} = 12.473 - \frac{196.01}{RT}$
<b>Titanium</b>	Mg <sub>2</sub> Si: 0.02Ti (X <sub>Mg</sub> = 0.662, X <sub>Si</sub> = 0.331, X <sub>Ti</sub> = 0.006)	$\ln \frac{g(\alpha)}{T^2} = 12.535 - \frac{196.86}{RT}$
	Mg <sub>2</sub> Si: 0.04Ti (X <sub>Mg</sub> = 0.657, X <sub>Si</sub> = 0.328, X <sub>Ti</sub> = 0.013)	$\ln \frac{g(\alpha)}{T^2} = 12.612 - \frac{197.91}{RT}$
	Mg <sub>2</sub> Si: 0.08Ti (X <sub>Mg</sub> = 0.649, X <sub>Si</sub> = 0.324, X <sub>Ti</sub> = 0.025)	$\ln \frac{g(\alpha)}{T^2} = 12.689 - \frac{198.97}{RT}$
<b>Niobium</b>	Mg <sub>2</sub> Si: 0.02Nb (X <sub>Mg</sub> = 0.662, X <sub>Si</sub> = 0.331, X <sub>Nb</sub> = 0.006)	$\ln \frac{g(\alpha)}{T^2} = 12.344 - \frac{194.25}{RT}$
	Mg <sub>2</sub> Si: 0.04Nb (X <sub>Mg</sub> = 0.657, X <sub>Si</sub> = 0.328, X <sub>Nb</sub> = 0.013)	$\ln \frac{g(\alpha)}{T^2} = 12.252 - \frac{193.01}{RT}$
	Mg <sub>2</sub> Si: 0.08Nb (X <sub>Mg</sub> = 0.649, X <sub>Si</sub> = 0.324, X <sub>Nb</sub> = 0.025)	$\ln \frac{g(\alpha)}{T^2} = 12.178 - \frac{191.99}{RT}$
<b>Manganese</b>	Mg <sub>2</sub> Si: 0.02Mn (X <sub>Mg</sub> = 0.662, X <sub>Si</sub> = 0.331, X <sub>Mn</sub> = 0.006)	$\ln \frac{g(\alpha)}{T^2} = 12.413 - \frac{195.20}{RT}$
	Mg <sub>2</sub> Si: 0.04Mn (X <sub>Mg</sub> = 0.657, X <sub>Si</sub> = 0.328, X <sub>Mn</sub> = 0.013)	$\ln \frac{g(\alpha)}{T^2} = 12.357 - \frac{194.43}{RT}$
	Mg <sub>2</sub> Si: 0.08Mn (X <sub>Mg</sub> = 0.649, X <sub>Si</sub> = 0.324, X <sub>Mn</sub> = 0.025)	$\ln \frac{g(\alpha)}{T^2} = 12.316 - \frac{193.87}{RT}$
<b>Cobalt</b>	Mg <sub>2</sub> Si: 0.02Co (X <sub>Mg</sub> = 0.662, X <sub>Si</sub> = 0.331, X <sub>Co</sub> = 0.006)	$\ln \frac{g(\alpha)}{T^2} = 12.554 - \frac{197.12}{RT}$
	Mg <sub>2</sub> Si: 0.04Co (X <sub>Mg</sub> = 0.657, X <sub>Si</sub> = 0.328, X <sub>Co</sub> = 0.013)	$\ln \frac{g(\alpha)}{T^2} = 12.625 - \frac{198.09}{RT}$
	Mg <sub>2</sub> Si: 0.08Co (X <sub>Mg</sub> = 0.649, X <sub>Si</sub> = 0.324, X <sub>Co</sub> = 0.025)	$\ln \frac{g(\alpha)}{T^2} = 12.835 - \frac{200.98}{RT}$

was considered to (a) model the reaction kinetics, and (b) to understand the effect of metal-dopants on the formation activation energy of Mg<sub>2</sub>Si: mX samples. Table 7.2 provides the list of CR equations for the formation kinetics of Mg<sub>2</sub>Si: mX samples. All the reactions follow 3-D diffusion controlled mechanism, and the conversion function,  $g(\alpha) = [1-(1-\alpha)^{1/3}]^2$  was calculated for five different degree of conversions ( $\alpha = 0.1, 0.3, 0.5, 0.7, \text{ and } 0.9$ ). The formation activation energies of Mg<sub>2</sub>Si: mX samples were obtained from the slopes of straight line  $\{\ln [g(\alpha)]/T^2\}$  vs  $-1/RT$  plots and are listed in the Table 7.2.

From the Figure 7.5 and Table 7.2, the positive shifts in the peak maximum of the DTA curves are related to the increase in formation activation energy of Mg<sub>2</sub>Si: mTi and Mg<sub>2</sub>Si: mCo, which are resulted from the increase in concentration of Ti- and Co-dopants respectively. As shown in Figure 7.6, the % increase in the formation activation energy of Mg<sub>2</sub>Si: mTi and Mg<sub>2</sub>Si: mCo is because of the proportional increase in dopant concentration ( $m$ ). The formation activation energy of the Mg<sub>2</sub>Si: mCo system is higher than the formation activation energy the Mg<sub>2</sub>Si: mTi

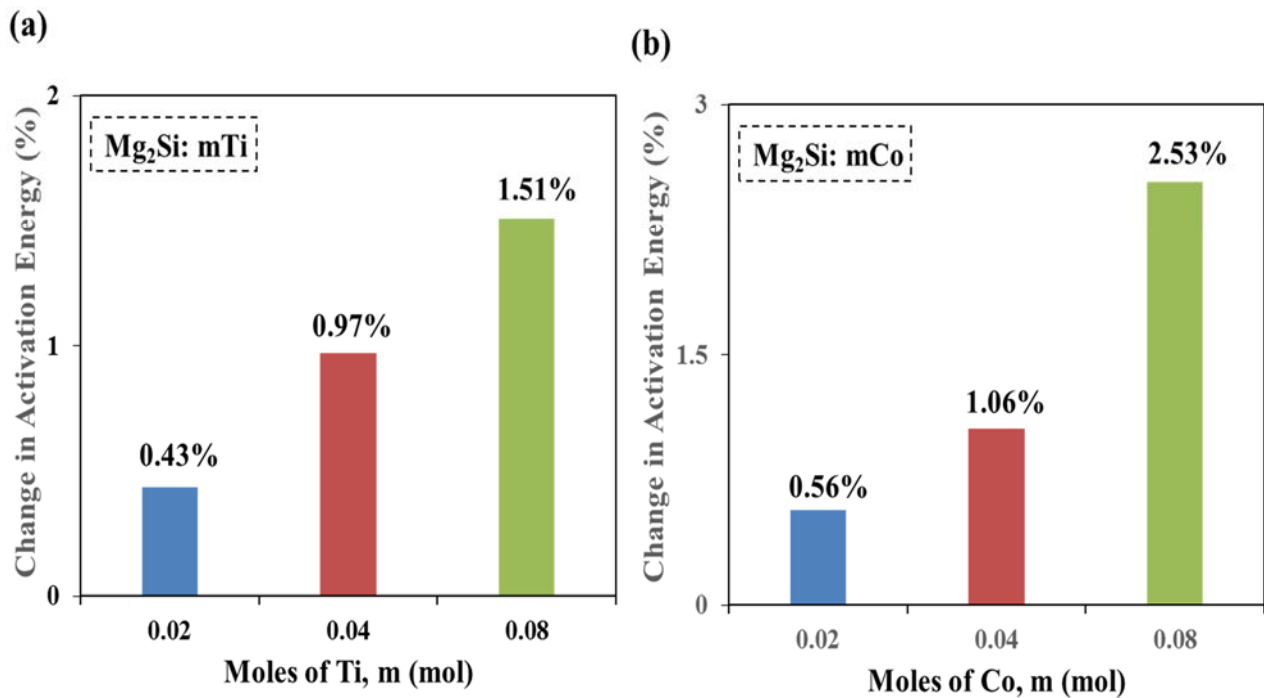


Figure 7.6: Formation Activation Energy vs. Dopant Moles of (a) Mg<sub>2</sub>Si: mTi & (b) Mg<sub>2</sub>Si: mCo

system. Similarly, the negative shifts in the peak maximum of the DTA curves are associated with the decrease in formation activation energy of  $\text{Mg}_2\text{Si: mNb}$  and  $\text{Mg}_2\text{Si: mMn}$ , which are caused from the increase in concentration of Nb- and Mn-dopants respectively. As shown in Figure 7.7, the % decrease in the formation activation energy of  $\text{Mg}_2\text{Si: mNb}$  and  $\text{Mg}_2\text{Si: mMn}$  are due to the proportional increase in the dopant concentration ( $m$ ). The formation activation energy of the  $\text{Mg}_2\text{Si: mNb}$  system is lower than the formation activation energy of the  $\text{Mg}_2\text{Si: mMn}$  system.

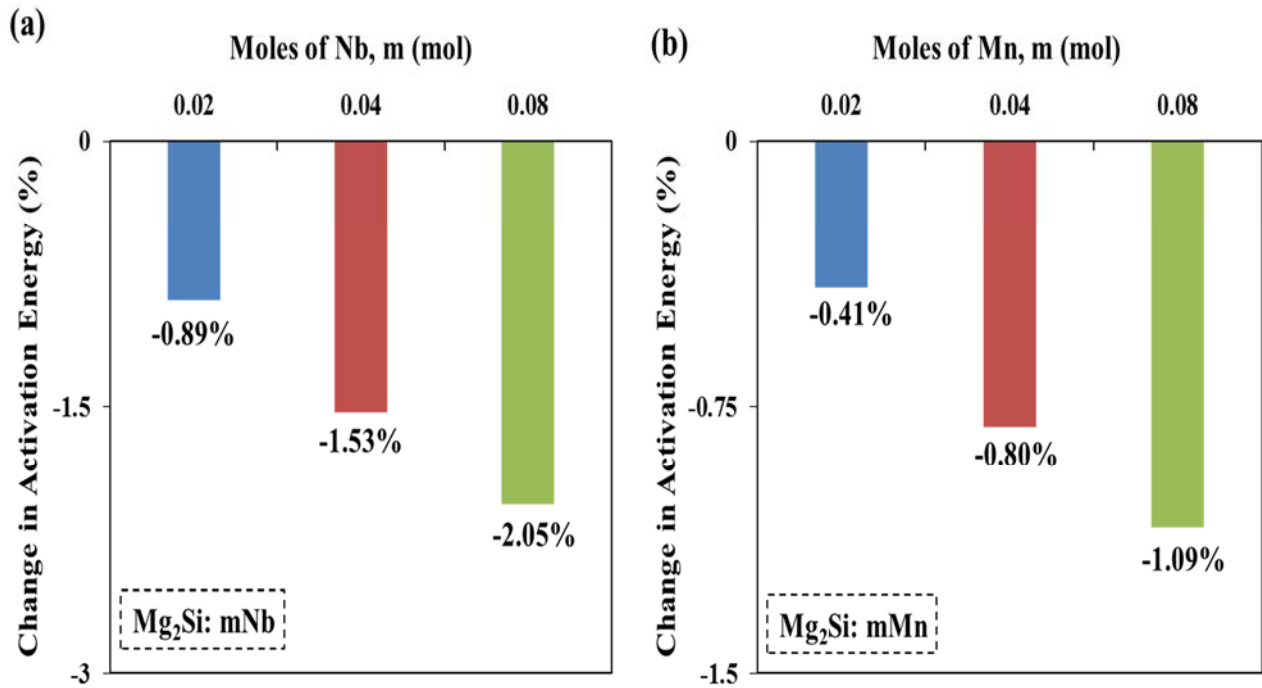


Figure 7.7: Formation Activation Energy vs. Dopant Moles of (a)  $\text{Mg}_2\text{Si: mNb}$  & (b)  $\text{Mg}_2\text{Si: mMn}$

The presence of small amounts of metal-dopants (Ti, Nb, Mn, and Co) in the reactant mixture ( $2\text{Mg} + \text{Si}$ ) effects the reaction kinetics, and 3-D diffusion of Mg/Si atoms during the formation of  $\text{Mg}_2\text{Si: mX}$  powders. Metals like Ti and Co have an inhibitor-type role, while metals such as Nb and Mn have catalytic-type role on the formation activation energy of  $\text{Mg}_2\text{Si: mX}$  powders. In addition, the concentration of the metal-dopants have significant role in either increasing or decreasing the formation activation energy of the  $\text{Mg}_2\text{Si: mX}$  samples.

### 7.4.2. Thermodynamic Properties of $\text{Mg}_2\text{Si}:0.08\text{X}$

To study the effect of addition of metal-dopants (Ti, Nb, Mn and Co) on the thermodynamic properties of  $\text{Mg}_2\text{Si}$ , we choose the maximum dopant concentration ( $m = 0.08$  mol) for the DTA heat flow measurements. All the conditions for DTA experiments are similar to those discussed in the previous section (6.3.3). As shown in Figure 7.8, the DTA curves of  $\text{Mg}_2\text{Si}:0.08\text{X}$  samples show enhanced heat flow in comparison to that of un-doped  $\text{Mg}_2\text{Si}$  sample. This suggests that the doping of  $\text{Mg}_2\text{Si}$  with 0.08 mol of metal-dopants also effects the thermodynamic properties of  $\text{Mg}_2\text{Si}:0.08\text{X}$ , since the enthalpy of sample is proportional to its DTA signal. The mass difference baseline method (from earlier section 6.3.3) was used to calculate the thermodynamic properties of  $\text{Mg}_2\text{Si}:0.08\text{X}$  samples. A linear relationship between  $C_p(T)$  and  $T$  was established for all the

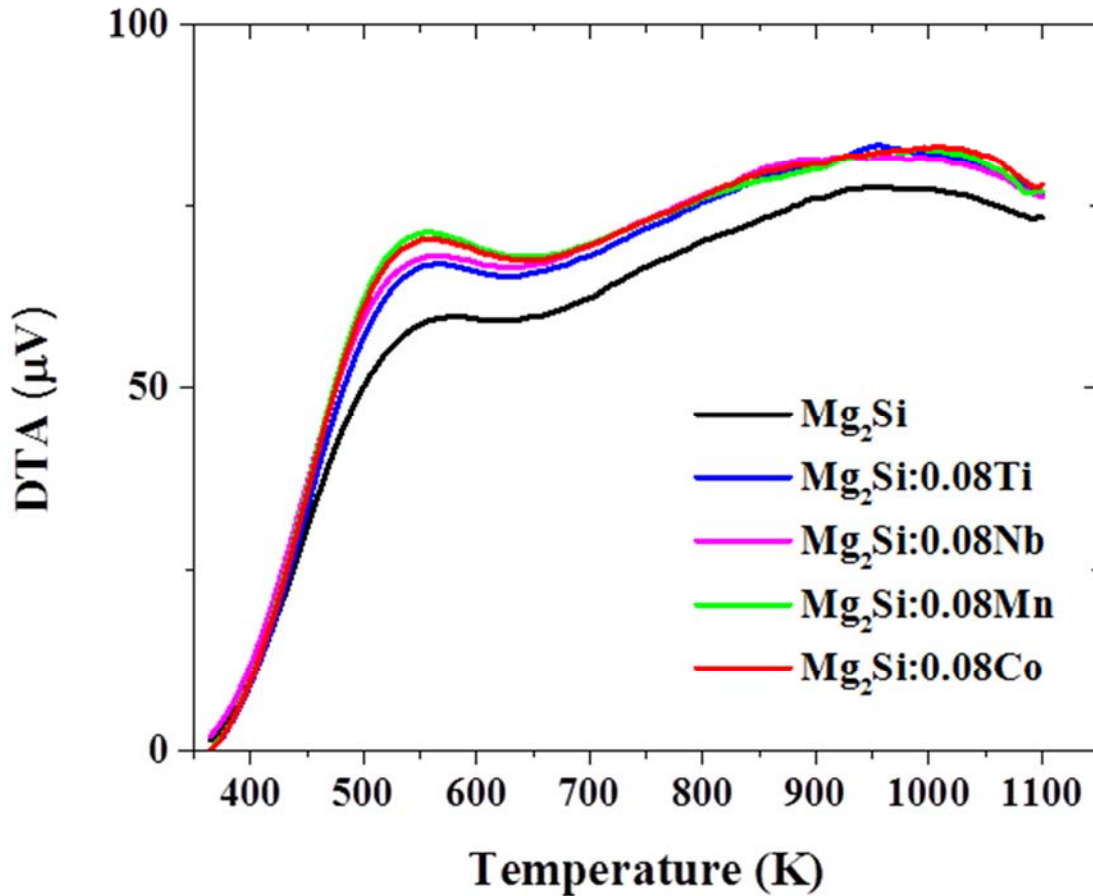


Figure 7.8: DTA Curves of  $\text{Mg}_2\text{Si}$  &  $\text{Mg}_2\text{Si}:0.08\text{X}$ ; X = Ti, Nb, Mn & Co at 20 K/min.

Mg<sub>2</sub>Si: mX samples, in analogous to the equation (7.6) for un-doped Mg<sub>2</sub>Si sample. Table 7.5 provides the general formula for the change in standard enthalpy, standard entropy, and standard Gibbs energy derived from  $C_p(T)$  at any arbitrary temperature, T (473 K < T < 1073 K). Table 7.4 lists the calculated values of the parameters (A, B, C, and D) from the Table 7.3 for un-doped Mg<sub>2</sub>Si and Mg<sub>2</sub>Si: 0.08X samples. The metal-doped samples (Mg<sub>2</sub>Si: 0.08X; X =Ti, Nb, Mn, and Co) samples exhibited better thermal stability, while compared to the un-doped Mg<sub>2</sub>Si sample. The values of thermodynamic properties of Mg<sub>2</sub>Si: 0.08X samples can be determined from 473 K to 1073 K using the formula of Table 7.3 and from the parameters listed in the Table 7.4.

Table 7.3: Thermodynamic Properties given as Function of Temperature from 473 K to 1073 K.

Thermodynamic Property	Associated Formula
Specific Heat , $C_p(T)$	$C_p(T) = A + 2B \times T$
Change in Std. Enthalpy, $\Delta H^o(T)$	$\Delta H^o(T) = C + A \times T + B \times T^2$
Change in Std. Entropy, $\Delta S^o(T)$	$\Delta S^o(T) = D + A \times \ln T + 2B \times T$
Change in Std. Gibbs Energy, $\Delta G^o(T)$	$\Delta G^o(T) = C + (A - D) \times T - A \times T \ln T - B \times T^2$

Table 7.4: Parameters (A, B, C and D) of Thermodynamic Property Functions from Table 7.3.

Sample	A	B	C	D
Mg <sub>2</sub> Si [143]	67.79	0.0099	-34291.20	-426.92
Mg <sub>2</sub> Si	68.89	0.0100	-34834.00	-433.79
Mg <sub>2</sub> Si:0.08Ti	80.51	0.0066	-39570.90	-502.14
Mg <sub>2</sub> Si:0.08Nb	81.63	0.0063	-40022.40	-508.71
Mg <sub>2</sub> Si:0.08Mn	83.92	0.0062	-41094.70	-522.77
Mg <sub>2</sub> Si:0.08Co	84.46	0.0060	-41305.50	-525.90

## **7.5. Summary of Metal-doped Magnesium Silicides Study**

In this chapter, we studied the effect of four metal-dopants ( $X = \text{Ti, Nb, Mn, and Co}$ ) and three dopant concentration ( $m = 0.02, 0.04$  and  $0.08$ ) on synthesis, characterization, kinetic and thermal studies of  $\text{Mg}_2\text{Si: mX}$  samples. Lattice parameters, formation activation energies, thermodynamic properties of  $\text{Mg}_2\text{Si: mX}$  samples were investigated. The Coats-Redfern equation model, and mass difference baseline method of DTA technique were used to study the effect of metal-dopants on activation energies and thermodynamic properties of  $\text{Mg}_2\text{Si: mX}$  respectively.

## CHAPTER 8

### TRANSITION METAL BORIDES AND SILICIDES

As discussed in the chapter 2, the transition metal borides and silicides are promising candidates for high-temperature thermoelectric applications. Borides and silicides of transition metals (Ti, Nb, Mn, and Co) are considered in the current study. As shown in the schematic of Figure 8.1, binary and ternary alloys comprising a specific combination of these elements i.e., (Ti/Nb/Mn)-Co-(B/Si), were chosen as a first step of the screening process because of their similarity with the half-auler (ABX-type) alloys [173, 174]. Table 8.1 provide the list of reported binary and ternary alloy phases of (Ti/Nb/Mn)-Co-(B/Si) system [29].



Figure 8.1: A Schematic of Transition Metal Boride/Silicide System Considered in Current Study.

Table 8.1 A Comprehensive List of Binary & Ternary Metal Boride & Silicide Alloy Phases [29].

System	Binary alloy phases	Ternary alloy phases
<b>Ti-Co-B</b>	Co <sub>3</sub> B, Co <sub>2</sub> B, CoB, TiB, Ti <sub>3</sub> B <sub>4</sub> , TiB <sub>2</sub>	Ti <sub>3</sub> Co <sub>5</sub> B <sub>2</sub> , Ti <sub>3</sub> Co <sub>20</sub> B <sub>6</sub> , Ti <sub>7</sub> Co <sub>7</sub> B <sub>6</sub>
<b>Nb-Co-B</b>	Nb <sub>3</sub> B <sub>2</sub> , NbB, Nb <sub>3</sub> B <sub>4</sub> , NbB <sub>2</sub>	Nb <sub>3</sub> Co <sub>5</sub> B <sub>2</sub> , NbCoB <sub>2</sub> , Nb <sub>2</sub> Co <sub>21</sub> B <sub>6</sub> , NbCoB, Nb <sub>3</sub> Co <sub>4</sub> B <sub>7</sub>
<b>Mn-Co-B</b>	Mn <sub>3</sub> B, Mn <sub>2</sub> B, MnB, Mn <sub>3</sub> B <sub>4</sub> , MnB <sub>2</sub> , MnB <sub>4</sub>	Mn <sub>3</sub> Co <sub>20</sub> B <sub>6</sub>
<b>Ti-Co-Si</b>	Ti <sub>3</sub> Si, Ti <sub>5</sub> Si <sub>3</sub> , Ti <sub>5</sub> Si <sub>4</sub> , TiSi, TiSi <sub>2</sub> , CoSi <sub>2</sub> , CoSi, Co <sub>2</sub> Si	TiCoSi, Ti <sub>4</sub> Co <sub>4</sub> Si <sub>7</sub> , TiCo <sub>2</sub> Si, Ti <sub>2</sub> Co <sub>3</sub> Si TiCo <sub>4</sub> Si <sub>3</sub> , Ti <sub>3</sub> CoSi <sub>8</sub> , Ti <sub>6</sub> Co <sub>16</sub> Si <sub>7</sub>
<b>Nb-Co-Si</b>	NbSi <sub>2</sub> , Nb <sub>5</sub> Si <sub>3</sub>	Nb <sub>4</sub> Co <sub>4</sub> Si <sub>7</sub> , NbCoSi, Nb <sub>6</sub> Co <sub>16</sub> Si <sub>7</sub> Nb <sub>4</sub> CoSi, NbCo <sub>4</sub> Si <sub>3</sub>
<b>Mn-Co-Si</b>	Mn <sub>11</sub> Si <sub>19</sub> , MnSi, MnSi <sub>2-x</sub> , Mn <sub>5</sub> Si <sub>3</sub> , Mn <sub>3</sub> Si, Mn <sub>25.2</sub> Si <sub>5.8</sub> , Mn <sub>0.85</sub> Si <sub>0.15</sub>	Mn <sub>0.53</sub> Co <sub>0.20</sub> Si <sub>0.27</sub> , Mn <sub>16.5</sub> Co <sub>14.8</sub> Si <sub>5.7</sub> , MnCo <sub>1.33</sub> Si <sub>0.67</sub> , MnCoSi, MnCo <sub>2</sub> Si Mn <sub>29</sub> Co <sub>14</sub> Si <sub>14</sub> , Mn <sub>16</sub> Co <sub>2</sub> Si <sub>7</sub> , Mn <sub>3</sub> Co <sub>3</sub> Si

### 8.1. Thermodynamic Study of Borides and Silicides

Thermodynamic modeling tools (161, 162) were used to model the thermodynamic properties of the metal borides and silicides. In particular, Gibbs energy minimization was performed on 9 binary metal borides (Co<sub>2</sub>B, CoB, TiB, TiB<sub>2</sub>, NbB<sub>2</sub>, Mn<sub>2</sub>B, MnB, Mn<sub>3</sub>B<sub>4</sub>, and MnB<sub>2</sub>) and 12 binary silicides (NbSi<sub>2</sub>, Nb<sub>5</sub>Si<sub>3</sub>, CoSi<sub>2</sub>, CoSi, Co<sub>2</sub>Si, Ti<sub>5</sub>Si<sub>3</sub>, TiSi, TiSi<sub>2</sub>, MnSi, Mn<sub>5</sub>Si<sub>3</sub>, Mn<sub>3</sub>Si, and MnSi<sub>1.73</sub>) using HSC tool over a wide temperature range of 0 – 1500 °C [161]. Figure 8.2(a) shows the change in Gibbs energy of the selected borides from 0 to 1500 °C. The negative value of the change in Gibbs energy shows that the metal borides are stable at higher temperatures. Among all borides, TiB<sub>2</sub> shows more negative change in Gibbs energy and thus, it is thermally stable transition metal boride suitable for thermoelectric study. Also, thermodynamic calculations were conducted to estimate the change in Gibbs energy of selected metal silicides. Figure 8.2(b) shows change in Gibbs energy of selected silicides from 0 to 1200 °C.

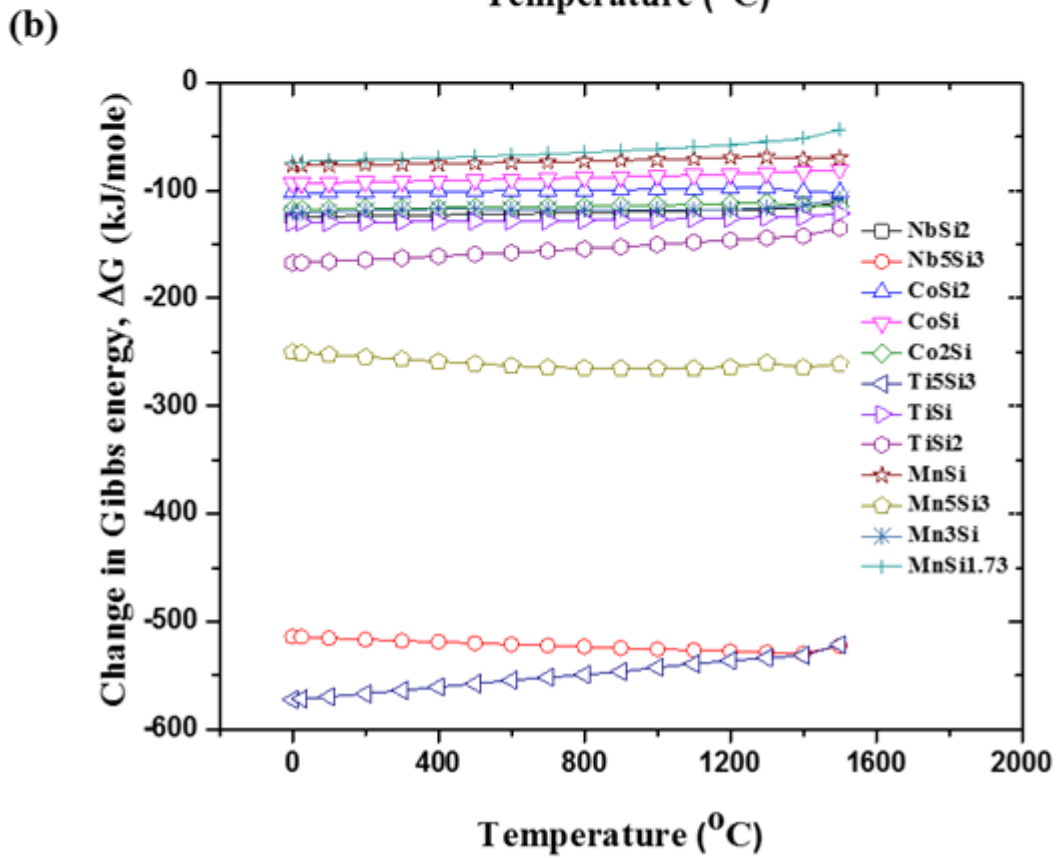
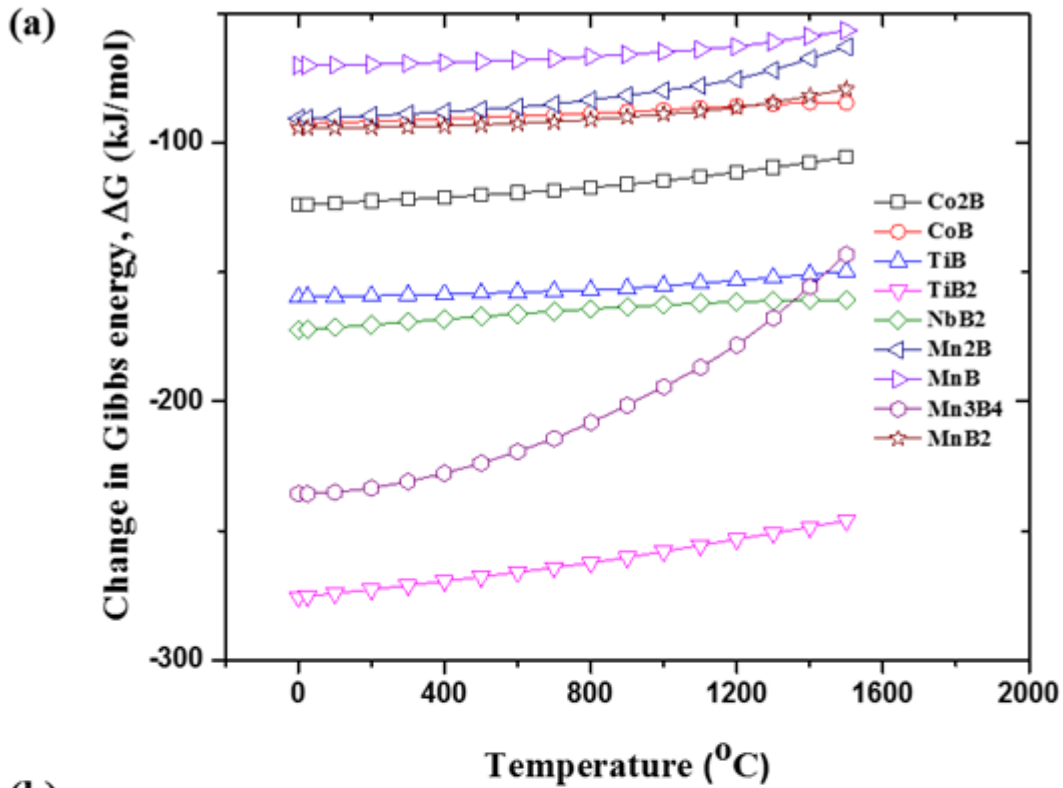


Figure 8.2: Change in Gibbs energy of Selected (a) Borides, and (b) Silicides [143]

Table 8.2: Gibbs Energy Function Parameters of Selected Borides [144].

<b>Borides</b>	<b>A (J/mol)</b>	<b>B (J/mol.K)</b>	<b>C (J/mol .K<sup>2</sup>)</b>	<b>D (J K/mol)</b>	<b>E (J/mol.K)</b>
<b>Co<sub>2</sub>B</b>	-151681	412.75	-0.01	713372	-68.37
<b>CoB</b>	-111365	267.67	-0.00732	562748	-68.37
<b>TiB</b>	-177652	212.32	-0.03044	778017	-33.18
<b>TiB<sub>2</sub></b>	-294439	181.18	-0.05685	412450	-26.02
<b>NbB<sub>2</sub></b>	-269919	293.82	-0.01927	470700	-46.98

Table 8.3: Gibbs Energy Function Parameters of Selected Silicides [144].

<b>Silicides</b>	<b>A (J/mol)</b>	<b>B (J/mol.K)</b>	<b>C (J/mol .K<sup>2</sup>)</b>	<b>D (J K/mol)</b>	<b>E (J/mol.K)</b>
<b>CoSi</b>	-90238	311.08	-0.00414	200333	-53.52
<b>Ti<sub>5</sub>Si<sub>3</sub></b>	-646360	1122.32	-0.02238	1004160	-196.43
<b>TiSi</b>	-146382	279.77	-0.00571	271960	-48.11
<b>TiSi<sub>2</sub></b>	-193045	406.08	-0.00815	-1477660	-69.33
<b>MnSi</b>	-92278	276.72	-0.00926	246494	-46.29
<b>Mn<sub>5</sub>Si<sub>3</sub></b>	-269849	1136.90	-0.02708	980102	-201.35
<b>Mn<sub>3</sub>Si</b>	-144109	534.88	-0.02396	386148	-93.20
<b>NbSi<sub>2</sub></b>	-158529	359.42	-0.00768	139745	-63.17
<b>Nb<sub>5</sub>Si<sub>3</sub></b>	-514695	1033.52	-0.01539	753956	-189.15

The negative value of change in Gibbs energy shows that the metal silicides are stable at higher temperatures. Among all the silicides studied, Ti<sub>5</sub>Si<sub>3</sub> and Nb<sub>5</sub>Si<sub>3</sub> shows more negative change in Gibbs energy value and thus, are thermally stable transition metal silicides.

Another important modelling tool for estimating the thermodynamic properties of TE materials is FactSage [162]. From all the stable binary alloys of (Ti/Nb/Mn) - Co- (B/Si) system, 5 borides (Co<sub>2</sub>B, CoB, TiB, TiB<sub>2</sub>, and NbB<sub>2</sub>) and 9 silicides (CoSi, Ti<sub>5</sub>Si<sub>3</sub>, TiSi, TiSi<sub>2</sub>, MnSi, Mn<sub>5</sub>Si<sub>3</sub>, Mn<sub>3</sub>Si, NbSi<sub>2</sub> and Nb<sub>5</sub>Si<sub>3</sub>) were selected to obtain Gibbs energy as a function of

temperature. The Gibbs energy function is given by equation (4.4), and the parameters (A, B, C, D, and E) of the polynomial were estimated for each alloy. Tables (8.2 and 8.3) gives the values of the Gibbs energy function parameters for the transition metal borides and silicides respectively.

## 8.2. Synthesis of TiB<sub>2</sub> and Mn<sub>4</sub>Si<sub>7</sub>

Based on the thermodynamic modelling calculations (section 8.1) for selected binary alloys of (Ti/Mn/Nb) – Co – (B/Si) system, and from the available information on crystal structure data, energy band diagrams and other TE properties from the literature [29], we selected transition metal boride (TiB<sub>2</sub>), and transition metal silicide (Mn<sub>4</sub>Si<sub>7</sub>) for the experimental studies.

Reddy *et al.* synthesized TiB<sub>2</sub> using both thermal plasma and arc-melting methods [175, 176]. The thermal plasma process resulted in nanopowders of TiB<sub>2</sub>, whereas the arc melting method produced ingots of TiB<sub>2</sub>. In the current study, arc-melting method was chosen for the synthesis of TiB<sub>2</sub> and Mn<sub>4</sub>Si<sub>7</sub>. Pellets of (Ti + 2B) mixture, and (4Mn + 7Si) were arc-melted, at 200 A under partial Ar pressure of 2 psi, to synthesize TiB<sub>2</sub> and Mn<sub>4</sub>Si<sub>7</sub> alloys using one step self-propagating high-temperature synthesis (SHS) method. Both the reactions of equations (8.1) and (8.2) are exothermic and the formation of the products are very favorable with the initiation of an electric arc or heat to start the self-propagating reaction [176].



## 8.3. Characterization of TiB<sub>2</sub> and Mn<sub>4</sub>Si<sub>7</sub>

The synthesized TiB<sub>2</sub> and Mn<sub>4</sub>Si<sub>7</sub> alloys were characterized using XRD technique. Figure 8.3 (a) and (b) shows the XRD spectra and images of TiB<sub>2</sub> and Mn<sub>4</sub>Si<sub>7</sub> alloys respectively using arc-melting technique. No other binary Ti-B, and Mn-Si alloy phases were observed in the spectra.

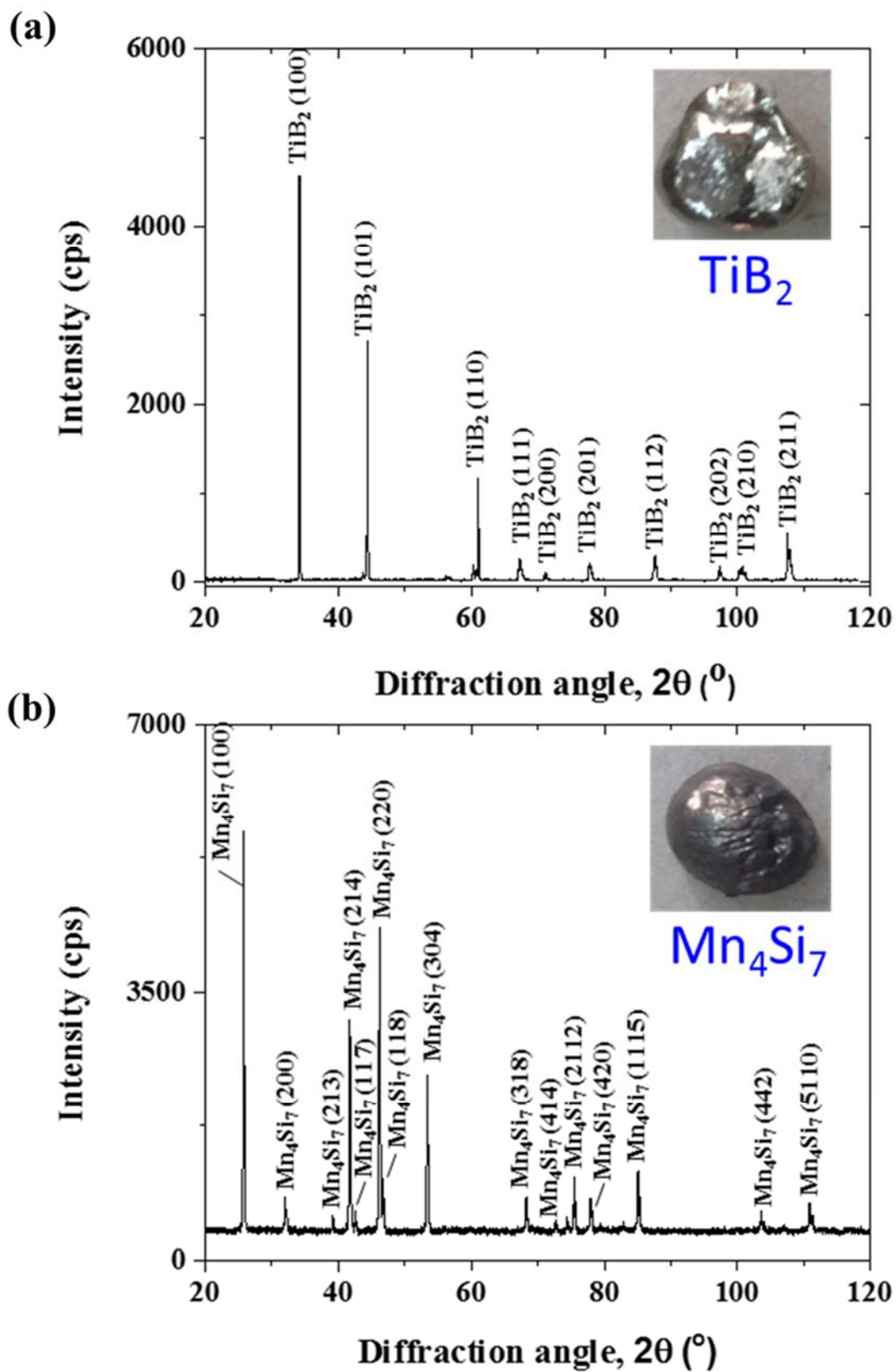


Figure 8.3: XRD Spectrum and Image of (a)  $\text{TiB}_2$  and (b)  $\text{Mn}_4\text{Si}_7$  obtained by Arc-Melting Method.

#### 8.4. Thermoelectric properties of TiB<sub>2</sub> and Mn<sub>4</sub>Si<sub>7</sub>

The arc-melted samples of TiB<sub>2</sub> and Mn<sub>4</sub>Si<sub>7</sub> were further tested for measurement of their thermoelectric properties. Specimen of dimensions (~ 3 - 6 mm height, 10 - 30 mm<sup>2</sup> cross-section area) were used to measure Seebeck coefficient ( $S$ ), electrical conductivity ( $\sigma$ ), thermal conductivity ( $\kappa$ ), and figure of merit ( $ZT$ ) of TiB<sub>2</sub> and Mn<sub>4</sub>Si<sub>7</sub> using  $ZT$ -Scanner instrument [177]. As shown in the Figure 8.4, the thermoelectric properties are plotted as a function of temperature from 300 K to 700 K. TiB<sub>2</sub> alloy showed high electrical conductivity and low thermal conductivity values, but exhibited poor negative Seebeck coefficient values. As a result, the figure of merit ( $ZT$ )

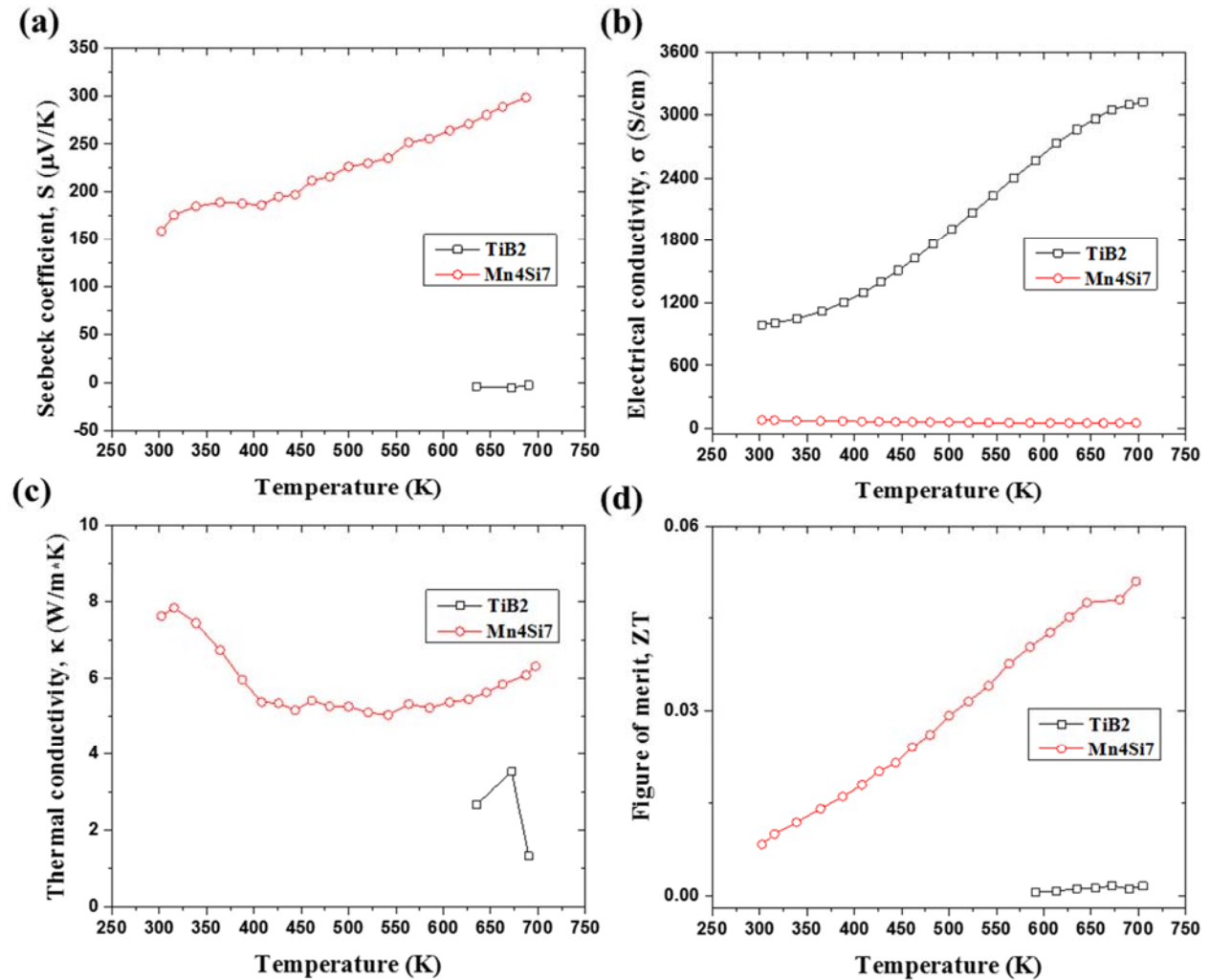


Figure 8.4: Thermoelectric Properties (a) Seebeck Coefficient ( $S$ ), (b) Electrical Conductivity ( $\sigma$ ), (c) Thermal Conductivity ( $\kappa$ ), and (d) Figure of Merit ( $ZT$ ) of TiB<sub>2</sub>, and Mn<sub>4</sub>Si<sub>7</sub>.

is low for the *n*-type TiB<sub>2</sub> material. Because of its good electrical and thermal conductivities, TiB<sub>2</sub> is used as an additive to enhance the transport properties of other thermoelectric materials [96, 97].

High manganese silicide (Mn<sub>4</sub>Si<sub>7</sub>) exhibited good positive Seebeck coefficient, and low thermal conductivity values, however it displayed poor electrical conductivity values. Hence, the *p*-type Mn<sub>4</sub>Si<sub>7</sub> have low figure of merit values (maximum  $ZT = 0.05$ ), which are comparatively higher than the  $ZT$  values of *n*-type TiB<sub>2</sub> alloy. One reason for the low thermoelectric performance of the alloys may be due to the high porosity or low density of the arc-melted samples. Further improvements in the synthetic and processing methods may enhance the  $ZT$  of *n*-type TiB<sub>2</sub>, and *p*-type Mn<sub>4</sub>Si<sub>7</sub> to much higher values.

#### **8.4. Summary of Transition Metal Borides and Silicides**

In the Chapter 8, efforts were made to study transition metal borides and metal silicides of the (Ti/Nb/Mn) – Co – (B/Si) system through initial screening of the alloys *via* thermodynamic modelling approach and from the available information in literature. Gibbs energy minimization method was used to study the thermal studies of selected metal borides and silicides. One transition metal boride (TiB<sub>2</sub>) and one transition metal silicide (Mn<sub>4</sub>Si<sub>7</sub>) were chosen for the experimental studies. One step self-propagating high-temperature synthesis (SHS) method was used to produce ingots of TiB<sub>2</sub> and Mn<sub>4</sub>Si<sub>7</sub> from the electric arc-melter furnace. Characterization of the alloy phases were done from the XRD spectra. Furthermore, thermoelectric properties ( $S$ ,  $\sigma$ ,  $\kappa$ , and  $ZT$ ) of TiB<sub>2</sub> and Mn<sub>4</sub>Si<sub>7</sub> samples were determined using the  $ZT$ -Scanner instrument. Both TiB<sub>2</sub> and Mn<sub>4</sub>Si<sub>7</sub> exhibited low thermal conductivity values. Good values of Seebeck coefficient and electrical conductivity were achieved for Mn<sub>4</sub>Si<sub>7</sub> and TiB<sub>2</sub> respectively. A maximum  $ZT$  of 0.05 was achieved for Mn<sub>4</sub>Si<sub>7</sub> sample produced from the arc-melting apparatus.

## CHAPTER 9

### CONCLUSIONS AND FUTURE WORK

#### 9.1. Conclusions

In the current research project, we studied the metal borides and silicides as potential materials for thermoelectric application at high temperature (400 – 1000 °C). The basic principles of thermoelectric effect, transport properties, figure of merit, conversion efficiency, synthesis and characterization, and thermodynamic properties of metal borides and silicides was reviewed. The preliminary study mainly focused on the development of Arrhenius model for the evaluation of TE properties of alkaline earth metal borides and silicides. Based on the results, Mg<sub>2</sub>Si was selected as a promising candidate for further experimental studies.

A simple and rapid synthesis of Mg<sub>2</sub>Si powders was carried out using pelletizing and sintering methods. Mg<sub>2</sub>Si was produced by cold-pressing of 2:1 molar mixture of Mg and Si, followed by sintering of the pellet at optimum conditions of 500 °C for 5 min. The Mg<sub>2</sub>Si sample was characterized using XRD, SEM, and EDS methods. Lattice parameter for Mg<sub>2</sub>Si was calculated from the XRD data. Formation of uniform and fine micro-aggregates of pure nanoMg<sub>2</sub>Si was observed for the sintered sample obtained at 500 °C and 5 min.

Thermal analysis of (2Mg + Si) mixture was carried out at different scan rates ( $\beta = 5, 10, 15, \text{ and } 20 \text{ K/min}$ ) to study the reaction kinetics of Mg<sub>2</sub>Si using DTA technique. A positive shift in the peak maximum temperature of DTA heat-flow curves with the increase in the scan rates. The activation energy for the formation of Mg<sub>2</sub>Si was calculated from the slopes of Ozawa

equation and KAS equation plots. The solid-state reaction proceed *via* 3-D diffusion mechanism of reactants and CR equation plots were obtained for different reaction rates based on peak temperatures corresponding to six different degree of conversion ( $\alpha = 0.1, 0.3, 0.5, 0.7, \text{ and } 0.9$ ). The activation energy obtained from CR plot (196.01 kJ/mol) is in good agreement with those obtained from the Ozawa equation, and KAS equation plots.

In addition, the thermal stability of the  $\text{Mg}_2\text{Si}$  powders was studied using both DSC and DTA techniques. The DTA heat-flow curve of  $\text{Mg}_2\text{Si}$  prepared from sintering at 500 °C and 5 min shows that the alloy melts at 850 - 1000 °C, which also corresponds to the evaporation temperature of pure Mg metal. The Gibbs energy function [ $\Delta G(T)$ ], and room temperature thermodynamic quantities ( $C_p$ ,  $\Delta H^\circ$ ,  $\Delta S^\circ$ , and  $\Delta G^\circ$ ) were determined for  $\text{Mg}_2\text{Si}$  using DSC ( $T = 323 - 623$  K; *iso-scan-iso*) and DTA ( $T = 473 - 1073$  K; *mass difference baseline*) methods. The heat capacity ( $C_p$ ), and change in Gibbs energy ( $\Delta G^\circ$ ) data suggests that  $\text{Mg}_2\text{Si}$  powders are thermally stable from 323 K - 1073 K.

The solid-state galvanic cell or EMF cell experiments were performed using the cell assembly, which consists of  $\text{CaF}_2$  crystal stacked in between  $\sim 1$  g pellets of six reference electrodes [(0.4 g Mg + 0.6 g ( $\text{CaF}_2 + \text{MgF}_2$ ))], and six different working electrodes [0.4g of  $\text{Mg}_x\text{Si}_{1-x}$  ( $X = 0.10, 0.23, 0.43, 0.67, 0.84, \text{ and } 0.98$  mol) + 0.6 g ( $\text{CaF}_2 + \text{MgF}_2$ )] respectively. The EMF vs. temperature plots show a linear dependence of the cell potential as a function of the temperature. The EMF data was used to determine the thermodynamic properties, such as activities, activity coefficients, change in Gibbs energy, enthalpy, and entropy of mixing for the Mg-Si system.

Similar to the  $\text{Mg}_2\text{Si}$  studies, synthesis, characterization, and thermal stability investigations were carried out on metal-doped silicides ( $\text{Mg}_2\text{Si}: mX$ ). Four metals ( $X = \text{Ti, Nb, Mn, and Co}$ ) were chosen as the dopants, and three dopant concentrations ( $m = 0.02, 0.04, \text{ and}$

0.08 moles) were considered for the current studies. A fast synthesis of  $\text{Mg}_2\text{Si}:\text{mX}$  powders was achieved using cold-pressing, and sintering methods. The sintering temperature, and the time for the formation of  $\text{Mg}_2\text{Si}:\text{mX}$  powders are 500 – 550 °C, and 5 min respectively.

Characterization of the sintered powders of  $\text{Mg}_2\text{Si}:\text{mX}$  was performed using XRD, SEM, and EDS techniques. The XRD spectra of all metal-doped  $\text{Mg}_2\text{Si}:\text{mX}$  samples resemble very similar to that of un-doped  $\text{Mg}_2\text{Si}$ , except that a small shift in the peak maxima was observed in the XRD pattern of the doped samples. Based on the peak shifts of major characteristic XRD reflection (220) of  $\text{Mg}_2\text{Si}$  at  $2\theta \sim 40^\circ$ , the lattice parameters were estimated for the  $\text{Mg}_2\text{Si}:\text{mX}$  samples. A decrease in the linear trend of lattice constants for Nb -, Mn -, and Co-doped  $\text{Mg}_2\text{Si}$  samples was observed with the increase in the dopant concentration. An increase in the trend of lattice constants were noticed for Ti-doped  $\text{Mg}_2\text{Si}$  sample with increase in concentration of Ti.

The DTA studies show that the Ti and Co dopants increase the formation activation energy of  $\text{Mg}_2\text{Si}:\text{mX}$ , while Nb and Mn dopants decrease the formation activation energy of  $\text{Mg}_2\text{Si}:\text{mX}$ . The thermal stabilities of  $\text{Mg}_2\text{Si}:\text{0.08X}$  are higher than that of un-doped  $\text{Mg}_2\text{Si}$ . The thermodynamic properties were determined for  $\text{Mg}_2\text{Si}:\text{0.08X}$  based on the mass difference baseline method of DTA technique.

Based on the thermodynamic modelling data and the information available from the literature,  $\text{TiB}_2$ , and  $\text{Mn}_4\text{Si}_7$  (HMS) alloys were selected for further experimental studies. Both  $\text{TiB}_2$ , and  $\text{Mn}_4\text{Si}_7$  alloys were synthesized, from the green pellets of elemental powder mixture, by using SHS procedure of electric arc-melting technique. The XRD analysis of the arc-melted ingots indicates the presence of pure  $\text{TiB}_2$  and  $\text{Mn}_4\text{Si}_7$  phases in the samples. Furthermore, measurement of TE properties (Seebeck coefficient, electrical conductivity, thermal conductivity, and figure of merit of *n*-type  $\text{TiB}_2$  and *p*-type  $\text{Mn}_4\text{Si}_7$  were done using *ZT*-Scanner instrument.

## 9.2. Future Work

The present research work was mainly focused on the development of binary metal borides and silicides as thermoelectric materials for high temperature applications. From the theoretical and practical knowledge of this research, a fundamental study on development of other potential binary and ternary alloys of metal borides and silicides can further be explored. A similar methodology can be used for synthesis, characterization, phase stability, reaction kinetics, and thermodynamic and thermoelectric properties study. Since, the metal borides and silicides are attractive due to their low cost, high-abundance, good stability, eco-friendly and good thermoelectric properties, they are envisioned as materials for heat recovery at high temperatures.

Further improvements in the direction of current research would be to use other processing techniques such as spark plasma sintering (SPS) and hot isostatic pressing (HIP), which have additional advantages of producing samples with high density, uniformity, better morphology and improved mechanical, thermodynamic and thermoelectric properties. Using these synthetic techniques, simultaneous synthesis and alteration of material properties *via* process variables such as sintering temperature, time, pressure, current or voltage etc. is possible to achieve the desired TE properties.

In the current research, four metal-dopants (Ti, Nb, Mn and Co) were used to study the effect of the dopants on reaction kinetics, thermodynamic properties of  $\text{Mg}_2\text{Si}$ . The effect of these metal-dopants on the TE properties of  $\text{Mg}_2\text{Si}$  will be an interesting study. Also, other metals from periodic table can be used as dopants of metal borides and silicides to alter the carrier concentration and thereby, further improve the figure of merit (ZT) of the TE alloys.

In present research, thermoelectric property measurements were conducted at low/mid temperatures of 300 K to 700 K. Enhancements in the design of the instrumentation will allow

accurate measurement of the thermoelectric properties i.e., Seebeck coefficient, electrical conductivity, thermal conductivity and figure of merit at much higher temperatures of 1200 K.

After making the aforementioned amendments, the subsequent steps in the current thermoelectric research would be to scale-up the production process of high ZT alloys, construction of TE modules from the *p*- and *n*-type TE elements, fabrication and assembly of TE devices, testing and development of proto-type TE model for heat recovery application in the laboratory.

## REFERENCES

- [1] Dough Robbins, “Wealth of Nations”, <http://dougrobbins.blogspot.com/2011/08/wealth-of-nations.html>.
- [2] Gaonosi Lemphole, “Energy Sources, and Power and Transmission” <http://glemphole.blogspot.com/2014/01/energy-sources-power-and-transmission.html>.
- [3] Annual Energy Outlook 2015, “U.S. Energy Information Administration”, [http://www.eia.gov/forecasts/aeo/section\\_elecgeneration.cfm](http://www.eia.gov/forecasts/aeo/section_elecgeneration.cfm).
- [4] Hoffert, Martin I., Ken Caldeira, Gregory Benford, David R. Criswell, Christopher Green, Howard Herzog, Atul K. Jain, Haroon S. Kheshgi, Klaus S. Lackner, John S. Lewis, H. Douglas Lightfoot, Wallace Manheimer, John C. Mankins, Michael E. Mauel, L. John Perkins, Michael E. Schlesinger, Tyler Volk, Tom M. L. Wigley, "Advanced Technology Paths to Global Climate Stability: energy for a greenhouse planet," *Science*, 298, 5595 (2002): 981-987.
- [5] REN21 (2014). "Renewables 2014: Global Status Report" (PDF). 13, 17, 21, 25. ISBN 978-3-9815934-2-6. Archived from the original on 4 September 2014.
- [6] Ellabban, Omar, Haitham Abu-Rub, and FredeBlaabjerg, "Renewable Energy Resources: Current Status, future prospects and their enabling technology, “Renewable and Sustainable Energy Reviews, 39, (2014): 748-764.
- [7] World Energy Outlook 2012, [www.iaea.org](http://www.iaea.org).
- [8] Lawrence Livermore National Lab., U.S. Energy flow: 2013, <https://flowcharts.llnl.gov/>
- [9] Johnson, Ilona, T. William, W. T. Choate, and A. Amber Davidson, "Waste Heat Recovery: Technology and Opportunities in US Industry," US Department of Energy, Office of Energy Efficiency and Renewable Energy, Industrial Technologies Program (2008).
- [10] Seebeck, Thomas Johann, "Magnetische Polarisation der Metalle und Erzedurch Temperatur-Differenz," *Abh. K. Akad. Wiss. Berlin*, 1822, 289 (1821).
- [11] Thomson, William, "On a Mechanical Theory of Thermo-Electric Currents," *Proceedings of the Royal Society of Edinburgh*, 3, (1851): 91-98.

- [12] Nolas, George S., Jeffrey Sharp, and Julian Goldsmid, "Thermoelectrics: Basic Principles and New Materials Developments," 45, Springer Science and Business Media, 2013.
- [13] Peltier, Jean Charles Athanase, "Nouvelles expériences sur la calorificité des courants électriques," In *Annales de Chimie et de Physique*, 56 (1834), 371-386.
- [14] Tritt, Terry M, "Thermoelectric Materials: Principles, Structure, Properties, and Applications," *Encyclopedia of Materials: Science and Technology*, (2002): 1-11.
- [15] Snyder, G. Jeffrey, James R. Lim, Chen-Kuo Huang, and Jean-Pierre Fleurial, "Thermoelectric Microdevice Fabricated by a MEMS-like Electrochemical Process." *Nature Materials*, 2, 8 (2003): 528-531.
- [16] Rowe, D. M, "Thermoelectrics and its Energy Harvesting—Modules, Systems, and Applications in Thermoelectrics, Vol. 1 and 2," (2012).
- [17] Ioffe, A. F., Stil'bans, L. S., Iordanishvili, E. K., and Stavitskaya T. S, "Termoelektricheskoe Okhlazhdenie," U.S.S.R Acad. Sci. Press (1949).
- [18] Rosi, F. D, "Thermoelectricity and Thermoelectric Power Generation," *Solid-State Electronics*, 11, 9 (1968): 833-868.
- [19] Minnich, A, Dresselhaus, M. S, Ren, Z. F, and Chen, G, "Bulk Nanostructured Thermoelectric Materials: Current Research and Future prospects," *Energy and Environmental Science*, 2, 5 (2009): 466-479.
- [20] Tritt, T. M., Böttner, H and Chen, L, "Thermoelectrics: Direct Solar Thermal Energy Conversion," *MRS bulletin*, 33, 4 (2008): 366-368.
- [21] Snyder, G. J, and Toberer, E. S, "Complex Thermoelectric Materials," *Nature Materials*, 7, 2 (2008): 105-114.
- [22] Mott, N. F, and Jones, H, "The Theory of the Properties of Metals and Alloys," Courier Corporation, 1958.
- [23] Schroder, Dieter K, "Semiconductor Material and Device Characterization," John Wiley & Sons, 2006.
- [24] <http://www.sardarsinghsir.com/MSc/MSc%20pdf%20files/Four-Probe-Method.pdf>.
- [25] Noda, Yasutoshi, Hiroyuki Kon, Yoshitaka Furukawa, Isao A. Nishida, and Katashi Masumoto, "Temperature Dependence of Thermoelectric Properties of  $Mg_2Si_{0.6}Ge_{0.4}$ ," *Materials Transactions, JIM*, 33, 9 (1992): 851-855.

- [26] Kim, Hyun-Sik, Zachary M. Gibbs, Yinglu Tang, Heng Wang, and G. Jeffrey Snyder, "Characterization of Lorenz Number with Seebeck Coefficient Measurement," *APL Materials*, 3, 4 (2015): 041506.
- [27] Haynes, William M., "CRC Handbook of Chemistry and Physics," CRC Press, 2016, <http://www.hbcpnetbase.com/>.
- [28] Villars, P., Cenzual, K., Gladyshevskii, R., "Handbook of Inorganic Substances," De Gruyter, 2013, <https://app.knovel.com/web/toc.v/cid:kpHIS0000B/>.
- [29] Pierre Villars, Material Phases Data System (MPDS), CH-6354 Vitznau, Switzerland (ed.) Springer Materials, <http://www.springermaterials.com/docs/index.html>, accessed on 22 October 2014.
- [30] Kim, H. C., T. S. Oh, and D-B. Hyun, "Thermoelectric Properties of the p-type Bi<sub>2</sub>Te<sub>3</sub>-Sb<sub>2</sub>Te<sub>3</sub>-Sb<sub>2</sub>Se<sub>3</sub> Alloys Fabricated by Mechanical Alloying and Hot Pressing," *Journal of Physics and Chemistry of Solids*, 61, 5 (2000): 743-749.
- [31] Gelbstein, Y., O. Ben-Yehuda, E. Pinhas, T. Edrei, Y. Sadia, Z. Dashevsky, and M. P. Dariel, "Thermoelectric Properties of (Pb, Sn, Ge) Te-based Alloys," *Journal of Electronic Materials*, 38, 7 (2009): 1478-1482.
- [32] Katsuyama, S., M. Watanabe, M. Kuroki, T. Maehata, and M. Ito, "Effect of NiSb on the Thermoelectric Properties of Skutterudite CoSb<sub>3</sub>," *Journal of Applied Physics*, 93 (2003): 2758-2764.
- [33] Anno, H., M. Hokazono, M. Kawamura, J. Nagao, and K. Matsubara, "Thermoelectric Properties of Ba<sub>8</sub>Ga<sub>x</sub>Ge<sub>46-x</sub> Clathrate Compounds," In *Thermoelectrics, 2002. Proceedings ICT'02. Twenty-First International Conference on*, 77-80. IEEE, 2002.
- [34] Kurosaki, Ken, Atsuko Kosuga, Hiroaki Muta, Masayoshi Uno, and Shinsuke Yamanaka, "Ag<sub>9</sub>TlTe<sub>5</sub>: a High-performance Thermoelectric Bulk Material with Extremely Low Thermal Conductivity," *Applied Physics Letters*, 87, 6 (2005).
- [35] Caillat, T., J-P. Fleurial, and G. J. Snyder, "Potential of Chevrel Phases for Thermoelectric Applications," *Solid State Sciences*, 1, 7 (1999): 535-544.
- [36] Tayebi, Lobat, Zahra Zamanipour, Masoud Mozafari, Payam Norouzzadeh, Jerzy S. Krasinski, Kenneth F. Ede, and Daryoosh Vashae, "Thermal and Thermoelectric Properties of Nanostructured versus Crystalline SiGe," In *Green Technologies Conference, 2012 IEEE*, 1-4. IEEE, 2012.
- [37] Koumoto, Kunihito, Ichiro Terasaki, and Ryoji Funahashi, "Complex Oxide Materials for Potential Thermoelectric Applications," *MRS Bulletin*, 31, 3 (2006): 206-210.

- [38] Brown, Shawna R., Susan M. Kauzlarich, Franck Gascoin, and G. Jeffrey Snyder, "Yb<sub>14</sub>MnSb<sub>11</sub>: New High Efficiency Thermoelectric Material for Power Generation," *Chemistry of Materials*, 18, 7 (2006): 1873-1877.
- [39] Caillat, Th, J-P. Fleurial, and A. Borshchevsky, "Preparation and Thermoelectric Properties of Semiconducting Zn<sub>4</sub>Sb<sub>3</sub>," *Journal of Physics and Chemistry of Solids*, 58, 7 (1997): 1119-1125.
- [40] Liu, Weishu, Xiao Yan, Gang Chen, and Zhifeng Ren, "Recent Advances in Thermoelectric Nanocomposites," *Nano Energy*, 1, 1 (2012): 42-56.
- [41] Liu, Huili, Xun Shi, Fangfang Xu, Linlin Zhang, Wenqing Zhang, Lidong Chen, Qiang Li, Ctirad Uher, Tristan Day, and G. Jeffrey Snyder, "Copper Ion Liquid-like Thermoelectrics," *Nature Materials*, 11, 5 (2012): 422-425.
- [42] May, Andrew F., Jean-Pierre Fleurial, and G. Jeffrey Snyder, "Thermoelectric Performance of Lanthanum Telluride produced *via* Mechanical Alloying," *Physical Review B*, 78, 12 (2008): 125205.
- [43] Venkatasubramanian, Rama, Edward Siivola, Thomas Colpitts, and Brooks O'quinn, "Thin-film Thermoelectric Devices with High Room-temperature Figures of Merit," *Nature*, 413, 6856 (2001): 597-602.
- [44] Biswas, Kanishka, Jiaqing He, Ivan D. Blum, Chun-I. Wu, Timothy P. Hogan, David N. Seidman, Vinayak P. Dravid, and Mercouri G. Kanatzidis, "High-performance Bulk Thermoelectrics with all-scale Hierarchical Architectures," *Nature*, 489, 7416 (2012): 414-418.
- [45] Blake, Nick P., Susan Lattner, J. Daniel Bryan, Galen D. Stucky, and Horia Metiu, "Band Structures and Thermoelectric Properties of the Clathrates Ba<sub>8</sub>Ga<sub>16</sub>Ge<sub>30</sub>, Sr<sub>8</sub>Ga<sub>16</sub>Ge<sub>30</sub>, Ba<sub>8</sub>Ga<sub>16</sub>Si<sub>30</sub>, and Ba<sub>8</sub>In<sub>16</sub>Sn<sub>30</sub>," *The Journal of Chemical Physics*, 115, 17 (2001): 8060-8073.
- [46] Funahashi, Ryoji, Ichiro Matsubara, Hiroshi Ikuta, Tsunehiro Takeuchi, Uichiro Mizutani, and Satoshi Sodeoka, "An Oxide Single Crystal with High Thermoelectric Performance in Air," *Japanese Journal of Applied Physics*, 39, 11B (2000): L1127.
- [47] Sakurada, S., and N. Shutoh, "Effect of Ti Substitution on the Thermoelectric Properties of (Zr, Hf) NiSn Half-Heusler compounds," *Applied Physics Letters* 86, 8 (2005): 082105.
- [48] Zhao, Li-Dong, Shih-Han Lo, Yongsheng Zhang, Hui Sun, Gangjian Tan, Ctirad Uher, Christopher Wolverton, Vinayak P. Dravid, and Mercouri G. Kanatzidis, "Ultralow Thermal Conductivity and High Thermoelectric Figure of Merit in SnSe crystals," *Nature*, 508, 7496 (2014): 373-377.

- [49] Rogl, G., A. Grytsiv, K. Yubuta, S. Puchegger, E. Bauer, C. Raju, R. C. Mallik, and P. Rogl, "In-doped Multifilled N-type Skutterudites with  $ZT = 1.8$ ," *Acta Materialia*, 95 (2015): 201-211.
- [50] Tritt, Terry M., and M. A. Subramanian, "Thermoelectric Materials, Phenomena, and Applications: A Bird's Eye View," *MRS Bulletin*, 31, 03 (2006): 188-198.
- [51] Chau, K. T., and C. C. Chan, "Emerging Energy-efficient Technologies for Hybrid Electric Vehicles," *Proceedings of the IEEE*, 95, 4 (2007): 821-835.
- [52] Steel manufacture, [http://www.steelconstruction.info/Steel\\_manufacture](http://www.steelconstruction.info/Steel_manufacture).
- [53] EERE, Waste Heat Recovery: Technol. & Opp. in U.S. Industry, [www1.eere.energy.gov/](http://www1.eere.energy.gov/).
- [54] Haxel, G. B., Boore, S., Mayfield, S, "Relative Abundance of Elements in the Earth's Upper Crust," 2003, [https://en.wikipedia.org/wiki/Abundance\\_of\\_elements\\_in\\_Earth%27s\\_crust/](https://en.wikipedia.org/wiki/Abundance_of_elements_in_Earth%27s_crust/).
- [55] Khan, A. U., N. Vlachos, and T. Kyratsi, "High Thermoelectric Figure of Merit of  $Mg_2Si_{0.55}Sn_{0.4}Ge_{0.05}$  Materials Doped with Bi and Sb," *Scripta Materialia*, 69, 8 (2013): 606-609.
- [56] Liu, Wei, Xinfeng Tang, Han Li, Kang Yin, Jeff Sharp, Xiaoyuan Zhou, and Ctirad Uher, "Enhanced Thermoelectric Properties of N-type  $Mg_{2.16}(Si_{0.4}Sn_{0.6})_{1-y}Sb_y$  due to Nano-sized Sn-rich Precipitates and an Optimized Electron Concentration," *Journal of Materials Chemistry*, 22, 27 (2012): 13653-13661.
- [57] Zaitsev, V. K, "Thermoelectric Properties of Anisotropic  $MnSi_{1.75}$ ," *CRC Handbook of Thermoelectrics* (1995): 299-309.
- [58] Joshi, Giri, Hohyun Lee, Yucheng Lan, Xiaowei Wang, Gaohua Zhu, Dezhi Wang, Ryan W. Gould, Diana C. Cuff, Ming Y. Tang, Mildred S. Dresselhaus, Gang Chen, and Zhifeng Ren, "Enhanced Thermoelectric Figure-of-Merit in Nanostructured p-type Silicon Germanium Bulk Alloys," *Nano letters*, 8, 12 (2008): 4670-4674.
- [59] Wang, X. W., H. Lee, Y. C. Lan, G. H. Zhu, G. Joshi, D. Z. Wang, J. Yang, A.J. Muto, M.Y. Tang, J. Klatsky, S. Song, M.S. Dresselhaus, G. Chen, and Z.F. Ren "Enhanced Thermoelectric Figure of Merit in Nanostructured n-type Silicon Germanium Bulk Alloy," *Applied Physics Letters*, 93, 19 (2008): 193121.
- [60] Allred, D. D., C. B. Vining, and G. A. Slack. "Modern Perspectives on Thermoelectrics and Related Materials," Pittsburgh, PA (United States), Materials Research Society, 1991.
- [61] Terasaki, I, "Thermoelectric Materials in Layered Transition-metal Oxides," In *Thermoelectrics, 2005. ICT 2005. 24<sup>th</sup> International Conference on IEEE*, 301-306, 2005.

- [62] Funahashi, Ryoji, and Saori Urata, "Fabrication and Application of an Oxide Thermoelectric System," *International Journal of Applied Ceramic Technology*, 4, 4 (2007): 297-307.
- [63] Takeda, Masatoshi, Tadahiro Fukuda, and Yosuke Kurita, "Thermoelectric Properties of Divalent Hexaborides," In *Thermoelectrics, 2003 Twenty-Second International Conference on-ICT*, 259-262. IEEE, 2003.
- [64] Sussardi, Alif, Takaho Tanaka, A. Ullah Khan, Louis Schlapbach, and Takao Mori, "Enhanced Thermoelectric Properties of Samarium Boride," *Journal of Materiomics*, 1, 3 (2015): 196-204.
- [65] Rowe, David Michael, "CRC Handbook of Thermoelectrics," CRC press, 1995.
- [66] Imai, Yoji, Masakazu Mukaida, Minoru Ueda, and Akio Watanabe, "Screening of the Possible Boron-based N-type Thermoelectric Conversion Materials on the Basis of the Calculated Densities of States of Metal Borides and Doped  $\beta$ -Boron," *Intermetallics*, 9, 8 (2001): 721-734.
- [67] Takeda, Masatoshi, Tadahiro Fukuda, Ferrer Domingo, and Takahiro Miura, "Thermoelectric Properties of Some Metal Borides," *Journal of Solid State Chemistry*, 177, 2 (2004): 471-475.
- [68] Fedorov, M. I., and V. K. Zaitsev, "The Features of Silicide Thermoelectrics Development," In *6th European Conference on Thermoelectrics. Articles Proceeding*. 2008.
- [69] Lange, H, "Electronic Properties of Semiconducting Silicides," *Physica Status Solidi (b)*, 201, 1 (1997): 3-65.
- [70] Ivanenko, L. I., V. L. Shaposhnikov, A. B. Filonov, A. V. Krivosheeva, V. E. Borisenko, D. B. Migas, L. Miglio, G. Behr, and J. Schumann, "Electronic Properties of Semiconducting Silicides: Fundamentals and Recent Predictions," *Thin Solid Films*, 461, 1 (2004): 141-147.
- [71] Zhang, Q., X. B. Zhao, H. Yin, and T. J. Zhu, "Thermoelectric Performance of  $Mg_{2-x}Ca_xSi$  Compounds," *Journal of Alloys and Compounds*, 464, 1 (2008): 9-12.
- [72] Imamura, Yasushi, Hiroaki Muta, Ken Kurosaki, and Shinsuke Yamanaka, "Thermoelectric Properties of Calcium Silicides," In *Thermoelectrics, 2006. ICT'06. 25th International Conference on*, 535-538. IEEE, 2006.
- [73] Maruyama, Satofumi, Yuzuru Miyazaki, Kei Hayashi, Tsuyoshi Kajitani, and Takao Mori, "Excellent P-N Control in a High Temperature Thermoelectric Boride," *Applied Physics Letters*, 101, 15 (2012): 152101.

- [74] Gruen, D. M., P. Bruno, R. Arenal, J. Routbort, D. Singh, and M. Xie, "Thermoelectric Power Factors of Nanocarbon Ensembles as a Function of Temperature," *Journal of Applied Physics*, 105, 7 (2009): 073710.
- [75] Gunjishima, Itaru, Takaya Akashi, and Takashi Goto, "Thermoelectric Properties of Single Crystalline B<sub>4</sub>C Prepared by a Floating Zone Method," *Materials Transactions*, 42, 7 (2001): 1445-1450.
- [76] Werheit, H., R. Schmechel, V. Kueffel, and T. Lundström, "On the Electronic Properties of  $\beta$ -Rhombohedral Boron Interstitially Doped with 3d Transition Metal Atoms," *Journal of Alloys and Compounds*, 262 (1997): 372-380.
- [77] Nakayama, Takahiro, K. Tanaka, J. Shimizu, and K. Kimura, "Thermoelectric Properties of Metal-doped  $\beta$ -Rhombohedral Boron," In *Thermoelectrics, 1998. Proceedings ICT 98. XVII International Conference on*, 570-573. IEEE, 1998.
- [78] Mori, Takao, David Berthebaud, Toshiyuki Nishimura, Akiko Nomura, Toetsu Shishido, and Kazuo Nakajima, "Effect of Zn Doping on Improving Crystal Quality and Thermoelectric Properties of Borosilicides," *Dalton Transactions*, 39, 4 (2010): 1027-1030.
- [79] Mori, T, "Boride Thermoelectrics; High temperature Thermoelectric Materials," *Modules, Systems, and Applications in Thermoelectrics*, CRC Press/Taylor and Francis, London (2012): 14.
- [80] Cahill, David G., Henry E. Fischer, S. K. Watson, R. O. Pohl, and G. A. Slack, "Thermal Properties of Boron and Borides," *Physical Review B*, 40, 5 (1989): 3254.
- [81] Mori, Takao, "Thermal Conductivity of a Rare-Earth B<sub>12</sub>-Icosahedral Compound," *Physica B: Condensed Matter*, 383, 1 (2006): 120-121.
- [82] Slack, Glen A, "The Thermal Conductivity of Nonmetallic Crystals," *Solid State Physics*, 34 (1979): 1-71.
- [83] Takeda, Masatoshi, Manabu Terui, Norihito Takahashi, and Noriyoshi Ueda, "Improvement of Thermoelectric Properties of Alkaline-Earth Hexaborides," *Journal of Solid State Chemistry*, 179, 9 (2006): 2823-2826.
- [84] Rogl, P, "Existence and crystal chemistry of borides," *Inorganic Reactions and Methods: Formation of Bonds to Group-I, -II, and -III B Elements*, Wiley, Volume 13 (1991): 85-98.
- [85] Mori, T, "Handbook on the Physics and Chemistry of Rare Earths," Gschneidner, KA, Jr (2008): 105.

- [86] Kim, Hongki, and Kaoru Kimura, "Vanadium Concentration Dependence of Thermoelectric Properties of  $\beta$ -Rhombohedral Boron Prepared by Spark Plasma Sintering," *Materials Transactions*, 52, 1 (2011): 41-48.
- [87] Hein, Hiltrud, Koepfel, Claus, Vetter, Ursula, and Warkentin. Sc, Y, La-Lu, "Rare Earth Elements: Compounds with Boron," Springer Science and Business Media, 2013.
- [88] Huang, Bo, Yong-Hua Duan, Yong Sun, Ming-Jun Peng, and Shuai Chen, "Electronic Structures, Mechanical and Thermodynamic Properties of Cubic Alkaline-Earth Hexaborides from First Principles Calculations," *Journal of Alloys and Compounds*, 635 (2015): 213-224.
- [89] Wikipedia search of materials, <https://en.wikipedia.org/wiki/>.
- [90] Thermtest, <https://www.thermtest.com/material-property-search>.
- [91] Gürsoy, M., M. Takeda, and B. Albert, "High-pressure Densified Solid Solutions of Alkaline Earth Hexaborides (Ca/Sr, Ca/Ba, Sr/Ba) and their High-temperature Thermoelectric Properties," *Journal of Solid State Chemistry*, 221 (2015): 191-195.
- [92] Samsonov, G. V., Yu B. Paderno, and V. S. Fomenko, "Hexaborides of the Rare-Earth Metals," *Powder Metallurgy and Metal Ceramics*, 2, 6 (1963): 449-454.
- [93] Wang, Weimin, Zhengyi Fu, Hao Wang, and Runzhang Yuan, "Influence of Hot Pressing Sintering Temperature and Time on Microstructure and Mechanical properties of TiB<sub>2</sub> Ceramics," *Journal of the European Ceramic Society*, 22, 7 (2002): 1045-1049.
- [94] Williams, R. K., R. S. Graves, and F. J. Weaver, "Transport Properties of High Purity, Polycrystalline Titanium Diboride," *Journal of Applied Physics*, 59, 5 (1986): 1552-1556.
- [95] Jain, A., Ong, S. P., Hautier, G., Chen, W., Richards, W. D., Dacek, S., Cholia, S., Gunter, D., Skinner, D., Ceder, G., and Persson, K. A, Commentary: The Materials Project: A Materials Genome Approach to Accelerating Materials Innovation. *APL Materials*, 1 (2013), 011002. <https://materialsproject.org/materials/>.
- [96] Feng, Bing, Hans-Peter Martin, and Alexander Michaelis, "In Situ Preparation and Thermoelectric Properties of B<sub>4</sub>C<sub>1-x</sub>-TiB<sub>2</sub> Composites," *Journal of Electronic Materials*, 42, 7 (2013): 2314-2319.
- [97] Cai, K. F., E. Mueller, C. Drasar, and C. Stiewe, "The Effect of Titanium Diboride Addition on the Thermoelectric Properties of  $\beta$ -FeSi<sub>2</sub> Semiconductors," *Solid State Communications*, 131, 5 (2004): 325-329.
- [98] Nikitin, E. N, "Study of Temperature Dependencies of Electrical Conductivity and Thermal Power of Silicides," *Zhurnal Tekhnicheskoy Fiziki*, 28, 23 (1958).

- [99] Fedorov, M. I, "Thermoelectric Silicides: Past, Present and Future," *J Thermoelectr*, 2 (2009): 51-60.
- [100] Fedorov, Mikhail I., and Grigory N. Isachenko, "Silicides: Materials for Thermoelectric Energy Conversion," *Japanese Journal of Applied Physics*, 54, 7S2 (2015): 07JA05.
- [101] Opahle, Ingo, Alessandro Parma, Eunan J. McEniry, Ralf Drautz, and Georg K. H. Madsen, "High-throughput Study of the Structural Stability and Thermoelectric Properties of Transition Metal Silicides," *New Journal of Physics*, 15, 10 (2013): 105010.
- [102] Borisenko, Victor, "Semiconducting Silicides: Basics, Formation, Properties," 39. Springer Science and Business Media, 2013.
- [103] Vining, Cronin B, "Thermoelectric Properties of Silicides," *CRC Handbook of Thermoelectrics* (1995): 277-86.
- [104] Lien, C-D., M. Finetti, M. A. Nicolet, and S. S. Lau, "Electrical Properties of Thin  $\text{Co}_2\text{Si}$ ,  $\text{CoSi}$ , and  $\text{CoSi}_2$  Layers Grown on Evaporated Silicon," *Journal of Electronic Materials*, 13, 1 (1984): 95-105.
- [105] LaBotz, Richard J., and Donald R. Mason, "The Thermal Conductivities of  $\text{Mg}_2\text{Si}$  and  $\text{Mg}_2\text{Ge}$ ," *Journal of The Electrochemical Society*, 110, 2 (1963): 121-126.
- [106] Tani, Jun-ichi, and Hiroyasu Kido, "Thermoelectric Properties of Bi-doped  $\text{Mg}_2\text{Si}$  Semiconductors," *Physica B: Condensed Matter*, 364, 1 (2005): 218-224.
- [107] You, Sin-Wook, Kwan-Ho Park, Il-Ho Kim, Soon-Mok Choi, Won-Seon Seo, and Sun-Uk Kim, "Solid-State Synthesis and Thermoelectric Properties of Al-doped  $\text{Mg}_2\text{Si}$ ," *Journal of Electronic Materials*, 41, 6 (2012): 1675-1679.
- [108] Tani, Jun-ichi, and Hiroyasu Kido, "Thermoelectric Properties of Sb-doped  $\text{Mg}_2\text{Si}$  Semiconductors," *Intermetallics*, 15, 9 (2007): 1202-1207.
- [109] Fan, Wenhao, Ruixue Chen, Liqi Wang, Peide Han, and Qingsen Meng, "First-principles and Experimental Studies of Y-doped  $\text{Mg}_2\text{Si}$  prepared using Field-activated Pressure-assisted Synthesis," *Journal of Electronic Materials*, 40, 5 (2011): 1209-1214.
- [110] Akasaka, Masayasu, Tsutomu Iida, Atsunobu Matsumoto, Kohei Yamanaka, Yoshifumi Takanashi, Tomohiro Imai, and Noriaki Hamada, "The Thermoelectric Properties of Bulk Crystalline N-and P-type  $\text{Mg}_2\text{Si}$  prepared by the Vertical Bridgman Method," *Journal of Applied Physics*, 104, 1 (2008): 013703.
- [111] Higgins, Jeremy M., Andrew L. Schmitt, Ilia A. Guzei, and Song Jin, "Higher Manganese Silicide Nanowires of Nowotny Chimney Ladder Phase," *Journal of the American Chemical Society*, 130, 47 (2008): 16086-16094.

- [112] Zaitsev, V. K., K. A. Rakhimov, and A. E. Engalychev, "Higher Manganese Silicide: Material for Thermoelectric Converters," *Geliotekhnika*, 3 (1983): 15-17.
- [113] Wang, Tao, Divakar Mantha, and Ramana G. Reddy, "Thermodynamic Properties of  $\text{LiNO}_3\text{-NaNO}_3\text{-KNO}_3\text{-2KNO}_3\cdot\text{Mg}(\text{NO}_3)_2$  system," *Thermochim Acta*, 551 (2013): 92-98.
- [114] Wang, T., and R. G. Reddy, "Thermodynamic Properties of Novel Low Melting Point  $\text{LiNO}_3\text{-NaNO}_3\text{-KNO}_3$  Ternary Molten Salt for Parabolic Trough Solar Power Generation," *Energy Technology 2013: Carbon Dioxide Management and Other Technologies* (2013): 1-16.
- [115] Reddy, Ramana G., Tao Wang, and Divakar Mantha, "Thermodynamic Properties of Potassium Nitrate–Magnesium Nitrate compound [ $2\text{KNO}_3\cdot\text{Mg}(\text{NO}_3)_2$ ]," *Thermochimica Acta* 531 (2012): 6-11.
- [116] Zhang, Mingming, Venkat Kamavaram, and Ramana G. Reddy, "Thermodynamic Properties of 1-Butyl-3-Methylimidazolium Chloride ( $\text{C}_4\text{mim}[\text{Cl}]$ ) Ionic Liquid," *Journal of Phase Equilibria and Diffusion*, 26, 2 (2005): 124-130.
- [117] Zhang, M. M., and R. G. Reddy, "Thermodynamic Properties of  $\text{C}_4\text{mim}[\text{Tf}_2\text{N}]$  Ionic Liquids," *Mineral Processing and Extractive Metallurgy*, 119, 2 (2010): 71-76.
- [118] Parida, S. C., and R. G. Reddy, "Thermodynamic Properties of  $\text{CaTiF}_5$  (s)," *The Journal of Chemical Thermodynamics*, 39, 6 (2007): 888-892.
- [119] Kumar, S. G., R. G. Reddy, and L. Brewer, "Phase Equilibria in  $\text{Ti}_3\text{Al-Nb}$  alloys at  $1000^\circ\text{C}$ ," *Journal of Phase Equilibria*, 15, 3 (1994): 279-284.
- [120] Reddy, R. G., A. M. Yahya, and L. Brewer, "Thermodynamic Properties of Ti–Al Intermetallics," *Journal of Alloys and Compounds*, 321, 2 (2001): 223-227.
- [121] George, Pratheesh, S. C. Parida, and Ramana G. Reddy, "Thermodynamic Studies on the System Nb-Al," *Metallurgical and Materials Transactions B*, 38, 1 (2007): 85-91.
- [122] Kattner, Ursula R, "The Thermodynamic Modeling of Multicomponent Phase Equilibria," *JOM*, 49, 12 (1997): 14-19.
- [123] Bogala, Mallikharjuna R., and Ramana G. Reddy, "Phase Stability of Thermoelectric Alkaline Earth Metal Borides and Silicides," *TMS2015 Supplemental Proceedings*: 623-633.
- [124] Morris, Robert Gemmill, R. D. Redin, and G. C. Danielson, "Semiconducting Properties of  $\text{Mg}_2\text{Si}$  Single Crystals," *Physical Review*, 109, 6 (1958): 1909.
- [125] LaBotz, Richard J., Donald R. Mason, and Daniel F. O'Kane, "The Thermoelectric Properties of Mixed Crystals of  $\text{Mg}_2\text{Ge}_x\text{Si}_{1-x}$ ," *Journal of the Electrochemical Society*, 110, 2 (1963): 127-134.

- [126] Kajikawa, Takenobu, Keisuke Shida, Kentaro Shiraishi, Tetsuya Ito, Mamoru Omori, and Toshio Hirai, "Thermoelectric Figure of Merit of Impurity Doped and Hot-pressed Magnesium Silicide Elements," In *Thermoelectrics, 1998. Proceedings ICT 98. XVII International Conference on*, 362-369. IEEE, 1998.
- [127] Zaitsev, V. K., M. I. Fedorov, E. A. Gurieva, I. S. Eremin, P. P. Konstantinov, A. Yu Samunin, and M. V. Vedernikov, "Highly Effective  $Mg_2Si_{1-x}Sn_x$  Thermoelectrics," *Physical Review B*, 74, 4 (2006): 045207.
- [128] Bux, Sabah K., Michael T. Yeung, Eric S. Toberer, G. Jeffrey Snyder, Richard B. Kaner, and Jean-Pierre Fleurial, "Mechanochemical Synthesis and Thermoelectric Properties of High Quality Magnesium Silicide," *Journal of Materials Chemistry*, 21, 33 (2011): 12259-12266.
- [129] Wang, L., X. Y. Qin, W. Xiong, and X. G. Zhu, "Fabrication and Mechanical Properties of Bulk Nanocrystalline Intermetallic  $Mg_2Si$ ," *Materials Science and Engineering: A*, 459, 1 (2007): 216-222.
- [130] Satyala, Nikhil, and Daryoosh Vashaee, "Modeling of Thermoelectric Properties of Magnesium Silicide ( $Mg_2Si$ )," *Journal of Electronic Materials*, 41, 6 (2012): 1785-1791.
- [131] Nakamura, Shigeyuki, Yoshihisa Mori, and Ken'ichi Takarabe, "Analysis of the Microstructure of  $Mg_2Si$  Thermoelectric Devices," *Journal of Electronic Materials*, 43, 6 (2014): 2174-2178.
- [132] Zhang, Qian, Jian He, T. J. Zhu, S. N. Zhang, X. B. Zhao, and Terry M. Tritt, "High Figures of Merit and Natural Nanostructures in  $Mg_2Si_{0.4}Sn_{0.6}$  based Thermoelectric Materials," *Applied Physics Letters*, 93, 10 (2008): 102109.
- [133] Xiong, Wei, Xiao-Ying Qin, and Li Wang, "Preparation and Microstructural Characterization of Nanocrystalline  $Mg_2Si$  Intermetallic Compound Bulk," *Chinese Journal of Nonferrous Metals*, 15, 3 (2005): 380-385.
- [134] Niu, Xiaoping, and Li Lu, "Formation of Magnesium Silicide by Mechanical Alloying," *Advanced Performance Materials*, 4, 3 (1997): 275-283.
- [135] Jiang, Hong-yi, Hai-shan Long, and Lian-meng Zhang, "Effects of Solid-state Reaction Synthesis Processing Parameters on Thermoelectric Properties of  $Mg_2Si$ ," *Journal of Wuhan University of Technology Mater. Sci. Ed.*, 19, 2 (2004): 55-56.
- [136] Tani, Jun-ichi, and Hiroyasu Kido, "Thermoelectric Properties of Sb-doped  $Mg_2Si$  Semiconductors," *Intermetallics*, 15, 9 (2007): 1202-1207.

- [137] Han, Li-qin, Mei-jun Yang, Qiang Shen, and Lian-meng Zhang, "Reaction Sintering of Magnesium Silicide Thermoelectric Material by the Spark Plasma Sintering Technique," *Journal of the Chinese Ceramic Society*, 36, 3 (2008): 337.
- [138] Yoshinaga, M., T. Iida, M. Noda, T. Endo, and Y. Takanashi, "Bulk Crystal Growth of Mg<sub>2</sub>Si by the Vertical Bridgman Method," *Thin Solid Films*, 461, 1 (2004): 86-89.
- [139] Zhou, Shu-Cai, and Chen-Guang Bai, "Microwave Direct Synthesis and Thermoelectric Properties of Mg<sub>2</sub>Si by Solid-state Reaction," *Transactions of Nonferrous Metals Society of China* 21, 8 (2011): 1785-1789.
- [140] Wang, L., and X. Y. Qin, "The Effect of Mechanical Milling on the formation of Nanocrystalline Mg<sub>2</sub>Si through Solid-state Reaction," *Scripta Materialia*, 49, 3 (2003): 243-248.
- [141] Ioannou, M., K. Chrissafis, E. Pavlidou, F. Gascoin, and Th Kyratsi, "Solid-state Synthesis of Mg<sub>2</sub>Si *via* Short-duration Ball-milling and Low-temperature Annealing," *Journal of Solid State Chemistry*, 197 (2013): 172-180.
- [142] Sun, Bin, Shufeng Li, Hisashi Imai, Junko Umeda, and Katsuyoshi Kondoh, "Synthesis Kinetics of Mg<sub>2</sub>Si and Solid-state Formation of Mg–Mg<sub>2</sub>Si Composite," *Powder Technology*, 217 (2012): 157-162.
- [143] Ozawa, Takeo, "Kinetic Analysis of Derivative Curves in Thermal Analysis," *Journal of Thermal Analysis and Calorimetry*, 2, 3 (1970): 301-324.
- [144] Kissinger, Homer E, "Reaction Kinetics in Differential Thermal Analysis," *Analytical Chemistry*, 29, 11 (1957): 1702-1706.
- [145] Coats, A. W., and J. P. Redfern, "Kinetic Parameters from Thermogravimetric Data," (1964): 68-69.
- [146] Dang, Jie, Guo-Hua Zhang, Kuo-Chih Chou, Ramana G. Reddy, Yu He, and Yuanjun Sun, "Kinetics and Mechanism of Hydrogen Reduction of MoO<sub>3</sub> to MoO<sub>2</sub>," *International Journal of Refractory Metals and Hard Materials*, 41 (2013): 216-223.
- [147] Gao, Xiang, and David Dollimore, "The thermal Decomposition of Oxalates: Part 26. A Kinetic Study of the Thermal Decomposition of Manganese (II) Oxalate Dihydrate," *Thermochimica Acta*, 215 (1993): 47-63.
- [148] Niu, Xiaoping, and Li Lu, "Formation of Magnesium Silicide by Mechanical Alloying," *Advanced Performance Materials*, 4, 3 (1997): 275-283.
- [149] Wang, L., and X. Y. Qin, "The Effect of Mechanical Milling on the Formation of Nanocrystalline Mg<sub>2</sub>Si through Solid-State Reaction," *Scripta Materialia*, 49, 3 (2003): 243-248.

- [150] Horvitz, D., L. Klinger, and I. Gotman, "New Approach to Measuring the Activation Energy of Thermal Explosion and its Application to Mg–Si System," *Scripta Materialia*, 50, 5 (2004): 631-634.
- [151] Savary, Etienne, Franck Gascoin, and Sylvain Marinel, "Fast Synthesis of Nanocrystalline Mg<sub>2</sub>Si by Microwave Heating: A New Route to Nano-structured Thermoelectric Materials," *Dalton Transactions*, 39, 45 (2010): 11074-11080.
- [152] Yang, J., and C. Roy, "Using DTA to Quantitatively Determine Enthalpy Change over a Wide Temperature Range by the "Mass-Difference Baseline Method," *Thermochimica Acta*, 333, 2 (1999): 131-140.
- [153] Zhang, Mingming, Venkat Kamavaram, and Ramana G. Reddy, "Thermodynamic Properties of 1-Butyl-3-Methylimidazolium Chloride (C<sub>4</sub>MIm [Cl]) Ionic Liquid," *Journal of Phase Equilibria and Diffusion*, 26, 2 (2005): 124-130.
- [154] Zhang, M. M., and R. G. Reddy, "Thermodynamic Properties of C<sub>4</sub>MIm [Tf<sub>2</sub>N] Ionic Liquids," *Mineral Processing and Extractive Metallurgy*, 119, 2 (2010): 71-76.
- [155] Vold, Marjorie J, "Differential Thermal Analysis," *Analytical Chemistry*, 21, 6 (1949): 683-688.
- [156] Smothers, William Joseph, and Yao Chiang, "Handbook of Differential Thermal Analysis," New York: Chemical Publishing Company, 1966.
- [157] Yang, J., and C. Roy, "A New Method for DTA Measurement of Enthalpy Change during the Pyrolysis of Rubbers," *Thermochimica Acta*, 288, 1 (1996): 155-168.
- [158] Binnewies, M., and Milke, E, "Data Section M, in *Thermochemical Data of Elements and Compounds*," Second, Revised and Extended Edition, Wiley-VCH Verlag GmbH, Weinheim, Germany. (2002):674.
- [159] Gerstein, B. C., F. J. Jelinek, M. Habenschuss, W. D. Shickell, J. R. Mullaly, and P. L. Chung, "Thermal Study of Groups II—IV Semiconductors. Lattice Heat Capacities and Free Energies of Formation. Heat Capacity of Mg<sub>2</sub>Si from 15—300 K," *The Journal of Chemical Physics*, 47, 6 (1967): 2109-2115.
- [160] Ihsan, Barin, "Thermochemical Data of Pure Substances," 934 (1995): 587.
- [161] Outotec HSC Chemistry, Pori, Finland. Available at: <http://www.hsc-chemistry.com>.
- [162] The FactSage system. Available at: <http://www.factsage.com>.
- [163] Alcock, C. B., and Baozhen Li, "A Fluoride-based Composite Electrolyte," *Solid State Ionics*, 39, 3 (1990): 245-249.

- [164] Skelton, W. H., N. J. Magnani, and J. F. Smith, "Thermodynamics of Formation of Th-Ni Alloys," *Metallurgical Transactions*, 1, 7 (1970): 1833-1837.
- [165] Kumar, S. G., R. G. Reddy, and L. Brewer, "Phase Equilibria in Ti<sub>3</sub>Al-Nb Alloys at 1000° C," *Journal of Phase Equilibria*, 15, 3 (1994): 279-284.
- [166] Reddy, R. G., A. M. Yahya, and L. Brewer, "Thermodynamic Properties of Ti-Al Intermetallics," *Journal of Alloys and Compounds*, 321, 2 (2001): 223-227.
- [167] George, Pratheesh, S. C. Parida, and Ramana G. Reddy, "Thermodynamic Studies on the System Nb-Al," *Metallurgical and Materials Transactions B*, 38, 1 (2007): 85-91.
- [168] The Thermo-Calc 2015b. Available at: <http://www.thermocalc.com>.
- [169] Eldridge, J. M., E. Miller, and K. L. Komarek, "Thermodynamic Properties of Liquid Magnesium-Silicon Alloys. Discussion of the Mg-Group IVB Systems," *Aime Met Soc Trans*, 239, 6 (1967): 775-781.
- [170] Geffken, R., and E. Miller, "Phase Diagrams and Thermodynamic Properties of the Mg-Si and Mg-Ge Systems," *Trans Met Soc AIME*, 242, 11 (1968).
- [171] Y.K. Rao, G.R. Belton, N.A. Gokcen, "Chemical Metallurgy: A Tribute to Carl Wagner," *The Metallurgical Society of AIME* (1981):75-96.
- [172] Sryvalin, I. T., O. A. Esin, and B. M. Lepinskikh, "Thermodynamic Properties of Solutions of Magnesium in Nickel, Lead, and Silicon," *Zhurnal Fizicheskoi Khimii*, 38 (1964): 637-641.
- [173] Han, Chao, Zhen Li, and Shixue Dou, "Recent Progress in Thermoelectric Materials," *Chinese Science Bulletin*, 59, 18 (2014): 2073-2091.
- [174] Yang, Haoxing, and Ramana Reddy, "Transport Properties of ABX Type Thermoelectric Alloys," *TMS2015 Supplemental Proceedings*: 601-611.
- [175] Ramachandran, Muralidharan, and Ramana G. Reddy, "Production of Nanoscale Titanium Diboride Powders," *Journal for Manufacturing Science and Production*, 11, 1-3 (2011): 15-22.
- [176] Ramachandran, Muralidharan, and Ramana G. Reddy, "In-Situ Synthesis and Characterization of TiB<sub>2</sub> and Ti-Al-B Composites," In *TMS 2014 143<sup>rd</sup> Annual Meeting & Exhibition, Annual Meeting Supplemental Proceedings*, 57, John Wiley & Sons, 2014.
- [177] ZT-Scanner, Thermoelectric Materials and Technology (TEMTE Inc., Canada), <http://www.temte.ca/ZT-Scan.html>. Accessed on May 2016.

## APPENDIX A

### Lattice Constant:

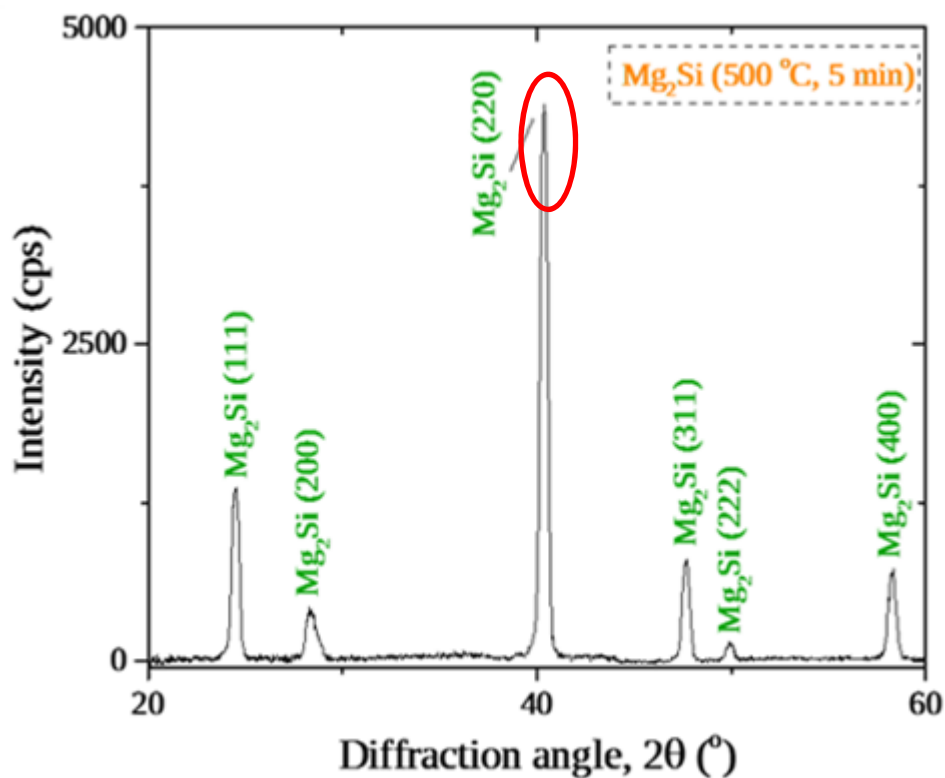


Figure A1: XRD Spectra Mg<sub>2</sub>Si Powder from Sintering at 500 °C for 5 min

In order to calculate the lattice constant of product (Mg<sub>2</sub>Si or Mg<sub>2</sub>Si: mX), we need the XRD spectrum of the sample. Figure A1 provide the XRD spectrum of Mg<sub>2</sub>Si sintered at 500 °C and 5 min. For lattice constant determination, we choose the strongest reflection (220) at 2θ ~ 40° from the XRD spectra. The lattice constant is calculated from equation (A.1) for cubic crystal as:

$$a(\text{\AA}) = d_{hkl}(\text{\AA}) \times (h^2 + k^2 + l^2)^{1/2} = \frac{\lambda}{2 \times \sin(\theta_{hkl})} \times (h^2 + k^2 + l^2)^{1/2} \quad (\text{A.1})$$

The values of (hkl) are obtained from the XRD reflection (220) as h = 2, k = 2, and l = 0.

Upon substituting these values in equation (A.1) we obtain,

$$a(\text{\AA}) = \frac{\lambda}{2 \times \sin(\theta_{hkl})} \times (2 + 2^2 + 0)^{1/2}$$

$$a(\text{\AA}) = \frac{\lambda}{2 \times \sin(\theta_{hkl})} \times 2(2)^{1/2} = \frac{2.8284 \times \lambda}{2 \times \sin(\theta_{hkl})} \quad (\text{A.2})$$

The values of wave length ( $\lambda = 1.54 \text{\AA}$ ) of Cu-K $\alpha$  X-ray radiation, and diffraction angle ( $\theta_{hkl} = \frac{40.6}{2} = 20.3$ ) are substituted in equation (A.2) to give

$$a(\text{\AA}) = \frac{2.8284 \times 1.54 \text{\AA}}{2 \times \sin(20.3)}$$

$$\boxed{a(\text{\AA}) = 6.278 \text{\AA}}$$

## APPENDIX B

### Formation Activation Energy:

To estimate the formation activation energy of  $Mg_2Si$  from elemental powders of Mg and Si as given in equation (B.1), the reaction kinetics  $Mg_2Si$  was studied using the DTA technique.

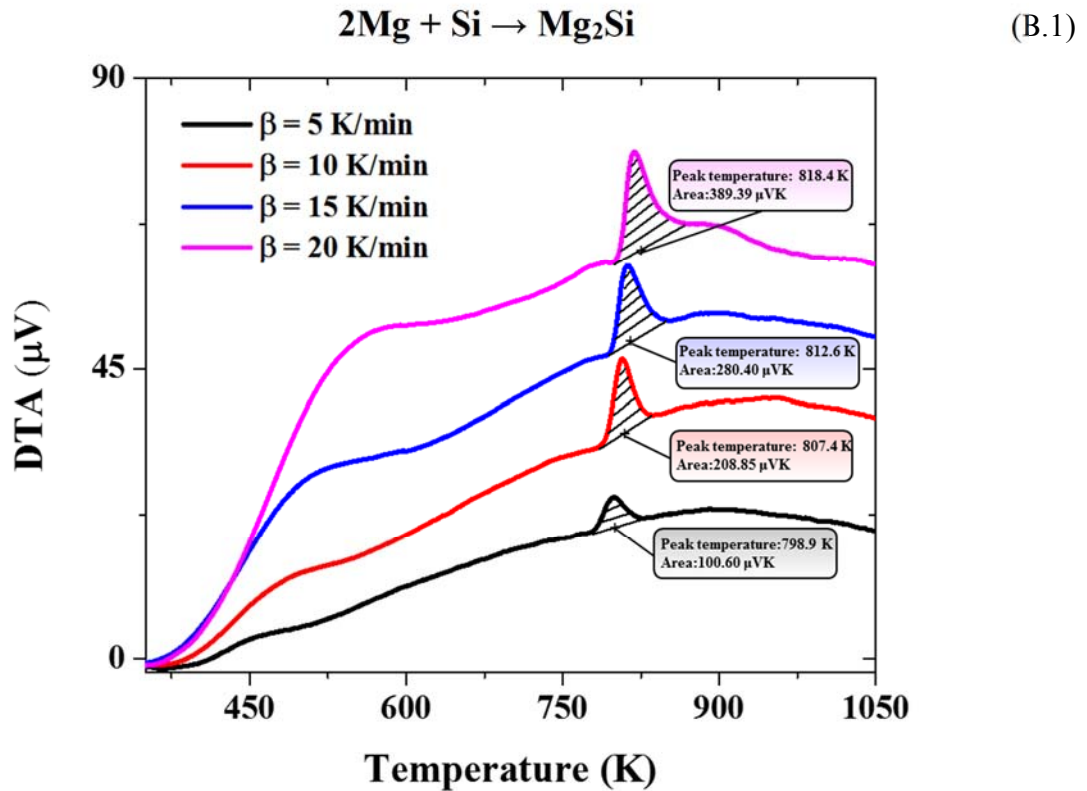


Figure B1: XRD Spectra  $Mg_2Si$  Powder from Sintering at 500 °C for 5 min

As shown in Figure B1, The DTA heat flow curves provide the variation in the temperature for peak maxima at different scan rates ( $\beta = 5, 10, 15,$  and  $20$  K/min). To calculate the activation energy of the solid-state reaction are: (i) Ozawa equation, (ii) Kissinger-Akahira-Sunrose (KAS) and (iii) Coats-Redfern equations are used in current study.

**Ozawa equation:**

$$\ln \beta = \ln \left[ \frac{0.0048 \times A \times E_a}{g(\alpha) \times R} \right] - 1.0516 \frac{E_a}{RT_{max}} \quad (\text{B.2})$$

**KAS equation:**

$$\ln \frac{\beta}{T_{max}^2} = \ln \left[ \frac{A \times E_a}{g(\alpha) \times R} \right] - \frac{E_a}{RT_{max}} \quad (\text{B.3})$$

**CR equation:**

$$\ln \frac{g(\alpha)}{T^2} = \ln \left[ \frac{A \times R}{\beta \times E_a} \right] - \frac{E_a}{RT} \quad (\text{B.4})$$

Table B.1 lists the scan rate and peak temperature used in the study.

$\beta$	$T_{max}(\text{K})$	$\ln \beta$	$\ln \beta / T_{max}^2$
5	798.9	1.60	-11.56
10	807.4	2.30	-10.89
15	812.6	2.70	-10.51
20	818.4	2.99	-10.25

From Table B.1 and using the Ozawa equation (B.2) and KAS equation (B.3), the straight lines were obtained for  $\log (\beta)$  vs  $-1.0516 /RT_{max}$  and  $\ln (\beta/T_{max}^2)$  vs  $1/RT_{max}$  respectively. The slopes of the straight line gives the formation activation energy of reaction (B.1). Ozawa equation plot and KAS equation plot gives activation energy of 196.97 kJ/mol, and 194.87 kJ/mol respectively.

Table B.2 lists the degree of conversion, temperature and conversion function.

<b>T(K)</b>	<b><math>\alpha</math></b>	<b><math>g(\alpha)</math></b>	<b><math>\ln [g(\alpha)/T^2]</math></b>
811.6	0.1	0.0011	-19.91
817.4	0.3	0.0125	-17.69
822.6	0.5	0.0425	-16.55
829.4	0.7	0.1092	-15.66
840.5	0.9	0.2871	-14.78

To obtain activation energy from the CR equation, five degree of conversions ( $\alpha$ ), and conversion function,  $g(\alpha) = [1-(1-\alpha)^{1/3}]^2$  was used for ( $\beta = 20$  K/min) and is listed in the Table B.2. Similar, tables (data not listed) were obtained for other scan rates ( $\beta = 5, 10, \text{ and } 15$ ). The slope of CR equation plot  $\{\ln [g(\alpha)/T^2]\}$  vs  $1/RT$  gives the formation activation energy as 196.01 kJ/mol, which is in good agreement with the formation activation energies (Ozawa, and KAS equations) and reported literature data.

<b><u>Kinetics Method</u></b>	<b><u>Activation Energy</u></b>
<b>Ozawa Equation :</b>	196.97 kJ/mol
<b>KAS Equation:</b>	194.87 kJ/mol
<b>CR Equation:</b>	196.01 kJ/mol

## APPENDIX C

### Thermodynamic Properties:

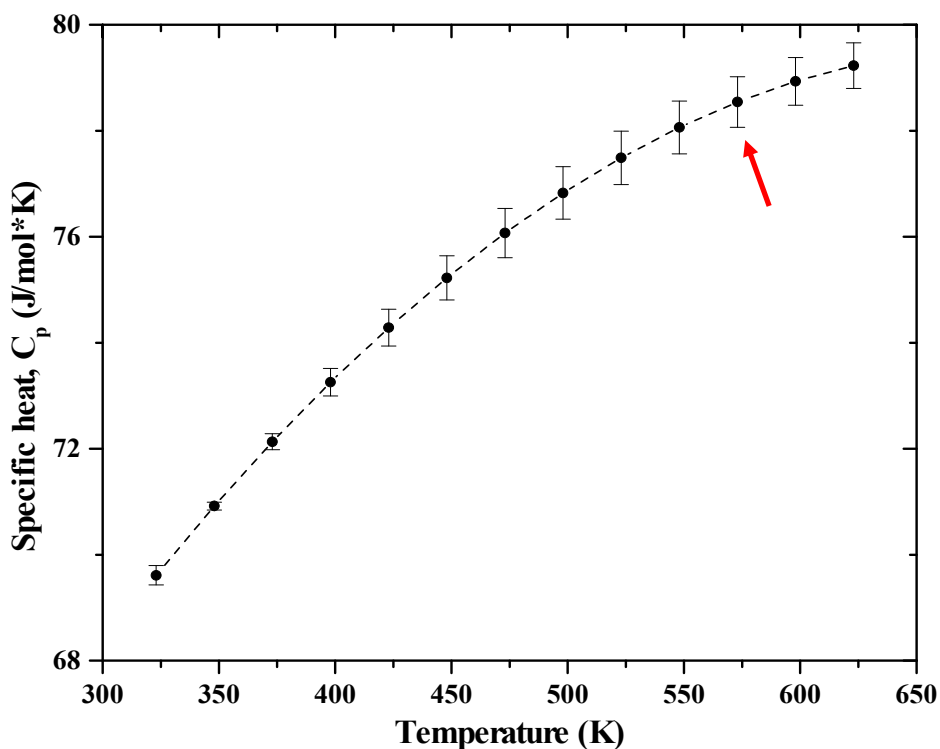


Figure C1 Specific Heat vs  $T$  plot of  $Mg_2Si$  obtained from DSC.

In order to calculate the thermodynamic properties from DSC (*iso-scan-iso*) the specific heat ( $C_p$ ) vs temperature plot of Figure C.1 or Figure 6.19 is considered. The calculations are shown in the following sections for a data point (DSC – red arrow) at the chosen common temperature of  $T = 573.15$  K. Similar calculations on thermodynamic properties of  $Mg_2Si$  can also be performed using the  $C_p(T)$  data from DTA method (not shown in the Appendix C).

**Using DSC method:**

The expression for  $C_p(T)$  is given by equation (C.1) for  $T < 623$  K as:

$$C_p(T), Jmol^{-1}K^{-1} = -0.0001T^2 + 0.1282T + 38.429 \quad (C.1)$$

$$C_p \text{ at } 573 \text{ K} = -0.0001 \times 573^2 + 0.1282 \times 573 + 38.429$$

$$\boxed{C_p(573.15 \text{ K}) = 79.05 \text{ Jmol}^{-1}\text{K}^{-1}}$$

Using  $C_p(T)$ , the change in standard enthalpy of  $Mg_2Si$ ,  $\Delta H^o(T)$  is calculated from equation (C.2) as:

$$\begin{aligned} \Delta H^o(T), Jmol^{-1} &= H_T^o - H_{298.15 \text{ K}}^o = \int_{298.15 \text{ K}}^T C_p(T) dT \\ &= -16272.2 + 38.429 \times T + 0.0641 \times T^2 - 0.00003333 \times T^3 \quad (C.2) \end{aligned}$$

On substituting the  $T$  ( $275 \text{ K} = 573.15 \text{ K} - 298.15 \text{ K}$ ) in equation (C.2), and from  $\Delta_f H^o$  ( $298.15 \text{ K}$ ) =  $-77.80 \text{ kJ/mol}$  for  $Mg_2Si$  (Table 6.7), the  $\Delta H^o(573.15 \text{ K})$  is obtained from equation (C.3) as

$$\Delta H^o = -16272.2 + 38.429 \times 275 + 0.0641 \times 275^2 - 0.00003333 \times 275^3$$

$$\Delta H^o(573 - 298 \text{ K}) = -1.55 \text{ kJmol}^{-1}$$

$$\Delta H^o(573.15 \text{ K}) = \Delta H^o(573.15 - 298.15 \text{ K}) + \Delta H_f^o(298.15 \text{ K}) \quad (C.3)$$

$$= -1.55 \text{ kJmol}^{-1} - 77.80 \text{ kJmol}^{-1}$$

$$\boxed{\Delta H^{\circ}(573.15\text{ K}) = -79.35\text{ kJmol}^{-1}}$$

The change in standard entropy of Mg<sub>2</sub>Si,  $\Delta S^{\circ}(T)$ , is obtained from the equation (C.4) as:

$$\begin{aligned}\Delta S^{\circ}(T), \text{Jmol}^{-1}\text{K}^{-1} &= S_T^{\circ} - S_{298.15\text{ K}}^{\circ} = \int_{298.15\text{ K}}^T [C_p(T)/T] dT \\ &= -252.731 + 0.1282 \times T - 0.00005 \times T^2 + 38.429 \times \log(T) \quad (\text{C.4})\end{aligned}$$

On substituting the T (275 K = 573.15 K – 298.15 K) in C.4, and from  $\Delta_f S^{\circ}$  (298.15 K) = -8.05 J/mol\*K for Mg<sub>2</sub>Si (Table 6.7), the  $\Delta S^{\circ}(573.15\text{ K})$  is obtained from equation C.5 as

$$\Delta S^{\circ} = -252.731 + 0.1282 \times 275 - 0.00005 \times 275^2 + 38.429 \times \log(275)$$

$$\Delta S^{\circ}(573 - 298\text{ K}) = -0.464\text{ Jmol}^{-1}\text{K}^{-1}$$

$$\Delta S^{\circ}(573.15\text{ K}) = \Delta S^{\circ}(573.15 - 298.15\text{ K}) + \Delta S_f^{\circ}(298.15\text{ K}) \quad (\text{C.5})$$

$$= -0.463\text{ Jmol}^{-1}\text{K}^{-1} - 8.05\text{ Jmol}^{-1}\text{K}^{-1}$$

$$\boxed{\Delta S^{\circ}(573.15\text{ K}) = -8.513\text{ Jmol}^{-1}\text{K}^{-1}}$$

From  $\Delta H^{\circ}(573.15\text{ K})$  and  $\Delta S^{\circ}(573.15\text{ K})$  values, the change in standard Gibbs energy of Mg<sub>2</sub>Si,  $\Delta G^{\circ}(573.15\text{ K})$ , is calculated using equation (C.6) as

$$\Delta G^{\circ}(T), \text{Jmol}^{-1} = \Delta H^{\circ}(573.15\text{ K}) - 573.15\text{ K} \times \Delta S^{\circ}(573.15\text{ K}) \quad (\text{C.6})$$

$$= -79.35\text{ kJmol}^{-1} - 573.15\text{ K} \times (-8.513\text{ Jmol}^{-1}\text{K}^{-1})$$

$$\boxed{\Delta G^{\circ}(573.15) = -74.47\text{ kJmol}^{-1}}$$

## APPENDIX D

### EMF Cell Calculations:

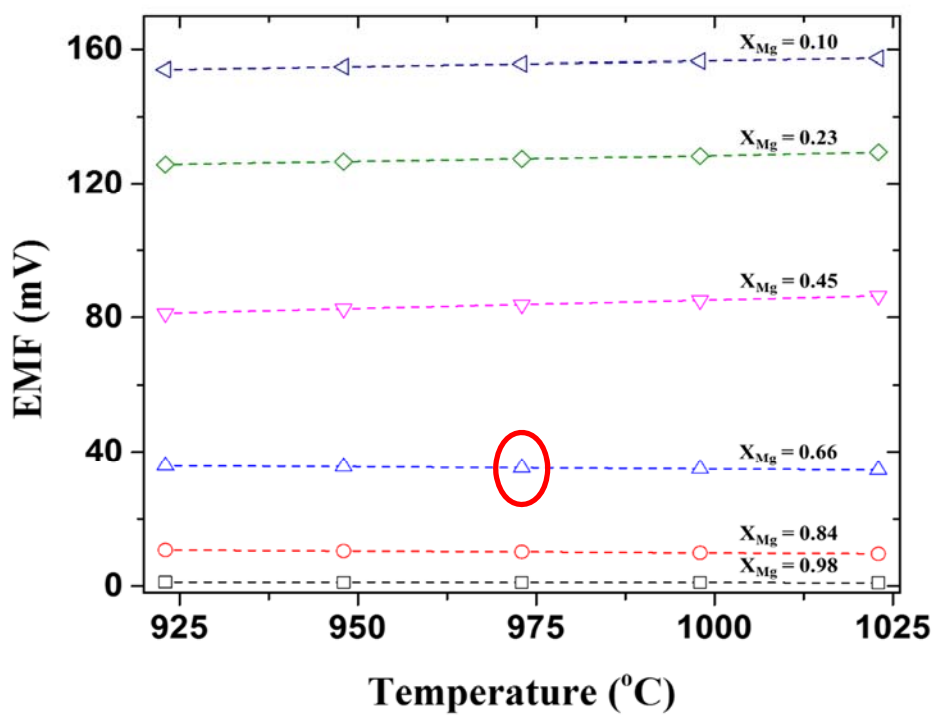


Figure D1: A Plot of EMF vs Temperature for Different Compositions of Mg-Si System

Using solid-state galvanic cell method or EMF cell method, thermodynamic quantities such as activities, activity coefficients, change in enthalpy, change in entropy, and change in Gibbs energy of mixing for Mg-Si system were determined in the current study. As shown in Figure D1, the EMF vs Temperature plot gives straight lines for different alloy composition of  $Mg_xSi_{1-x}$ . In the Appendix D, we focus on calculation of thermodynamic quantities for the highlighted composition at 973 °C.

From the plot, cell EMF for the  $Mg_{0.67}Si_{0.33}$  composition is obtained as 38.94 mV. The partial Gibbs energy of Mg in Mg-Si system can be calculated using equation (D.1) as

$$\Delta\bar{G}_{Mg} = -nFE \quad (D.1)$$

$$\Delta\bar{G}_{Mg} = -2 \times 96845 \text{ J/mol} \times V \times 38.94 \text{ mV}$$

$$\boxed{\Delta\bar{G}_{Mg} = -7.54 \text{ kJ}}$$

The activity of Mg is related to the partial Gibbs energy by equation (D.2) as follows.

$$a_{Mg} = \exp \left[ \frac{\Delta\bar{G}_{Mg}}{RT} \right] \quad (D.2)$$

$$a_{Mg} = \exp \left[ \frac{-7.54 \text{ kJ}}{8.314 \text{ J/mol} \cdot K \times 1246 \text{ K}} \right]$$

$$\boxed{a_{Mg} = 0.432}$$

The activity coefficient of Mg is calculated from the activity of Mg using the following relationship given by equation (D.3) as

$$\gamma_{Mg} = \frac{a_{Mg}}{X_{Mg}} = \frac{0.432}{0.667} \quad (D.3)$$

$$\boxed{\gamma_{Mg} = 0.647}$$

The activity coefficient of Si is calculated from Gibbs –Duhem relation, and is given by equation (D.4) as:

$$\ln \gamma_{Si} = -X_{Mg} \times X_{Si} \times \left[ \frac{\ln \gamma_{Mg}}{X_{Si}^2} \right] - \int_1^{X_{Si}} \left[ \frac{\ln \gamma_{Mg}}{X_{Si}^2} \right] dX_{Si} \quad (D.4)$$

$$\ln \gamma_{Si} = -0.667 \times 0.333 \times \left[ \frac{\ln 0.647}{0.333^2} \right] - \int_1^{0.333} \left[ \frac{\ln \gamma_{Mg}}{X_{Si}^2} \right] dX_{Si}$$

$$\ln \gamma_{Si} = -1.374; \Rightarrow \boxed{\gamma_{Si} = 0.257}$$

The activity of silicon is calculated from the activity coefficient values using the following relationship given by equation (D.5) as

$$a_{Si} = \gamma_{Si} \times X_{Si} \quad (D.5)$$

$$a_{Si} = 0.257 \times 0.333; \Rightarrow \boxed{a_{Si} = 0.0855}$$

The Gibbs energy of mixing ( $\Delta G^M$ ) for [Mg-Si]<sub>alloy</sub> system is given by equation (D.6) as

$$\Delta G^M = RT[X_{Mg} \times \ln a_{Mg} + X_{Si} \times \ln a_{Si}] \quad (D.6)$$

$$\Delta G^M = 8.314 \times 1246 K [0.667 \times \ln 0.432 + 0.333 \times \ln 0.0855]$$

$$\boxed{\Delta G^M = -14.63 \text{ kJ/mol}}$$

The enthalpy of mixing ( $\Delta H^M$ ) was calculated using the  $\Delta G^M(T)$  for the composition in the binary Mg-Si system using the equation (D.7) as:

$$\Delta H^M = \frac{\partial \left( \frac{\Delta G^M}{T} \right)}{\partial \left( \frac{1}{T} \right)} \quad (D.7)$$

$$\boxed{\Delta H^M = -17.47 \text{ kJ/mol}}$$

The entropy of mixing ( $\Delta S^M$ ) of a solution is also related to the enthalpy of mixing ( $\Delta H^M$ ), and the Gibbs energy of mixing ( $\Delta G^M$ ) as given by equation (D.8):

$$\Delta S^M = \frac{\Delta H^M - \Delta G^M}{T} \quad (D.8)$$

$$\Delta S^M = \frac{-17.47 \text{ kJ/mol} + 14.63 \text{ kJ/mol}}{1246 \text{ K}}$$

$$\boxed{\Delta S^M = -2.28 \text{ J/mol} \cdot \text{K}}$$